# Supersymmetry with decoupled scalars and reconstruction and identification of electrons in the ATLAS detector

E. Turlay

LAL 09-37

2009

UNIVERSITÉ PARIS XI
UFR SCIENTIFIQUE D'ORSAY

**THÈSE**

présentée pour l'obtention du titre de

**DOCTEUR EN SCIENCES DE L'UNIVERSITÉ PARIS XI ORSAY**

par

**Emmanuel Turlay**

# Supersymétrie avec scalaires découplés et reconstruction et identification des électrons dans le détecteur ATLAS

Soutenue le 2 avril 2009 devant la commission d'examen composée de

| | |
|---|---|
| Claude Charlot | Rapporteur |
| Marie-Claude Cousinou | |
| Abdelhak Djouadi | Directeur de thèse |
| Ulrich Ellwanger | |
| Giacomo Polesello | Rapporteur |
| Guy Wormser | Président du jury |
| Dirk Zerwas | Directeur de thèse |

# Résumé

Le LHC est un collisionneur de protons avec une énergie de 14 TeV disponible dans le centre de masse, situé au CERN (Genève, Suisse). Les premières collisions sont attendues à l'été 2009. L'expérience ATLAS est, avec CMS, l'une des deux expériences généralistes installées sur le LHC. L'énergie disponible ainsi que la haute luminosité de celui-ci permettra aux expériences ATLAS et CMS de rechercher le boson de Higgs ainsi que d'autres nouvelles particules prédites par les modèles de physique au-delà du modèle standard tels que la supersymétrie.

Les électrons occupent une place importante pour la mesure des paramètres du modèle standard ainsi que la recherche de la nouvelle physique. Ils procurent également de nombreux indicateurs des performances du détecteur, grâce notament à la reconstruction de la désintégration du boson $Z$ en deux électrons, à l'étude du rayonnement de freinage ou de la conversion des photons en paires électron-positron. D'autre part, avec $10^5$ jets hadroniques attendus pour chaque électron, une sévère discrimination du bruit de fond est nécessaire.
Dans cette thèse, la reconstruction et l'identification des électrons dans le détecteur ATLAS est présentée. Un certain nombre de variables sont étudiées pour rejeter le bruit de fond hadronique et électromagnétique tout en optimisant l'efficacité du signal. Les performances d'identification des électrons et de réjection du bruit de fond sont estimés dans un environement de détection potentiellement dévaforable.

La supersymétrie est une extension du modèle standard dans laquelle chaque particule standard de spin $s$ s'associe à une nouvelle particule de spin $|s - \frac{1}{2}|$. La recherche de la supersymétrie est l'un des objectifs primaires de l'expérience ATLAS. Dans cette thèse, les signatures d'un modèle supersymétrique dans lequel les scalaires sont découplés sont étudiés. Le potentiel de découverte est quantifié. Les mesures réalisables, leurs bruits de fonds et leurs incertitudes sont investigués. Ces observables sont ensuite utilisées pour estimer le potentiel de détermination des paramètres du modèle au LHC.

Le modèle standard supersymétrique minimal est le modèle le plus largement utilisé pour étudier la phénoménologie de la supersymétrie au LHC ainsi qu'aux futurs collisionneurs linéaires. Dans cette thèse, la précision sur la détermination de ses paramètres apportée par deux futurs collisioneurs linéaire $e^+e^-$ par rapport au LHC est estimée.

Mots clefs : LHC, ATLAS, supersymétrie, éléctrons, split supersymétrie, détermination des paramètres

# Remerciements

*"Merci!"* - Proverbe ouzbek

Qui l'eût cru? Certainement pas M. Cossavella ou Mme. Seinturier dont la dure tâche d'enseigner la physique au lycée a perdu toute rationalité lors de mon passage sur leur bancs. Je les entend encore : "M. Turlay, vous n'aurez pas votre bac en passant les séances de TP à chercher CANAL+ sur les oscilloscopes!", ou encore "Réduisez votre entropie et fournissez plus de travail!". Good times! Evidemment, c'est toujours trop tard qu'on se rend compte du mérite de ces professeurs et du tort qu'on a pu leur causer. Merci et désolé... le jeu n'en valait-il pas la chandelle? Mais ils ne furent pas les seules victimes du fardeaux de mon éducation. Merci à mes parents dont la clairvoyance et la lucidité m'a épargné de nombreux échecs prévisibles ("Science po? Mais hier tu voulais être ingénieur du son!").

La physique fondamentale est apparue naturellement comme le meilleur moyen d'assouvir ma curiosité dans un environnement sérieux et convivial. Ces adjectifs résument bien l'atmosphère dans laquel j'ai effectué ma thèse au LAL. Ainsi, je remercie Guy Wormser de m'y avoir accueilli pendant trois ans et d'avoir accepté de présider le jury de ma thèse. Je remercie également Giacomo Polesello et Claude Charlot pour leur lecture attentive de mon manuscrit. Leurs commentaires constructifs ont contribué à l'amélioration de ce travail. Je remercie Marie-Claude Cousinou et Ulrich Ellwanger d'avoir accepté de faire partie de mon jury.

Merci à Abdelhak Djouadi pour sa connaissance de la physique du Higgs et de la supersymétrie ainsi que pour sa bonne humeur perpétuelle. Cette thèse n'aurait pas été sans la supervision active de Dirk Zerwas. Sa diplomatie, sa pédagogie, sa rigueur, son professionalisme, sa connaissance encyclopédique de la physique des collisionneurs ainsi que son humour à toute épreuve ont rendu ces trois ans agréables, productifs et très enrichissant. Un merci spécial à Claire Adam Bourdarios pour sa bonne humeur et sa relecture approfondie du manuscrit. La vie au LAL ne serait pas ce qu'elle est sans son équipage. Je remercie Daniel Fournier, Laurent Serin, Laurent Duflot, David Rousseau, RD Schaffer, la Fayard family, Patrick Puzo, Dimitris Varouchas, Caroline Collard, Ilija Ivukotic et les autres.

La thèse est une épreuve épanouissante car elle amène souvent à faire face à ses démons. Cela génère évidemment son lot de doutes, de peur de l'échec, de remises en question, de stress et de junk-food. Tout cela ne serait pas supportable sans des soupapes de sécurité. Merci à Nikola et Christophe O. d'avoir par moment joué le rôle de la

soupape. Merci à Mathieu d'avoir partagé avec moi ce bureau pendant plus de deux ans, et n'oublie pas tes gosses dans ton char!

Ces trois ans n'auraient pas non plus été possibles sans la soupape rock'n'roll. Merci à The League (Florent Mercury, Vincent Clapton, Antoine Chad Smith et Lionel Beefheart) et à Black Northern Beat (Axel et Cyril) d'avoir accepté et supporté ma tyranie.

Merci à la team Camille Vernet (Poncho, David et Christophe G.) pour avoir toujours été dans le coin. Merci également à la Glasgow crew (Francesco, Christian, Diego et Mitja) pour nos meetings annuels. J'espère qu'ils dureront encore longtemps.

Un grand merci aux clans Turlay et Arnaud pour leur soutien et leur affection. Merci à Damien, Maylis, Delphine, Cyril, Maxime, Papeu, Mayoune, Madé, les Laurent, les Gueret, Michel, Marie-Claire, Sonia, Laurent, Eric, Adeline, Tom et Rémi.

Ces dernières lignes sont pour Céline que je remercie d'être là, toujours. Merci pour ton soutien permanent et inconditionnel. *Where would I be without your arms around me?*

# Contents

The Standard Model (SM) of particle physics has reached an unprecedented level of understanding of Nature down to the attometre scale. It beautifully accounts for observed phenomena and predicts the behaviour of physical systems on energy scales spanning from the few electron-volts (eV) of classical physics to the hundred GeV interactions occuring instants after the Big Bang. The SM describes the behaviour of matter under electromagnetic, weak and strong interactions in a mathematically consistent framework based on quantum field theory, local gauge invariance and the Higgs-Englert-Brout mechanism.

The part of the SM describing the electromagnetic and weak nuclear forces, the electroweak model, was established in the sixties in parallel by Glashow [1], Salam [2] and Weinberg [3] after works by Yang and Mills in the fifties [4]. It is the last step in a series of attempts at explaining the behaviour of matter at increasingly lower distance scales, including Maxwell's electromagnetism and Fermi's theory of weak interaction. It leans on a number of theoretical tools such as quantum mechanics and special relativity [5] for the description of dynamics, group theory for the classification of symmetries and the path integral method [6] for the computation of elementary processes. The SM accounts for matter through a number of elementary fermions, quarks and leptons, many of which were well known before its advent. In the leptonic sector, electrons were discovered and their charge and mass measured in 1896. Muons were seen fourty years later in cosmic rays but were initially classified as mesons. Unpredicted, taus were discovered at Stanford Linear Accelerator Center (SLAC, Stanford, USA) in the mid-seventies. The SM does not give any prediction as to the number of generations of fermions, measured to be three by the Large Electron Positron Collider (LEP, CERN, Geneva, Switzerland). The main prediction of the electroweak model is the existence of intermediate vector bosons as interaction carriers. Although the existence of the photon was long known and charged current had already been theorized to explain weak nuclear decays, neutral currents as well as the existence of $W^{\pm}$ and $Z^0$ bosons were postulated by the electroweak theory. Weak neutral currents were first seen in the Gargamelle bubble chamber at CERN in 1973 [7]. The UA1 and UA2 collaborations later produced and measured the masses of the $W$ and $Z$ bosons in $p\overline{p}$ collisions at the SPS (CERN) in 1983 [8, 9]. The currently most accurate determination of the $W$ mass and decay width is the result of a combination of LEP and TeVatron (Fermilab, Chicago, USA) measurements. The mass of the $Z$ boson was also very well measured by LEP. Figure 1 shows the agreement between the measured value of a number of electroweak observables and their value predicted by a global fit. Most measurements lie withing one standard deviation of the predicted values showing an excellent agreement between the SM and experiments.

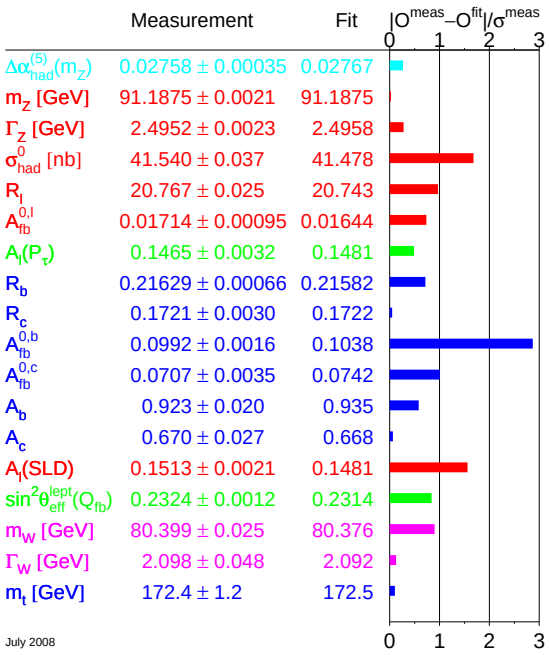


Figure 1: Latest agreements between the predicted values of some electroweak observables and their measurements [10].

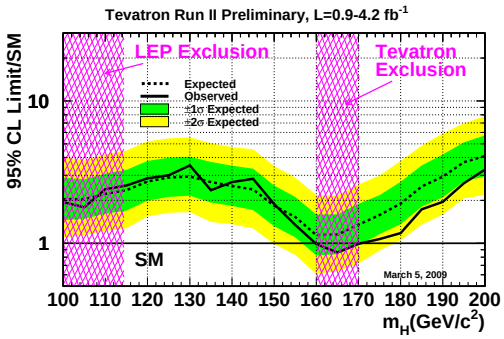


Figure 2: Limits on the production rate of the Higgs boson at TeVatron with respect to the theoretical SM production rate. The pink areas are excluded at 95% C.L. [11].

The strongly interacting sector of the SM was formulated in parallel to the electroweak theory. In the sixties, hadronic physics bloomed as many different states bound by strong interaction were discovered in the recently invented bubble and spark chambers. The classification of these states led to the formulation of the quark model by Gell-Mann [12] and Zweig [13] in 1964. However this model was incomplete as it did not provide any explanation for the existence of states such as the $\Delta^{++}$ that were forbidden by Fermi statistics. In 1965, Han and Nambu [14] and Greenberg [15] independently proposed that quarks should bear an extra degree of freedom, namely a colour charge, allowing them to form specific bound states. The gluon would be the interaction vector for the strong force. In 1968, the first generation of quarks (up and down quarks) were identified as those providing a substructure to the proton as measured at SLAC. In 1970, the Glashow-Iliopoulos-Maiani mechanism gave strong support to the prediction of the existence of a second generation that would include the charm quark. The discovery of the $J/\Psi$ in 1974 at SLAC and Brookhaven National Laboratory (BNL, Brookhaven, USA) demonstrated the existence of the charm. The third generation of quarks (the top and bottom quarks) was predicted in 1973 when Kobayashi and Maskawa noted that a third pair could explain experimental observation of CP violation. The $b$ quark was discovered in 1977 in the $\Upsilon$ resonnances at Fermilab. In 1973, Wilczek, Gross [16] and Politzer [17] found that a consequence of quantum chromodynamics (QCD) was that the strong coupling constant became small at short distances. This paved the way for the application of perturbation theory to QCD and gluons were discovered at the PETRA accelerator (DESY, Hamburg, Ger-

many) in 1979 [18]. The last particle to be discovered tied the knot on the fermionic sector of the SM as it was the last quark of the third generation, the top quark. It was seen in the DØ [19] and CDF [20] experiments at the TeVatron in 1995.

Despite this collection of experimental successes, the SM cannot claim a thorough understanding of Nature. Indeed, three major aspects remain unexplained.

Firstly, the SM is believed to provide mass to elementary particles through the Higgs-Englert-Brout mechanism [21, 22, 23], the main prediction of which is the existence of a new scalar particle, the Higgs boson. Its mass is a free parameter. No experimental indications emerged so far but limits were set. Four experiments searched for the Higgs boson at LEP. No firm evidence for a SM Higgs boson were found but a lower limit on its mass was set to 114.4 GeV with 95% of confidence level [24]. At TeVatron, the DØ and CDF experiments search for the Higgs boson in the gluon fusion channel and in association with a vector bosons. Below a mass of 135 GeV, the dominant decay is to $b\bar{b}$ and $WW^*$ for higher masses. Searches including up to 4.2 fb$^{-1}$ of data have not found any evidence for a SM Higgs. As shown on figure 2, a Higgs boson mass between 160 and 170 GeV was excluded at 95% of confidence level by a combination of results from both experiments [11]. Indirect measurements from SLD, LEP and the Tevatron, favor a light Higgs boson with a mass of $87^{+36}_{-27}$ GeV at 68% C.L. and constrain its mass to be below 182 GeV at 95% C.L. when including the LEP 2 exclusion [25]. A light Higgs boson around 120 GeV would accomodate well with all current bounds and fits. The search for the Higgs boson is one of the main goals of the ATLAS experiment at the Large Hadron Collider (CERN). With 14 TeV available in the center-of-mass, the LHC can produce the Higgs boson if its mass lies within 1 TeV, which corresponds to the theoretical upper bound. It is expected to be produced via gluon or vector boson fusion or in associated production with a vector boson or a $t\bar{t}$ pair. Search channels include its decay into a photon pair, four leptons, tau lepton pairs and $W$ boson pairs. The confirmation of the Higgs mechanism through a discovery of the Higgs boson would be a success but would not tie up the model as it would, if discovered alone, render the electroweak scale unstable through quantum loop corrections. This issue is beautifully addressed by different higher scale extensions to the SM, the most popular of which is supersymmetry.

Secondly, the SM only accounts for 4% of the energy density of the Universe. Observations such as those of the motion of astrophysical objects (stars, gas clouds or galaxies) and of the gravitational lensing effect show that part of this missing energy could be in the form of cold, massive non-baryonic matter, dark matter, interacting only through the weak and gravitational forces. The latest measurement of the density of dark matter in the Universe results from measurements of the Cosmic Microwave Background realized by the WMAP probe [26]. It states that approximately 20% of the energy in the Universe is in the form of dark matter. Candidates for non-baryonic dark matter include primordial black holes, axions but the most favoured candidates are so-called Weakly Interacting Massive Particles (WIMPs). These are expected to be massive in order to interact gravitationally (with massed from a few GeV to a few TeV), neutral to avoid annihilation and colourless. No candidate stands out within the

SM. The most favoured candidate arises in the context of $R$–parity conserving supersymmetry. WIMP are searched for directly through their elastic scattering on nuclei by experiments and indirectly through the increased flux of high-energy neutrinos due to their annihilation in the sun by numerous experiments. No concording results were presented so far.

Finally, observations of type Ia supernovae in the last ten years showed that the Universe is expanding at an increasing rate [27, 28]. This lead to the claim that the remaining 76% of the energy density of the Universe is of unknown kind and tends to pull matter apart, dark energy. Candidates include the addition of a cosmological constant to Einstein's equation or space-time dependent scalar fields, neither of which belong in the SM. Indeed, the description of gravitational interactions lies beyond the scope of the SM. Moreover, the vaccum energy of the only scalar field in the SM, the Higgs boson, is tenth of orders of magnitude larger than that required to account for the observed amount of dark energy. Discovered only ten years ago, dark energy remains a mystery as its theoretical description does not accomodate easily with known physics. The LHC is not expected to provide much experimental input to the problem but new physics it may unravel might provide clues as to the nature of dark energy.

Supersymmetry sprang in the early seventies. It was quickly adapted to weak scale phenomenology and became the most popular extension to the SM as it successfuly adress some of the aforementionned issues. Indeed, supersymmetry predicts the existence of a new particle for each particle of the SM. The fields associated to these new particles allow for a cancellation of divergent loop corrections and stabilizes the electroweak scale. Also, supersymmetry can predict that one of the new particles is stable and weakly interacting. Its mass could account for the dark matter in the Universe. In some supersymmetric models, gauge couplings can be made to unify at the high scale. In addition, supersymmetry accomodates well with a Higgs boson mass in the region favoured by global electroweak fits. The apparition of supersymmetry at the TeV scale is a necessary condition for the resolution of these two problems. Direct searches for supersymmetry were performed by experiments at LEP and TeVatron without success. The current lower limits for the mass of new particles is around 50 GeV for the lightest, 100 GeV for lepton and weak boson partners and 400 GeV for quark partners. With 14 TeV available in the center-of-mass, the LHC can produce supersymmetric particles with masses up to several TeV.

The ATLAS experiment [29] is one of the two general-purpose experiments installed on the LHC accelerator at CERN. The other one is the CMS experiment. The ATLAS detector is a very large multi-component system, set to record the outcome of high-energy proton-proton collisions produced by the LHC. It is now fully installed and all sub-detectors are currently completing or consolidating their commissioning. Collision data are expected to be recorded in 2009. The aim of the ATLAS and CMS experiments is to search for the Higgs boson and possible extensions to the SM such as supersymmetry.

The Standard Model and its most popular extension is presented. I describe the ATLAS detector and present the methods used to reconstruct and identify electrons. The

potential for discovery, measurement and determination of the parameters of a supersymmetric model with decoupled scalars in ATLAS is shown. Eventually, I estimate the gain in precision for the determination of the parameters of a popular supersymmetric model from a multi-TeV linear collider with respect to the LHC and the ILC.

# Chapter 1

# The Standard Model

*"Born a poor young country boy, Mother Nature's son*
*All day long I'm sitting singing songs for everyone"*

Paul McCartney – *Mother Nature's son*

The Standard Model (SM) of particle physics describes matter and its interactions at the elementary scale. It is a Quantum Field Theory (QFT) invariant under the Poincaré group and the $SU(3)_C \times SU(2)_L \times U(1)_Y$ local gauge group. Fermionic fields describe matter, vector fields represent interactions. Electromagnetic and weak interactions are unified and arise through the postulate that laws of motion are invariant under field transformations belonging to the $SU(2)_L \times U(1)_Y$ symmetry group (Special Unitary group of dimension two tensorialy multiplied by the Unitarity group of dimension one). Strong interaction results from the assumption that the model is invariant under field transformations belonging to the $SU(3)_C$ group. Vector bosons stem from the locality of these groups. Mass is provided via the Higgs mechanism.

## 1.1 Symmetries

Fields live in a four dimensional Minkowski space. That is a three space plus one time dimensional space with the metric $ds^2 = dt^2 - \sum_{i=1}^{3} x_i^2$. It is symmetric under the Poincaré group which insures that physics are invariant under translations, rotations and constant motion with respect to any inertial frame. This implies that energy, momentum and angular momentum are conserved.

In addition, laws of motion are invariant under a number of local gauge symmetries. The Lagrangian density for a free mass-less spin half field $\psi$

$$\mathcal{L} = i\overline{\psi}(x)\gamma^\mu \partial_\mu \psi(x),$$

is invariant under the transformation $\psi(x) \rightarrow e^{i\alpha}\psi(x)$. That is a change of phase or a global gauge transformation as $\alpha$ is a free parameter, constant over all space-time.

However, if the transformation is made local, that is $\alpha \rightarrow \alpha(x)$, $\mathcal{L}$ is not invariant anymore :

$$\mathcal{L} \rightarrow \mathcal{L} - \overline{\psi}(x)\psi(x)\gamma^{\mu}\partial_{\mu}\alpha(x) \tag{1.1}$$

This extra term can be avoided by a redefinition of the derivative $\partial_\mu$ to $D_\mu = \partial_\mu - ieA_\mu(x)$ where $D_\mu$ is a covariant derivative and $A_\mu(x)$ is a so–called gauge field. It is a vector field and transforms as $A_\mu(x) \rightarrow A_\mu(x) + \frac{1}{e}\partial_\mu\alpha(x)$, hence cancelling the extra term in equation (1.1). Replacing $\partial_\mu$ by $D_\mu$ in the Lagrangian density gives

$$\mathcal{L} = i\overline{\psi}\gamma^{\mu}\partial_{\mu}\psi + e\overline{\psi}\gamma^{\mu}A_{\mu}\psi,$$

hence generating an interaction term between the spinor field and the gauge field. The concept of local gauge invariance is of major importance for the SM. It states that choosing the symmetries of a physical system predicts its dynamics, or, put differently, nature is not invariant under local gauge transformation unless interactions are present [4]. Thus every interaction in the SM is generated by a specific symmetry, also providing vector gauge boson.

Gauge symmetries are continuous and are classified in Lie groups. These are equipped with infinitesimal generators which set the basis for any transformation within the group. A set of generator is minimal and complete. Their commutator is set by the Lie algebra associated with the group $[T_a, T_b] = if_{abc}T_c$ where $f_{abc}$ is the structure constant characteristic of the group. Space-time transformations that leave physics invariant are all fitted into the Poincaré group which is a Lie group. It is a combination of the translations group $\mathcal{R}^{1,3}$ and the Lorentz group O(1,3).
The transformations that provide the SM with interactions can be fitted into a combination of three local gauge groups : $\mathrm{SU(3)_C}\times\mathrm{SU(2)_L}\times\mathrm{U(1)_Y}$. The subscript indicates the quantum operator on which the transformation operates. C stands for color charge, L for left–handed weak isospin and Y for weak hypercharge. The requirement that the amplitude $\langle\psi|\phi\rangle$ must remain unchanged under the transformation $\phi \rightarrow V\phi$ forces the matrix $V$ to be unitary. The general form of transformations under these groups are the following :

$$\begin{aligned}
\mathrm{U(1)_Y}: &\quad \psi(x) \rightarrow e^{i\alpha Y}\psi(x) \\
\mathrm{SU(2)_L}: &\quad \psi(x) \rightarrow e^{i\theta_i\tau_i/2}\psi(x) \\
\mathrm{SU(3)_C}: &\quad \psi(x) \rightarrow e^{i\rho_j\lambda_j/2}\psi(x)
\end{aligned}$$

where $\alpha$, $\theta_i$ and $\rho_j$ are free space–time dependent parameters. $i$ runs from 1 to 3 and $j$ from 1 to 8. $\tau_i$ are the three Pauli matrices and are a representation of the infinitesimal generators of the group SU(2). $\lambda_j$ are the eight Gell-Mann matrices and are a representation of the infinitesimal generators of the group SU(3). SU($n$) group have $n^2 - 1$ generators which are traceless Hermitian matrices. This combination of symmetry group sets the bosonic field content of the SM as one vector field will be required for each generator in order to keep the Lagrangian density symmetric (see section 1.2). Furthermore, it is the spontaneous breakdown of the $\mathrm{SU(2)_L}\times\mathrm{U(1)_Y}$ group into $\mathrm{U(1)_Q}$, the electromagnetic gauge symmetry, that provides masses for the particles of the SM (see section 1.4).

## 1.2 Field content

In the SM, fields are classified according to their spin. It specifies the role of the field in the model and also the way it transforms under the gauge groups. Matter fields are described by spin half fermions. Interactions are described by vector bosons (spin one). One extra boson emerges as the result of the spontaneous breaking of the electroweak symmetry. That is the Higgs-Englert-Brout scalar boson (spin zero). These fields are coupled as allowed by the gauge symmetries and their quantum numbers.

Fermions are ordered into three families. Each of these contains one left-handed lepton doublet, one left-handed quark doublet, one right-handed charged lepton singlet and two right-handed quark singlet. Singlets and doublets refer to their behaviour under $\mathrm{SU(2)_L}$. Left and right-handedness refers to the helicity of the field, that is the projection of its spin along its momentum.

$$\begin{array}{ccc} \begin{pmatrix} \nu_e \\ e \end{pmatrix}_{\mathrm{L}} & \begin{pmatrix} \nu_\mu \\ \mu \end{pmatrix}_{\mathrm{L}} & \begin{pmatrix} \nu_\tau \\ \tau \end{pmatrix}_{\mathrm{L}} \\ e_{\mathrm{R}} & \mu_{\mathrm{R}} & \tau_{\mathrm{R}} \\ \begin{pmatrix} u^i \\ d^i \end{pmatrix}_{\mathrm{L}} & \begin{pmatrix} c^i \\ s^i \end{pmatrix}_{\mathrm{L}} & \begin{pmatrix} t^i \\ b^i \end{pmatrix}_{\mathrm{L}} \\ u^i_{\mathrm{R}} & c^i_{\mathrm{R}} & t^i_{\mathrm{R}} \\ d^i_{\mathrm{R}} & s^i_{\mathrm{R}} & b^i_{\mathrm{R}} \end{array} \tag{1.2}$$

Expression (1.2) displays the three families of fermions in order of increasing mass. The first, the lighter, contains the electron, its associated neutrino, up and down quarks. The second contains the muon, its neutrino, charm and strange quarks and the last is made of the tau, its neutrino, the top and bottom quarks. There are no right-handed neutrinos. Doublets have helicity one half while singlets have zero. Quark fields bear colour indices $i = 1...3$ as they are $\mathrm{SU(3)_C}$ triplets while leptons $\ell$ and $\nu_\ell$ transform as singlet.

One vector boson is needed for each generator of the three gauge group.

$$\begin{array}{cc} \mathrm{SU(3)_C} & G^a_\mu,\ a = 1...8 \\ \mathrm{SU(2)_L} & W^i_\mu,\ i = 1...3 \\ \mathrm{U(1)_Y} & B_\mu \end{array}$$

$\mathrm{SU(3)_C}$ generates eight neutral gluons. $\mathrm{SU(2)_L}$ generates three gauge fields $W^i_\mu$, the third of which is neutral. $\mathrm{U(1)_Y}$ generates one neutral gauge field $B_\mu$.
The Lagrangian density for the SM is

$$\mathcal{L}_{\mathrm{SM}} = \mathcal{L}_{\mathrm{dyn}} + \mathcal{L}_G + \mathcal{L}_{\mathrm{mass}}.$$

$\mathcal{L}_{\mathrm{dyn}}$ describes the dynamics of the model. It includes kinetic terms for fermions as well as coupling terms.

$$\mathcal{L}_{\mathrm{dyn}} = i\overline{f}_\kappa \gamma^\mu D_\mu f_\kappa,$$

where $\kappa$ should be summed over all singlets and doublets listed in (1.2). The covariant derivative $D_\mu$ is

$$\begin{aligned} D_\mu &= \partial_\mu + ig_1 T^k W_\mu^k + ig_2 \frac{Y}{2} B_\mu + ig_3 \Theta^a G_\mu^a \\ &= \partial_\mu + ieQA_\mu + \frac{ie}{\sin\theta_W \cos\theta_W}(T^3 - \sin^2\theta_W Q) Z_\mu \\ &\quad + \frac{ie}{\sqrt{2}\sin\theta_W} \tau^1 (W_\mu^-, W_\mu^+)^T + ig_3 \Theta^a G_\mu^a \end{aligned}$$

where $g_1$, $g_2$ and $g_3$ are the $\mathrm{U(1)_Y}$, $\mathrm{SU(2)_L}$ and $\mathrm{SU(3)_C}$ coupling constants. The following definitions

$$\begin{aligned} T^k &= \frac{\tau^k}{2}, k = 1...3 \\ \Theta^a &= \frac{\lambda^a}{2}, a = 1...8 \\ e &= g_1 \cos\theta_W = g_2 \sin\theta_W = \frac{g_1 g_2}{\sqrt{g_1^2 + g_2^2}} \\ Q &= T^3 + \frac{Y}{2} \end{aligned}$$

and the following field redefinitions

$$\begin{aligned} A_\mu &= \frac{1}{\sqrt{g_1^2 + g_2^2}}(g_2 W_\mu^3 + g_1 B_\mu) \\ Z_\mu &= \frac{1}{\sqrt{g_1^2 + g_2^2}}(g_2 W_\mu^3 - g_1 B_\mu) \\ W_\mu^\pm &= \frac{1}{2}(W_\mu^1 \mp i W_\mu^2). \end{aligned}$$

are applied in order to display mass eigenstates $A_\mu$, $Z_\mu$ and $W_\mu^\pm$. They correspond to the photon, $Z^0$ and $W^\pm$ bosons. $Q$ is the electric charge operator and $e$ the elementary electric charge. $\theta_W$ is the Weinberg mixing angle. Once $\kappa$ has been summed over, $D_\mu$ developed and fields redefined, the remaining terms are the following

$$\begin{aligned} \mathcal{L}_{\mathrm{dyn}} &= i\overline{\nu}\gamma^\mu \partial_\mu \nu + i\overline{\ell}\gamma^\mu \partial_\mu \ell + i\overline{u}\gamma^\mu \partial_\mu u + i\overline{d}\gamma^\mu \partial_\mu d \\ &\quad - eA_\mu \left( -\overline{\ell}\gamma^\mu \ell + \frac{2}{3}\overline{u}\gamma^\mu u - \frac{1}{3}\overline{d}\gamma^\mu d \right) \\ &\quad - \frac{e}{2 s_W c_W} Z_\mu \left[ \overline{\nu}_{\mathrm{L}} \gamma^\mu \nu_{\mathrm{L}} + \overline{\ell}\gamma^\mu \left( 2s_W^2 - \frac{1+\gamma^5}{2} \right) \ell \right] \\ &\quad - \frac{e}{2 s_W c_W} Z_\mu \left[ \overline{u}\gamma^\mu (\frac{2}{3} s_W^2 - \frac{1+\gamma^5}{2}) u + \overline{d}\gamma^\mu \left( \frac{1-\gamma^5}{2} - \frac{4}{3} s_W^2 \right) d \right] \\ &\quad - \frac{e}{\sqrt{2} s_W} \left( \overline{\nu}_{\mathrm{L}} \gamma^\mu W_\mu^+ \ell_{\mathrm{L}} + \overline{\ell}_{\mathrm{L}} \gamma^\mu W_\mu^- \nu_{\mathrm{L}} + \overline{u}_{\mathrm{L}} \gamma^\mu W_\mu^+ d_{\mathrm{L}} + \overline{d}_{\mathrm{L}} \gamma^\mu W_\mu^- u_{\mathrm{L}} \right) \\ &\quad - g_3 G_\mu^a \left( \overline{u}_i \gamma^\mu T_{ij}^a u_j + \overline{d}_i \gamma^\mu T_{ij}^a d_j \right) \end{aligned}$$

where leptons and quarks fields are summed over the three generations. The first line contains kinetic terms while the second describes electromagnetic interactions. The third and fourth lines describes weak interactions and the last stands for strong interactions.

$\mathcal{L}_G$ contains the kinetic and self–interaction terms for the gauge bosons :

$$\mathcal{L}_G = -\frac{1}{4}\left(B_{\mu\nu}B^{\mu\nu} + W^i_{\mu\nu}W^{\mu\nu}_j + G^a_{\mu\nu}G^{\mu\nu}_a\right)$$

where

$$\begin{aligned} B_{\mu\nu} &= \partial_\mu B_\nu - \partial_\nu B_\mu \\ W^i_{\mu\nu} &= \partial_\mu W^i_\nu - \partial_\nu W^i_\mu + i g_2 \epsilon^{ijk} W^j_\mu W^k_\nu \\ G^a_{\mu\nu} &= \partial_\mu G^a_\nu - \partial_\nu G^a_\mu - g_3 f^{abc} G^b_\mu G^c_\nu \end{aligned}$$

are the strength tensors of the gauge fields. $\epsilon^{ijk}$ and $f^{abc}$ are the SU(2) and SU(3) structure constants. They describe the Lie algebra of the group. The last term in $W^i_{\mu\nu}$ and $G^a_{\mu\nu}$ provide self–coupling terms. The terms proportional to $gX^3$ are three legged self–interaction vertices and the $g^2X^4$ terms are four legged vertices. The absence of a third term in $B_{\mu\nu}$ means that the only self–coupling terms in the electroweak sector will be of the form $ZWW$, $AWW$, $WWWW$, $ZZWW$, $AAWW$ and $AZWW$. Only QCD allows a term of the form $GGG$.

## 1.3 Renormalizability

The problem of renormalization arises in the context of perturbation theory. Indeed, the quantities of interest in fundamental physics such as scattering amplitude, masses, couplings, etc... are all computed as expansions in orders of the coupling constants

$$\mathcal{M} = \sum_{i=0}^{\infty} g^i M_i \tag{1.3}$$

where $M_i$ is the contribution to $\mathcal{M}$ bearing $i$ vertices. Individual contributions $M_i$'s can diverge. For instance, in a diagram featuring a loop

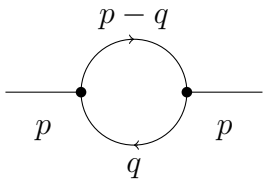


the momentum $q$ is not bounded and must therefore be integrated over from 0 to infinity. Divergences then arise in the case of 2-, 3- and 4-point functions. Such divergences in individual amplitudes are cancelled out by higher order contributions. This however becomes an issue when $\mathcal{M}$ is approximated to the first few orders in perturbation

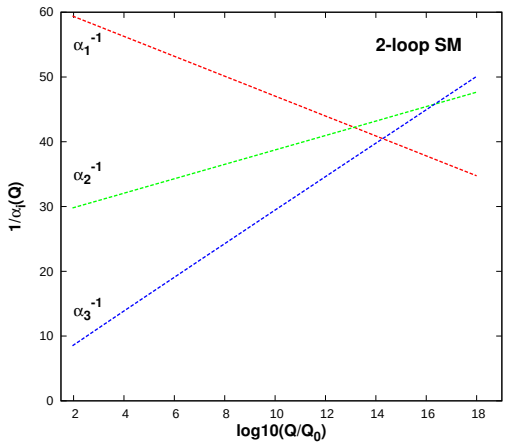


Figure 1.1: Running of the SM gauge couplings as a function of the renormalization scale $Q$ for $Q_0 = m_Z$.

theory. The solution is to rewrite $\mathcal{M}$ in terms of *effective* renormalized parameters (mass, couplings, ...) at the specific scale $\mu$ of the interaction instead of the *bare* non-renormalized quantities. The remaining contributions including divergences are canceled by higher-order so-called counter-terms. A model is said to be renormalizable if, at any order $n$ in perturbation theory, divergences can be isolated and canceled in counter-terms of order $n+1$. This is only possible in theories featuring systematic structured divergences, orders after orders. Effective renormalized parameters incorporate higher-order contributions with respect to bare parameters. The magnitude of these contributions varies with the chosen renormalization scale. Figure 1.1 shows the value of the renormalized coupling constants of the SM as a function of the renormalization scale. The slope of the evolution of couplings is related to the sign of the so-called $\beta$ functions which incorporate higher-orders corrections. The non-Abelian nature of QCD allows for three-legged gluon self-coupling terms. These contribute to a negative $\beta$ function, pulling the QCD coupling constant to lower values as the energy scale increase. The three gauge couplings do not unify at high scale. However, unification can be achieved in the framework of supersymmetry, see section 2.2.2.

It was shown [30] that the electroweak part of the Standard Model is renormalizable. One condition for that is the existence of a neutral scalar boson coupling to weak vector bosons. Indeed, the amplitude for the elastic scattering of $W$ bosons is divergent unless a graph with an intermediate scalar boson such as the Higgs boson is introduced.

## 1.4 The Higgs boson

Given the way vector field transform under gauge transformation, mass terms of the form $\frac{1}{2}m^2 Z_\mu Z^\mu$ would violate gauge invariance. Similarly, a mass term for fermions

of the form $m\overline{f}f = m(\overline{f}_{\rm R}f_{\rm L} + \overline{f}_{\rm L}f_{\rm R})$ breaks gauge invariance as $f_{\rm R}$ is part of a weak isospin single whereas $f_{\rm L}$ is part of a doublet.
In the SM, fermions and bosons masses are generated by the Higgs-Englert-Brout mechanism [21, 22, 23], that is a spontaneous breakdown of the gauge symmetry. The by product of such a mechanism is a new scalar field, the Higgs boson. The idea is to generate masses through a coupling to a scalar field whose vacuum expectation value is non-zero. The following terms are added to the Lagrangian density

$$\begin{aligned}\mathcal{L}_{\rm mass} = |D_\mu\phi|^2 - V(\phi) \quad &- \quad y_\ell \left[\overline{\ell}_{\rm R}\phi^\dagger(\nu,\ell)^T_{\rm L} + (\nu,\ell)_{\rm L}\phi\ell_{\rm R}\right] \\ &- \quad y_u \left[\overline{u}_{\rm R}\epsilon\phi(u,d)^T_{\rm L} + (\overline{u},\overline{d})_{\rm L}\epsilon\phi^\dagger u_{\rm R}\right] \\ &- \quad y_d \left[\overline{d}_{\rm R}\phi^\dagger(u,d)^T_{\rm L} + (\overline{u},\overline{d})_{\rm L}\phi d_{\rm R}\right]\end{aligned} \tag{1.4}$$

where leptons and quarks are summed over the three families. $\epsilon$ is an antisymmetric matrix and $\phi$ is a complex scalar doublet

$$\phi = \begin{pmatrix} \phi^+ \\ \phi^0 \end{pmatrix} = \frac{1}{\sqrt{2}} \begin{pmatrix} \phi_1 + i\phi_2 \\ \phi_3 + i\phi_4 \end{pmatrix}$$

and $V(\phi)$ is the scalar potential. Yukawa couplings $y$ link fermions and the scalar field together.
In order to break gauge symmetry, the scalar potential must be written

$$V(\phi) = -\mu^2\phi^\dagger\phi + \lambda(\phi^\dagger\phi)^2 \tag{1.5}$$

where $\mu$ and $\lambda$ are positive free parameters. The minus sign before the $\mu^2$ term ensures the spontaneous breakdown since it forces $\phi$ to take a non-vanishing vacuum expectation value. $V(\phi)$ is minimal for $\frac{1}{2}(\phi_1^2 + \phi_2^2 + \phi_3^2 + \phi_4^2) = \mu^2/2\lambda$. Any choice along this four-sphere will break the gauge symmetry. Choosing $\phi_1 = \phi_2 = \phi_4 = 0$, the ground state of the scalar field is

$$\langle\phi\rangle = \begin{pmatrix} 0 \\ \frac{\mu}{\sqrt{2\lambda}} \end{pmatrix} = \begin{pmatrix} 0 \\ v \end{pmatrix}$$

This choice breaks both $\mathrm{SU(2)_L}$ and $\mathrm{U(1)_Y}$ but not $\mathrm{U(1)_Q}$ as $\rho_0$ is neutral. Hence, the photon will remain mass-less whereas weak gauge bosons will acquire mass. Similarly, $\phi$ does not carry any colour charge : gluons will also remain mass-less. From there, weak gauge bosons will become massive through the development of the $D_\mu\phi$ term while fermions become massive through the Yukawa terms. The scalar boson field has weak hypercharge $Y = 1$ and weak isospin $T = \frac{1}{2}$ so that

$$\begin{aligned}|D_\mu\langle\phi\rangle|^2 &= \left|\left(-i\frac{g_1}{2}B_\mu - i\frac{g_2}{2}\tau^a W^a_\mu\right)\begin{pmatrix} 0 \\ v \end{pmatrix}\right|^2 \\ &= \frac{1}{2}\left(\frac{1}{2}vg_2\right)^2 W^+_\mu W^{-\mu} + \frac{1}{2}\left(\frac{1}{2}v\sqrt{g_1^2+g_2^2}\right)^2 Z_\mu Z^\mu\end{aligned}$$

The masses of the weak gauge bosons can be identified as

$$m_W = \frac{1}{2}vg_2 \qquad \text{and} \qquad m_Z = \frac{1}{2}v\sqrt{g_1^2+g_2^2} \qquad \text{so that} \qquad \frac{m_W}{m_Z} = \cos\theta_W.$$

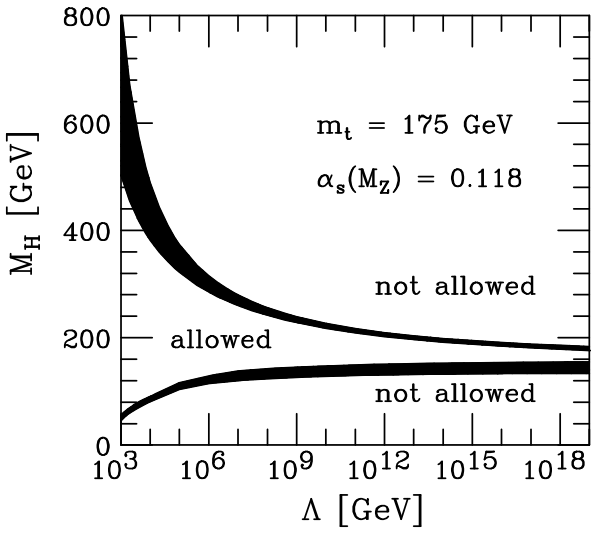


Figure 1.2: Theoretical bounds on the Higgs boson mass as a function of the ultra-violet cut-off $\Lambda$ [31].

The fermions masses can be identified upon replacement of $\phi$ by its ground state in the Yukawa terms

$$m_f = y_f v.$$

The two charged components $\phi_1$ and $\phi_2$ of $\phi$ are absorbed as a longitudinal polarization component by the $W_\mu$ field and the neutral $\phi_4$ is absorbed by the $Z_\mu$ field. The $\phi_3$ component can be expended around its minimum

$$\phi = \begin{pmatrix} 0 \\ v + \frac{h}{\sqrt{2}} \end{pmatrix}.$$

Plugging this expansion in the potential $V(\phi)$ yields

$$V(\phi) = -\frac{1}{2}v^2\lambda h^2 - \lambda v h^3 - \frac{\lambda}{4}h^4.$$

The first term gives the Higgs mass and the last two terms provide the three and four legged self-interaction coupling terms. The Higgs mass being

$$m_h^2 = v^2\lambda.$$

The vacuum expectation value of the Higgs field can be estimated through a measurement of electroweak bosons mass and couplings. However $\lambda$, or $m_h$, remains a free parameter of the model. Constraints arise from a number of theoretical considerations. For instance, the production rate of the elastic diffusion of longitudinal $W$'s, $W_L^+W_L^- \to W_L^+W_L^-$, without an intermediate Higgs boson diverges like $s$, the center-of-mass energy of the scattering, which violates unitarity. The latter can be restored if the mass of the Higgs boson satisfies [32, 33]

$$m_h < \left(\frac{8\pi\sqrt{2}}{3G_F}\right)^{1/2} \sim 1 \text{ TeV}$$

where $G_F$ is the Fermi constant.
Furthermore, the Higgs self-coupling $\lambda$ appearing in the Higgs potential (1.5) diverges for large values of the renormalization scale $q^2$. Requiring that $\lambda(\Lambda)$ be finite for some ultra-violet cut-off $\Lambda$ results in the following upper bound on the mass of the Higgs boson

$$m_h^2 = \lambda(v^2)v^2 = \sqrt{2}\frac{\lambda(v^2)}{G_F} < \frac{4\sqrt{2}\pi^2}{3G_F \ln \Lambda^2/v^2}$$

where $\Lambda$ is the ultra-violet cut-off of the theory. Figure 1.2 shows the allowed values of the Higgs boson mass as a function of the cut-off scale. If the SM is to be valid up to the Planck scale, the limit translates into an upper bound of about 180 GeV for the Higgs boson mass. If however new physics are to enter at, e.g., the TeV scale, the Higgs boson mass should be lower than about 750 GeV.
On the other hand, when $q^2$ goes to zero, $\lambda(q^2)$ can become negative due to the contribution from the top quark giving rise to a new minimum in the Higgs potential [34, 35]. Requiring $\lambda(q^2)$ to remain positive gives a lower bound on $\lambda(v^2)$ yielding

$$m_h^2 > \frac{v^2}{8\pi^2}\left[-12\frac{m_t^4}{v^4} + \frac{3}{16}\left(2g_2^4 + (g_2^2 + g_1^2)^2\right)\right]\ln\frac{q^2}{v^2}.$$

If the SM is to be valid up to the Planck scale, the Higgs boson should be heavier than around 130 GeV. If however new physics come into play around the TeV scale, this lower bound drops to around 70 GeV.
Figure 1.2 shows the upper and lower theoretical bounds on the Higgs boson mass as a function of $\Lambda$.

## 1.5 Quark flavours

Yukawa coupling matrices $y_u$ and $y_d$ in equation (1.4) have no reason to be diagonal. Hence, quark mass eigenstates are different from their gauge eigenstates. Since neutrinos are mass-less in the SM, the matrix $y_\ell$ can always be made diagonal and leptons mass eigenstates are identical to their gauge eigenstates. In order to have diagonal mass matrix for quarks, one should rotate the quark fields in the following fashion

$$u'^i_{\mathrm{L/R}} = U^{ij}_{\mathrm{L/R}} u^i_{\mathrm{L/R}} \qquad d'^i_{\mathrm{L/R}} = D^{ij}_{\mathrm{L/R}} d^i_{\mathrm{L/R}}$$

where $i$ and $j$ run over generations. Consequently, the actual mass terms for the quark fields are

$$\mathcal{L}^q_{\mathrm{mass}} = -y_d v(\overline{d}_L D_L^\dagger D_R d_R + \overline{d}_R D_R^\dagger D_L d_L) - y_u v(\overline{u}_L U_L^\dagger U_R u_R + \overline{u}_R U_R^\dagger U_L u_L)$$

rather than the one mentioned in 1.4. Similarly, the coupling term between quark fields and the $W^\pm_\mu$ fields reshapes as

$$\mathcal{L}^{qW}_{\mathrm{dyn}} = -\frac{e}{\sqrt{2}s_W} u^i_L V^{ij} W^+_\mu d^j_L + \text{Hermitian conjugate}$$

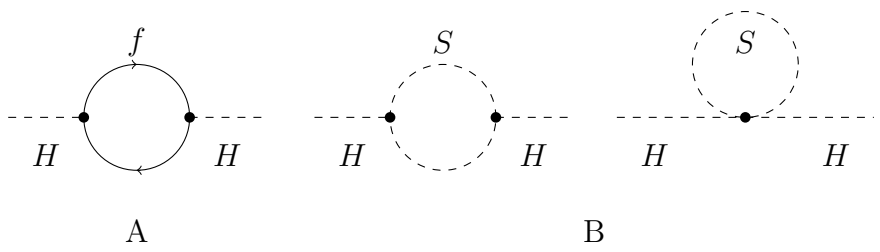


Figure 1.3: Diagrams for the contributions of fermions (A) and scalars (B) to the Higgs boson mass.

where $i$ and $j$ run over the three generations and $V^{ij} = U_L^{ik} D_L^{kj}$ or explicitly

$$V = \begin{pmatrix} V_{ud} & V_{us} & V_{ub} \\ V_{cd} & V_{cs} & V_{cb} \\ V_{td} & V_{ts} & V_{tb} \end{pmatrix}.$$

$V$ is a unitary matrix which can be parametrized by three angles and one complex phase generating CP violation. The consequence of such a term is that charged currents can change the flavour. Namely, in addition to standard $Zu_i d_i$ couplings, off-diagonal $Wu_i d_j$ with $i \neq j$ can occur. In $V$, diagonal terms are close to unity, thus, off-diagonal terms are small and $V_{td}$ and $V_{ub}$ are of second order of an expansion parameter. $V$ being unitary, so are $U_L$ and $D_L$. Terms coupling quarks to $Z_\mu$ will include the product $U_L U_L^\dagger = 1$ or $D_L D_L^\dagger = 1$. Hence, no flavour changing neutral currents are expected in the Standard Model.

## 1.6 The hierarchy problem

One fundamental issue in the SM is that its energy scale is more than ten orders of magnitude smaller than the Planck scale. Indeed, a theory that would unify all four interactions has to be valid up to scales of $10^{18}$ GeV whereas the typical scale of the SM is around 300 GeV. Gauge symmetry prevents fermions and vector bosons from acquiring masses. Oppositely, scalar bosons are not protected and could, in theory, have very large mass [36, 37, 38, 39], i.e. they become unnatural. Yet, as mentioned in section 1.4, in the SM, a Higgs boson mass larger than 1 TeV would violate unitarity. The hierarchy problem is very much related to the naturalness problem which arises in the SM in the calculation of contributions from fermionic loops to the Higgs boson mass. Namely, contribution to $m_h^2$ from a fermion $f$ (diagram A in figure 1.3) with Yukawa coupling $\lambda_f = \sqrt{2} m_f / v$ and multiplicity $N_f$ reads [40]

$$\Delta m_h^2 = N_f \frac{\lambda_f^2}{8\pi^2} \left[ -\Lambda^2 + 6m_f^2 \ln \frac{\Lambda}{m_f} - 2m_f^2 \right] + \mathcal{O}(1/\Lambda^2)$$

where $\Lambda$ is the ultra-violet cutoff of the loop integral. These corrections are quadratically divergent. Being the heaviest, the top quark is the main contributor. If the SM

were to be valid up to say the Planck scale, the Higgs mass would be enormous. The counter-terms needed to keep it below the TeV scale would have to be adjusted with a precision of $\mathcal{O}(10^{-30})$ which is unnatural. In turn, the contribution from a scalar boson $S$ (diagrams B in figure 1.3) with trilinear and quadrilinear couplings to the Higgs boson $v\lambda_S$ and $\lambda_S$ and multiplicity $N_S$ reads

$$\Delta m_h^2 = \frac{\lambda_S N_S}{16\pi^2}\left[-\Lambda^2 + 2m_S^2 \ln\frac{\Lambda}{m_S}\right] + \frac{\lambda^2 N_S}{16\pi^2} v^2 \left[-1 + 2\ln\frac{\Lambda}{m_S}\right] + \mathcal{O}(1/\Lambda^2).$$

Now if we assume that $\lambda_S = -\lambda_f^2$ and $N_S = 2N_f$, the total contribution to the Higgs mass squared is

$$\Delta m_h^2 = \frac{\lambda_f^2 N_f}{4\pi^2}\left[(m_f^2 - m_S^2)\ln\frac{\Lambda}{m_S} + 3m_f^2 \ln\frac{m_S}{m_f}\right] + \mathcal{O}(1/\Lambda^2).$$

Now the quadratic divergence has vanished and the remaining logarithmic divergence can be led to zero if $m_f = m_S$. Evidently, there is no such scalar boson in the SM. However, supersymmetry (see chapter 2) readily provides two scalar bosons for each fermion in the model. This cancellation of divergences is one of the main motivation for extending the SM to supersymmetry.

## 1.7 High-energy hadronic interactions

Interactions in quantum field theory arise as small perturbations to the free Lagrangian density. Calculations of physical processes are achieved via the perturbation theory where coupling constants play the role of the expansion parameter. The dominant process (graph) to a given set of initial and final states will be the one including the smallest power of the coupling constants or equivalently, the smallest number of vertices in the corresponding Feynman graph. The "tree level" designates the leading order (LO), where the coupling constants appear with a power of one. Common processes such as electroweak processes, hard QCD processes or Higgs boson and supersymmetry production have now been calculated to the "one loop" level, that is the next-to-leading order (NLO). The number of loops and hence the number of different graphs increase with the order of the contribution. Going further than NLO (NNLO) requires tools for automatic generation and calculation of graphs. Perturbation theory is not suitable for low-energy QCD where the coupling constant $\alpha_S$ becomes large. Consequently, perturbative calculations cannot be performed in certain energy domains such as that of nuclear physics or low-energy hadronic physics. Numeric tools such as Lattice QCD are necessary to describe such systems. The energy scale of the interactions at the LHC places $\alpha_S$ in a domain where perturbation theory can be comfortably trusted.

The dominant uncertainties on the calculation of hadronic cross-section are due to higher-order contributions and parton density functions (PDFs) $f(x)$. The latter correspond to the probability distribution of the fraction $x$ of the energy of the incoming protons that is carried by a given parton. PDFs are not computable analytically but their

evolution as a function of the transferred momentum is predicted by the Dokshitzer-Gribov-Lipatov-Altarelli-Parisi (DGLAP) equations [41, 42, 43]. Their evolution as a function of $x$ is predicted by the Balitsky-Fadin-Kuraev-Lipatov (BFKL) equations [44, 45, 46]. From there, PDFs can be predicted from a fit to experimental data. Two collaboration provide a set of PDFs : the Coordinated Theoretical-Experiment Project on QCD (CTEQ) [47, 48] and the Martin-Robert-Stirling-Thorne (MRST) group.
Once PDFs are known, the cross-section for the production of a final-state $X$ in $pp$ collisions can be expressed from the perturbative partonic cross-section $\sigma(ab \to X)$, where $a$ and $b$ are quarks or gluons, thanks to the factorisation theorem

$$\sigma(pp \to X) = \sum_{a,b} \int_{x_{\min}}^{1} dx_1 dx_2 f_a(x_1, \mu_F) f_b(x_2, \mu_F) \sigma(ab \to X; s x_1 x_2, \mu_R, \mu_F, \text{masses})$$

where $f_{a(b)}$ is the PDF for parton $a(b)$, $s$ is the square of the energy in the center of mass and $\mu_R$ and $\mu_F$ are the renormalization and factorization scales. The later represents the scale above which interactions are treated perturbatively and incorporated into $\sigma(ab \to X)$ and below which interactions are incorporated in the PDFs.
Most of the available softwares for the generation of Monte Carlo samples of physical processes are based on the calculation of the tree-level matrix element. Final states of hard scattering are then matched to a parton shower generator. The latter computes the hadronization of final state partons. LO samples are then normalized to the NLO cross-section thanks to so-called $K$–factors computed by dedicated codes.
Once the cross-section $\sigma(pp \to X)$ for some final-state $X$ is known, the expected number of events produced is

$$N_X = \sigma(pp \to X) \times \int dt \mathcal{L}$$

where $\mathcal{L}$ is the instantaneous collision luminosity. Experimentally, this number should be multiplied a number of efficiency factors corresponding to detector effects (acceptance, reconstruction, identification, etc...) and analysis requirements.
Figure 1.4 shows cross-sections for typical processes as a function of the energy in the center of mass. At the LHC, the total inelastic cross-section is clearly dominated by jet production. Production rates for new particles such as the Higgs bosons are about ten orders of magnitude smaller than the total cross-section.

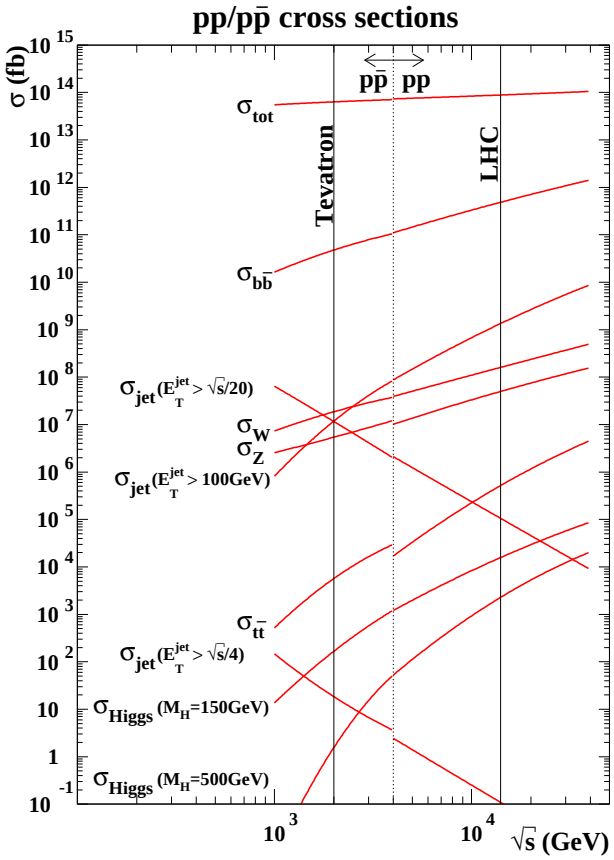


Figure 1.4: Cross-sections for typical processes as a function of the energy in the center of mass $\sqrt{s}$.

# Chapter 2

# Supersymmetry

*"One's idea must be as broad as nature if they are to interpret nature"*

Sherlock Holmes – *A study in scarlet*

Supersymmetry is the most popular extension to the Standard Model. This status is mostly due to the way it tackles a number of issues of the SM : it allows for a stabilization of the weak scale, provides a candidate for the dark matter of the Universe [49], can unify gauge couplings at the high scale [50] and occur naturally in some higher scale theories. If it is realized, supersymmetry could be probed in the energy domain accessible at the LHC.

Supersymmetry establishes a symmetry between fermions and bosons. It extends the SM via models such as the Minimal Supersymmetric extension to the SM (MSSM, section 2.2) and its universal branch mSUGRA (minimal supergravity, section 2.2.3). In such models, each field of spin $s$ in the SM is associated to a new field of spin $|s - \frac{1}{2}|$ with identical quantum numbers. These models propose a candidate for the dark matter of the Universe, unify gauge couplings at the high scale and address the hierarchy problem of the electroweak scale (section 1.6) by cancelling divergence. The latter implies that new particles must lie in the TeV range. By their coupling to the SM they may be produced experimentally at colliders such as the TeVatron or the LHC. Signatures include high-energy jets and leptons and missing transverse energy. No evidence were seen at the TeVatron but, with a reach of several TeV for the production of new particles, the LHC is the ideal tool for the search for supersymmetry.

In 1967, Coleman and Mandula showed that the only possible extension of the Poincaré group, is by a product with an internal symmetry group. They did not consider supersymmetry as this internal symmetry yet [51]. Separately, in 1971 Gol'fand and Likhtman introduced the idea of spinorial translation as a possible extension to the Poincaré algebra [52]. They built a four-dimensions Quantum Field Theory (QFT) containing massive quantum electrodynamics. In 1973, Volkov and Akulov proposed another model along with the concept of spontaneous breakdown. Eventually in 1974, Wess and Zumino [53] as well as Salam and Strathdee [54] adapted the so-called super-gauge

transformations emitted in the early seventies by string theorists to four-dimensions QFT. Subsequently in 1975, Haag, Lopuszanski and Sohnius combined these works with the Coleman-Mandula theorem to demonstrate that supersymmetry is the only possible extension of space-time symmetries [55]. The next year, Fayet designed what a minimal supersymmetric QFT including the SM should look like [56, 57].

## 2.1 Construction

One of the major theoretical reasons for the interest in supersymmetry is that it was proved to be the only possible extension of the Poincaré group. The first step towards that statement is the Coleman-Mandula (CM) theorem. It is the last and most powerful in a series of no-go theorems [58, 59, 60].
It was shown in [58] that any internal symmetry that does not commute with the Poincaré group leads to infinite numbers of states with equal four-momentum eigenvalues. That is, multiplets of the symmetry group containing both the Poincaré group and some new internal symmetries would contain an infinite number of particles. Subsequently, the CM theorem states that if $G$ is a symmetry group of the scattering matrix, if it contains the Poincaré group, if there is a finite number of particles of a given mass, if any two-particle state undergoes scattering at almost all energies and if its amplitude is an analytic function of the center-of-mass energy and momentum transfer, then $G$ is the direct product[1] of the Poincaré group with an internal symmetry group[2]. That is, space-time symmetries of quantum field theories cannot be extended in any but a trivial way. A proof of this theorem is provided in [51] and [61].

From there, the last step was provided by [52]. The CM theorem can be circumvented by extending Lie algebras to superalgebras, i.e., algebras containing both commuting and anti-commuting relations. [55] proved that this was the only possible way of extending the Poincaré group.
The commuting part of the algebra identifies with the internal symmetry group to which the CM theorem applies. However, the anti-commuting part escapes the scope of the CM theorem and is left free to combine with space–time symmetries. Hence, the only way to extend the Poincaré group is to include superalgebras, that is, supersymmetries.

Let $Q_\alpha$ be the generators of the considered extension. $Q_\alpha$'s are two–components Weyl spinors. They act on the first two components of Dirac spinors while $Q^\dagger_{\dot\alpha}$'s act on the last two components. By construction, they anti-commute, that is

$$\{Q_\alpha, Q_\beta\} = \{Q^\dagger_{\dot\alpha}, Q^\dagger_{\dot\beta}\} = 0. \tag{2.1}$$

The structure of superalgebras imposes that the anti-commutator of two fermionic operators should close into a bosonic operator. Thus, $\{Q_\alpha, Q^\dagger_{\dot\alpha}\}$ should close into a linear combination of the two bosonic operators at hand, namely $P_\mu$ and $M_{\mu\nu}$. However,

[1] Their generator commute.
[2] a group which elements are diagonal in and independent of momentum and spin.

by virtue of Jacobi identities, the $M_{\mu\nu}$ part vanishes [62] so that

$$\{Q_\alpha, Q^\dagger_{\dot\alpha}\} = 2\sigma^\mu_{\alpha\dot\alpha} P_\mu. \tag{2.2}$$

Then, the commutator of a fermionic operator with a bosonic one must close into a fermionic one. Hence, $[Q_\alpha, P_\mu]$ must be proportional to $Q_\alpha$. However, so far, supersymmetries are global and as so, are independent of position in space–time. Consequently,

$$[Q_\alpha, P_\mu] = [Q^\dagger_{\dot\alpha}, P_\mu] = 0. \tag{2.3}$$

Eventually, $M_{\mu\nu}$ and $Q_\alpha$ must commute into an expression proportional to $Q_\alpha$'s, that is [62]

$$[M_{\mu\nu}, Q_\alpha] = -(\sigma_{\mu\nu})^\beta_\alpha Q_\beta \qquad \text{and} \qquad [M_{\mu\nu}, Q^{\dot\alpha\dagger}] = -(\sigma^\dagger_{\mu\nu})^{\dot\alpha}_{\dot\beta} Q^{\dot\beta}. \tag{2.4}$$

One can notice that relations (2.1), (2.2), (2.3) and (2.4) are invariant under the transformations

$$Q_\alpha \to e^{-i\psi} Q_\alpha \qquad \text{and} \qquad Q^\dagger_{\dot\alpha} \to e^{i\psi} Q^\dagger_{\dot\alpha}$$

which are those of a global U(1) with generator say $R$ leading to the relation

$$[Q_\alpha, R] = Q_\alpha \qquad \text{and} \qquad [Q^\dagger_{\dot\alpha}, R] = Q^\dagger_{\dot\alpha}. \tag{2.5}$$

This U(1) global symmetry known as $R$–symmetry accommodates perfectly with the CM theorem since

$$[R, P_\mu] = [R, M_{\mu\nu}] = 0.$$

Relations (2.1), (2.2), (2.3), (2.4) and (2.5) define the supersymmetry algebra. It is possible to include more than one (say $n$) supersymmetry generator in which case it is refereed to as $N = n$ extended supersymmetry. Most if not all studies and analysis are performed in the framework of $N = 1$ supersymmetry.

As a fermionic operator, $Q$ transforms fermionic fields into bosonic fields and vice-versa. Fields that transform into one another under supersymmetric transformations are *superpartners* and can be fitted into *supermultiplets*. A consequence of eq. (2.3), is that $[Q_\alpha, P^2] = 0$ so that fields that belong to the same irreducible representation of supersymmetry, i.e. superpartners, have the same mass. The situation is identical for all internal symmetry generators so that superpartners carry the same set of quantum numbers except for spin. Another straightforward consequence of the supersymmetry algebra is that each supermultiplet should have an equal number of bosonic and fermionic degrees of freedom. This can be proved by considering the trace of the operator $(-1)^{2s}P^\mu$ where $s$ is the spin of the state, across a supermultiplet containing the fermionic or bosonic states $|i\rangle$.

$$\begin{aligned}
\sum_i \langle i|(-1)^{2s}P^\mu|i\rangle &= \sum_i \langle i|(-1)^{2s}QQ^\dagger|i\rangle + \langle i|(-1)^{2s}Q^\dagger Q|i\rangle \\
&= \sum_i \langle i|(-1)^{2s}QQ^\dagger|i\rangle + \sum_i\sum_j \langle i|(-1)^{2s}Q^\dagger|j\rangle\langle j|Q|i\rangle \\
&= \sum_i \langle i|(-1)^{2s}QQ^\dagger|i\rangle - \sum_j \langle j|(-1)^{2s}QQ^\dagger|j\rangle \\
&= 0 \quad = \quad p_\mu \sum_i \langle i|(-1)^{2s}|i\rangle \quad = \quad p_\mu(n_B - n_F)
\end{aligned}$$

using the completeness relation and remembering that, as a fermionic operator, $(-1)^{2s}$ anti-commutes with $Q$. Hence, $n_B = n_F$. The two simplest way to construct supermultiplet with $n_B = n_F$ are matter and gauge supermultiplets. The former contain a Weyl chiral fermion ($n_F = 2$) and a complex scalar ($n_B = 2$). Gauge supermultiplets are made of a mass-less vector boson ($n_B = 2$) and a Weyl fermion ($n_F = 2$).

The simplest supersymmetric field theory is the Wess-Zumino model. It contains a matter supermultiplet : a left-handed Weyl fermion $\psi$ and a complex scalar $\phi$. An infinitesimal supersymmetry transformation on $\phi$ gives

$$\phi \to \epsilon\psi \qquad \text{and} \qquad \phi^* \to \epsilon^\dagger\psi^\dagger$$

where $\epsilon$ is an infinitesimal anti-commuting Weyl fermion object which parametrizes the transformation. An infinitesimal supersymmetry transformation on $\psi$ gives

$$\psi \to i\sigma^\mu\epsilon^\dagger\partial_\mu\phi + \epsilon F \qquad \text{and} \qquad \psi^\dagger \to -i\epsilon\sigma^\mu\partial_\mu\phi^* + \epsilon^\dagger F^*.$$

$F$ is an auxiliary complex scalar field introduced in order for the supersymmetry algebra to close off–shell, i.e. when $\overline{\sigma}^\mu\partial_\mu \neq 0$. Without this field, the commutator of two supersymmetric transformation on a fermion is not equal to a derivative of the original field. Auxiliary fields do not propagate and can be eliminated neatly through the equations of motion they generate. They supersymmetricaly transform as follows

$$F \to e\epsilon^\dagger\overline{\sigma}^\mu\partial_\mu\psi \qquad \text{and} \qquad F^* \to -i\partial_\mu\psi^\dagger\overline{\sigma}^\mu\epsilon.$$

The free mass-less Lagrangian density

$$\mathcal{L}_{\text{free}} = -\partial^\mu\phi^*\partial_\mu\phi - i\psi^\dagger\overline{\sigma}^\mu\partial_\mu\psi + F^*F$$

is invariant under supersymmetry transformations. A similar exercise can be performed with a gauge supermultiplet made of a mass-less gauge boson $A^a_\mu$ and a Weyl fermion $\lambda^a$ ($a$ is the gauge index). An extra real bosonic auxiliary field $D^a$ is required to close the algebra off–shell. These fields transform as

$$A^a_\mu \to -\frac{1}{\sqrt{2}}\left[\epsilon^\dagger\overline{\sigma}_\mu\lambda^a + \lambda^{\dagger a}\overline{\sigma}_\mu\epsilon\right] \quad , \quad \lambda^a \to -\frac{i}{2\sqrt{2}}\sigma^\mu\overline{\sigma}^\nu\epsilon F^a_{\mu\nu} + \frac{1}{\sqrt{2}}\epsilon D^a$$

$$\text{and} \quad D^a \to \frac{i}{\sqrt{2}}\left[\epsilon^\dagger\overline{\sigma}^\mu D_\mu\lambda^a - D_\mu\lambda^{\dagger a}\overline{\sigma}^\mu\epsilon\right]$$

where $F_{\mu\nu}$ and $D_\mu$ are the field strength tensor and the covariant derivative respectively. The following Lagrangian density is invariant under supersymmetry transformations

$$\mathcal{L}_{\text{gauge}} = -\frac{1}{4}F^a_{\mu\nu}F^{\mu\nu a} - i\lambda^{\dagger a}\overline{\sigma}^\mu D_\mu\lambda^a + \frac{1}{2}D^aD^a.$$

Gauge interactions happen through the standard covariant derivative. In order to include new terms coupling scalar fields beyond gauge interaction, the *superpotential* must be introduced

$$W = \frac{1}{2}M^{ij}\phi_i\phi_j + \frac{1}{6}y^{ijk}\phi_i\phi_j\phi_k$$

where $M_{ij}$ is a mass matrix and $y_{ijk}$ a so–called Yukawa coupling matrix. $W$ is an analytic function of the scalar fields $\phi_i$ and represents the most general set of renormalizable interactions. It enters the Lagrangian density in the following way

$$\mathcal{L} \supset -\frac{1}{2}\left(\frac{\delta^2 W}{\delta\phi_i\phi_j}\psi^i\psi^j + \text{c.c.}\right) - \frac{\delta W}{\delta\phi^i}\frac{\delta W^*}{\delta\phi_i^*}.$$

The building of a supersymmetric model lies in the design of its superpotential, so that it is the most general expression respecting the desired symmetries.

## 2.2 The minimal supersymmetric extension to the SM

In order to design a supersymmetric QFT that would include the SM, supermultiplets should be constructed as accommodating the existing fields.
Each existing chiral quark and lepton are fitted into a supermultiplet along with one complex scalar, a so-called *squark* or *slepton*. For instance, a left-handed top quark $t_{\text{R}}$ can be associated with a so-called *stop* right $\tilde{t}_{\text{R}}$. As scalars do not feature handedness, the right or left tag refers to the handedness of the associated standard fermion.
Similarly, gauge bosons are included in gauge multiplets along with Weyl fermions, the *gauginos*. The gluon, $W$ and $B$ bosons are associated with the gluino, wino and bino which after gauge symmetry breaking mix into the zino and photino.
The Higgs boson could belong to a matter multiplet along with another Weyl fermion but two problems arise here. The Yukawa terms in eq. (1.4) should be re-implemented in the context of the superpotential, bearing in mind that in order to be supersymmetric $W$ should be an analytic function of left matter superfields. This forbids the Higgs field to provide mass to both $u$–type and $d$–type quarks simultaneously. Parallely, a single Higgs doublet would lead to triangle gauge anomalies in the electroweak sector, i.e. a violation of the gauge symmetry in quantum corrections. The condition for the cancellation of these anomalies is that there are two Higgs doublet with opposite hypercharge. Hence, it is necessary to have two Higgs doublet, $H_u$ to generate the mass of $T_3 = \frac{1}{2}$ fermions ($u$–type quarks) and $H_d$ with opposite hypercharge for $T_3 = -\frac{1}{2}$ fermions ($d$–type quarks and massive leptons). Table 2.1 summarizes the additional fields of the MSSM.

Thus, supersymmetry predicts the existence of one sfermion for each chiral fermion and one gaugino for each gauge boson in the SM. Each of this superpartners should have the same mass as their standard partners. These states have not been discovered experimentally. If they exist, their mass must lie beyond the reach of current experiments, well above that of their standard partners. This implies that supersymmetry must be broken below some scale. Many breaking scenarios have been envisioned but no consensus exist. In fact, it can be shown that spontaneous breakdown of supersymmetry cannot be realized in the context of the MSSM without introducing new fields. The latter are phenomenologically believed to be gauge singlet with masses well beyond the electroweak scale. They constitute the so-called hidden or secluded sector. However, in order to study the MSSM without knowing the exact supersymmetry breaking scheme, so-called *soft* supersymmetry breaking terms must be introduced in

| spin 0 | spin $\frac{1}{2}$ |
|---|---|
| squarks | quarks |
| $(\tilde{u}_{\mathrm{L}} \quad \tilde{d}_{\mathrm{L}})$ | $(u_{\mathrm{L}} \quad d_{\mathrm{L}})$ |
| $\tilde{u}^*_{\mathrm{R}}$ | $u^\dagger_{\mathrm{R}}$ |
| $\tilde{d}^*_{\mathrm{R}}$ | $d^\dagger_{\mathrm{R}}$ |
| sleptons | leptons |
| $(\tilde{\nu} \quad \tilde{e}_{\mathrm{L}})$ | $(\nu \quad e_{\mathrm{L}})$ |
| $\tilde{e}^*_{\mathrm{R}}$ | $e^\dagger_{\mathrm{R}}$ |
| Higgs | higgsinos |
| $(H_u^+ \quad H_u^0)$ | $(\tilde{H}_u^+ \quad \tilde{H}_u^0)$ |
| $(H_d^0 \quad H_d^-)$ | $(\tilde{H}_d^0 \quad \tilde{H}_d^-)$ |

| spin $\frac{1}{2}$ | spin 1 |
|---|---|
| gluino | gluon |
| $\tilde{g}$ | $g$ |
| winos | $W$ bosons |
| $\tilde{W}^i$ | $W^i_\mu$ |
| bino | $B$ boson |
| $\tilde{B}$ | $B_\mu$ |

Table 2.1: Matter (left) and gauge (right) supermultiplets in the MSSM

the Lagrangian density. These terms include mass terms for all superpartners and bilinear and trilinear scalar couplings

$$\begin{aligned}\mathcal{L} \supset\ & -\frac{1}{2}(M_1\tilde{B}\tilde{B} + M_2\tilde{W}\tilde{W} + M_3\tilde{g}\tilde{g}) + \text{c.c.} \\ & -\tilde{q}^*_{\mathrm{L}} m_q^2 \tilde{q}_{\mathrm{L}} - \tilde{u}^*_{\mathrm{R}} m_u^2 \tilde{u} - \tilde{d}^*_{\mathrm{R}} m_d^2 \tilde{d}_{\mathrm{R}} - \tilde{l}^*_{\mathrm{L}} m_\ell^2 \tilde{l}_{\mathrm{L}} - \tilde{e}^*_{\mathrm{R}} m_e^2 \tilde{e}_{\mathrm{R}} \\ & -m^2_{H_u} H_u^* H_u - m^2_{H_d} H_d^* H_d - (b H_u H_d + \text{c.c.}) \\ & -(\tilde{u}^*_{\mathrm{R}} A_u y_u \tilde{q}_{\mathrm{L}} H_u - \tilde{d}^*_{\mathrm{R}} A_d y_d \tilde{q}_{\mathrm{L}} H_d - \tilde{e}^*_{\mathrm{R}} A_e y_e \tilde{l}_{\mathrm{L}} H_d) + \text{c.c.}.\end{aligned} \tag{2.6}$$

Here, $M_{1,2,3}$ are the gaugino mass parameters. The second line contains the scalar mass parameters $m^2_{q,u,d,\ell,e}$. These are 3×3 hermitian matrices in family space. In the third line, $m^2_{H_{u,d}}$ are the Higgs mass parameters and $b$ is a bilinear coupling between $H_u$ and $H_d$. The last line contains trilinear $H\tilde{f}\tilde{f}$ coupling parametrized by the 3×3 Yukawa matrices $y_{u,d,e}$ and $A_{u,d,e}$.
The superpotential for the MSSM reads

$$\begin{aligned}W_{\mathrm{MSSM}} \ =\ & y_u(\tilde{u}^*_{\mathrm{R}}\tilde{u}_{\mathrm{L}} H_u^0 - \tilde{u}^*_{\mathrm{R}}\tilde{d}_{\mathrm{L}} H_u^+) - y_d(\tilde{d}^*_{\mathrm{R}}\tilde{u}_{\mathrm{L}} H_d^- - \tilde{d}^*_{\mathrm{R}}\tilde{d}_{\mathrm{L}} H_d^0) \\ & -y_e(\tilde{e}^*_{\mathrm{R}}\tilde{\nu} H_d^- - \tilde{e}^*_{\mathrm{R}}\tilde{e}_{\mathrm{L}} H_d^0) + \mu(H_u^+ H_d^- - H_u^0 H_d^0).\end{aligned}$$

The terms in $W$ containing fermions should also be included but they vanish upon derivation and therefore do not enter the Lagrangian density. Disregarding any assumptions on the phenomenology of the model, eq (2.6) contains 105 parameters[3] all defined at the breaking scale. Nevertheless, it is possible and phenomenologically desirable to constrain a number of these. For instance, Flavour Changing Neutral Currents, CP violation and flavour mixing can be avoided by assuming a somehow universal supersymmetry breaking scheme. Masses and trilinear coupling matrices can be made diagonal, reducing the number of parameters to 24. This constrained MSSM is referred to as the phenomenological MSSM (pMSSM). Table 2.2 lists its parameters. Gaugino

[3] 3 gaugino mass parameters, 2 Higgs mass parameters, 45 scalar mass parameters, 54 trilinear couplings and one bilinear coupling.

| | |
|---|---|
| Gaugino mass parameters | $M_{1,2,3}$ |
| Higgs mass parameters | $\mu$ and $M_A$ |
| Trilinear couplings | $A_{\tilde{\tau},\tilde{b},\tilde{t}}$ |
| Sfermion soft-breaking terms | $m^{1,2,3}_{\tilde{l}_\mathrm{R}}$ and $m^{1,2,3}_{\tilde{l}_\mathrm{L}}$ |
| | $m^{1,2,3}_{\tilde{q}_\mathrm{L}}$, $m^{1,2,3}_{\tilde{u}_\mathrm{R}}$ and $m^{1,2,3}_{\tilde{d}_\mathrm{R}}$ |
| Ratio $v_1/v_2$ | $\tan\beta$ |

Table 2.2: The 24 parameters of the phenomenological MSSM.

mass parameters remain non-universal. All trilinear coupling associated with light SM fermions vanish and the matrices are diagonalized. Only the trilinear couplings from the third generation remain. $\tan\beta$ can be seen as the rotation angle between the two Higgs doublets and $M_A$ relates to the bilinear coupling $b$.

### 2.2.1 Mass spectrum

#### The Higgs sector

After rotating the components of the two Higgs doublets in order for the charged component not to get VEVs, the Higgs potential in the MSSM reads

$$V = \left(|\mu|^2 + m^2_{H_u}\right)|H^0_u|^2 + \left(|\mu|^2 + m^2_{H_d}\right)|H^0_d|^2 - \left(bH^0_u H^0_d + \text{c.c.}\right) + \frac{g^2+g'^2}{8}\left(|H^0_u|^2 - |H^0_d|^2\right)^2 .$$

Terms in $\mu$ and $g$ arise from the equations of motion of the auxiliary fields. Terms in $b$ and $m_H$ are those included in the soft terms of equation 2.6. The condition for a spontaneous breakdown of the symmetry ($H^0_u = H^0_d = 0$ is not a stable minimum) and for a potential bounded from below are

$$b^2 > \left(|\mu|^2 + m^2_{H_u}\right)\left(|\mu|^2 + m^2_{H_d}\right) \quad \text{and} \quad 2b < 2|\mu|^2 + m^2_{H_u} + m^2_{H_d}$$

respectively. The VEVs of $H_u$ and $H_d$ satisfy $v_u^2 + v_d^2 = v^2 = 2m_Z^2/(g^2+g'^2)$. The condition for the Higgs potential to have a minimum satisfying this relation reads

$$|\mu|^2 + m^2_{H_u} = \cot\beta + (m_Z^2/2)\cos 2\beta \quad \text{and} \quad |\mu|^2 + m^2_{H_d} = b\tan\beta - (m_Z^2/2)\cos 2\beta$$

where $\tan\beta = v_u/v_b$. These requirements indicate that $\mu$ would be of the order of the electroweak scale. However, similarly to the hierarchy problem in the Higgs sector of the SM, no symmetry protects $\mu$ from being of the order of the Planck scale. This is known as the $\mu$ problem and can be solved in the context of the next-to-minimal supersymmetric extension to the SM (NMSSM).
Two Higgs doublet provide eight real, scalar degrees of freedom, three of which provide longitudinal modes to the massive gauge bosons. The remaining five mass eigenstates are the CP–even neutral scalars $h$ and $H^0$, two charged scalar $H^\pm$ and the CP–odd

neutral scalar $A$. Their tree-level masses are

$$\begin{aligned} m_h^2 &= \frac{1}{2}\left(m_A^2 + m_Z^2 - \sqrt{\left(m_A^2 + m_Z^2\right)^2 - 4m_Z^2 m_A^2 \cos^2 2\beta}\right) \\ m_H^2 &= \frac{1}{2}\left(m_A^2 + m_Z^2 + \sqrt{\left(m_A^2 + m_Z^2\right)^2 - 4m_Z^2 m_A^2 \cos^2 2\beta}\right) \\ m_A^2 &= 2b/\sin 2\beta \\ m_{H^\pm}^2 &= m_A^2 + m_W^2 \end{aligned} \tag{2.7}$$

A knowledge of $m_A$ and $\tan\beta$ provides the masses of all Higgs bosons. Expression 2.7 leads to $m_h$ being bounded from above by $m_Z$ at tree-level. Quantum corrections induced by fermion and sfermion loops such as those in figure 1.3 are non negligible [63, 64] leading to an upper bound of 130 GeV if sfermions are lighter than 1 TeV. This bound gets weaker if sfermions have very large mass, see section 5.1.

### Neutralinos and charginos

The weak eigenstates of the neutral higgsinos and gauginos mix into four mass eigenstates, neutralinos $\tilde{N}_{1,\ldots,4}$ with $m_{\tilde{N}_i} < m_{\tilde{N}_{i+1}}$. The mass matrix

$$M_{\tilde{N}} = \begin{pmatrix} M_1 & 0 & -c_\beta s_W m_Z & s_\beta s_W m_Z \\ 0 & M_2 & c_\beta c_W m_Z & -s_\beta c_W m_Z \\ -c_\beta s_W m_Z & c_\beta c_W m_Z & 0 & -\mu \\ s_\beta s_W m_Z & -s_\beta c_W m_Z & -\mu & 0 \end{pmatrix}$$

with $\{c, s\}_\theta = \{\cos, \sin\}\theta$ can be diagonalized using a $4 \times 4$ unitary matrix to provide the neutralino masses $m_{\tilde{N}_i}$. Charged higgsinos and winos mix into two charged mass eigenstates, charginos $\tilde{C}_{1,2}$ with $m_{\tilde{C}_1} < m_{\tilde{C}_2}$. Similarly, the chargino mass matrix

$$M_{\tilde{C}} = \begin{pmatrix} 0 & 0 & M_2 & \sqrt{2}c_\beta m_W \\ 0 & 0 & \sqrt{2}s_\beta m_W & \mu \\ M_2 & \sqrt{2}s_\beta m_W & 0 & 0 \\ \sqrt{2}c_\beta m_W & \mu & 0 & 0 \end{pmatrix}$$

can be diagonalized to give the following mass eigenstates

$$\begin{aligned} m_{\tilde{C}_1}^2, m_{\tilde{C}_2}^2 &= \frac{1}{2}\left(|M_2|^2 + |\mu|^2 + 2m_W^2\right) \\ &\quad \mp \frac{1}{2}\sqrt{\left(|M_2|^2 + |\mu|^2 + 2m_W^2\right)^2 - 4|\mu M_2 - m_W^2 \sin 2\beta|^2} \end{aligned}$$

The radiative corrections to the neutralino and chargino masses are due in equivalent part to the fermion/sfermion and gauge/Higgs sectors and are lower than 10% [65].

### Gluinos

Gluinos are color octets and as so, do not mix with any other fields. The gluino one-loop mass is

$$m_{\tilde{g}} = M_3(Q)\left(1 + \frac{\alpha_S}{4\pi} A(Q/M_3)\right)$$

where $A$ accounts for the coupling to all quarks and squarks in the model. This term can contribute to a fourth or more of the total mass [65].

#### Supersymmetric scalars

Although in principle, up/down–type squarks and charged sleptons can mix within each group, it is possible to limit the number of free parameters by assuming flavour-blind soft parameters. From there the difference in Yukawa and soft couplings between third generations and others predict that mixing should only occur within $(\tilde{t}_{\mathrm{L}}, \tilde{t}_{\mathrm{R}})$, $(\tilde{b}_{\mathrm{L}}, \tilde{b}_{\mathrm{R}})$ and $(\tilde{\tau}_{\mathrm{L}}, \tilde{\tau}_{\mathrm{R}})$ leaving the other generations unmixed. For instance, the mass matrix for the stop reads

$$m_{\tilde{t}}^2 = \begin{pmatrix} m_{\tilde{q}_{\mathrm{L}}^3}^2 + m_t^2 + \left(\frac{1}{2} - \frac{2}{3}\sin^2\theta_W\right)\cos 2\beta m_Z^2 & m_t(A_t - \mu\cot\beta) \\ m_t(A_t - \mu\cot\beta) & m_{\tilde{t}_{\mathrm{R}}}^2 + m_t^2 + \frac{2}{3}\sin^2\theta_W\cos 2\beta m_Z^2 \end{pmatrix}.$$

Off-diagonal terms are proportional to trilinear couplings and fermion masses. Thus, little mixing is expected in the first two generations. The matrices $m_{\tilde{\tau}}^2$ and $m_{\tilde{b}}^2$ are equivalent with $\tan\beta$ instead of $\cot\beta$. The mass eigenstates are label $\tilde{f}_1$ and $\tilde{f}_2$ in order of increasing mass.

### 2.2.2 Interesting features

#### Hierarchy problem

The appearance of two real scalar degrees of freedom for each SM Weyl fermion is indeed of great help to solve the hierarchy problem of the electroweak scale. After inclusion of the supersymmetric field spectrum, the leading divergences in the loop corrections to the Higgs mass are proportional to $m_f^2 - m_{\tilde{f}}^2$. Since supersymmetry must be broken, these contributions do not vanish entirely, they are merely kept under control. If the mass of the new particles are not much heavier than the TeV scale, the radiative corrections should be of the same order as the tree–level Higgs boson mass. Otherwise, a fine–tuning of the counter-terms will be necessary to keep $m_h$ sufficiently low not to break unitarity.

#### $R$–parity

As briefly mentioned in 2.1, another symmetry can be imposed : $R$–parity. It prevents terms that would violate baryon or lepton number conservation to enter the super-potential. These would allow protons to decay in a matter of hours. $R$–parity is a multiplicative quantum number defined for each particle as

$$R = (-1)^{3B+L+2s}$$

where $B$ is the baryon number, $L$ the lepton number and $s$ the spin of the particle. Particles in the SM all have $R = 1$. New supersymmetric particles all have $R = -1$. Requiring $R$–parity to be conserved in supersymmetric models has two consequences. Firstly, supersymmetric particles can only be produced in pairs. Secondly, the decay

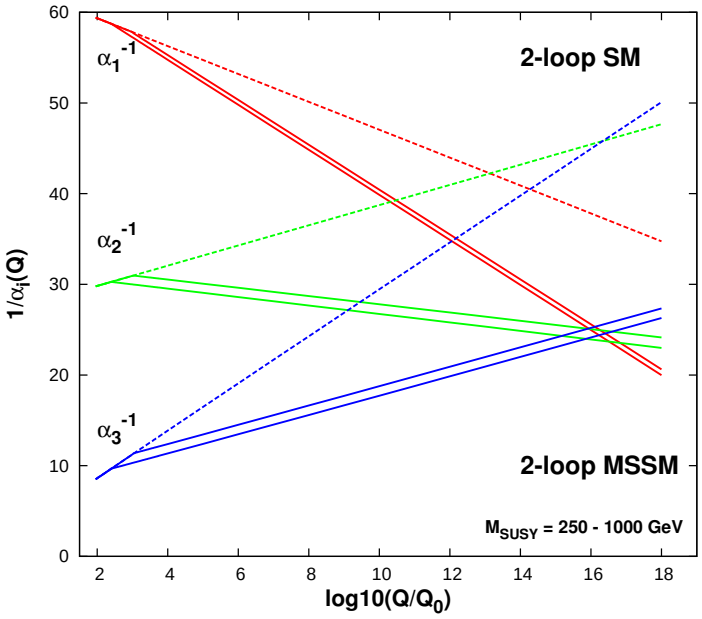


Figure 2.1: Running of the SM gauge couplings as a function of the renormalization scale in the case of the MSSM (solid) and of the SM (dashed). The supersymmetry mass scale was varied from 250 to 1000 GeV.

products of any supersymmetric particle must include one sparticle. The immediate consequence is that the lightest supersymmetric particle (LSP) is stable. Incidentally, were the LSP to be colourless and neutral, it would qualify as a WIMP candidate [49]. This constitutes one of the major reasons for the interest for supersymmetry. If this weakly interacting LSP were to be produced in a colliding experiment, it would escape detection and energy would be missing in the recorded event. This is one of the major discriminating variable in any search for $R$–parity conserving supersymmetry at colliders.

### Gauge coupling unification

Figure 2.1 shows the SM coupling of the three gauge groups ($\alpha_i^{-1} = g_i^2/(4\pi)$) according to the renormalization group equations as a function of the renormalization group scale for the SM (dashed) and for the MSSM (solid). In the case of the SM, they do not intersect in one point. This means that if a unified gauge theory is desired above some scale, the SM cannot be the effective model valid up to that scale. Namely, an intermediate scale with a new particle content is necessary. The solid lines on figure 1.1 shows the same couplings but with the inclusion of the MSSM corrections above some scale. Below that scale, the couplings are equal to those in figure 1.1, above, they differ. The couplings intersect at $M_{\mathrm{GUT}} \approx 10^{16}$ GeV. The gauge couplings are then universal above the GUT scale and break down into the three known couplings below

that scale [50].
In the one-loop MSSM, the gauge couplings and the gaugino mass parameters run like

$$\frac{\mathrm{d}}{\mathrm{d}t}g_i = \frac{b_i}{16\pi^2}g_i^3 \quad \text{and} \quad \frac{\mathrm{d}}{\mathrm{d}t}M_i = \frac{b_i}{8\pi^2}g_i^2 M_i \quad \text{with} \quad i = 1,2,3$$

where $t = Q/Q_0$ ($Q_0$ is the input scale) and $b_i$ are some factors. Hence, the gaugino mass parameters can be unified at $M_{\mathrm{GUT}}$

$$M_{1,2,3}(M_{\mathrm{GUT}}) = m_{1/2}$$

where $m_{1/2}$ denotes the universal gaugino mass parameter. Therefore

$$M_i(Q) = \frac{g_i^2(Q)}{g_i^2(Q_0)}m_{1/2}$$

and for any input scale $Q_0$, $M_i/g_i^2$ are all identical at any RG scale.

### 2.2.3 Minimal supergravity

The MSSM parameters are defined at the breaking scale which should be rather close to the electroweak scale in order to keep control on the Higgs mass. However, assuming unification is realized at $M_{\mathrm{GUT}}$, it is possible to define universal parameters at that scale and thereby greatly reduce the number of parameters. Namely

- gaugino mass parameters $M_i$ unify into a universal parameter $m_{1/2}$,
- scalar masses $m_{\tilde{f}}$ and $m_{H_{u,d}}$ unify into a universal parameter $m_0$,
- trilinear couplings $A_{\tilde{f}}$ unify into a universal coupling $A_0$ and
- $\tan\beta$ and the sign of $\mu$ remain free.

More generally, supergravity comes into play when one tries to render supersymmetry local [66, 67, 68, 69]. In doing this, unification of space-time symmetries of general relativity and local supersymmetry can be achieved. The new local symmetry necessarily gives rise to a new spin–2 gauge boson, the graviton which superpartner is the spin–3/2 gravitino. The latter acquires mass by absorbing the goldstino[4] as supersymmetry gets spontaneously broken in a similar fashion to the Higgs mechanism. It would solely interact gravitationally and therefore only be of interest for cosmological considerations. In this context, $m_{1/2}$, $m_0$ and $A_0$ arise naturally as a parametrization of the soft terms. Yet, such models are not theoretically viable for they are not renormalizable. Still, non-renormalizable terms are suppressed by powers of the Planck mass, making mSUGRA a perfectly well behaved low-energy phenomenological model. With as few as five free parameters, phase space scans are easily achievable and experimental analysis are greatly facilitated. mSUGRA stands as a very convenient reference model for benchmark studies in the experimental community.

[4]The goldstino intrinsically arises from the breaking of supersymmetry.

The masses of new particles can be re-written using this new set of parameters unified at the GUT scale. For the first two generations of squarks where mixing is small, masses read [70]

$$\begin{aligned}
m^2_{\tilde{e}_\mathrm{R}} = m^2_{\tilde{\mu}_\mathrm{R}} &= m_0^2 + 0.15 m_{1/2}^2 - s_W m_Z^2 \cos 2\beta \\
m^2_{\tilde{e}_\mathrm{L}} = m^2_{\tilde{\mu}_\mathrm{L}} &= m_0^2 + 0.52 m_{1/2}^2 - \left(\frac{1}{2} - s_W\right) m_Z^2 \cos 2\beta \\
m^2_{\tilde{\nu}_e} = m^2_{\tilde{\nu}_\mu} &= m_0^2 + 0.52 m_{1/2}^2 + \frac{1}{2} m_Z^2 \cos 2\beta \\
m^2_{\tilde{u}_\mathrm{R}} = m^2_{\tilde{c}_\mathrm{R}} &= m_0^2 + (0.07 + c_{\tilde{g}}) m_{1/2}^2 + \frac{2}{3} s_W m_Z^2 \cos 2\beta \\
m^2_{\tilde{d}_\mathrm{R}} = m^2_{\tilde{s}_\mathrm{R}} &= m_0^2 + (0.02 + c_{\tilde{g}}) m_{1/2}^2 - \frac{1}{3} s_W m_Z^2 \cos 2\beta \\
m^2_{\tilde{u}_\mathrm{L}} = m^2_{\tilde{c}_\mathrm{L}} &= m_0^2 + (0.47 + c_{\tilde{g}}) m_{1/2}^2 + \left(\frac{1}{2} - \frac{2}{3} s_W\right) m_Z^2 \cos 2\beta \\
m^2_{\tilde{d}_\mathrm{L}} = m^2_{\tilde{s}_\mathrm{L}} &= m_0^2 + (0.47 + c_{\tilde{g}}) m_{1/2}^2 - \left(\frac{1}{2} - \frac{1}{3} s_W\right) m_Z^2 \cos 2\beta
\end{aligned}$$

where $s_W = \sin\theta_W$. The coefficient $c_{\tilde{g}}$ describes the contribution from gluino-quark loops to the running of squark masses

$$c_{\tilde{g}} = \frac{8}{9}\left[\left(\frac{\alpha_s(m_{\tilde{q}})}{\alpha_s(M_\mathrm{GUT})}\right)^2 - 1\right] \approx 5. \tag{2.8}$$

It provides a large contribution from $m_{1/2}$ to squark masses. Also, via the expression $M_i(Q) = m_{1/2}\alpha_i(Q)/\alpha_i(M_\mathrm{GUT})$ for $i = 1, 2$, gaugino masses at the weak scale read [70]

$$\begin{aligned}
M_1 &\approx 0.41 m_{1/2} \\
M_2 &\approx 0.84 m_{1/2}.
\end{aligned}$$

As mentioned in 2.2.1, the gluino mass receives large contributions from quark and squark loops. Due to large Yukawa couplings, the masses of the third generation sfermions and Higgs bosons cannot be easily computed analytically.

## 2.3 Experimental constraints

### 2.3.1 Constraints from colliders experiments

#### Sparticle masses

In the context of the mSUGRA, the strongest experimental bound on the mass of sparticles is due to the non-observation of charginos at LEP with energies in the center-of-mass of up to $\sqrt{s} \approx 208$ GeV. If the lightest chargino is produced in pairs, $e^+e^- \to \tilde{C}_1^+\tilde{C}_1^-$ and $\Delta m \equiv m_{\tilde{C}_1} - m_{\tilde{N}_1}$, the bound reads [72]

$$m_{\tilde{C}_1} \gtrsim 103 \text{ GeV if } \Delta m \sim 1 \text{ GeV}, \quad m_{\tilde{C}_1} \gtrsim 92 \text{ GeV otherwise.}$$

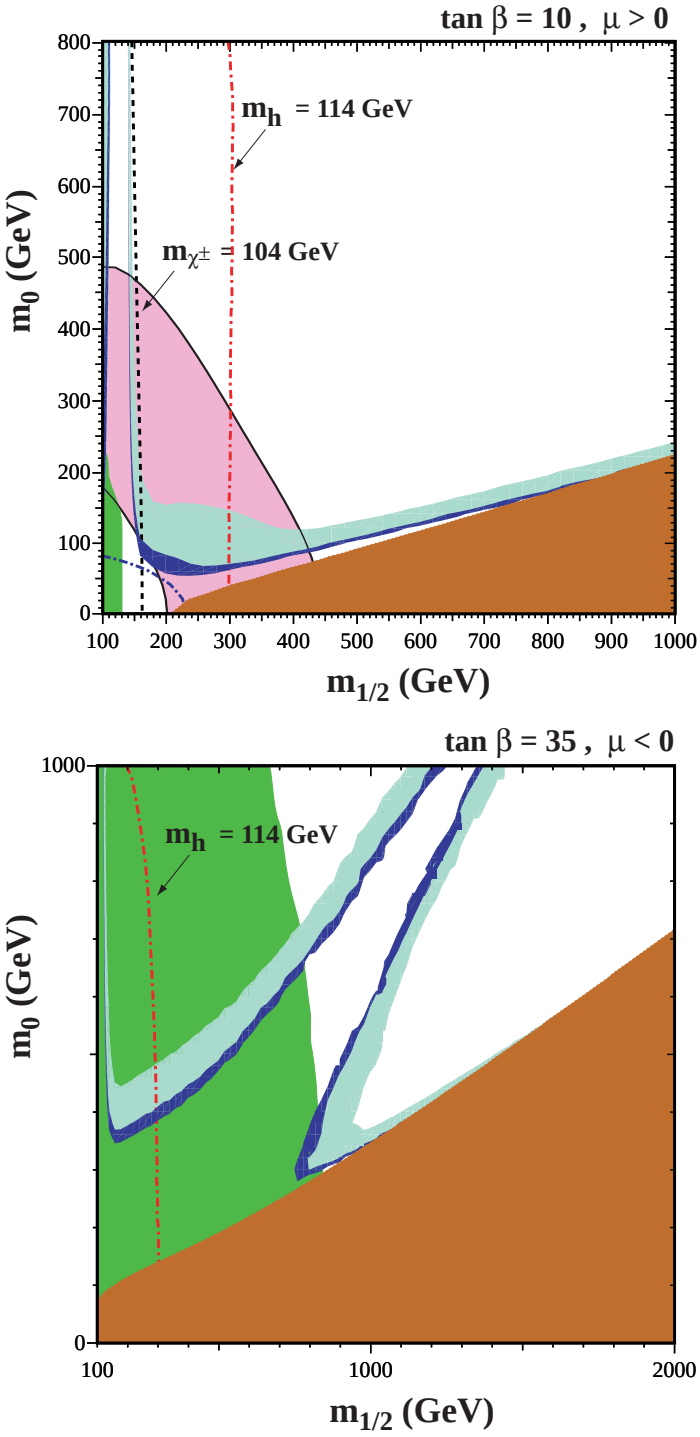


Figure 2.2: Allowed region for mSUGRA in the $m_0 - m_{1/2}$ plane [71]. Only the dark blue region is allowed. In the brown region, the LSP is not the $\tilde{N}_1$, there is no radiative electroweak symmetry breaking and $m_{\tilde{N}_1}$, $m_{\tilde{e}_1}$ or $m_{\tilde{\tau}_1}$ lie below the limits set by LEP. The pink and green regions are favoured by $g_\mu - 2$ and $b \to s\gamma$ measurements respectively. The light blue zone corresponds to previous constraints on the relic density. The dark blue area takes into account updated measurements.

If gaugino masses are universal at the GUT scale, their hierarchy at the weak scale is $M_1 : M_2 : M_3 \sim 1 : 2 : 8$. Hence, the bound on $m_{\tilde{C}_1}$ translates into a lower limit on the mass of the $\tilde{N}_1$:

$$m_{\tilde{N}_1} \gtrsim 50 \text{ GeV if } \tilde{N}_1 \approx \tilde{B}, \quad m_{\tilde{N}_1} \gtrsim 92 \text{ GeV otherwise.}$$

It also translates into a limit on the gluino mass

$$m_{\tilde{g}} \gtrsim 350 \text{ GeV}.$$

The search for stop and sbottom squarks in their decay to neutralino at LEP set a lower limit of around 100 GeV on their mass.
TeVatron experiments CDF and DØ search for the supersymmetry in $p\overline{p}$ collisions with $\sqrt{s} = 1.96$ TeV. In typical mSUGRA parameter sets, the dominant channels for the production of supersymmetry at the TeVatron are chargino and neutralino pairs or associated production followed by quark and gluino pairs.
Charginos and neutralinos associated production is searched for in the tri-lepton channel. Recent studies include 2.3 fb$^{-1}$ of data and did not show any evidence for such a signal [73]. Gluinos are searched for in their decay to $\tilde{b}b$. Studies with 2.5 fb$^{-1}$ of data excluded gluinos lighter than 350 GeV for $m_{\tilde{b}} = 300$ GeV, $m_{\tilde{N}_1} = 60$ GeV and $m_{\tilde{q}} = 500$ GeV [74]. Another study excluded $m < 392$ GeV for $m = m_{\tilde{q}} = m_{\tilde{g}}$ and $m_{\tilde{g}} > 280$ GeV for $m_{\tilde{q}} < 600$ GeV [75]. Stops lighter than 132 GeV were excluded for $m_{\tilde{N}} = 48$ GeV and sbottoms lighter than 193 GeV were excluded for $m_{\tilde{N}} = 40$ GeV.

### Light Higgs boson mass

The limit on the mass of the SM-like Higgs boson set by LEP2 of $m_h > 114$ GeV [25] imposes a stringent constraint on supersymmetric models. Contributions from fermion and sfermion loops should be sufficiently large to lead to a mass above that limit leading to a lower bound . Figure 2.2 shows the allowed regions in the mSUGRA parameter space for low (left) and high (right) $\tan\beta$. The lower bound induced by the Higgs boson mass is shown in red. The largest one-loop correction to the Higgs boson mass is due to top and stop loops. Incidentally, the stop mass depends mostly on $m_{1/2}$ due to its coupling to quarks and gluon via $\alpha_S$. This corresponds to the $c_{\tilde{g}}$ factor is equation 2.8. A lower bound on $m_h$ yields a lower bound on $m_{1/2}$. This limit almost entirely excludes the bulk region.

### Anomalous magnetic moment of the muon

The anomalous magnetic moment of the muon $a_\mu = \frac{g_\mu - 2}{2}$ as measured by the E821 experiment (BNL) deviates from the SM prediction by 2.6 $\sigma$ [76]. This discrepancy can easily be accounted for were supersymmetry to be realized. Consequently, the reproduction of the experimental value constitutes an additional constraint for model building. Supersymmetric contributions to $a_\mu$ involve chargino-sneutrino and neutralino-smuon loops. They are of the form

$$\Delta a_\mu^{\text{SUSY}} \propto \frac{m_\mu^2 \mu m_{1/2} \tan\beta}{M_{\text{SUSY}}^4}.$$

The region favoured by the experimental measurement at the 2 $\sigma$ level is shown in pink on figure 2.2. No such region appear on the $\mu < 0$ plot since in such a case, $\Delta a_\mu^{\mathrm{SUSY}}$ is negative, thus not accounting for the discrepancy.

#### The $b \to s\gamma$ decay

In the case of exact supersymmetry (non-broken), all magnetic moment-transition operator vanish [77]. The direct consequence is that the branching ratio of the $b \to s\gamma$ decay is exactly zero. Yet, as supersymmetry breaks, contributions due to charged Higgs boson/top loops and chargino/stop loops are non-negligible. The approximate agreement between the measured value of the branching ratio of $\overline{B} \to X_s\gamma$ and the prediction of the SM imposes constraint on supersymmetric one-loop contributions, namely, they should cancel. The green domain on figure 2.2 is favoured by this constraint.

### 2.3.2 Constraints from dark matter

It is now well established that a large fraction of the matter content of the Universe is non-baryonic. The motion of many astrophysical objects (stars, gas clouds, globular clusters, or entire galaxies) cannot be fully accounted for by gravitational interacting radiative matter. Also, the observed gravitational lensing effect cannot be explained if only visible matter is considered. The latest measurement of the density of dark matter in the Universe results from a fit of a $\Lambda$CDM cosmological model[5] on the WMAP three-years data [26]. It states that approximately 20% of the energy in the Universe is in the form of dark matter.
Candidates for non-baryonic dark matter include primordial black holes or axions but the most favoured candidates are Weakly Interacting Massive Particles (WIMPs). These are expected to be massive in order to interact gravitationally (a few GeV to a few TeV), neutral to avoid annihilation and colourless. No candidate stands out within the SM and the most favoured candidate is the LSP arising in the context of $R$–parity conserving supersymmetry.

The WIMP relic density can be calculated assuming they were in thermal and chemical equilibrium after inflation. WIMPs drop out of thermal equilibrium once the rate of reactions that change SM particles into WIMPs becomes smaller than the expansion rate of the Universe. After freeze-out, the number of WIMPs to entropy ratio remains constant. A good approximation for the WIMP relic density reads

$$\Omega_{\mathrm{WIMP}} h^2 \approx \frac{0.1 \text{ pb } c}{\langle \sigma_A v \rangle}$$

where $c$ is the speed of light, $\sigma_A$ is the total WIMP annihilation cross-section and $v$ the relative velocity between the WIMPs.

WIMPs are searched for directly through their elastic scattering on nuclei. Although no groundbreaking results were published for the direct detection of WIMPs, the

[5]Cold Dark Matter with a cosmological constant.

DAMA/LIBRA experiment claimed to have observed an annual modulation of its signal with a significance of 8.2 $\sigma$ [78]. This controversial result is believed to be a signal for WIMPs as earth pass through the galactic dark matter cloud. On the other hand, the ATIC balloon experiment reports an excess of galactic cosmic ray electrons with energies of 300 to 800 GeV [79]. These could arise from the annihilation of WIMPs with a mass of around 600 GeV. WIMPs can also be searched for indirectly. They can be captured by massive celestial objects and annihilate into neutrinos, gamma rays, positrons, antiprotons or antinuclei. For instance, an increased flux of high-energy neutrinos coming from the sun or the earth could sign the presence of WIMPs. Current experiments could not set competitive limits in the mass domain proposed by supersymmetry. The Fermi Gamma-ray Space Telescope (formerly GLAST) was launched in June 2008 and provides an interesting sensitivity in that domain. It will search for an excess of gamma rays from the center of the galaxy in the 30 MeV to 300 GeV range.

The occurrence of a candidate for dark matter, i.e. with the right mass and couplings, is a strong discriminator to constrain parameter spaces. For instance, in the $m_0 - m_{1/2}$ plane of the mSUGRA parameter space, four regions can be designed according to the behaviour of their LSP:

- The bulk region corresponds to the low–$m_0$ and low–$m_{1/2}$ domain. In this area, all sparticles and the Higgs bosons are light. This domain was dramatically reduced by WMAP results [71] due to the large neutralino annihilation cross-section. This region can be seen on figure 2.2 as a blob on the lower left corner of the upper plot.

- The co-annihilation region corresponds to the low–$m_0$ horizontal blue stripe on the upper plot of figure 2.2. In that domain, $m_{\tilde{\tau}_1} \approx m_{\tilde{N}_1}$ and $\tilde{\tau}_1 - \tilde{N}_1$ and $\tilde{\tau}_1 - \tilde{\tau}_1$ annihilation contribute to reduce the relic density to sufficiently low values [80].

- The rapid annihilation funnel region is the domain where $\tan\beta$ is large and $m_A$ and $m_H \approx 2m_{\tilde{N}_1}$. Hence, neutralinos rapidly annihilate into heavy Higgs bosons leading to large di-fermion resonances. On figure 2.2, this region can be seen on the lower plot, corresponding to the large $\tan\beta$ case.

- The focus point region corresponds to the high–$m_0$ area were scalars are heavy. The LSP has a large higgsino component leading to a large annihilation rate through a Higgs boson.

## 2.4 Supersymmetry at the LHC

If it is realized, supersymmetry is expected to appear in the energy range probed by the LHC. With an energy of 14 TeV in the centre-of-mass, the LHC can produce new particles with masses up to several TeV.
The search for supersymmetry at the LHC has been intensively prepared by dedicated working groups and is articulated around a number of benchmark parameter points in

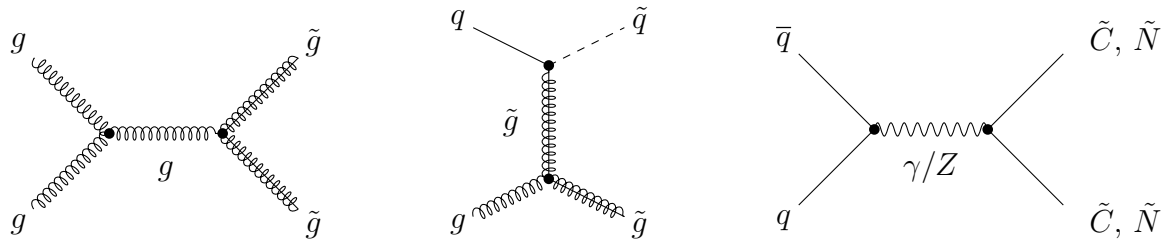


Figure 2.3: Typical processes contributing to the production of supersymmetry at the LHC.

the mSUGRA phase space such as the SPS1a point (see section 5.2.1). However, the variety of resulting signatures covers a larger range of possible theoretical scenarios. In such points, new particles have masses of the order of 100 GeV for the $\tilde{N}_1$ LSP, 115 GeV for the Higgs boson to 800 GeV for the gluino allowing for total supersymmetry production cross-sections varying from 2 to 300 pb. The dominant contributions arise from the production of gluino pairs, squark pairs or gluino-squark associated production by gluon or gluon-quark fusion. Also, chargino or neutralino pairs or associated production can proceed through the annihilation of a quark pair. Figure 2.3 shows three typical processes to produce supersymmetry at the LHC. After production, supersymmetric particles decay into other supersymmetric particles along with jets or lepton with large transverse momenta. These decay chains proceed until the LSP is produced and escapes the detector leading to large missing transverse energy. Hence, typical studied signatures include numerous jets with high transverse momenta, large missing transverse energy and possibly isolated leptons. The typical SM backgrounds for search topologies include QCD multi-jets production, $t\bar{t}$ events, vector bosons plus jets, or vector boson pairs.

Figure 2.4 shows the 1 fb$^{-1}$ reach for a $5\sigma$ discovery of mSUGRA in the $m_0 - m_{1/2}$ plane for different search strategies and for two different parameter sets. $m_0$ can be probed up to values of a few TeV and $m_{1/2}$ up to about 500 GeV.

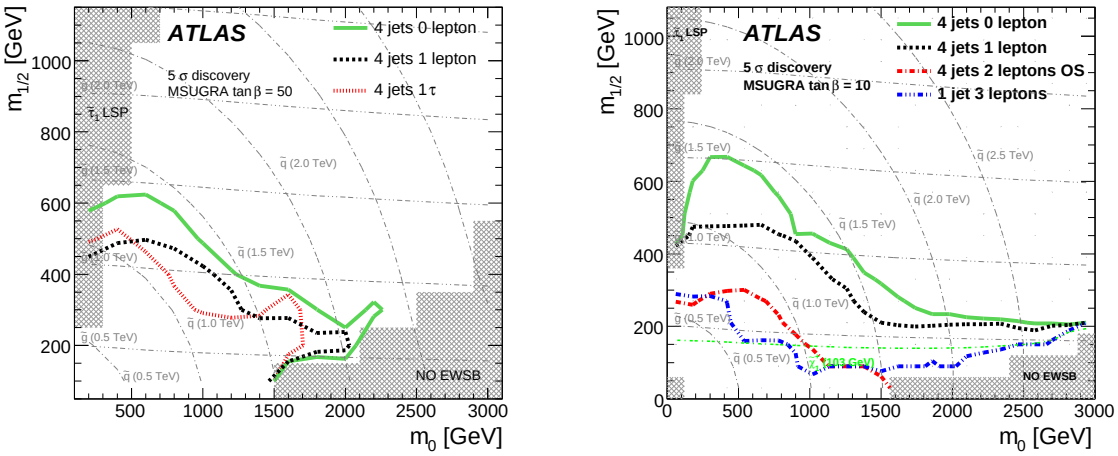


Figure 2.4: 1 fb$^{-1}$ reach for a $5\sigma$ discovery of mSUGRA in the ATLAS experiment in the $m_0 - m_{1/2}$ plane for different search strategies. On the left $\tan\beta = 50$ while on the right $\tan\beta = 10$. The horizontal and curved grey lines indicate gluino and squark mass contours respectively in steps of 500 GeV [81].

# Chapter 3

# A Toroidal LHC ApparatuS

*"Some kind of happiness is measured out in miles*
*Some kind of innocence is measured out in years"*

John Lennon – *Hey bulldog*

*"Success is the ability to go from one failure to another with no loss of enthusiasm"*

Winston Churchill

The ATLAS Collaboration is one of the four experiments installed along the Large Hadron Collider (LHC) at CERN (Geneva, Switzerland). Its purpose is to search for the Higgs boson as well as supersymmetry or other extensions to the Standard Model. The development of the detector started in 1990, the installation in 2000 and the commissioning in 2004. In 2008, the detector was installed and commissioned. ATLAS immediately started and is still recording cosmic muons crossing the detector. The LHC is now is a phase of consolidation of its magnet system and collision are expected in 2009. As of now, the ATLAS Collaboration counts more than 2000 signing authors in more than 160 institutes in 37 countries.

## 3.1 The Large Hadron Collider

The LHC is a proton-proton collider with a nominal center-of-mass energy of 14 TeV and a design luminosity of $10^{34}$ cm$^{-2}$ s$^{-1}$. It is installed in the LEP circular tunnel under the French-Swiss border. Its installation started in 2000 and its assembly ended in 2007. It is 27 km in circumference and lies between 50 and 175 meters below the surface. The beam trajectory is bent by 1232 14.3 meters long 35 tons superconducting dipole magnets which contain the two beam pipes. The dipoles generate a magnetic field of 8.4 T at a current of around 11.7 kA. 392 quadrupoles magnets are used to focus the beams. Magnets are cooled down to 1.9 K by liquid Helium.

The acceleration complex comprises several steps. 50 MeV protons are generated by the LINAC 2 linear accelerator. The Proton Synchrotron booster (PS) increases the

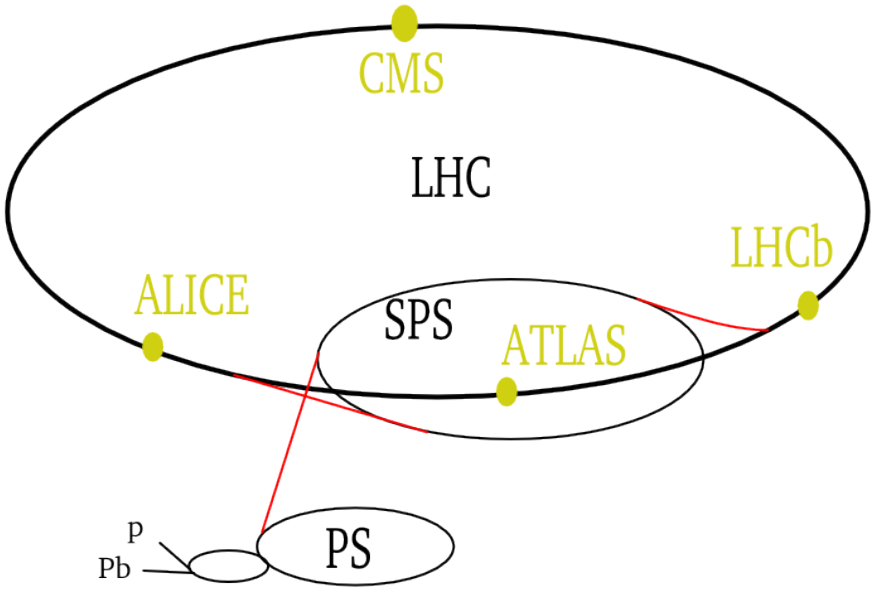


Figure 3.1: Configuration of the acceleration complex and locations of the four LHC experiments.

energy to 1.4 GeV before the SPS accelerates the beam to 450 GeV and injects it into the LHC. Beams are expected to stay in the ring for ten to twenty hours. Protons are grouped in bunches of $10^{10}$, 2808 of which will circulate in the ring separated by 25 ns. The total inelastic proton-proton cross section at the LHC is 80 mb, that is $10^9$ events per second at design luminosity. For each bunch crossing, an average of 23 interactions will occur simultaneously, inducing pile-up (see section 3.4.1).

On September 10, 2008, the LHC injected its first proton. They travelled several times around the ring, allowing experiments to record splash events[1]. On September 29, during the test of the last magnet sector of the LHC, a faulty splice between two superconducting bus bar caused the release of a large amount of helium in the tunnel. Several magnets were damaged or displaced. The LHC subsequently switched to shutdown mode in order to replace, fix or realign the magnets. The LHC is expected to start injecting protons again in 2009. The beam energy will be pushed to a few TeV and the luminosity progressively raised to $10^{33}$ cm$^{-2}$ s$^{-1}$. Table 3.1 summarize the general parameters of the LHC. Table 3.2 list typical cross-sections expected at the LHC for standard processes as well as new physics.

Four experiments are installed along the LHC. Two general purpose detectors, ATLAS and CMS (Compact Muon Solenoid) are located one across the other respectively at Point 1 (Meyrin, Switzerland) and 5 (Cessy, France). Experimental techniques are

[1] A splash event occurs when protons hit the collimators placed before the detector, triggering large forward showers.

| | Nominal values | Early runs |
|---|---|---|
| Beam energy | 7 TeV | 5 TeV |
| Luminosity | $10^{34}$ cm$^{-2}$ s$^{-1}$ | up to $10^{33}$ cm$^{-2}$ s$^{-1}$ |
| Protons per bunch | $10^{10}$ | $10^{10}$ |
| Bunch separation | 25 ns | 75 ns |

Table 3.1: General parameters of the LHC. Values for the early running phase are also reported.

| Final state | Cross–section |
|---|---|
| $b\bar{b}$ | $\mathcal{O}(100\ \mu\text{b})$ |
| Jets | $\mathcal{O}(1\ \mu\text{b})$ |
| $t\bar{t}$ | $\mathcal{O}(1\ \text{nb})$ |
| Higgs | $\mathcal{O}(1\ \text{pb})$ |
| Supersymmetry | $\mathcal{O}(10\ \text{pb})$ |

Table 3.2: Typical cross-sections at the LHC

complementary while physics goals are the same. In CMS, calorimetry is realized by scintillating lead tungstate crystal located within a solenoid coil, whereas ATLAS chose liquid argon as sampling material and lead and stainless steel as absorbers (see section 3.3.2) situated outside of a solenoid coil.

At Point 8, LHCb will study $b$–physics and aims at measuring the parameters of CP violation in an asymmetric detector. At Point 2, ALICE (A Large Ion Collider Experiment) is a heavy ion experiment. For this experiment, the LHC will switch to lead ion accelerator. Pb-Pb nuclei collisions will be studied at a centre of mass energy of 5.5 TeV per nucleon. The resulting temperature and energy density are expected to be large enough to generate a quark-gluon plasma.

## 3.2 Design overview

The LHC provides a rich physics potential, ranging from more precise measurements of Standard Model parameters to the search for the Higgs boson and new physics. Requirements for the ATLAS detector system have been defined using a set of standard or new processes which will be or might be observed. The high luminosity and large cross-sections at the LHC enable high precision tests of QCD, electroweak interactions, and flavour physics. The top quark is produced at the LHC at a rate of a few tens of Hertz, providing the opportunity to test its couplings and spin. The search for the Higgs boson and supersymmetry have been used as benchmarks to establish the performance of ATLAS.
A promising channel for the search of the Higgs boson at low mass ($m_h < 130$ GeV) is the $h \to \gamma\gamma$. Above 130 GeV, $h \to ZZ^* \to 4\ell$ is the golden channel. For low scalar

mass ($m_0 < 1$ TeV), supersymmetric production is dominated by gluino and squark pairs. These decay into other squarks or neutralinos/charginos along with one or more jets or leptons. In turn, neutralinos and charginos will cascade down to the Lightest Supersymmetric Particle (LSP), producing again many jets and isolated leptons on the way. The remaining LSPs will escape the detector leading to large missing transverse energy ($\not\!\!E_{\mathrm{T}}$). $Z'$ and $W'$ heavy objects predicted by other models of new physics will produce lepton or jet pairs with very high transverse momenta ($p_{\mathrm{T}}$). Thus, both the Higgs boson and new physics produce events featuring numerous jets, isolated leptons and photons and $\not\!\!E_{\mathrm{T}}$ in a very busy multi-interaction environment. Fundamental requirements for the detector include :

- very good electromagnetic calorimetry for electron and photon measurements,
- full-coverage hadronic calorimetry for accurate jet and missing transverse energy measurements,
- good muon identification and momentum resolution over a wide range of momenta,
- good charged-particle momentum resolution and reconstruction efficiency in the tracking detector and secondary vertex detection close to the interaction point for $\tau$ and $b$ tagging,
- highly efficient triggering on low–$p_{\mathrm{T}}$ objects with sufficient background rejection,
- fast, radiation resistant electronics and sensors elements.

The ATLAS detector [29] is 44 meters long, 25 meters high and weighs about 7000 tons. It is a cylinder whose axis ($z$ axis) is the beam pipe. The $x$ axis points towards the center of the LHC ring and the $y$ axis points upwards. In polar coordinates, two quantities are used : The azimuthal angle $\phi$ and the pseudo-rapidity $\eta = -\ln\tan\frac{\theta}{2}$. $\theta$ is the polar angle. The positive $\eta$ half of the detector is called A and the other half C. The transverse plan is the $xy$ plan.

Figure 3.2 shows the overall layout of the detector. The magnet configuration comprises a thin superconducting solenoid surrounding the tracking detector cavity, and three large superconducting toroidal coils (one barrel and two end-caps) arranged with an eight-fold azimuthal symmetry around the calorimeters.
The tracking detector (section 3.3.1) is immersed in a 2 T solenoidal field and covers the range $|\eta| < 2.5$. Pattern recognition, momentum and vertex measurements and electron identification are achieved with a combination of discrete, high-resolution semiconductor pixel and strip detectors in the inner part of the tracking volume, and straw-tube tracking detectors with the capability to generate and detect transition radiation in its outer part.
High granularity liquid-argon (LAr) electromagnetic sampling calorimeters (section 3.3.2), with excellent performance in terms of energy and position resolution, cover the pseudo-rapidity range $|\eta| < 3.2$. The hadronic calorimetry in the range $|\eta| <$

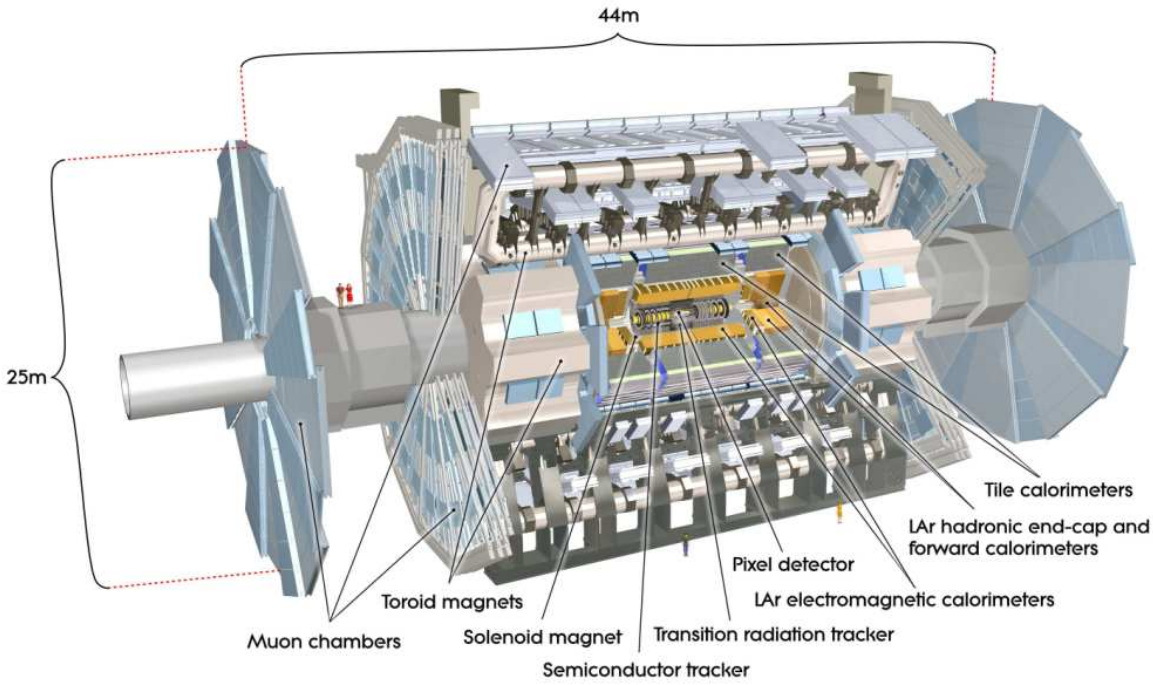


Figure 3.2: Cut-away view of the ATLAS detector.

1.7 is provided by a scintillator-tile calorimeter, which is separated into a large barrel and two smaller extended barrel cylinders, one on either side of the central barrel. In the end-caps ($|\eta| > 1.5$), LAr technology is also used for the hadronic calorimeters, matching the outer $|\eta|$ limits of end-cap electromagnetic calorimeters. The LAr forward calorimeters provide both electromagnetic and hadronic energy measurements, and extend the pseudo-rapidity coverage to $|\eta| = 4.9$.
The calorimeter is surrounded by the muon spectrometer (section 3.3.3). The air-core toroid system, with a long barrel and two inserted end-cap magnets, generates strong bending power in a large volume within a light and open structure. Multiple-scattering effects are thereby minimised, and excellent muon momentum resolution is achieved with three layers of high precision tracking chambers. The muon instrumentation includes trigger chambers with very good timing resolution. The muon spectrometer defines the overall dimensions of the ATLAS detector.

## 3.3 Detectors

### 3.3.1 Tracking

With approximately one thousand particles emerging from the interaction point every bunch crossing at design luminosity, high-precision measurement must be made with fine detector granularity to achieve momentum and vertex resolution requirements. This performance is achieved by combining three sub-systems.

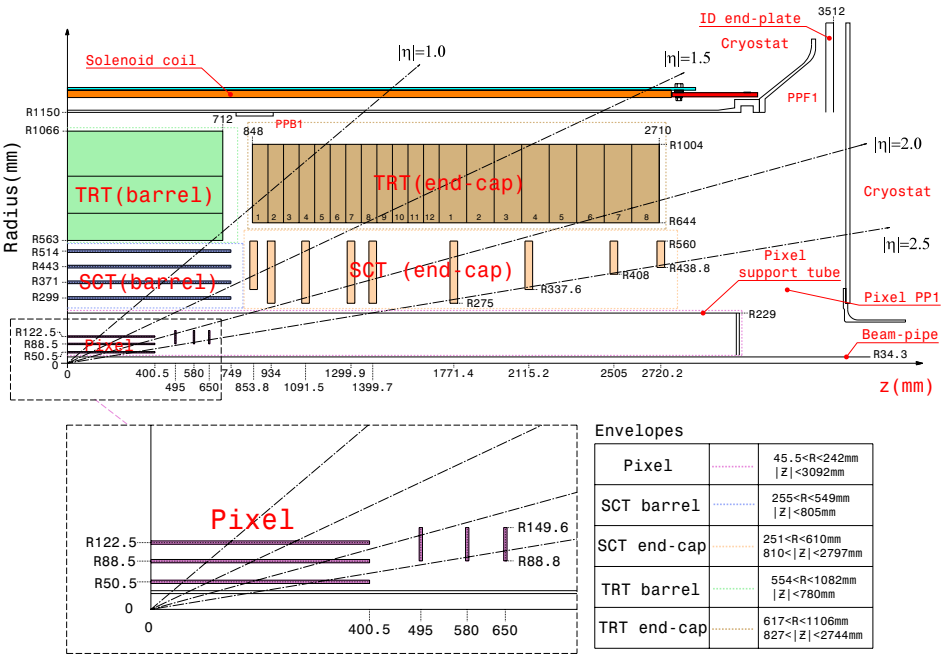


Figure 3.3: Plan view of a quarter of the ATLAS tracking detector.

### Pixels

Closest to the beam axis is the silicon pixel detector. Three layers of silicon pixels located 50.5, 88.5 and 122.5 mm away from the beam axis cover a pseudo-rapidity range of $|\eta| < 2.5$. Each layer is paved with $50 \times 400$ $\mu$m$^2$ pixels for a total of 80.4 million readout channels. The first layer starting from the beam axis is called the vertexing-layer, also called $B$–layer, as it allows for a very precise determination of primary and secondary vertices, hence helpful for the tagging of $b$–jets. The vertexing-layer is also used to separate electrons from photons (see section 4.3.2). Three end-cap rings are situated in the $x - y$ plane at $z = 495$, 580 and 650 mm. Each ring spans in radii from 89 to 150 mm. The accuracies in the barrel are 10 $\mu$m in $R\phi$ and 115 $\mu$m in $z$ and 10 $\mu$m ($R\phi$) and 115 $\mu$m ($R$) in the rings.

### Semi–Conductor Tracker

Around the pixel detector is the the Semi-Conductor Tracker (SCT). In the barrel ($|z| < 749$ mm for the SCT), four concentric layers ($r = 299$, 371, 443 and 514 mm) host two sets of silicon strips each. Each set is 80 $\mu$m wide, up to 126 mm long. One of the strip is parallel to the beam axis while the other is twisted with an angle of 40 mrad to measure both $z$ and $R - phi$ with a resolution of 580 $\mu$m and 17 $\mu$m respectively. In the end-cap, nine rings ($z = 854$ to 2720 mm) bear radial strips as well as 40 mrad twisted strips. The combination of hits from strips in the same layer constitutes a space-point.

#### Transition Radiation Tracker

The last sub-detector before the solenoid is the Transition Radiation Tracker (TRT). It covers $|\eta| < 2$, its barrel extends to $|z| = 712$ mm and its end cap from $|z| = 848$ to 2710 mm. The TRT is made of 4 mm diameter straw tubes filled with 70% xenon, 20% methane and 10% $CO_2$. In the centre of each straw runs a gold clad tungsten wire, the anode, while the tube plays the role of the cathode. In the barrel, straws run parallely to the beam axis and the wires split at $z = 0$. In the end-cap, they run along $\phi$ in a concentric fashion around the $z$ axis. The TRT solely provides a measurement of $R - \phi$ the resolution of which is 130 $\mu$m per straw. Each particle coming from the interaction point crosses 36 tubes on its way out. For each tube, the drift time of signal is measured leading to an information on perigee of the particle with respect to anode. Without any information, only a drift circle centered on the anode can be reconstructed. Approximately 351,000 channels read information from the TRT.

### 3.3.2 Calorimetry

The ATLAS calorimeters consist of a number of sampling detectors with $\phi$–symmetry and pseudo-rapidity coverage up to 4.9. The calorimeters closest to the beam line are housed in three cryostats, one barrel and two end-caps. The barrel cryostat contains the electromagnetic barrel calorimeter, whereas the two end-cap cryostats each contain an electromagnetic end-cap calorimeter (EMEC), a hadronic end-cap calorimeter (HEC), located behind the EMEC, and a forward calorimeter (FCal) to cover the region closest to the beam. All these calorimeters use liquid argon as the active detector medium; liquid argon has been chosen for its intrinsic linear behaviour, its stability of response over time and its intrinsic radiation-hardness. Figure 3.4 shows a cut-away view of the ATLAS calorimeter system. Figure 3.5 details the granularity in each layer.

#### Presampler

The presampler is a 11 mm thick liquid argon layer located inside the barrel cryostat, covers $|\eta| < 1.8$ and has a granularity of $\Delta\eta \times \Delta\phi = 0.025 \times 0.098$. It provides an estimation of the energy lost by particles in the tracking detector and solenoid in order to correct the measurements of the barrel calorimeters.

#### Electromagnetic calorimeter

The electromagnetic (EM) calorimeter aims at detecting and measuring electrons and photons. Yet, it is also helpful in the reconstruction of muons and jets. It was designed to optimize resolution and efficiency for the measurement of photons in the $h \to \gamma\gamma$ channel and electrons in supersymmetric cascades as well as in the $h \to 4\ell$ channel. Its very fine granularity ($\Delta\eta \times \Delta\phi = 0.025 \times 0.0245$) and its pseudo-rapidity coverage ($|\eta| < 2.5$) allow for a very strong jet rejection and $e/\gamma$ identification.
Upon entering the calorimeter, incoming particles hit the lead, triggering an electromagnetic shower. The particles in the shower ionize the liquid argon (LAr) which consequently drifts toward kapton electrodes. The latter collect the signal. The barrel

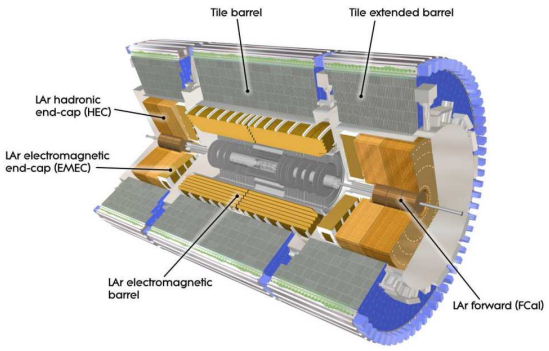


Figure 3.4: Cut-away view of the ATLAS calorimeter system.

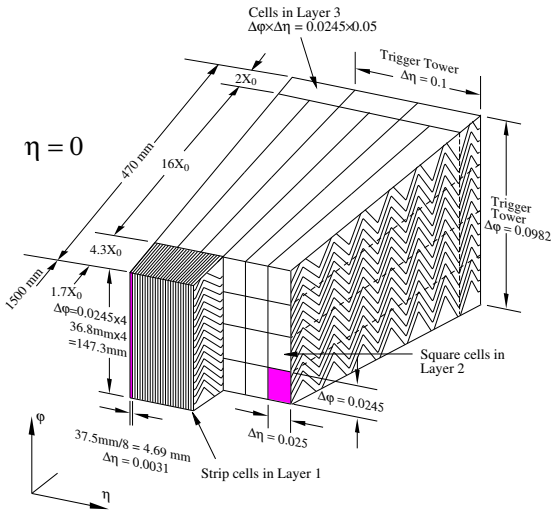


Figure 3.5: Sketch of a barrel module where the different layers are visible along with their granularity.

EM calorimeter covers $|\eta| < 1.475$ and is made of two half-barrels, one for $\eta > 0$ and the other for $\eta < 0$. Each half is 3.2 m long and extends from $R = 1.5$ to 1.97 m. It consists of 1024 accordion-shaped lead absorbers providing perfect continuity in $\phi$, interleaved with liquid argon and readout electrodes in the centre. The total depth starts from 22 radiation length ($X_0$) at $\eta = 0$ and increases to 30 $X_0$ at $|\eta| = 0.8$. Then, from 24 to 33 $X_0$ for $0.8 < |\eta| < 1.3$.
The EM barrel calorimeter is divided in depth in three compartments, also called layers :

- The innermost compartment, the *strips*, is only 4.3 $X_0$ deep. Its very fine $\eta$ granularity ($\Delta\eta \times \Delta\phi = 0.0031 \times 0.098$) allows for an efficient $\gamma - \pi^0$ separation.

- The next compartment, the *middle*, is 16 $X_0$ deep and measures the largest part of the electromagnetic shower. Its $\phi$ granularity is finer than that of the strips ($\Delta\eta \times \Delta\phi = 0.025 \times 0.0245$).

- The last compartment, the *back*, is only 2 $X_0$ deep and receives the tail of the shower. Its granularity is $\Delta\eta \times \Delta\phi = 0.1 \times 0.0245$.

An elementary $\Delta\eta \times \Delta\phi$ pad is called a cell. They are the building blocks for clusters which in turn are used to reconstruct electrons and photons (section 3.4.4).

### Hadronic calorimeter

The hadronic calorimeter is located outside the EM calorimeter and extends out to $|\eta| = 4.9$. It aims at differentiating strongly interacting showers from electrons and photons which do not penetrate as deeply. It comprises two parts.

Tile calorimeter The tile calorimeter is placed directly outside the EM calorimeter envelope. Its barrel covers the region $|\eta| < 1$, and its two extended barrels the range $0.8 < |\eta| < 1.7$. It is a sampling calorimeter using 14 mm thick steel sheets as the absorber and 3 mm thick scintillating tiles as the active material. Radially, the tile calorimeter extends from $R = 2.28$ to 4.25 m. It is segmented in depth in three layers, approximately 1.5, 4.1 and 1.8 $X_0$ thick for the barrel and 1.5, 2.6, and 3.3 $X_0$ for the extended barrel. The total detector thickness at the outer edge of the tile-instrumented region is 9.7 $X_0$ at $\eta = 0$. The granularity is $\Delta\eta \times \Delta\phi = 0.1 \times 0.1$ for the two innermost layers and $0.2 \times 0.1$ for the outermost one.

LAr end-cap The Hadronic End-cap Calorimeter (HEC) consists of two independent wheels per end-cap, located directly behind the end-cap electromagnetic calorimeter and sharing the same LAr cryostats. It extends from $|\eta| = 1.5$ to 3.2, thereby overlapping with both the tile calorimeter and the forward calorimeter. Each wheel is divided into two segments in depth, for a total of four layers per end-cap. The wheels closest to the interaction point are built from 25 mm thick parallel copper plates, while those further away use 50 mm thick copper plates. The outer radius of the copper plates is 2.03 m, while the inner radius is 0.475 m (except in the overlap region with the forward calorimeter where this radius becomes 0.372 m). The copper plates are interleaved with 8.5 mm LAr gaps, providing the active medium for this sampling calorimeter. The granularity is $\Delta\eta \times \Delta\phi = 0.1 \times 0.1$ for $1.5 < |\eta| < 2.5$ and $0.2 \times 0.2$ for $2.5 < |\eta| < 3.2$.

Forward calorimeter The Forward Calorimeter (FCal) is integrated into the end-cap cryostats. It is approximately 10 interaction lengths deep, and consists of three modules in each end-cap: the first, made of copper, is optimised for electromagnetic measurements, while the other two, made of tungsten, measure predominantly the energy of hadronic interactions. Each module consists of a metal matrix, with regularly spaced longitudinal channels filled with the electrode structure consisting of concentric rods and tubes parallel to the beam axis. The LAr in the gap between the rod and the tube is the sensitive medium. The granularity is $\Delta\eta \times \Delta\phi = 0.2 \times 0.2$.

### 3.3.3 Muon spectrometry

The muon spectrometer is based on the magnetic deflection of muon tracks in the large superconducting air-core toroid magnets, instrumented with separate trigger and tracking chambers. Over the range $|\eta| < 1.4$, magnetic bending is provided by the large barrel toroid. For $1.6 < |\eta| < 2.7$, muon tracks are bent by two smaller end-cap magnets inserted into both ends of the barrel toroid. Over $1.4 < |\eta| < 1.6$, magnetic deflection is provided by a combination of barrel and end-cap fields. This magnet configuration provides a field which is mostly orthogonal to the muon trajectories.
In the barrel region, tracks are measured in chambers arranged in three cylindrical layers around the beam axis at radii of approximately 5, 7.5 and 10 m. In the transition between the barrel and end–cap regions, the chambers are installed in planes

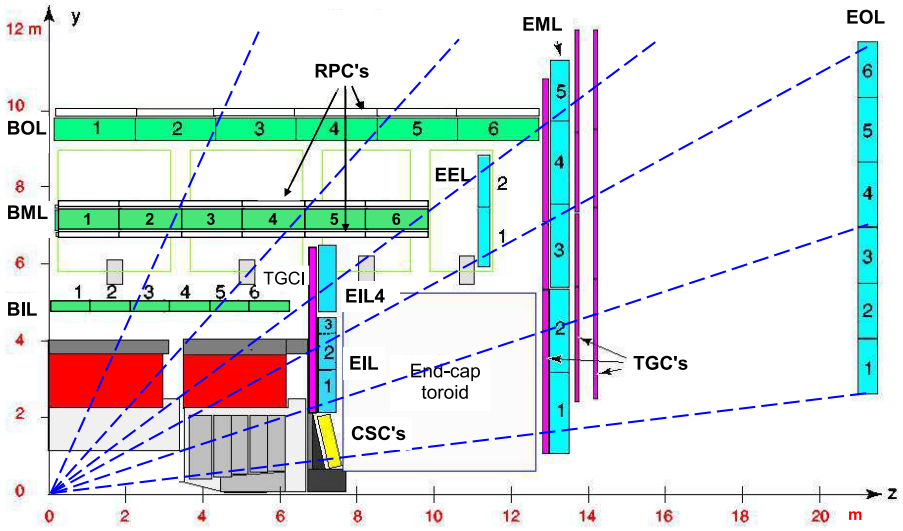


Figure 3.6: Plan view of a quarter of the ATLAS muon spectrometer. Monitored drift tubes are shown in green in the barrel and blue in the end–cap, cathode strips chambers in yellow, resistive plate chambers in white and thin gap chambers in magenta.

perpendicular to the beam at distances of 7.4, 10.8, 14 and 21.5 m from the interaction point.
The muon system is instrumented with two kinds of chambers, one for precision momentum measurement and the other for triggering.

### Precision chambers

Monitored Drift Tubes The 1150 MDT's constitute the bulk of the muon system as they are present on all layers of both barrel and end–cap. The basic element of the MDT chambers is a 0.9 to 6.2 m long pressurized drift tube with a diameter of 30 mm, operating with argon (93%) and $CO_2$ (7%) gas at 3 bars. Electrons resulting from the ionisation are collected at the central tungsten-rhenium wire. MDT's allow for a very good track reconstruction with a resolution of 300 $\mu$m.

Cathode Strips Chambers CSC's are used in the area where MDT's cannot bear the particle flux, that is $|\eta| > 2$. They are located in the innermost end–cap wheels, at $|z| = 7.4$ m. The CSC system consists of two disks with eight chambers each. Each chamber contains four CSC planes resulting in four independent measurements in $\eta$ and $\phi$ along each track.
The CSC's are multi-wire proportional chambers with the wires oriented in the radial direction. Both cathodes are segmented, one with the strips perpendicular to the wires, providing the precision coordinate, and the other parallel to the wires providing the transverse coordinate. The position of the track is obtained by interpolation between the charges induced on neighbouring cathode strips. Strips are 5.08 mm apart and the

gas is a mixture of argon (30%), $CO_2$ (50%) and $CH_4$ (20%). The CSC's provide a resolution of 50 to 70 $\mu$m.

#### Trigger chambers

Resistive Plate Chambers In the barrel, RPC's cover MDT's on both side in the second layer and alternatively on the inner and outer side in the third layer. In the end–caps, they cover the inner side of MDT's in the first and third layers. Two extra wheels are located between the third and fourth layers.
The RPC is a gaseous parallel electrode-plate detector. Two resistive plates, made of phenolic-melaminic plastic laminate, are kept parallel to each other at a distance of 2 mm by insulating spacers. The electric field between the plates allows avalanches to form along the ionising tracks towards the anode. The gas used is a mixture of $C_2H_2F_4$ (94.7%), Iso-$C_4H_{10}$ (5%) and $SF_6$ (0.3%). A RPC trigger chamber is made of two rectangular detectors, contiguous to each other, each of whom, consists of two independent detector layers read out by two orthogonal sets of pick-up strips. RPC's provide a resolution of 1 cm and 25 ns.

Thin Gap Chambers TGC's are similar in design to CSC's with 1.8 mm anode separation and 2.4 mm cathode separation. The gas is a mixture of $CO_2$ (55%) and n–$C_5H_{12}$. TGC provide level one trigger signal as well as $\eta$ and $\phi$ information for the offline reconstruction.

### 3.3.4 Magnets

ATLAS features a unique hybrid system of four large superconducting magnets. This magnetic system is 22 m in diameter and 26 m in length, with a stored energy of 1.6 GJ and provides a magnetic field over a volume or approximately 12,000 $m^3$. The ATLAS magnet system consists of

- a solenoid which is aligned on the beam axis and provides a 2 T axial magnetic field for the tracking detector. It is incorporated into the cryostat in order to minimize the radiative thickness in front of the barrel electromagnetic calorimeter,

- a barrel toroid and two end-cap toroids which produce a toroidal magnetic field of approximately 0.5 T and 1 T for the muon detectors in the central and end-cap regions, respectively.

## 3.4 Physics events

### 3.4.1 Collision environment

The analysis of final states at the LHC is very much complicated by the nature of hadronic interactions. Indeed, as protons collide, only one parton (gluon or quark) in

each proton is expected to take part in the hard scattering process. This is a high–$q^2$ interaction (high energy exchange) potentially leading to the production of heavy particles such as electroweak bosons, top quarks, the Higgs boson or new particles. However, as opposed to electron-positron colliders, the remaining partons (remnants) in the incoming protons are also expected to scatter onto one another. However, these interactions are expected to happen at much lower $q^2$ and will not produce any interesting final state. Then, outgoing objects are not very much deviated from the initial beam direction and hence are mostly expected in the forward region. Hence, interesting physics are expected in the central region of detectors, that is at high transverse momenta. The central region can also be populated with gluon jets and photons springing from initial and final state radiation (ISR and FSR). Indeed, partons bearing a large fraction of the energy of the incoming protons ($x$) are naturally the one participating in the hard scatter. These or those produced in the scattering are likely to emit gluons or photons before or after the interaction took place leading to additional jets or photons in the detector. ISR, FSR and low–$q^2$ scatterings from remnants constitute the underlying event.

In addition, the high luminosity of the LHC causes events to pile-up in the detectors leading to minimum bias events. Indeed, as mentioned in section 3.1, protons in the LHC beams are packed into bunches of $10^{10}$. Hence, many proton pairs can collide simultaneously leading to multiple interactions. An efficient trigger system (section 3.4.2) is necessary to filter non-interesting events. Some of them can still make it to the recorded data if they are simultaneous with an interesting hard scattering leading to a minimum bias event.

### 3.4.2 Trigger

As show in table 3.2, new physics are expected to occur at the frequency of one event in about $10^{10}$. Thereby, the combination of very high luminosity and underlying events forces the use of an efficient trigger system.
The trigger system has three distinct levels: level one (L1), level two (L2) and the event filter (EF). Each trigger level refines the decisions made at the previous level and, where necessary, applies additional selection criteria. The first level uses a limited fraction of the total detector information to make a decision in less than 2.5 $\mu$s, reducing the rate from 40 MHz at design luminosity to about 75 kHz. The two higher levels access more detector information for a final rate of up to 200 Hz with an event size of approximately 1.3 Mbyte.

- The L1 trigger searches for high transverse-momentum muons, electrons, photons, jets, and $\tau$ decaying into hadrons, as well as large missing and total transverse energy. Its selection is based on information from a subset of detectors. High transverse-momentum muons are identified using trigger chambers in the barrel and end-cap regions of the spectrometer. Calorimeter selections are based on reduced granularity ($\Delta\eta \times \Delta\phi = 0.1 \times 0.1$) information from all the calorimeters. Table 3.3 list examples of available trigger items for the start-up luminosity

| | | | | | | |
|---|---|---|---|---|---|---|
| $e/\gamma$ | EM3 | EM7 | EM13(i) | EM18(i) | EM23i | EM100 |
| | 2EM3 | 2EM7 | 2EM13(i) | 2EM18(i) | 2EM23i | 3EM7 |
| Jets | J10 | J18 | J23 | J42 | J70 | J120 |
| | 3J10 | 3J18 | 4J10 | 4J18 | 4J23 | |
| Muons | MU4 | MU6 | MU10 | MU15 | MU20 | MU40 |
| | 2MU4 | MU4/6 | 2MU6 | 2MU10 | 2MU20 | 3MU6 |
| Missing $E_{\mathrm{T}}$ | XE25 | XE30 | XE40 | XE50 | XE70 | XE80 |

Table 3.3: Examples of available trigger items for a luminosity of $10^{31}\mathrm{cm}^{-2}\mathrm{s}^{-1}$. The leading letter indicates the nature of the object, the following number indicates the $p_{\mathrm{T}}$-threshold and (i) indicates an optional isolation requirement.

of $10^{31}\mathrm{cm}^{-2}\mathrm{s}^{-1}$. Results from the L1 muon and calorimeter triggers are processed by the central trigger processor, which implements a trigger menu made up of combinations of trigger selections. The L1 trigger also defines one or more Regions-of-Interest (RoI's), that is the geographical coordinates in $\eta$ and $\phi$, of those regions within the detector where its selection process has identified interesting features. The RoI data include information on the type of feature identified and the criteria passed. This information is subsequently used by the high-level trigger.

- The L2 selection is seeded by the RoI information provided by the L1 trigger. L2 selections use, at full granularity and precision, all the available detector data within the RoI's (approximately 2% of the total event data). The L2 menus are designed to reduce the trigger rate to approximately 3.5 kHz, with an event processing time of about 40 ms, averaged over all events.

- The final stage of the event selection is carried out by the event filter, which reduces the event rate to roughly 200 Hz. Its selections are implemented using offline analysis procedures. The average event processing time is of the order of four seconds.

### 3.4.3 Event simulation

In order to study the response of the detector to expected physics events and prepare their analysis, Monte Carlo samples are generated. They are then submitted to a full simulation of the detector.

Over 1300 different physics samples were generated. The principal general-purpose Monte Carlo generators employed were `PYTHIA` [82], `HERWIG` [83], `Sherpa` [84], `AcerMC` [85], `ALPGEN` [86], `MadGraph/MadEvent` [87] and `MC@NLO` [88]. Parton-level Monte Carlo generators used either `PYTHIA` or `HERWIG/JIMMY` for hadronization and underlying event modelling. `HERWIG` hadronization was complemented by an underlying event simulation from the JIMMY program [89] (versions 4.2 and 4.31). The underlying event model

parameters were tuned, for PYTHIA and HERWIG/JIMMY, to published data from TeVatron and other experiments. For Sherpa, the default parton shower and underlying event modelling was used. LHAPDF, the Les Houches Accord PDF interface library [90], was used throughout, and was linked to all Monte Carlo event generators to provide the Parton Density Function set values. The PDF sets [47] used were CTEQ6L for leading order Monte Carlo event generators, and CTEQ6M for the next-to-leading order Monte Carlo event generator MC@NLO.

The response of the ATLAS detector to generated events was estimated using a dedicated Geant 4 simulation [91, 92]. One important aspect of the CSC challenge was the test of the alignment and calibration procedures with an imperfect description of the detector. The goal was to establish and validate the alignment and calibration procedures and to determine the known distortions. The used geometry includes misalignment's of the inner detector. The misalignment's were introduced as independent translations and rotations at three levels: (i) of the main sub-detector parts (pixels, SCT barrel, two SCT end-caps, TRT barrel and two TRT end-caps), (ii) of major detector sub-units, like pixel and SCT barrel layers, pixel and SCT end-cap disks and TRT barrel modules and (iii) of individual silicon detector modules. The sizes of displacements were chosen to lie within the expected build tolerances. The actual displacements were assigned randomly in most cases.

Additional material was added in different locations of the inner detector and in front of the electromagnetic calorimeter. Within the active tracking volume the material in regions of service routing was increased by 1–5% of a radiation length. For services outside the active tracking volume the material was increased by up to 15% of a radiation length. Additional material was also added in a $\phi$–asymmetric way in front of the calorimeter. In the region $\eta > 0$ additional material corresponding to 8–11% $X_0$ were added in front of the barrel cryostat, 5% $X_0$ between the barrel presampler and strip layers (in $\pi/2 < \phi < 3\pi/2$), and 7–11% $X_0$ behind the cryostat. In the region $\eta < 0$, additional material corresponding to 5% $X_0$ was added between the barrel presampler and the strip layer in the region $-\pi/2 < \phi < \pi/2$. The density of material in the gap between the barrel and the end-cap cryostat was increased by 70%. Among the important studies is the impact of the misalignment's on the $b$–tagging performance or on the reconstructed resolution of the $Z$ resonance in muon final states. In addition the impact on the mass resolution and reconstruction efficiencies was studied for $H \to \gamma\gamma$, $H \to ZZ \to 4\ell$ and $Z \to ee$ samples.

### 3.4.4 Event reconstruction

After a successful trigger decision, events' raw data are stored at CERN's Tier–0 in the ByteStream format. From there, reconstruction proceeds.
The goal of the reconstruction process is to infer the physics event at the interaction point given the quantities measured by the detector (energy deposits in the calorimeters, hits in the tracker...). It is the reverse process from that of simulating the detector response to a given physics event.

### Electrons

Electrons are reconstructed using a combination of information from the tracker and the calorimeters. A detailed account is provided in chapter 4.

### Muons

Muons are identified thanks to a combination of three track reconstruction strategies. The stand-alone method uses only tracks reconstructed in the muon spectrometer ($|\eta| < 2.7$). A combination of a muon spectrometer track with an tracking-detector track is also possible over $|\eta| < 2.5$. Eventually, the Segment tag technique combines an tracking-detector track with a muon spectrometer segment, i.e. a straight line track, in an inner muon station. The reconstruction of tracks in the muon spectrometer is essentially equivalent to that in the tracking detector. The overall muon reconstruction efficiency is around 95% and the resolution on the measurement of the momentum is around 4% for $p_{\mathrm{T}} > 25$ GeV.

### Jets

Jet reconstruction algorithm in ATLAS can be realized by two algorithms, a fixed cone jet finder or a sequential recombination technique, either on calorimeter towers or topological clusters. Towers are formed by collecting cells into bins of $\Delta\eta \times \Delta\phi = 0.1 \times 0.1$ and summing up their signals. For topological clusters, nearest neighbours are collected around seed cells with a significant absolute signal above the major seed threshold, i.e. $|E_{\mathrm{cell}}| > 4\sigma_{\mathrm{cell}}$ of the total noise. These neighbouring cells are collected independently of the magnitude of their own signal. If the absolute value of their signal significance is above a secondary seed threshold, typically such that $|E_{\mathrm{cell}}| > 4\sigma_{\mathrm{cell}}$, they are considered as secondary seeds and their direct neighbours are also collected. Finally, all surrounding cells above a very low threshold are added if no more secondary seeds are among the direct neighbours. A final analysis of the resulting cluster looks for multiple local signal maxima. In case of more than one maximum in a given cluster, it is split into smaller clusters, again in three dimensions, along the signal valleys between maxima. Once these input objects are built, jet finding algorithms are run. The fixed cone algorithm collects every input object (towers or topological clusters) around a seed ($> 1$ GeV) in a cone of $R_{\mathrm{cone}} = 0.4$ or 0.7 ($R = \sqrt{\Delta\eta^2 + \Delta\phi^2}$). The four-momentum of the resulting collection is computed and the cone is centered around it iteratively until convergence is reached. Infrared safety is ensured by splitting or merging overlapping jets. For the sequential recombination method, the $k_T$ algorithm is applied [93]. Jets are reconstructed with an efficiency of 100% from $p_{\mathrm{T}}$'s of 30 GeV and their energy is measured with a resolution of $\approx 15\%$ to 4% for low and high–$p_{\mathrm{T}}$ jets respectively.

Jets are calibrated by the application of weights to individual cells measurements. All calorimeter cells in tower or cluster jets are re-summed with weighting functions $w$ depending on the cell signal density $E_i/V_i$ , where $V_i$ is the volume of the cell considered, and on the cell location in the calorimeter, $\overrightarrow{X}_i$, consisting basically of module and layer identifiers. They are fitted using simulated QCD di-jet events, covering the whole

kinematic range expected at the LHC, and matching calorimeter cone-tower jets, with $\Delta R = 0.7$, with nearby truth-particle cone jets of the same size. The weighting functions determined in this way absorb all detector effects, including missing signals from charged truth particles with less than $\sim$ 400 MeV transverse momentum which are bent away from the calorimeter by the solenoid magnetic field in the tracking detector cavity.

#### Flavour tagging

It is not possible to identify the flavour of the parton giving rise to a jet except in the case of $b$–jets. $B$–hadrons are relatively long-lived and travel about 3 mm in the transverse plane before decaying. In addition, they are fairly heavy ($> 5$ GeV). Thus, their decay products may have a large transverse momentum with respect to the jet axis and the opening angle of the decay products is large enough to allow a separated reconstruction. A combination of a good reconstruction of secondary vertices or a measurement of the impact parameter of tracks with an efficient identification of soft leptons permits to tag jets containing a $b$–quarks. Using these measurements, a weight is computed as a sum of likelihood ratio. It was shown in [81] that $b$–jets can be identified in ATLAS with an efficiency of about 60% in the central region of the detector and for $p_{\mathrm{T}} > 100$ GeV.

#### Missing transverse energy

The reconstruction of the missing transverse energy is based on the calibrated calorimeter cells and combined muons, where care is taken not to double-count energy lost by the latter in the calorimeter. Then, energy lost in the cryostat between the electromagnetic calorimeter and the tile calorimeter is accounted for. Eventually, a refined calibration of $\not\!\!E_{\mathrm{T}}$ is performed through the association of each high–$p_{\mathrm{T}}$ object in the event to its globally calibrated cells. The refined calibration of $\not\!\!E_{\mathrm{T}}$ then replaces the initial contribution from globally calibrated cells by the contribution from the corresponding calibrated high–$p_{\mathrm{T}}$ objects themselves.

### 3.4.5 Data processing

The simulation of Monte Carlo samples, the reconstruction of simulated or recorded data as well as physics analysis are all performed with the unified `athena` framework [94].
`Athena` is a complex modular `C++` framework. It incorporates the various computing tasks as packages. It contains all on-line and offline algorithms allowing to transform raw measurements of the detector into high-level combined physics objects. Its package structure is very modular and allows for a great flexibility in the management of different releases. Major production versions are released every six month. Development sub-versions are released every month. `Athena` is highly customizable at run-time by an ergonomic `python` interface.

The first step of simulated data processing are Raw Data Objects (RDO) files. They contain events as output by the Event Filter in byte-stream format, reflecting the format in which data are delivered from the detector rather than in any object-oriented representation. RDO files weighs approximately 2 MB per event.

Event Summary Data (ESD) files contain the output of the reconstruction algorithms. They are intended to make access to RDOs unnecessary for most physics applications other than for some calibration or re-reconstruction. ESDs have an object-oriented representation, and are stored in POOL ROOT format. ESD files weighs approximately 750 kB per event.

Analysis Object Data (AOD) files contain reduced representations of events. They are derived from ESD and are suitable for analysis. They contain physics objects and other elements of analysis interest. They have an object-oriented representation, and is stored in POOL ROOT format. AOD files weighs approximately 170 kB per event.

Derived Physics Data (DPD) is an ntuple-style representation of event data for end-user analysis and histogramming.

Several standard methods co-exist for the analysis of data. The choice of method depends on the purpose of the analysis (performance study, physics analysis, etc...) and on user preferences.

The slowest and less flexible method consists in running a `C++` code embedded in an `athena` package on ESD or AOD files in order to produce ROOT histograms. A change in the constitution of histograms necessitates the edition and the recompilation of the `C++` code. Furthermore, the execution of this code is achieved within an `athena` process resulting in a very long overhead due to the initialization and loading of the detector geometry and conditions.

The fastest method consists in running a `C++` code embedded in an `athena` package on ESD or AOD file in order to generate a ROOT ntuple files such as an Event View ntuple or a DPD (Derived Physics Data). These files are generated once at the beginning of the study and in general need not be rebuilt. They are ROOT trees containing only the desired variable. Then, a ROOT `C++` macro is run on the ntuple files in order to build histograms. This method has almost no overhead and can process events at a rate of $\sim$ 1000 Hz.

The most flexible method consist in running a `python` code in the AthenaROOTAccess framework directly on AOD files to generate histograms. This method inherits the flexibility and user-friendly-ness of the `python` language and allows for a very fast and compact writing of the desired tasks. Also, this method provides a very direct way to have a rapid insight of any physics sample after downloading AOD files from the Grid. The drawback of this flexibility is that the method suffers from the heavy but necessary `C++` machinery of the AthenaROOTAccess framework. This results in a $\sim$ 100 Hz processing rate.

A personal method was used in the analysis presented in chapter 5. A `python` code was run in the AthenaROOTAccess framework to store desired variables in `python` shelve files. Then a `python` macro was run on the shelve files to generate histograms. This method allowed for a $\sim$ 1500 Hz processing rate.

### 3.4.6 Distributed computing

The amount of data to be recorded during the operation of the LHC experiments ($\approx$ 1 Pbyte/year) as well as the large Monte Carlo production required for a careful study of the expected backgrounds rule out a central concentration of computing resources. The Worldwide LHC Computing Grid project [95] aims at distributing the CPU and storage demand over a number of sites around the world.
The central node is CERN's Tier-0, a dedicated computing farm. It runs the event reconstruction withing 24 hours of their recording by the detector. The output of the reconstruction (ESD POOL files) and raw data are then sent over to eleven Tier-1 sites, each of them conserving a fifth of the data. Reprocessing of the reconstruction is achieved at Tier-1's. The analysis objects (AOD POOL files) are all distributed to all Tier-1's. 140 Tier-2 sites take care of user analysis jobs and Monte Carlo production. The French cloud includes one Tier-1 site (CCIN2P3-IRFU in Lyon) and four Tier-2 sites : GRIF (Ile-de-France), LAPP (Annecy), LPC (Clermont-Ferrand) and Subatech (Nantes).
From the user point of view, the Grid structure allows to send analysis jobs on any dataset (data or MC) from any machine to almost any grid site around the world in a very efficient and transparent manner. I used the Grid as a user to perform both physics analysis and performance studies. I used the PANDA interface to send `athena` (ATLAS software) jobs. I used raw grid commands to send non-`athena` jobs (`SFitter`). I sent jobs from the CERN computer farm or from the IN2P3 Computing Center in Lyon. If no site is specified, the job will be sent to one of the site containing the desired datasets, preferably on the French cloud. SFitter jobs do not require access to any ATLAS dataset and, as so, ran successfully on the French cloud. However, most of my `athena` jobs were voluntarily sent to the BNL computing center as it contains all MC samples and has the lowest job failure rate.

# Chapter 4

# Reconstruction and identification of electrons in ATLAS

*"Thunderbolts of lightning, very very frightening me"*

Freddy Mercury – *Bohemian Rhapsody*

*"They say that genius is an infinite capacity for taking pains, [...] It's a very bad definition, but it does apply to detective work."*

Sherlock Holmes – *A study in scarlet*

Electrons are of major importance in the ATLAS experiment, be it for the understanding of the detector performance, the measurement of Standard Model processes or the search for physics beyond the latter. Indeed, the measurement of electrons as the decay products of $Z$'s, $\Upsilon$'s or $J/\Psi$'s can provide robust constraints on the absolute electromagnetic energy scale. The study of photon conversions as well as the bremsstrahlung activity gives information as to the material distribution before the electromagnetic calorimeter. Electrons are also necessary for the measurement of the $W$ boson and top quark masses. Eventually, once the detector response is reasonably understood and the SM is measured, electrons will be used to probe the Higgs boson in its decay into four leptons ($h \to ZZ^* \to 4\ell$ and $h \to WW^* \to 2\ell 2\nu$). Also, electrons often appear in the long decay chains occurring in supersymmetric events. Namely, the supersymmetric tri-lepton channel (see chapter 2) is of great interest for both the discovery and the measurement of supersymmetry. Some models of new physics based on extra dimensions feature new very heavy gauge bosons, the decay of which will produce leptons with very high transverse momenta ($p_{\mathrm{T}}$).

Approximately $10^5$ QCD jets are expected for each isolated electron in the 20–50 GeV $p_{\mathrm{T}}$–range at the LHC. More generally, the QCD jet cross-section is a hundred times larger than at the TeVatron. On the other hand, cross-sections for electrons in new physics or Higgs events are of the order of a few fb. Thus, high reconstruction and identification efficiencies must be achieved against high jet rejections from $p_{\mathrm{T}}$'s of a

few GeV ($J/\Psi$, $h \to 4\ell$ or $b$–tagging) up to a few TeV ($Z' \to ee$). In the early data-taking phases, the performances of the reconstruction and identification processes will be assessed directly on recorded $Z \to ee$ events thanks to the in-situ tag-and-probe method. A good resolution and accuracy on the measurement of the electrons' energy is necessary to reconstruct resonances ($Z$, $J/\Psi$, $h$ or $t$) or other observables such as kinematic end-points and thresholds. This can be achieved by a combination of calibration techniques involving both Monte Carlo based and in-situ methods.

In this chapter, the methods used to reconstruct and identify electrons and discriminate jets in ATLAS are exposed [29, 81]. In particular, isolation studies, track-matching optimization, conversion reconstruction and the determination of signal efficiencies and jet rejection are discussed. The presented studies were performed in the context of the Computing System Commissioning (CSC) exercise [81]. This effort aimed at assessing the readiness of the reconstruction chain for data-taking. That included an optimization of trigger menus, reconstruction algorithms, physics studies and analysis tools. All results were published in [81].

## 4.1 Simulation

Signal samples for the study of the reconstruction and identification of electrons include single electron events as well as actual physics processes such as $Z \to ee$ events or supersymmetric (SUSY) events.
Single electron events were generated at fixed $p_{\mathrm{T}}$ or with $7 < p_{\mathrm{T}} < 80$ GeV. Unless stated otherwise, the hereafter mentions of "single electrons" refer to a simulated sample of single electron events with $7 < p_{\mathrm{T}} < 80$ GeV.

Samples of $Z \to ee$ events were also simulated by the `PYTHIA` event generator [82]. The new implementation of parton showering, commonly known as $p_{\mathrm{T}}$–ordered showering, was used as well as the new underlying event model where the phase-space is interleaved/shared between initial-state radiation (ISR) and the underlying event.

SUSY events were generated by the `HERWIG` code (releases 6.508 to 6.510) [83]. In this case, the underlying event was generated by `JIMMY` [89]. This sample will be referred to as "SUSY events". The underlying event model parameters were tuned, for `PYTHIA` and `HERWIG/JIMMY`, to published data from TeVatron and other experiments. The decay of $\tau$–leptons was treated via the `TAUOLA` package [96], version 2.7. The radiation of photons by charged leptons was treated using the `PHOTOS` QED radiation package, version 2.15 [97].

For the generation of $t\bar{t}$ events, the `MC@NLO` 3.3 code [88] was used to compute the NLO matrix elements including a next-to-leading log re-summation. This code is interfaced to the `HERWIG` parton shower generator for the hadronization of final states and to `JIMMY` for the underlying event.

For the study of the jet rejection, `PYTHIA` was used to produce the large QCD jet sample required to assess performance of the electron reconstruction and identification.

The filtered di-jets sample contains all hard-scattering QCD processes with $p_{\mathrm{T}} > 15$ GeV, e.g. $qg \to qg$, including heavy-flavour production, together with other physics processes of interest, such as the production of prompt photon or single $W/Z$. A filter was applied at the generator level to simulate the level 1 trigger requirements, with the goal of increasing in an unbiased manner the probability that the selected jets pass the electron identification cuts after the detector simulation. The summed transverse energy of all stable particles (excluding muons and neutrinos) with $|\eta| < 2.7$ in a region $\Delta\eta \times \Delta\phi = 0.12 \times 0.12$ was required to be greater than 17 GeV for an event to be retained. The filter retains 8.3% of the di-jet events. The total number of events available for analysis after filtering, simulation and reconstruction, amounts to 8.2 million. This sample will be referred to as "di-jet events".

The reconstruction of simulated events is accomplished by the ATLAS `athena` software. The starting point of this work was the reconstruction process contained in release 12.0.3 (September 2006). Improvements were incorporated, documented and maintained into successive releases up to 14.2.0 in June 2008.

The analysis of reconstructed samples was performed using two methods. Flat combined ntuples containing the quantities output by the reconstruction and identification processes were analysed by `ROOT C++` macros. From early 2008, the `AthenaROOTAccess` package was used to run `Python` codes directly on structured AOD files.

## 4.2 Electrons and photons in the detector

Upon production in a hard scattering process at the interaction point, electrons travel through the tracking detector where their trajectory is bent by the magnetic field produced by the solenoid. As charged particles, they leave hits in the silicon detectors as well as in the TRT drift tubes. As they cross material (see figure 4.1 for the material distribution in from of the calorimeter as a function of $|\eta|$), it is possible that a fraction of their energy be carried away by a photon emitted in a bremsstrahlung process. Such processes occur when charged particles (here electrons) are decelerated by nuclei and emit photons. After leaving the tracking detector and crossing the solenoid, they enter the presampler and the electromagnetic calorimeter. The interaction with the lead present in the calorimeter results in an electromagnetic shower. The secondary particles in the shower ionize the surrounding liquid argon. Ions drift thanks to an electric field towards the electrodes where the signal is measured. Most of the electrons' original energy is unloaded there and recorded in the calorimeter cells. The shower is mostly contained to the electromagnetic calorimeter and small amounts of energy in the hadronic calorimeter are detected only in the case of high $p_{\mathrm{T}}$ electrons. Figure 4.2 shows the amount of transverse energy deposited by $p_{\mathrm{T}} = 500$ GeV single electrons in the hadronic calorimeter as a function of $|\eta|$. Even where the amount of material in front of the calorimeter is minimal ($|\eta| \approx 0$), less than 1% of the $p_{\mathrm{T}}$ of the electron leaks into the hadronic calorimeter.

Photons behave very similarly to electrons except for the fact that they do not leave hits in the tracking detector and are not deflected by the magnetic field. In the presence

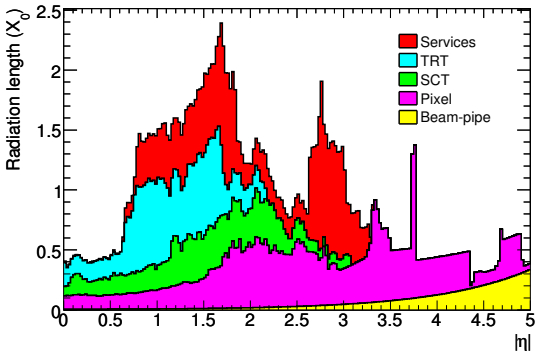


Figure 4.1: Material distribution at the exit of the tracking detector envelope, including the services and thermal enclosures. The distribution is shown as a function of $|\eta|$ and averaged over $\phi$. The breakdown indicates the contributions of external services and of individual subdetectors, including services in their active volume [29].

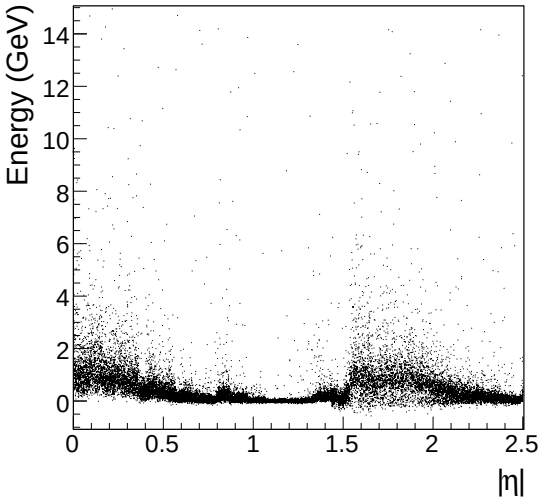


Figure 4.2: Transverse energy deposited in the hadronic calorimeter as a function of $|\eta|$ for single electrons with $p_{\mathrm{T}} = 500$ GeV.

of material (see figure 4.1), photons have a large tendency to convert. In such cases, an electron-positron pair is produced. They share the photon's energy in uneven parts leading to asymmetric conversions. Tracks from the electron-positron pair may not always be reconstructed, leading to single-track conversions. Late conversions occur when a photon travels a macroscopic distance in the tracking detector before decaying. In the calorimeter, photon showers are generally narrower than electron showers. Still, the main discrimination factor between the two arises from the tracking detector.

## 4.3 Reconstruction

Two measurements are at hand for the reconstruction of electrons : tracks and calorimetric information. They will be used to classify EM clusters as electron candidates, photon candidates or converted-photon candidates.

### 4.3.1 Track and cluster reconstruction

#### Tracks

Hits in the pixel and SCT detectors are assembled into clusters. The TRT raw timing information is turned into calibrated drift circles (see section 3.3.1). The SCT clusters are transformed into space-points (see section 3.3.1), using a combination of the cluster information from opposite sides of a SCT module. Then, different fitting strategies co-exist, each optimized for specific applications. The default technique proceeds outwards. It exploits the high granularity of the precision detectors to find prompt tracks

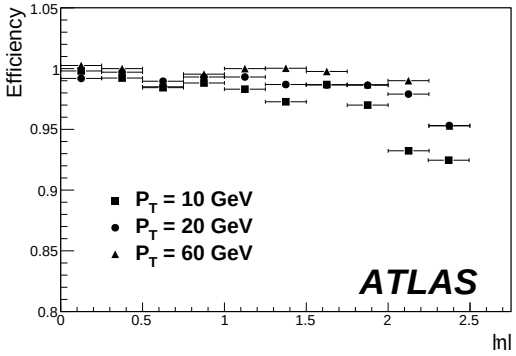


Figure 4.3: Track reconstruction efficiency as a function of $|\eta|$ obtained on single electrons.

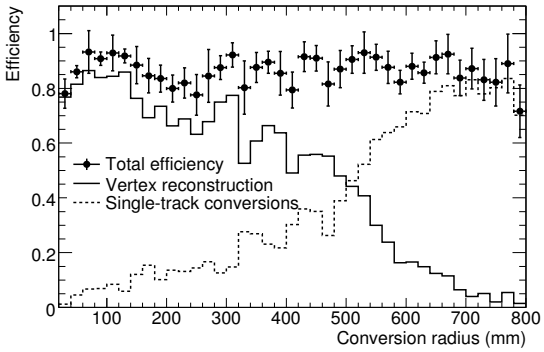


Figure 4.4: Conversion reconstruction efficiency as a function of conversion radius.

originating from the vicinity of the interaction region. Track seeds are formed from a combination of space-points in the pixel layers and the first SCT layer. These seeds are then extended throughout the SCT to form track candidates. Next, these candidates are fitted, outlier clusters are removed, ambiguities in the cluster-to-track association are resolved, and fake tracks are rejected. The selected tracks are extended into the TRT to associate drift circles around the extrapolation and to resolve the left-right ambiguities. Finally, the extended tracks are refitted with the full information of all three detectors. This method is adapted to tracks left by primary charged particles.

Another method, called back-tracking, proceeds inwards. It searches for unused track segments in the TRT. Such segments are extrapolated into the SCT and pixel detectors to improve the tracking efficiency for secondary tracks from conversions or decays of long-lived particles. The last technique consists in reconstructing TRT tracks in a standalone fashion. The use of such tracks is very recent and experimental. Therefore, they are not used in the electron reconstruction process for the results shown in this work.

Left-side plot of figure 4.3 shows the track reconstruction efficiency as a function of pseudo-rapidity obtained on single electrons. The rack reconstruction efficiency is defined as the fraction of MC truth electrons for which a track is reconstructed with a distance $R = \sqrt{\Delta\eta^2 + \Delta\phi^2}$ of 0.2. It is close to 100% as a function of pseudo-rapidity out to $|\eta| \approx 1.4$ where the material in the tracking detector increases substantially. It is also fairly uniform as a function of $p_{\mathrm{T}}$ down to low values, with a 97% efficiency for single electrons with a $p_{\mathrm{T}}$ of 10 GeV.

As the number of radiation lengths increases, the probability for an electron to undergo bremsstrahlung rises. The energy lost in the process can be recovered with dedicated fitting algorithms. The dynamic noise adjustment method [98] extrapolates track segments to the next layer, allowing for loss compatible with hard bremsstrahlung. The Gaussian-sum filter method takes into account non-Gaussian noise by modelling it as a weighted sum of Gaussian components [99].

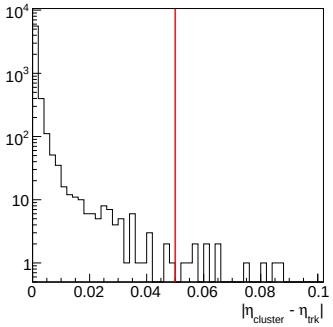


Figure 4.5: $\eta$ difference between the EM cluster and the track extrapolated to the calorimeter for single electrons. The red line represents the cut.

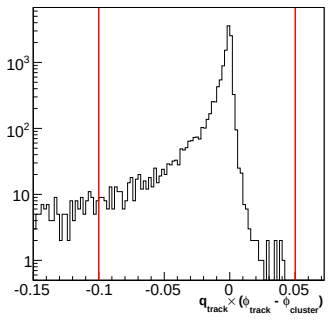


Figure 4.6: $\phi$ difference between the EM cluster and the track extrapolated to the calorimeter for single electrons. The red lines represent the cut.

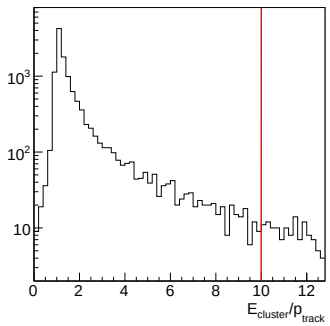


Figure 4.7: Ratio between the energy of the cluster and the momentum of the track for single electrons with. The red line represents the cut.

#### Electromagnetic clusters

EM clusters correspond to local energy deposits in the EM calorimeter. They are built by the sliding-window algorithm [100]. The latter proceeds in three steps. First, $200 \times 256$ calorimeter towers are built. Each of them is $\Delta\eta \times \Delta\phi = 0.025 \times 0.025$ wide. Within each tower, the energy of cells in all longitudinal layers is summed. Then a window of $5 \times 5$ towers is slid across each the previously built grid, one tower at a time. If the transverse energy summed over all layers in the window is above 3 GeV and is a local maxima, a pre-cluster is formed. Its position is the energy-weighted $\eta$ and $\phi$ barycentre's inside a $3 \times 3$ window centred on the central tower. If two pre-clusters lie within a distance of $2 \times 2$ of each other, the one with the smallest $E_{\mathrm{T}}$ is discarded as the final clusters would most likely overlap. Eventually, cells within a window of size $N_\eta \times N_\phi$ of a layer-dependent seed position are assigned to EM clusters. $N_\eta$ and $N_\phi$ are variable and depend on the physical object of interest. In the middle layer, the position of the seed is the position of the pre-cluster. In the strips and the back layers, the position of the seed is the barycentre of the cells selected in the middle layer. In the presampler, the barycentre of cells selected in the strips is used as seed. The number of cells included in the strips is $N_\eta \times 6$ if $N_\phi < 7$ and $N_\eta \times 8$ otherwise. In the back, $(N_\eta + 1) \times N_\phi$ cells are included. This is done in such a way that for a $5 \times 5$ clusters, if the seed is close to the boundary between two strips, then these two strips are included into the cluster in the $\phi$–direction, whereas if the seed is located in the middle of the strip, only one strip is included.

### 4.3.2 Electron and photon candidates

The selection of electron candidates can be seeded either by an EM cluster or by a track. In the former case, any $5 \times 5$ EM cluster with $p_{\mathrm{T}} > 3$ GeV constitutes a seed. For each of these, an attempt is made at finding a matching track in the tracking detector.

The track is extrapolated to the calorimeter in order to account for the curvature due to the magnetic field in the tracking detector[1].The track should not belong to any reconstructed object corresponding to a conversion, see section 4.3.3. The matching procedure is based on geometrical cuts ($\Delta\eta$ and $\Delta\phi$) as well as on the ratio of the energy of the cluster to the momentum of the track. The cuts' values are

$$|\Delta\eta| < 0.05, \qquad -0.10 < \Delta\phi < 0.05 \qquad \text{and} \qquad E/p < 10.$$

The $\Delta\phi$ cut is asymmetrical to retain electrons losing energy through bremsstrahlung. If a track is found, an electron candidate is defined, including the cluster and the associated track. Otherwise, a photon candidate is defined. Figures 4.5 and 4.6 show the $\eta$ and $\phi$–difference respectively between the EM cluster and the track for single electrons. This is mostly important for $\Delta\phi$. The latter is defined as $\Delta\phi = q_{\text{track}}(\phi_{\text{track}} - \phi_{\text{cluster}})$ in order for the tail due to bremsstrahlung effects to always be on the negative side. Indeed, as electrons radiate photons, they loose momentum and the bending of their track increases. However, the energy deposited in the calorimeter corresponds not only to the electron but also to the radiated photons, resulting in an increased $\Delta\phi$. Figure 4.7 shows the ratio between the energy of the cluster and the momentum of the track.

When reconstructing a track, the ATLAS software allows to keep a link to the MC truth particle originating it. The classification efficiency is defined as the fraction of MC truth electrons for which an electron candidate containing the associated track is found. For photons, the classification efficiency is simply defined as the fraction of MC truth photons for which a photon candidate is found within a distance $R = \sqrt{\Delta\eta^2 + \Delta\phi^2}$ of 0.2.

### 4.3.3 Conversion reconstruction

With a cluster in the EM calorimeter and hits in the inner tracker, electrons springing from photon conversions are likely to be reconstructed as isolated electrons candidates. Indeed, If one solely makes use of the cuts on combined variables ($\Delta\eta$, $\Delta\phi$ and $E/p$) for the electron/photon separation, 48% of conversions from single photons ($7 < p_{\text{T}} < 80$ GeV) are being classified as electrons. With 56% of photons converting, that means 27% of single photons end up as electron candidates. Those may off-course not pass identification cuts on the track as it does not initiate at the interaction point but may still constitute background in some analyses. Also, they should be reconstructed as isolated photons and not counted out in analyses with prompt photons in the final state such as the $H \to \gamma\gamma$ channel. For that purpose, it is necessary to match potential electron candidates to reconstructed conversions in order to re-route them properly and define them as photon candidates.

[1]Until 2008, the track was extrapolated from its outermost precision hit out to the calorimeter. As of early 2009, this will be replaced by a new technique in which the momentum of the track is scaled to the energy of the cluster and the extrapolation is applied from the perigee. The $E/p$ cut will be removed. This changes will help recover electrons which lost energy via bremsstrahlung.

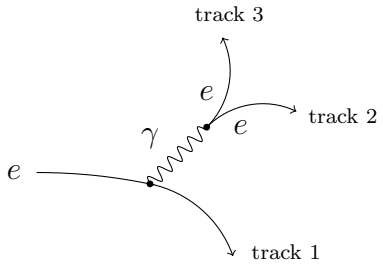


Figure 4.8: Sketch of a photon radiating of a primary electron. The photon converts into an electron pair.

### Conversion candidates

Conversions sign in the detector by leaving two tracks with opposite curvature. The vertex, that is the origin and intersection of the two tracks, is often far from the beam axis (late conversions). In addition to the charge constraint, a number of quality cuts are applied to the tracks and geometrical cuts are applied to the pairs (polar angle, vertex radius, arc length, etc...). This helps fight the background from the underlying event. Then, the vertex fitting procedure is applied. The default track perigee is the interaction point. This is incorrect in the case of late conversions. A new fit is performed including this new parameter. At this stage, fake conversions still widely outnumber real conversions. No efficient particle identification is achievable with the tracking detector only. Calorimetric information is needed in order to properly identify actual conversions and that is done at a later stage.

Once vertices have been reconstructed, the remaining tracks are further investigated in order to find potential single-track conversions. The latter can occur in the case of asymmetrical or late conversions. Figure 4.4 shows the conversion reconstruction efficiency as a function of the conversion radius. As expected, vertex finding works up to radii of $\sim 500$ mm (beginning of the TRT) where the single-track method picks up to add up to a flat overall efficiency of 90%. Indeed, many candidates correspond to fake combinations : this background will be rejected by further identification cuts.

### Conversion identification

The first step to would be to define an electron candidate if, in addition to passing the cuts on combined variables, the matching track does not belong to any reconstructed conversion. This requirement helps recover 30% of photon conversions that had been wrongfully classified as electron candidates. However, its by product is an absolute decrease of 4% of the classification efficiency of simulated single electrons in the same $p_{\mathrm{T}}$–range. The reason for that is that an ambiguity remains in the reconstruction of conversions in the case of the process sketched in figure 4.8. Indeed, when a signal electron radiates a bremsstrahlung photon, the latter can convert into an electron pair. When the conversion reconstruction algorithm searches for two crossing tracks with opposite charges, only tracks 2 and 3 should be associated. However, if the photon

does not travel and converts right after generation, tracks 1 and 3 can also constitute a potential conversion and are hence reconstructed as so. The difference is that while tracks 2 and 3 come from the same point, track 1 starts much closer to the beam axis than track 3. This mis-identification can be avoided by requiring that both tracks in the conversion candidate have the same number of hits in the vertexing-layer (see section 3.3.1). Indeed, while track 1 will feature a hit in that layer, track 2 will most likely not.
Looking at numbers, only 1% of true conversions have tracks with different numbers of hits in the vertexing-layer. However, in a sample of single electrons, 60% of fake conversions contain tracks with different numbers of hits in the vertexing-layer. In other words, this extra requirement does not impair the gain in the classification of true photons and helps recover 60% of the 4% drop due to the track requirement.

#### Final classification efficiency

| | Classification efficiencies | |
|---|---|---|
| | Photons | Electrons |
| Only combined cuts | 72.7% | 89.8% |
| + track requirement | 80.8% | 85.5% |
| + vertexing-layer requirement | 80.3% | 87.8% |
| Relative gain | +10% | −2% |

Table 4.1: Photon and electron classification efficiencies for different sets of cut. Numbers are quoted for single electrons and photons.

Table 4.1 summarizes the classification efficiencies for single electrons and photons. The classification efficiency includes the geometrical matching as well as the conversion identification procedure. The first line quotes numbers when only cuts on the combined variables are applied. The second line quotes efficiencies when, in addition, the track is required not to belong to any reconstructed conversion candidate. The last line shows efficiencies when both tracks in the conversion candidate are required to have the same number of hits in the vertexing-layer. This study changes the way converted photon are classified and defines them as photon candidates. This resulted in an 8% absolute increase in the photon classification efficiency for a 2% absolute loss in the electron classification efficiency.

Figures 4.9 and 4.10 show the efficiency of defining an electron candidate classification efficiency as a function of $p_{\mathrm{T}}$ and $|\eta|$. The drop in efficiency for $|\eta| > 1$ corresponds to the expected increase in the fraction of electrons undergoing bremsstrahlung as the amount of material crossed in the tracking detector increases. For such electrons, the track reconstruction and extrapolation is affected resulting in a poor geometrical matching. The integrated classification efficiency is around 92% for $p_{\mathrm{T}} > 30$ GeV.

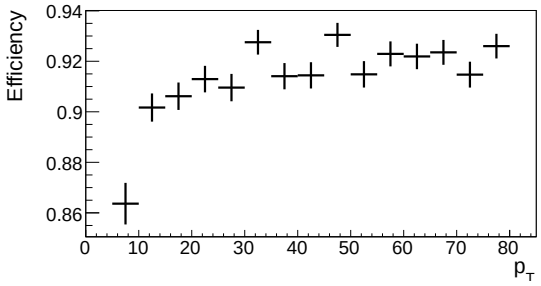


Figure 4.9: Classification efficiency versus $p_{\mathrm{T}}$ for single electrons.

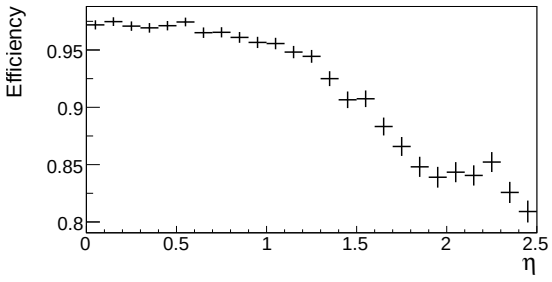


Figure 4.10: Classification efficiency versus $|\eta|$ for single electrons.

| Hypothesis | Barrel | End-cap |
|---|---|---|
| Electrons | $3 \times 7$ | $5 \times 5$ |
| Converted photons | $3 \times 7$ | $5 \times 5$ |
| Unconverted photons | $3 \times 5$ | $5 \times 5$ |

Table 4.2: Number of cells ($N_\eta \times N_\phi$) in EM clusters for each particle hypothesis.

### 4.3.4 Calibration

Once electron and photon candidates are separated, clusters are re-calibrated accordingly. For instance, electron clusters are enlarged in $\phi$ so as to recover energy that could have been lost by bremsstrahlung. The re-calibrated $\Delta\eta \times \Delta\phi$ sizes are reported in table 4.2. Electron clusters contain $3\times7$ ($5\times5$) cells in $\eta\times\phi$ in the barrel (end-cap). Being migrated over from the electron candidates, clusters for converted photons have the same dimensions as for electrons. Photons contain only $3 \times 5$ cells in the barrel. Cluster sizes were optimized for each particle type by comparing the contribution to the energy resolution coming from electronics noise and from the pile-up expected at high luminosity with the contribution coming from the energy leakage fluctuations outside the cluster [101]. Photon clusters are not square in order to account for converted photons for which the conversion was not identified.

A series of corrections are then applied to calibrate both the energy and position measurements. These corrections are derived from Monte-Carlo simulations and validated using test-beam data. On top of these corrections, a precise inter-calibration derived from $Z \rightarrow ee$ events will be applied. Offline calibration starts with the correction of cell measurements to take into account electronics non-linearities and non-nominal high voltage settings. Then, once clusters are built, their energy and position are calibrated.

#### Position calibration

The cluster $\eta$ position is first calculated in each layer as the energy-weighted barycentre of the cluster cells in that layer (In the first layer, only the three strips around the cluster centre are used, regardless of the specified cluster size). Due to the finite granularity of the readout cells, these measurements are biased towards the centers

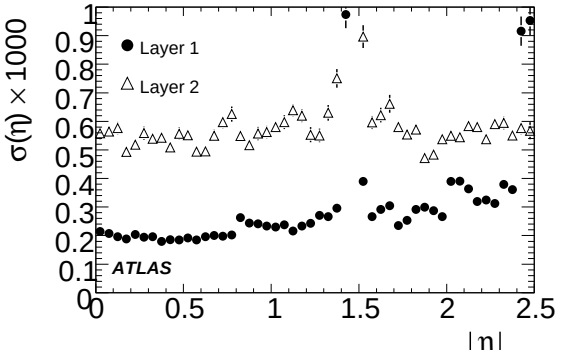


Figure 4.11: Expected $\eta$ position resolution versus $|\eta|$ for $E = 100$ GeV photons for the two main layers of the barrel and end-cap EM calorimeters [29].

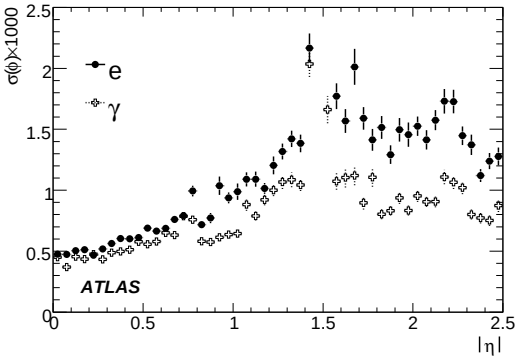


Figure 4.12: Expected $\phi$–position resolution as a function of $|\eta|$ for electrons and photons with an energy of 100 GeV [81].

of the cells leading to so-called S–shapes. The correction varies continuously over $\eta$, due to changes in the detector geometry. The correction will also depend on the cluster energy, as that affects the average shower depth. To derive the correction, the calorimeter is divided in $\eta$ into regions based on where the behaviour of the correction changes discontinuously. Within each region, an empirical function is constructed to describe the correction, and an unbinned fit is performed to simulated data for a particular cluster size, type, and energy. The correction also depends on energy; over the range 25–1000 GeV, the required correction varies by $\sim 20\%$. To apply the correction for a given cluster, the correction is first tabulated for each of the energies for which simulated data samples were available. The final correction is then found by doing a cubic polynomial interpolation within this table. Figure 4.11 shows the $\eta$–resolution as a function of $|\eta|$ for $E = 100$ GeV photons for the two main layers of the barrel and end-cap EM calorimeters. The calibration allows for precision on the $\eta$–position better than 1‰.

The measurement of the cluster $\phi$–position must also be corrected. These corrections are applied only in the second layer of the calorimeter where the $\phi$–granularity is the best. As opposed to the $\eta$ direction, the accordion geometry results in more energy sharing between cells in the $\phi$ direction, which washes out the S–shape in this direction. There is, however, a small bias in the $\phi$ measurement which depends on the average shower depth with respect to the accordion structure (and thus on $|\eta|$). Data are binned in $\eta$ and the resulting correction is interpolated in $\eta$ and energy. Figure 4.12 shows the expected $\phi$–resolution as a function of $|\eta|$ for electrons and photons with $E = 100$ GeV.

The individual layer $\eta$ and $\phi$ measurements are combined to produce the overall position of the cluster. For $\phi$, only the second is used. In the overlap region, the energy-weighted average of the barrel and end-cap $\phi$ measurements is used. For $\eta$, the first and second layers 1 are averaged. The first layer is weighted three times as much as the second to roughly take into account the better resolution. The $\eta$–combination implicitly assumes

that the incoming particle is projective. If its production vertex is shifted from the origin, then the combined $\eta$ will be biased.

### Energy calibration

The standard method to calibrate the energy of photons and electrons from simulated data, the so-called Calibration Hits method [102], is based on detailed Monte Carlo simulations. Dedicated single-particle simulations are used to record the energy deposited by particles in all detector materials, active or dead. Through these simulations, the energy depositions in the inactive material can be correlated with the measured quantities. For example, the energy lost in the material in front of the calorimeter (tracking detector, cryostat, etc...) can be estimated from the energy deposited in the presampler. This method provides a modular way to reconstruct the energies of electrons and photons by decoupling the different corrections. This approach eases comparisons between electrons and photons, and might be particularly useful in the initial stages of the experiment. This most precise method yields a 1 to 3% energy resolution for 100 GeV electrons versus $\eta$ and a linearity better than 0.5% in the barrel for electrons with energy below 500 GeV.

The cluster energy is decomposed into three components

$$E = E_{\text{cal}} + E_{\text{front}} + E_{\text{back}}$$

where $E_{\text{cal}}$ is the energy deposited in the EM calorimeter, $E_{\text{front}}$ is the energy deposited in the presampler and in the inactive material in front of the calorimeter, and $E_{\text{back}}$ is the energy that leaks out the rear of the EM calorimeter.
The energy deposited by a particle in the EM calorimeter is estimated as

$$E_{\text{cal}} = C_{\text{cal}}(X, \eta)(1 + f_{\text{out}}(X, \eta))E_{\text{cl}},$$

where $E_{\text{cl}}$ is the energy contained in the cluster, $X$ is the longitudinal barycentre or shower depth measured on the presampler and the EM calorimeter, $\eta$ is the calibrated pseudo-rapidity of the cluster, $f_{\text{out}}$ is the fraction of energy deposited outside the cluster and $C_{\text{cal}}$ is the calibration factor. The latter is defined as the average ratio between the true energy deposited in the EM calorimeter (both absorbers and ionisation medium) and the reconstructed cluster energy $E_{\text{cl}}$. It is within a few percent of unity, and takes into account effects such as the dependence of the sampling fraction on $\eta$ and on the longitudinal profile of the shower. Due to the presence of the magnetic field and bremsstrahlung, the fraction of energy deposited in the calorimeter outside the cluster is energy dependent. Since only single electrons and photons with no noise or underlying event are simulated, this fraction is easily calculated.

The energy lost in the material in front of the calorimeter (inner detector, cryostat, coil, and material between the presampler and strips) is parametrised as a function of the energy lost in the active material of the presampler $E_{\text{ps}}$ :

$$E_{\text{front}} = a(E_{\text{cal}}, \eta) + b(E_{\text{cal}}, \eta)E_{\text{ps}} + c(E_{\text{cal}}, \eta)E_{\text{ps}}.$$

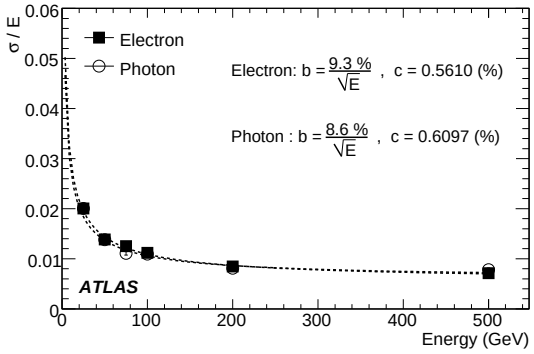


Figure 4.13: Resolution on the energy of electrons and photons as a function of the energy for $|\eta| = 0.3$ [81].

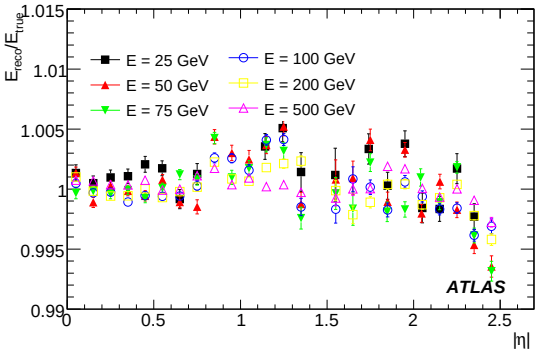


Figure 4.14: Linearity of the energy measurements for electrons as a function of $|\eta|$ for different energies [81].

Coefficients $a$, $b$ and $c$ are parametrised in terms of $E_{\text{cal}}$ and $\eta$. The coefficient $c$ is used only in the end-cap.

The energy deposited by the showers behind the EM calorimeter is computed as a fraction of the energy reconstructed in the calorimeter. This fraction, when parametrised as a function of $X$, is fairly energy independent both for electrons and photons. Averaged over the particle energies, it is parametrised by

$$f_{\text{leak}} = \frac{E_{\text{back}}}{E_{\text{cal}}} = f_0(\eta)X + f_1(\eta)e^X.$$

Figure 4.13 shows the resolution on the measurement of the energy of electrons and photons as a function of the energy for $|\eta| = 0.3$. The sampling term $b$ increases from 9% at low–$|\eta|$ to 20% at high–$|\eta|$. This is due to the increase of the material in front of the calorimeter. The constant term is in general lower than 0.6% and is related to the energy modulation in a cell which is not corrected at this stage. The linearity, the ratio between the fitted mean value and the true particle energy, is shown in figure 4.14. It is better than 0.5% over the full $|\eta|$ range and in the energy interval 25–500 GeV.

### In-situ calibration

It is also possible to provide a constraint on the absolute energy scale by inter-calibrating the calorimeter using real $Z \to ee$ events. A constant term of 0.7% and a precision on the energy scale of 0.2‰ can be achieved by fitting the reconstructed $Z$ peak to a reference line-shape for each $\eta \times \phi$ region for 200 pb$^{-1}$ of data, corresponding to 160,000 reconstructed $Z \to ee$ decays. Such a precision will only be achieved once the material in front of the electromagnetic calorimeter will have been determined to a high accuracy using e.g. photon conversions.

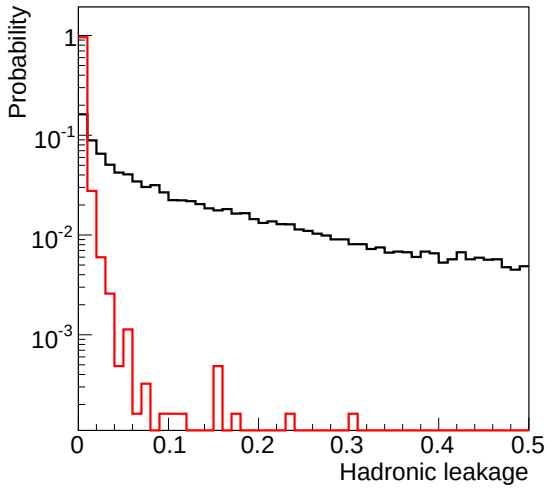


Figure 4.15: Distribution of the hadronic leakage for signal (red) and background (black).

## 4.4 Identification

Candidates corresponding to actual primary electrons can be identified against fakes by applying a series of $p_{\mathrm{T}}$ and $|\eta|$–dependent cuts or thanks to multivariate analyses. After describing the available identification variables, I will detail the cut-based method and present a cut optimization.

### 4.4.1 Identification variables

Identification variables include information from the calorimeters as well as from the inner tracker. In this section, "signal" will refer to single electrons ($7 < p_{\mathrm{T}} < 80$ GeV) and "background" will refer to di-jet events as described in 4.1.

Hadronic leakage Electrons lose most of their energy before reaching the hadronic calorimeter. On the other hand, hadronic jet are more likely to deposit a large amount of energy in the latter. The hadronic leakage is defined as the ratio of the transverse energy of the shower in the first sampling of the hadronic calorimeter in a region $\Delta\eta \times \Delta\phi = 0.12 \times 0.12$ to the transverse energy of the cluster. Figure 4.15 shows the distributions of the hadronic leakage for signal and background. As expected, electrons leave less than 10% of their $p_{\mathrm{T}}$ in the hadronic calorimeter while jets deposit a much larger fraction.

#### Second sampling of the EM calorimeter

Electromagnetic showers deposit most of their energy in the second layer of the electromagnetic calorimeter in which the following variables are used.

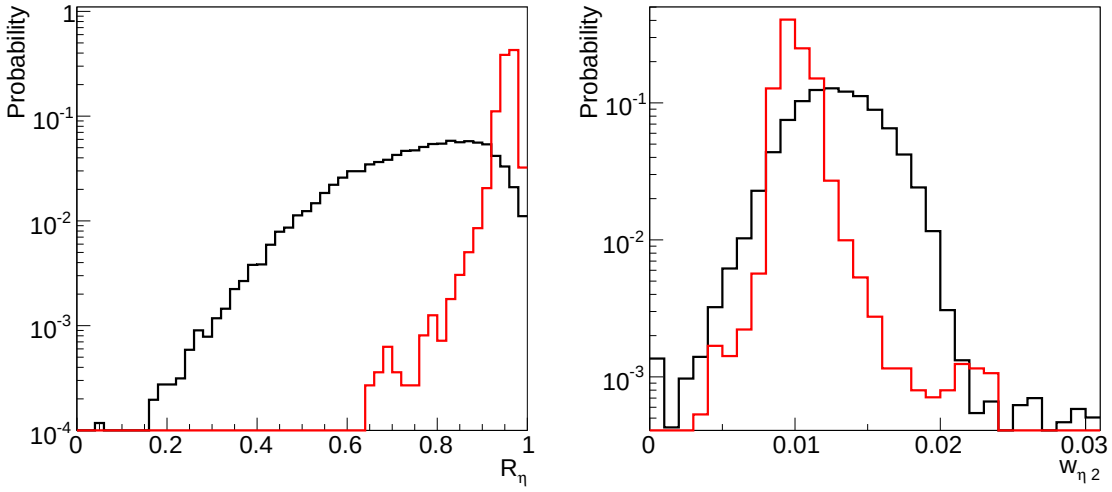


Figure 4.16: Left : distribution of the lateral shower shape in the second sampling of the EM calorimeter for signal (red) and background (black).Right : distribution of the weighted shower width in the second layer for signal (red) and background (black).

Lateral shower shape Energy deposit by electrons tend to be more local and concentrated in pseudo-rapidity. The lateral shower shape $R_\eta$ is defined as the ratio of the energy in the second layer of the EM calorimeter in a window of $3 \times 7$ cells to the energy in a window of $7 \times 7$ cells. The left-side plot in figure 4.16 shows $R_\eta$ for signal and background. For electrons, typically more than 60% of the energy is contained in the $3 \times 7$ window while for jets, $R_\eta$ can get as low as 20%.

Weighted shower width in the second layer Electrons are expected to shower into a more narrow deposit in the EM calorimeter. $w_{\eta 2}$ is the RMS of the pseudo-rapidity of the cells in the cluster weighted by their energy in the second layer of the EM calorimeter. The right-side plot in figure 4.16 shows $w_{\eta 2}$ for signal and background. For signal electrons, the distribution is narrow and peaks around 0.01 while for jets, it is much wider and peaks at a higher value.

### First sampling of the EM calorimeter

Information recorded in the hadronic calorimeter and the second sampling of the EM calorimeter rejects jets with pions of high energy and wide showers. After these cuts jets with single or multiple $\eta$ or $\pi^0$ are the main source of fake electrons. The first compartment, with its very fine granularity in rapidity, can be used to detect substructures within a shower and thus isolated $\pi^0$ and photons.

Maximum difference $\pi^0$ jets often feature two distinct maxima. The variable $\Delta E_s$ is defined as the difference between the energy of the second hottest cell in the first sampling and the energy of the cell with the lowest energy deposit between the two cells

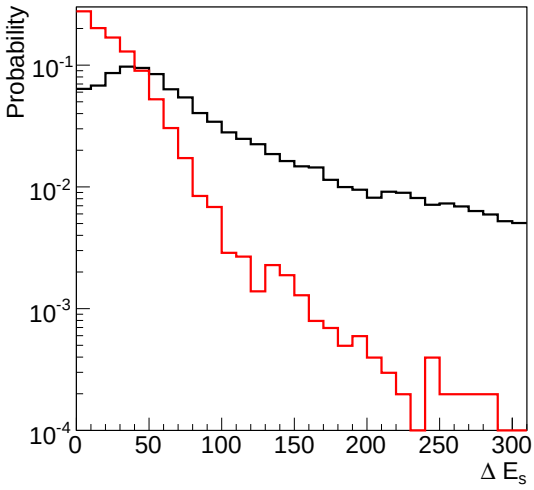


Figure 4.17: Distribution of $\Delta E_s$ for signal (red) and background (black).

with the largest energy deposit. Figure 4.17 shows $\Delta E_s$ in MeV for signal and background. As expected, for electrons, the distribution peaks at zero and the difference is never larger than 300 MeV while for jets it peaks around 50 MeV and spreads out to higher values.

Second largest deposit In order to be insensitive to fluctuations, the value of the second maximal energy deposition has to be greater than a threshold, which depends linearly on the transverse energy. $R_{\mathrm{max2}}$ is defined as $E_{\mathrm{max2}}/(1+9(5)\times 10^{-3}E_{\mathrm{T}})$ where $E_{\mathrm{max2}}$ is the energy of the second hottest cell and 9 (5) is for low (high) luminosity. Left-side plot in figure 4.18 shows $R_{\mathrm{max2}}$ for signal and background. For electrons, the distribution drops quickly and $R_{\mathrm{max2}}$ is seldom larger than 0.7 while for jets it extends to much higher values.

Weighted shower width in the first layer Same as $w_{\eta 1}$ but in the first compartment of the EM calorimeter. The right plot in figure 4.18 shows $w_{\eta 1}$ for signal and background.

Shower width The shower width is defined as $w_{\mathrm{tot1}} = \sqrt{\sum E_i (i - i_{\mathrm{max}})^2 / \sum E_i}$, where $i$ is the strip number and $i_{\mathrm{max}}$ the strip number of the first local maximum. The left-side plot in figure 4.19 shows $w_{\mathrm{tot1}}$ for signal and background.

Core shower shape The core shower shape is define as $F = (E(\pm 3) - E(\pm 1))/E(\pm 1)$, where $E(\pm n)$ is the energy in $\pm n$ strips around the hottest strip. The right-side plot in figure 4.19 shows $F$ for signal and background.

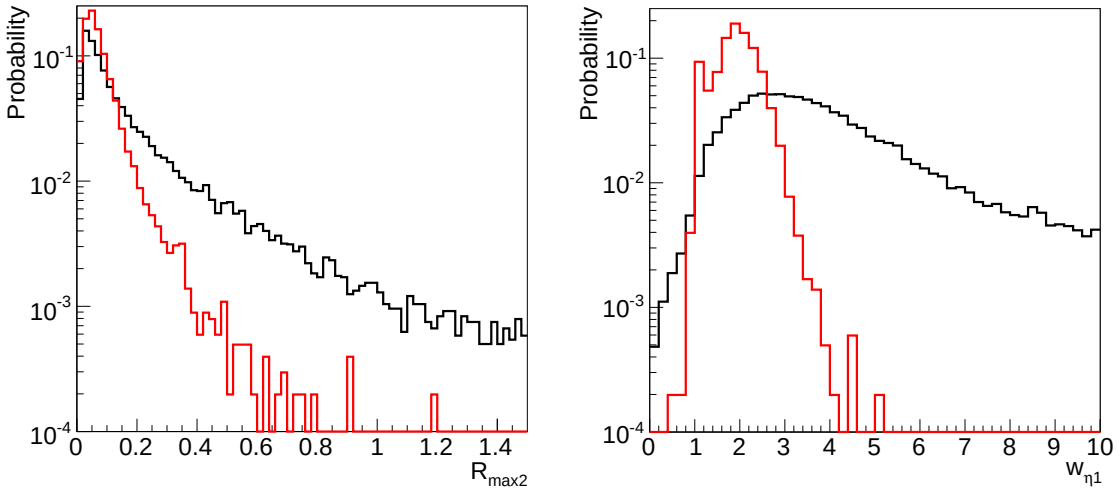


Figure 4.18: Left : distribution of the normalized second energy deposit in the first layer of the EM calorimeter for signal (red) and background (black). Right : distribution of the weighted shower width in the first layer of the EM calorimeter for signal (red) and background (black).

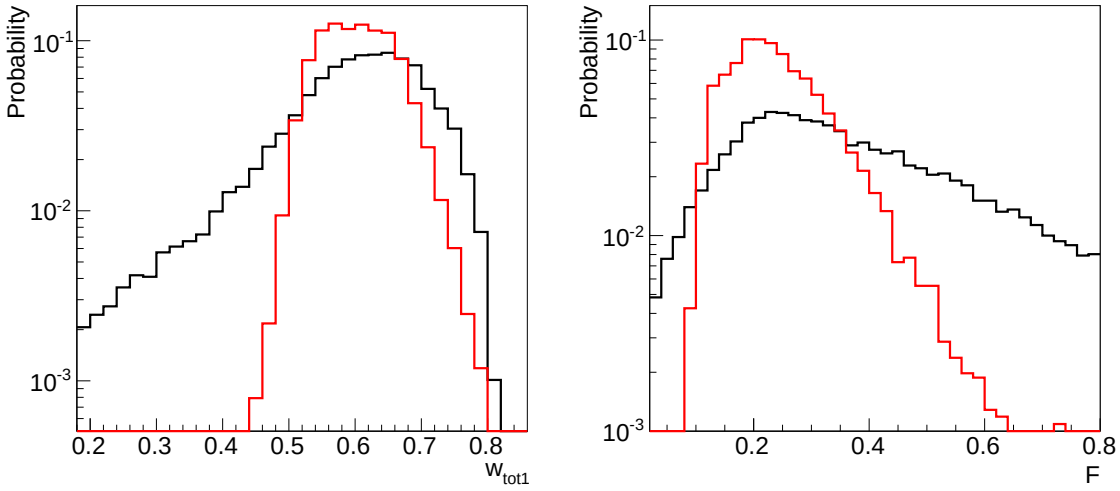


Figure 4.19: Left : distribution of the shower width in the first layer of the EM calorimeter for signal (red) and background (black). Right : distribution of the core shower shape in the first layer of the EM calorimeter for signal (red) and background (black).

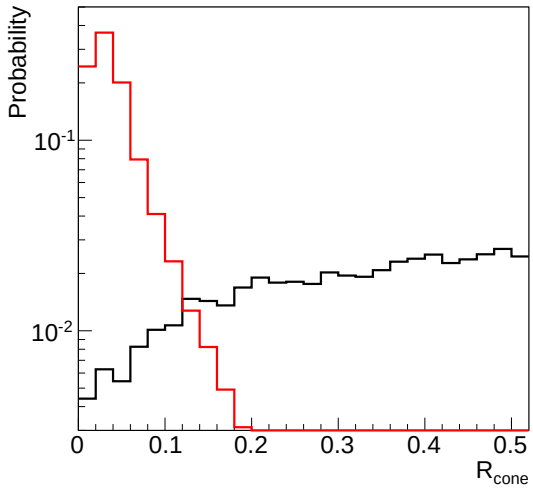


Figure 4.20:

### Calorimetric isolation

Another measure of the containment of the shower is $R_{\text{cone}}$. It is the ratio of the transverse energy in a cone of radius of 0.2 around the shower axis (excluding the cluster itself) to the transverse energy of the cluster. $R_{\text{cone}}$ is typically small for primary electrons. The lower right plot in figure 4.20 shows $R_{\text{cone}}$ for signal and background. An optimization of the cut on this variable is presented in section 4.4.3.

### Track quality

With the use of calorimetric variables, the contamination of the inclusive signal from charged hadrons can be greatly reduced. The remaining background is dominated by photon conversions and low multiplicity jets containing high-$p_{\text{T}}$ $\pi^0$ mesons. They can be eliminated using track requirements.

vertexing-layer $n_B$ indicates whether the track hit the vertexing-layer. This variable helps discriminating photon conversions.

Pixel detector $n_{\text{pixel}}$ is the number of hits on the track in the pixel detector.

Precision hits $n_{\text{Si}}$ is the number of hits on the track in the pixel and SCT detectors.

Impact parameter $A_0$ is the distance of the perigee to the beam axis. It helps discriminating tracks from secondary vertices.

### Track matching

The $\eta$ and $\phi$ difference between the cluster and the associated track are used again in the identification process. $E/p$ is also used. An optimization of the cut on $E/p$ is

| $\|\eta\|$ bins |
|---|
| 0 – 0.8 |
| 0.8 – 1.37 |
| 1.37 – 1.52 |
| 1.52 – 1.8 |
| 1.8 – 2 |
| 2 – 2.35 |
| 2.35 – 2.47 |

Table 4.3: List of bins in pseudo-rapidity.

| $p_{\mathrm{T}}$ bins (GeV) |
|---|
| 0 – 7.5 |
| 7.5 – 15 |
| 15 – 30 |
| 30 – 40 |
| 40 – 50 |
| $> 50$ |

Table 4.4: List of bins in transverse momentum.

presented is section 4.4.3.

#### Transition radiation

The total number of hits on the track in the TRT $n_{\mathrm{TRT}}$ as well as the fraction of high threshold hits $R_{\mathrm{TRT}}$ are used as discriminants. An optimization of the cut on $R_{\mathrm{TRT}}$ is presented in section 4.4.3.

### 4.4.2 Cut-based identification

The standard cut-based procedure is designed to identify electrons in the barrel ($|\eta| < 2.5$) with medium to large transverse momenta (say $p_{\mathrm{T}} > 15$ GeV). Its is robust and will be used as a reference in the early stages of data-taking, before any more subtle technique can be applied.

Cuts are optimized in $7 \times 6$ bins in $|\eta| \times p_{\mathrm{T}}$. Bins limits are listed in table 4.3 and 4.4. Three reference sets of cuts have been defined : loose, medium and tight, as summarised in Table 4.5. This provides flexibility in analyses, for example to improve the signal efficiency for rare processes which are not subject to large backgrounds.

#### Loose cuts

This set of cuts performs a simple electron identification based only on limited information from the calorimeters. Cuts are applied on the hadronic leakage and on shower-shape variables, derived from only the middle layer of the EM calorimeter. This set of cuts provides excellent identification efficiency, but low background rejection.

#### Medium cuts

This set of cuts improves the quality by adding cuts on the first layer of the EM calorimeter and on the tracking variables.
Strip-based cuts are effective in the rejection of $\pi^0 \to \gamma\gamma$ decays. Since the energy-deposit pattern from $\pi^0$'s is often found to have two maxima, showers are studied in a window $\Delta\eta \times \Delta\phi = 0.125 \times 0.2$ around the cell with the highest $E_{\mathrm{T}}$ to look for a second maximum. If more than two maxima are found, the second highest maximum

| Type | Description | Name |
|---|---|---|
| | **Loose cuts** | |
| Acceptance of the detector | $\|\eta\| < 2.47$ | |
| Tile calorimeter | Hadronic Leakage | $R_{\text{had}}$ |
| Second layer of EM calorimeter | Lateral shower shape | $R_{\eta}$ |
| | Weighted width in the second layer. | $w_{\eta 2}$ |
| | **Medium cuts** (includes loose cuts) | |
| First layer of EM calorimeter | Maximum multiplicity. | $\Delta E_s$ |
| | Second largest energy deposit. | $R_{\text{max2}}$ |
| | Weighted width in the first layer. | $w_{\eta 1}$ |
| | Shower width. | $w_{\text{tot1}}$ |
| | Core shower shape. | $F$ |
| Track quality | Number of hits in the pixel detector. | $n_{\text{pixel}}$ |
| | Number of precision hits. | $n_{\text{Si}}$ |
| | Transverse impact parameter. | $A_0$ |
| | **Tight cuts** (includes medium cuts) | |
| Isolation | Isolation in the calorimeter. | $R_{\text{cone}}$ |
| B–layer | Number of hits in the vertexing-layer. | $n_B$ |
| Track matching | $\Delta\eta$ between the cluster and the track. | $\Delta\eta$ |
| | $\Delta\phi$ between the cluster and the track. | $\Delta\phi$ |
| | Ratio of the cluster energy to the track momentum. | $E/p$ |
| TRT | Total number of hits in the TRT. | $n_{\text{TRT}}$ |
| | Ratio of the number of high threshold hits to $n_{\text{TRT}}$. | $R_{\text{TRT}}$ |
| | **Tight 90 cuts** (includes tight except for isolation) | |
| TRT | Same as TRT cuts above, but with tighter values corresponding to about 90% efficiency for isolated electrons. | |

Table 4.5: Definition of variables used for loose, medium and tight electron identification cuts. See section 4.4.1 for a detailed description.

is considered. The variables used include $\Delta E_s$, $R_{\mathrm{max2}}$, $w_{\mathrm{tot1}}$, $w_{\eta 1}$ and $F$. The tracking variables include $n_{\mathrm{pixel}}$, $n_{\mathrm{Si}}$ and $A_0$.
Medium cuts increase the jet rejection by a factor of 3 to 4 with respect to the loose cuts, while reducing the identification efficiency by $\sim 10\%$.
The baseline analysis for the search for the Higgs boson in the $H \to ZZ^* \to 4e$ channel makes use of the loose set of cuts for the two electrons springing from the on-shell $Z$. Electrons from the $Z^*$ are more subject to background. They are required to pass the medium set of cuts. Also, as part of signatures for supersymmetric events, electrons are required to pass the medium set as other cuts on the event are likely to reject most of the background ($\not{E}_{\mathrm{T}}$, jet $p_{\mathrm{T}}$,...).

#### Tight cuts

This set of cuts makes use of all the variable currently available for electrons. In addition to the cuts used in the medium set, candidates are required to have one hit in the vertexing-layer to reject conversions. Cuts on the TRT are applied to reject the dominant background from charged hadrons and more narrow track matching constraints are required ($\Delta\eta$, $\Delta\phi$ and $E/p$).
Two different final selections are available within this tight category: they are named tight and tight 90 and are optimised differently for isolated and non-isolated electrons. In the case of tight cuts, a cut on $R_{\mathrm{cone}}$ is applied. This set of cuts provides, in general, the highest isolated electron identification and the highest rejection against jets. The tight 90 cuts do not include the additional explicit energy isolation cut, but instead apply tighter cuts on the TRT information to further remove the background from charged hadrons.
Electrons passing the tight set of cuts are used in the analysis of processes with a large rate or that are subject to a large background such as $Z, \Upsilon, J/\Psi \to ee$, $W \to e\nu$ or $WH \to e\nu\gamma\gamma$. They are also used as "tag" electrons in the determination of identification efficiencies from data (see 4.5.4) or to reject electrons in the identification of $\tau$ leptons.

### 4.4.3 Cut optimization

Two studies leading to the optimization of the identification cuts on $R_{\mathrm{TRT}}$ and $E/p$ are presented in this section.

#### Transition radiation

As shown on figure 4.28, one of the most harmful identification cut for the signal is the requirement on $R_{\mathrm{TRT}}$, that is the ratio of the number of high-threshold hits in the TRT to the total number of hits therein. When fitting tracks in the TRT, hits that carry too large a contribution to the $\chi^2$ are excluded and tagged as outliers. As shown in the left-side and centre plots in figure 4.21 in black, when excluding outlier hits, around 21% of signal electrons do not feature any hit in the TRT after the rest of the tight set of cut has been applied (except TRT cuts). As shown on the right-side plot, this results in more than 22% of signal electrons with $R_{\mathrm{TRT}} = 0$. The inclusion of outlying

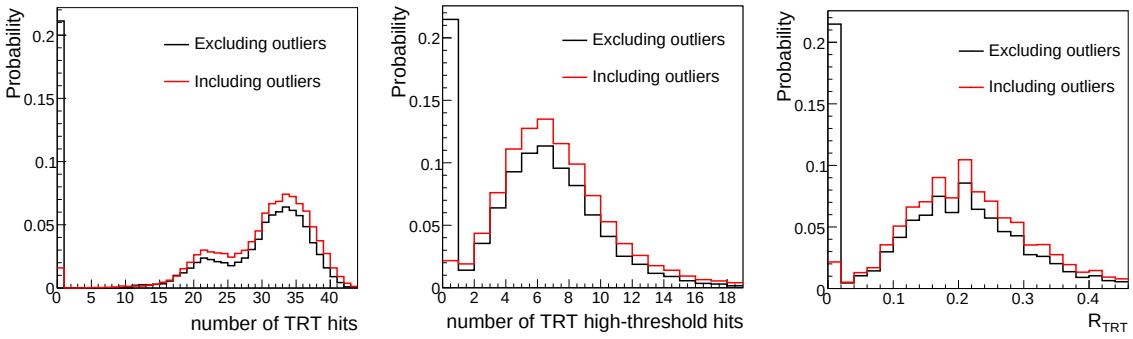


Figure 4.21: Distributions of the number of TRT hits (left), the number of high-threshold TRT hits (centre) and of $R_{\mathrm{TRT}}$ (right) for electrons found in SUSY events.

| $\lvert\eta\rvert$ | Cut value ($R_{\mathrm{TRT}}>$) |
|---|---|
| 0 – 0.1 | 0.08 |
| 0.1 – 0.625 | 0.085 |
| 0.625 – 1.07 | 0.085 |
| 1.07 – 1.304 | 0.115 |
| 1.304 – 1.752 | 0.13 |
| 1.752 – 2 | 0.155 |

Table 4.6: Optimized values for the lower cut on $R_{\mathrm{TRT}}$ for each TRT $|\eta|$ bin.

hits to the count decreases this fraction to around 2%, bringing back candidates within the acceptance of a cut on $R_{\mathrm{TRT}}$.
The $|\eta|$ bins design is slightly different for cuts applied on information from the TRT as they have to take into account its specific geometry rather than that of the calorimeter. The bin limits for TRT cuts are shown in the left column of table 4.6. Figure 4.22 shows $R_{\mathrm{TRT}}$ for signal electrons found in SUSY events (red) and fake electrons found in di-jet events (black). For the signal, candidates are selected after the tight set of cuts has been applied except for cuts on the TRT. For the background, no identification cut were applied in order to conserve significant statistics. The blue line indicates the chosen value for the lower cut on $R_{\mathrm{TRT}}$ for the corresponding $|\eta|$ bin. Table 4.6 lists the optimal value for the lower cut on $R_{\mathrm{TRT}}$ for each $|\eta|$ bins in the TRT.

### Cluster/track momentum matching

A constraint on the ratio of the energy of the cluster to the momentum of the associated track is an efficient tool to discriminate background from hadronic jets. Indeed, for the latter, the energy deposit in the calorimeter results from the showering of a number of constituents where as the tracks left in the tracking detector only sign the passage of one of the constituents. This results in $E/p$ values larger than unity which is expected in the case of signal electrons.

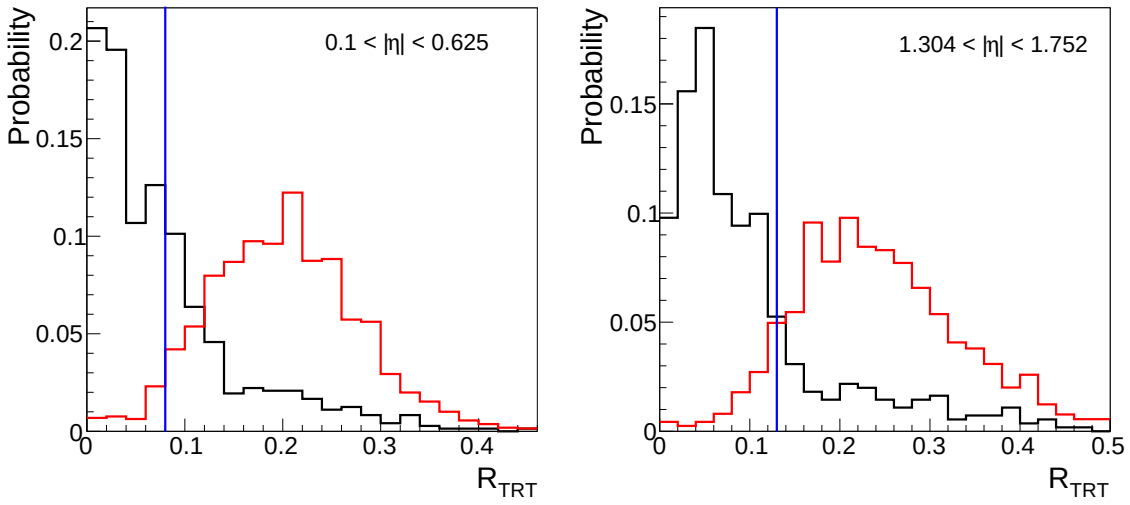


Figure 4.22: Distributions of $R_{\mathrm{TRT}}$ for signal electrons found in SUSY events (red) and fake electrons found in di-jet events (black). On the left-side, candidates with $0.1 < |\eta| < 0.625$ are selected while, on the right-side, candidates with $1.304 < |\eta| < 1.752$. For the signal, candidates are selected after the tight set of cuts has been applied except for cuts on the TRT. For the background, no identification cut were applied in order to conserve significant statistics. The blue line indicates the chosen value for the lower cut on $R_{\mathrm{TRT}}$ for the corresponding $|\eta|$ bin.

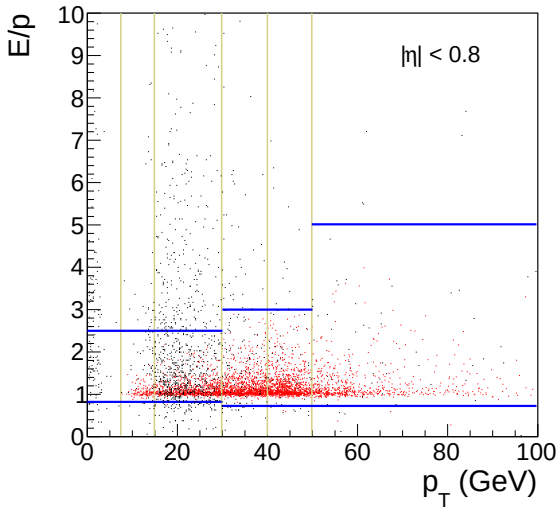


Figure 4.23: Distributions of $E/p$ versus $p_{\mathrm{T}}$ for signal electrons (red) found in $Z \rightarrow ee$ events and for fake electrons (black) found in di-jet events. Signal electrons were selected after the tight set of cuts has been applied (except for the cut on $E/p$) and fakes were selected before any identification cuts. Vertical lines indicates the $p_{\mathrm{T}}$–bins limits. Horizontal lines indicates the chosen values for the upper and lower cut on $E/p$.

| | $\|\eta\|$ | | | | | | |
|---|---|---|---|---|---|---|---|
| $p_T$ (GeV) | 0 – 0.8 | 0.8 – 1.37 | 1.37 – 1.52 | 1.52 – 1.8 | 1.8 – 2 | 2 – 2.35 | 2.35 – 2.47 |
| 0 – 7.5 | 0.8 | 0.8 | 0.8 | 0.8 | 0.8 | 0.8 | 0.8 |
| 7.5 – 15 | 0.8 | 0.8 | 0.8 | 0.8 | 0.8 | 0.8 | 0.8 |
| 15 – 30 | 0.8 | 0.8 | 0.8 | 0.8 | 0.8 | 0.8 | 0.8 |
| 30 – 40 | 0.7 | 0.7 | 0.7 | 0.7 | 0.7 | 0.7 | 0.7 |
| 40 – 50 | 0.7 | 0.7 | 0.7 | 0.7 | 0.7 | 0.7 | 0.7 |
| > 50 | 0.7 | 0.7 | 0.7 | 0.7 | 0.7 | 0.7 | 0.7 |
| | $E/p >$ | | | | | | |

| | $\|\eta\|$ | | | | | | |
|---|---|---|---|---|---|---|---|
| $p_T$ (GeV) | 0 – 0.8 | 0.8 – 1.37 | 1.37 – 1.52 | 1.52 – 1.8 | 1.8 – 2 | 2 – 2.35 | 2.35 – 2.47 |
| 0 – 7.5 | 2.5 | 2.5 | 2.5 | 3 | 3 | 3 | 3 |
| 7.5 – 15 | 2.5 | 2.5 | 2.5 | 3 | 3 | 3 | 3 |
| 15 – 30 | 2.5 | 2.5 | 2.5 | 3 | 3 | 3 | 3 |
| 30 – 40 | 3 | 3 | 3 | 3 | 4 | 4 | 3 |
| 40 – 50 | 3 | 3 | 3 | 4 | 5 | 5 | 4 |
| > 50 | 5 | 5 | 5 | 5 | 5 | 5 | 5 |
| | $E/p <$ | | | | | | |

Table 4.7: Optimized values for the lower and upper cut on $E/p$ for each $p_T$ and $|\eta|$ bin.

Figure 4.23 shows a scatter plot of $E/p$ versus the $p_T$ of candidates in the first $|\eta|$ bin ($|\eta| < 0.8$ as listed in 4.3) for electrons found in $Z \rightarrow ee$ events (red) and for fake electrons found di-jet events (black). Signal electrons were selected after the tight set of cuts was applied whereas fakes were selected before any identification cut. Evidently, the distribution for fake electrons extends to values up to 10 whereas it is well confined around unity for signal electrons. The blue vertical lines indicates the chosen values for the cut on $E/p$ in each $p_T$ bin. Table 4.7 lists optimized values for the lower and upper cut on $E/p$ for each $p_T$ and $|\eta|$ bin.

### Isolation in the calorimeter

In order to increase background rejections, a criterion can be applied on the isolation of the shower in the calorimeter. For that purpose, the transverse energy in a cone of radius $R$ can be measured. That quantity is defined as the sum of the transverse energy of all cells within $R$ of the object position, including those in the hadronic calorimeter minus the sum of the transverse energy of all cells in the cluster. It measures the transverse energy surrounding the cluster. This quantity is measured for $R = 0.2$, 0.3 and 0.4. Off course, it is very much dependant on the transverse energy of the cluster and hence, should be normalized to it. Let

$$R_{\text{cone } 20,30,40} = \frac{E_T(\text{cone } 20, 30, 40)}{E_T(\text{cluster})}.$$

Figure 4.24 shows $R_{\text{cone } 20}$, $R_{\text{cone } 30}$ and $R_{\text{cone } 40}$ for signal electrons found in SUSY events (red) and fake electrons found in di-jet events (black). Fakes are mostly composed of hadronic jets. No cuts are applied. Evidently, $R_{\text{cone}}$ is mostly gathered

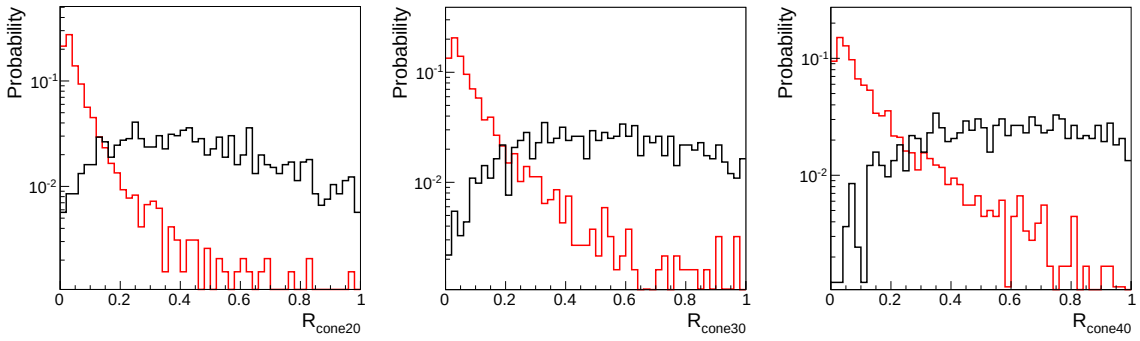


Figure 4.24: $R_{\text{cone }20}$ (left), $R_{\text{cone }30}$ (centre) and $R_{\text{cone }40}$ (right) for electrons found in SUSY events (red) and fake electrons found in di-jet events (black). Candidates are selected before the identification process.

| Cut | $R_{\text{cone }20} < 0.4$ | $R_{\text{cone }30} < 0.7$ | $R_{\text{cone }40} < 0.9$ |
|---|---|---|---|
| Gain in rejection | + 22% | + 13% | + 7% |

Table 4.8: Relative increase in rejection after a rudimentary cut on $R_{\text{cone}}$ for three values of the cone radius and with no loss of signal efficiency.

towards 0 for signal electrons and more widely spread in the case of fake electrons. This is due to the fact that hadronic jets deposit energy well outside the $5 \times 7$ clusters used to reconstruct electrons as well as in the hadronic calorimeter. For signal electrons, most of the energy is well contained within the cluster. As expected the bulk of the distribution for fake electrons is shifted towards greater values as the radius of the cone increases. However, the effect is more visible for signal electrons, for which the distribution broadens as the radius of the cone increases.

In order to choose which cone radius to use, we apply a rudimentary $p_{\text{T}}$ and $|\eta|$–independent cut and compare the variation in efficiencies and rejections. We want to improve the background rejection without causing any noticeable effect to the tight set efficiency for the signal. For each radius, the cut value is decreased until a significant drop in efficiency is observed. For the resulting cut value, the jet rejection is estimated. Table 4.8 shows the relative increase in jet rejection after applying the cut. A cut on $R_{\text{cone}}$ for a cone radius of 0.2 provides evidently the best gain in background rejection for no significant loss in signal efficiency. Furthermore, the amount of transverse energy in a $R = 0.2$ cone has been shown to be insensitive to pile-up as opposed to cone with larger radii [103].

Figure 4.25 shows the distribution of $R_{\text{cone }20}$ in the six $p_{\text{T}}$ bins defined in table 4.4. The optimized values for the cut in the different $p_{\text{T}}$ bins are listed in table 4.9. Cut values were chosen to minimize efficiency loss while maximizing the gain in background rejection.

In terms of performances, table 4.10 summarizes the effect on this isolation requirement on signal efficiencies and background rejections for the tight set of cuts. Eventually, the

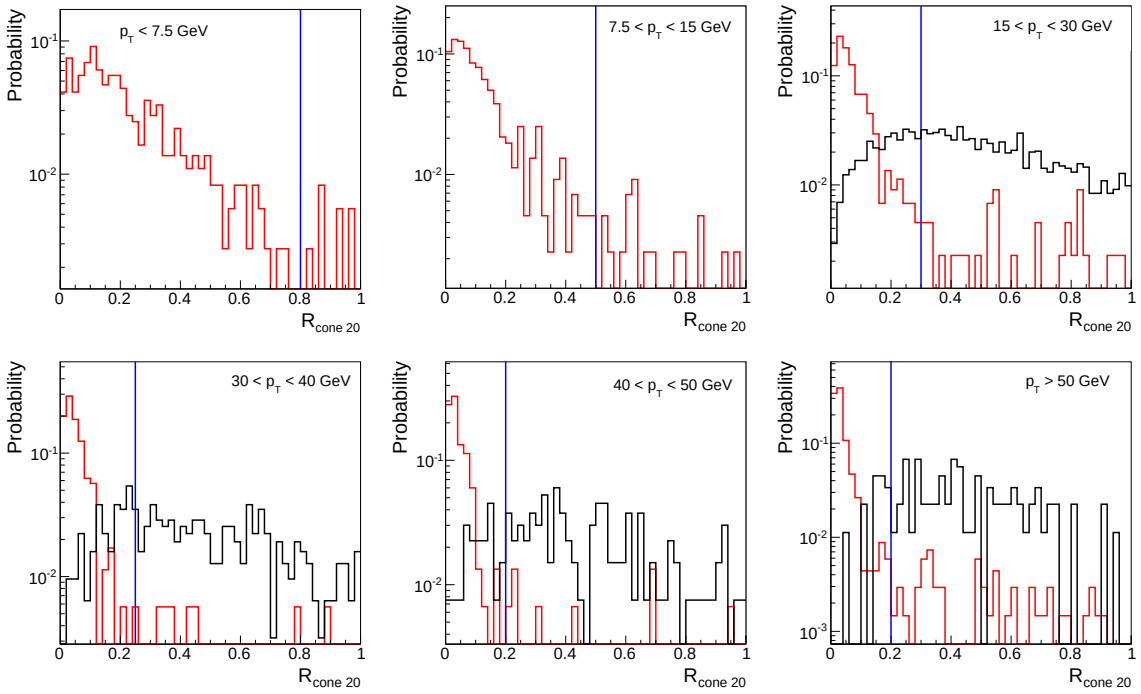


Figure 4.25: Distributions of $R_{\text{cone 20}}$ for electrons found in SUSY events (red) and for fake electrons found in di-jet events (black) for the six $p_{\text{T}}$ bins defined in table 4.4. The first two plots do not show background as there is a $p_{\text{T}} > 17$ GeV cut in the di-jet sample (see section 4.4.1). The blue lines indicate the chosen values for the cut.

application of an optimized $p_{\text{T}}$–dependent cut on the calorimetric isolation of electron candidates yields a 64% relative increase in background rejection at the cost of a 1.5% relative drop in signal efficiency. This isolation criterion stands as a refinement in the electron identification process and hence belongs in the tight set of cuts.

## 4.5 Identification performance

A trustworthy measure of the identification performance is crucial for the reduction of systematic uncertainties. This includes measuring signal efficiencies as well as background rejections. These must then be estimated as a function of $|\eta|$ and $p_{\text{T}}$ and confronted among different samples. The following definitions of the performance quantities constitute the baseline for all performance and physics analyses presented in the CSC challenge [81]. Quoted numbers were obtained with the 13.0.30 release of the `athena` software.

| $p_{\mathrm{T}}$ (GeV) | Cut value ($R_{\mathrm{cone\ 20}}$ <) |
|---|---|
| 0 – 7.5 | 0.8 |
| 7.5 – 15 | 0.5 |
| 15 – 30 | 0.3 |
| 30 – 40 | 0.25 |
| 40 – 50 | 0.2 |
| > 50 | 0.2 |

Table 4.9: Optimized value of the cut on $R_{\mathrm{cone\ 20}}$ for each $p_{\mathrm{T}}$ bin.

| | Efficiency (%) | Rejection |
|---|---|---|
| Tight set without isolation | 65.4 ± 0.6 | 59800 ± 2600 |
| Tight set | 64.4 ± 0.6 | 98000 ± 4000 |
| Relative difference | −1.5% | +64% |

Table 4.10: Effect of the isolation requirement on signal efficiencies and background rejections. Efficiencies are obtained on electrons found in SUSY events and rejections are obtained on fake electrons found in di-jet events.

### 4.5.1 Signal efficiency

The electron identification efficiency is defined as

$$\epsilon_{\mathrm{id}} = \frac{N_{\mathrm{id}}}{N_{\mathrm{truth}}} \tag{4.1}$$

where $N_{\mathrm{truth}}$ is the number of isolated electrons within the acceptance in the Monte Carlo truth and $N_{\mathrm{id}}$ is the number of reconstructed electrons passing a certain set of cut and matching one of the isolated electrons counted in $N_{\mathrm{truth}}$. The acceptance refers to $|\eta| < 2.47$, that is the coverage of the EM calorimeter, and a lower $p_{\mathrm{T}}$ cut which is usually quoted along with the efficiency. When the efficiency is quoted as a function of $p_{\mathrm{T}}$ or $|\eta|$, these corresponds to the MC truth particle.
Isolated electrons are searched for in the output of the Monte Carlo generators. They should not be a particle issued by the detector simulation as resulting from the interaction of the final state with matter. Table 4.11 describes the classification of Monte Carlo electrons depending on their parent particle. Isolated electrons should decay

| Category | Type of parent particle |
|---|---|
| Isolated | $Z$, $W$, $t$, $\tau$ or $\mu$ |
| Non-isolated | $J/\psi$, $b$–hadron or $c$–hadron decays |
| Background electron | $\gamma$, $\pi^0/\eta$ Dalitz decays, light hadron decays |

Table 4.11: Classification of electron according to parent particle.

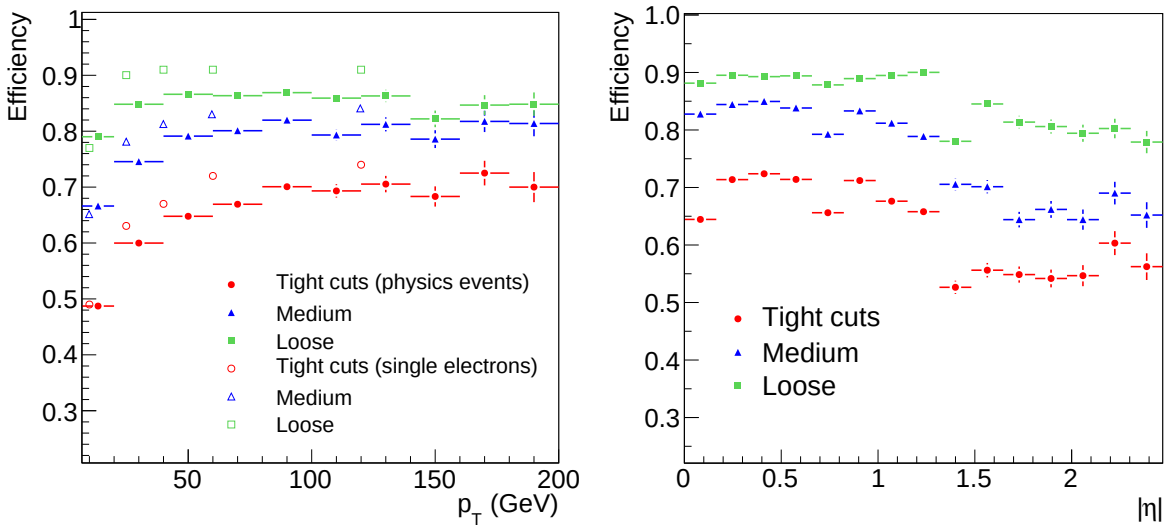


Figure 4.26: Electron identification efficiency as a function of $p_{\mathrm{T}}$ (left) and $|\eta|$ (right) for electrons in SUSY events (full markers) and fixed–$p_{\mathrm{T}}$ single electrons (hollow markers) [81].

from an electroweak vector boson, a top quark, a $\tau$ or a muon. Once an isolated electrons is found within the acceptance, the corresponding reconstructed track is searched for. Indeed, a direct software link exists between reconstructed tracks and the Monte Carlo truth particle that left it. Eventually, reconstructed electron candidates in the event are scanned until one contains the previously selected track. This procedure is more complicated but more stable than a geometrical matching, as it does not depend on any $\Delta R$ cut. Selected candidates are counted into $N_{\mathrm{id}}$ if they satisfy the set of cuts of interest.

Efficiencies can be measured on single electron events for sanity checks and software monitoring. However, realistic final states such as $Z \rightarrow ee$ or SUSY events should be used for a more robust measure. Indeed, the high jet and track multiplicity in SUSY events constitute a very hostile environment for the identification of isolated electrons. Figure 4.26 shows the electron identification efficiency as a function of transverse momenta and pseudo-rapidity. Efficiencies corresponding to the loose, medium and tight set of cuts are shown in green squares, blue triangles and red circles respectively. Efficiencies for fixed–$p_{\mathrm{T}}$ single electron events ($p_{\mathrm{T}} = 10$, 25, 40, 60 and 120 GeV) are shown in open markers while efficiencies for electrons in SUSY events are plotted in full markers. Efficiencies with the tight set of cuts reaches a plateau of 70% at high $p_{\mathrm{T}}$. The medium (loose) set of cuts reaches a plateau of 80% (85%). The efficiencies obtained for transverse momenta below say 20 GeV, are significantly lower than the plateau values, for which the cuts were initially optimised. As expected, single electrons display higher efficiencies than those in SUSY events because of the large hadronic activity in these events. The efficiencies as a function of $|\eta|$ show a drop in the end-cap region ($|\eta| > 1.5$). Specific drops can also be seen for $|\eta| \sim 1.35$, which corresponds to the

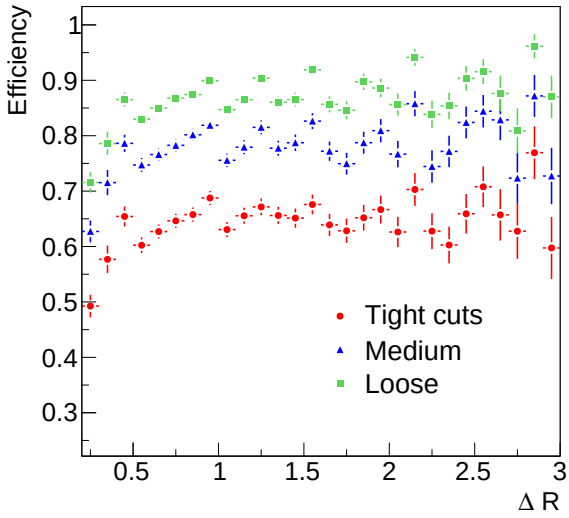


Figure 4.27: Electron identification efficiency as a function of the distance to the closest jet for electrons in SUSY events [81].

barrel/end-cap transition region, and for $|\eta| \sim 0.8$, which corresponds to the change in the lead thickness between the two types of electrodes in the barrel EM calorimeter. Figure 4.27 shows the electron identification efficiency as a function of the distance to the closest jet. Jets were reconstructed based on the MC truth and with a cone of $R = 0.4$. The efficiencies are uniform down to $\Delta R \sim 0.4$ from where the overlap between the electron and hadronic showers cause a drop. Jets are reconstructed from topological clusters using a $\Delta R = 0.4$ cone algorithm.
Figure 4.28 shows the effect of each cut on the identification efficiency of single electrons with $7 < p_{\mathrm{T}} < 80$ GeV. The efficiencies in this figure are normalized to the number of reconstructed electron candidates. On the upper plot, each cut is applied individually. On the lower plot, all cuts are applied but one. Evidently, the most impairing cuts are those applied on tracking variables such as $R_{\mathrm{TRT}}$, $n_{\mathrm{B}}$, $n_{\mathrm{pixel}}$ or $n_{\mathrm{Si}}$. These cuts are indeed stringent but are necessary in order to reach the required rejection on charged hadrons. Also, as shown on the upper plot, cuts on the combined variables ($\Delta\eta$, $\Delta\phi$ and $E/p$) are harmful but, as can be seen on the lower plot, are very correlated with other cuts as their release do not provide any gain in efficiency. Indeed, removed candidates are most likely electrons which underwent bremsstrahlung and did not leave any quality information in the TRT.
Table 4.13 provides signal efficiencies for the three sets of cuts. Evidently and as expected, efficiencies obtained on $Z \rightarrow ee$ events are consistent with those obtained on SUSY events and with those shown in figure 4.26 when integrated for $p_{\mathrm{T}} > 17$ GeV.

As mentioned is section 3.4.1, the high luminosity of the LHC will induce a pile-up of minimum bias events in the detector, even in the early phase. The effect of the pile-up resulting from a $10^{33}$ cm$^{-2}$s$^{-1}$ luminosity on the identification of electrons in $Z \rightarrow ee$ and $t\bar{t}$ events was investigated in [103]. The largest effect was seen in the track

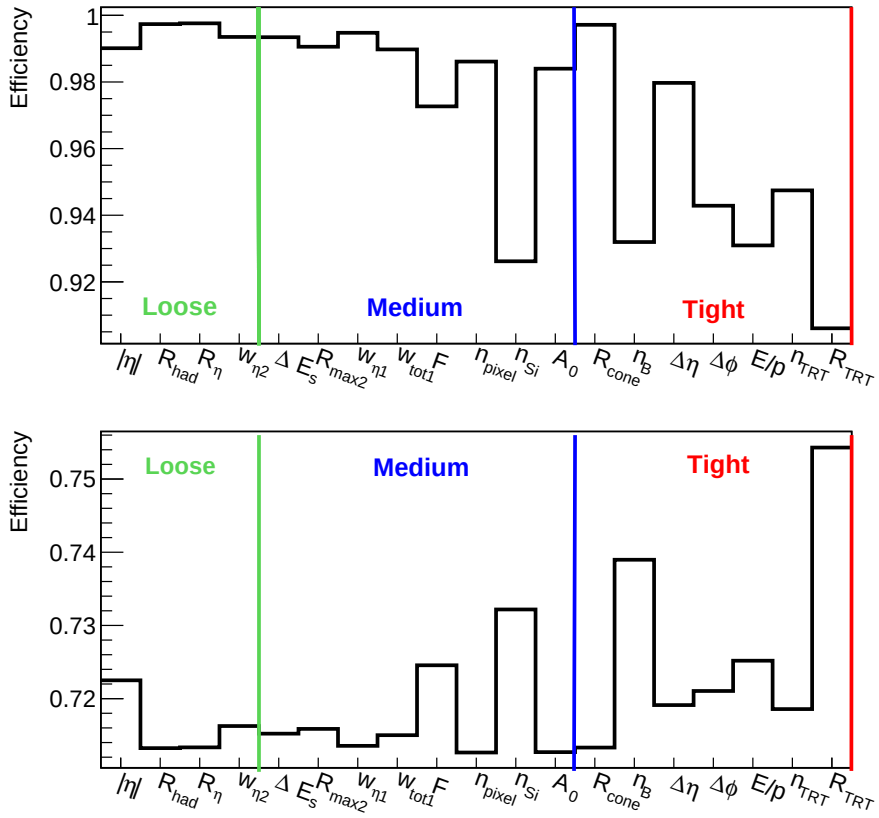


Figure 4.28: Effect of single cuts on the identification efficiency of single electrons. The classification efficiency was not included. On the top, cuts are applied one by one, on the bottom, all cuts but one are applied.

| $p_{\mathrm{T}} > 17$ GeV | | |
|---|---|---|
| Isolated | Non-isolated | Background |
| $W$ – 75.0% | $b$-hadrons – 38.7% | $\gamma$-conv. – 97.8% |
| $Z$ – 20.9% | $c$-hadrons – 60.6% | Dalitz decays – 1.8% |
| $\tau$ – 4.1% | $J/\psi$ – 0.7% | $u/d/s$-hadrons – 0.4% |

Table 4.12: Contribution and origin of isolated, non-isolated, and background electron candidates in the two di-jet samples before the identification criteria are applied [81].

| | $p_{\mathrm{T}} > 17$ GeV | | |
|---|---|---|---|
| | Efficiency (%) | | Jet rejection |
| | $Z \to ee$ | SUSY | di-jet |
| Loose | 87.96 ± 0.07 | 89.29 ± 0.36 | 567 ± 1 |
| Medium | 77.29 ± 0.06 | 77.35 ± 0.49 | 2,184 ± 13 |
| Tight | 64.22 ± 0.07 | 64.36 ± 0.56 | 98,000 ± 4,000 |

Table 4.13: Expected efficiencies for isolated electrons and corresponding jet background rejections for the three sets of cuts used for electron identification. The results are shown for $p_{\mathrm{T}} > 17$ GeV for electrons in $Z \to ee$ or SUSY events and fake electrons in di-jet events [81].

multiplicity and in the calorimeter isolation but did not result in any change on the efficiencies. The effect on photons from $H \to \gamma\gamma$ events was shown in [81] to be also negligible.

### 4.5.2 Background rejection

The jet rejections are obtained using di-jet events. See section 4.1 for a detailed description of the sample.
The jet rejections are normalised with respect to the number of particle jets reconstructed using particle four-momenta within a cone size $\Delta R = 0.4$ and derived from un-filtered di-jets events. The average number per generated event of such particle jets with $p_{\mathrm{T}}$ above 17 GeV and in the range $|\eta| < 2.47$ is 0.74. The jet rejection is defined as

$$R = \frac{N_j^{\mathrm{truth}}}{N_j^{\mathrm{e-id}}} = \frac{N_{\mathrm{events}} \times 0.74}{N_j^{\mathrm{e-id}} \times \epsilon_{\mathrm{filter}}}$$

where $N_j^{\mathrm{truth}}$ is the number of true jets in the non-filtered sample, $N_{\mathrm{events}}$ is the number of events under consideration after the filter has been applied, $\epsilon_{\mathrm{filter}} = 0.0828$ is the filter efficiency and $N_j^{\mathrm{e-id}}$ is the number of true jets reconstructed as electrons.

After reconstruction of electron candidates and before any of the identification cuts are applied, the signal is completely dominated by non-isolated electrons from $b$ and $c$–hadron decays. The expected signal-to-background ratios for the filtered di-jet sample

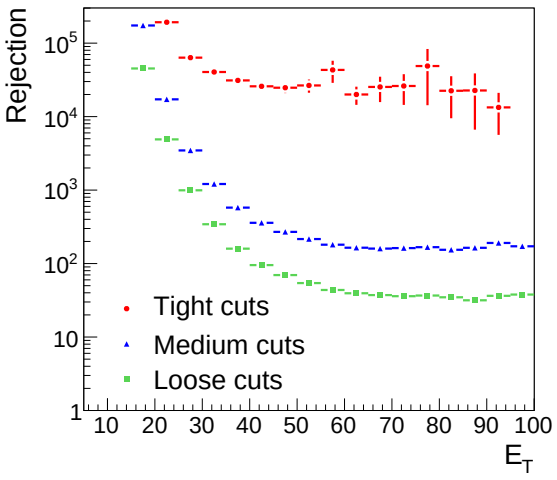


Figure 4.29: Jet rejection as a function of $E_{\mathrm{T}}$ obtained on di-jet events.

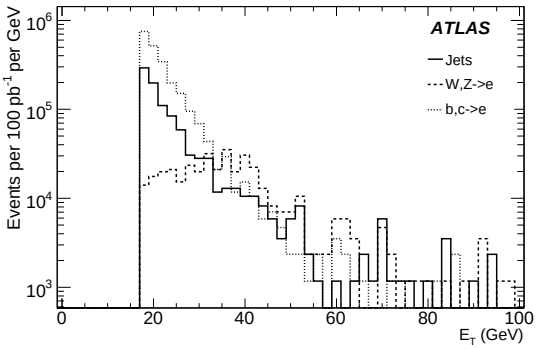


Figure 4.30: Differential cross-sections as a function of $E_{\mathrm{T}}$ after the tight set of cuts has been applied, shown separately for the expected components from isolated electrons, non-isolated electrons and residual di-jet background, for an integrated luminosity of 100 pb$^{-1}$ [81].

| $\lvert\eta\rvert$ | Jet rejection | | |
|---|---|---|---|
| | Loose | Medium | Tight ($\times 10^5$) |
| 0.00 – 0.80 | 600 ± 3 | 3740 ± 50 | 1.5 ± 0.1 |
| 0.80 – 1.35 | 353 ± 2 | 1581 ± 20 | 1.09 ± 0.09 |
| 1.35 – 1.50 | 353 ± 3 | 444 ± 5 | 0.9 ± 0.1 |
| 1.50 – 1.80 | 643 ± 6 | 2440 ± 40 | 2.3 ± 0.4 |
| 1.80 – 2.00 | 1300 ± 21 | 9800 ± 450 | 3.2 ± 0.8 |
| 2.00 – 2.35 | 1700 ± 24 | 8400 ± 300 | 0.40 ± 0.02 |
| 2.35 – 2.47 | 2170 ± 62 | 4050 ± 170 | 0.29 ± 0.03 |
| 0.00 – 2.47 | 567 ± 2 | 2184 ± 13 | 0.98 ± 0.04 |

Table 4.14: Jet rejections for each $|\eta|$ bin.

is 1:80. The residual jet background is dominated by charged hadrons. Only a small fraction of the background at this stage consists of electrons from photon conversions or Dalitz decays, namely 6.4%. Table 4.12 summarises the relative compositions of the filtered di-jet samples.

Table 4.13 shows jet rejections for the three sets of cuts. By construction, the loose set provides high signal efficiency but low rejection. It can be useful in the case of multi-lepton final states with non-dominant QCD background. The medium set provides intermediate efficiency and rejection while the tight set brings the required $10^5$ jet rejection for an overall efficiency of 64%.

Figure 4.29 shows the jet rejection as a function of $E_{\mathrm{T}}$ obtained on di-jet events for the three sets of cuts. Rejections are very high for low–$E_{\mathrm{T}}$ jets for which electromagnetic showers are expected to be broader and tracks of lesser quality. Rejections reach a

| Cuts | Cut-based method | | Likelihood method | |
|---|---|---|---|---|
| | $\epsilon_e$ (%) | $R_j$ | $\epsilon_e$ (%) at fixed $R_j$ | $R_j$ at fixed $\epsilon_e$ |
| Loose | $87.97 \pm 0.05$ | $567 \pm 1$ | $89.11 \pm 0.05$ | $2767 \pm 17$ |
| Medium | $77.29 \pm 0.06$ | $2184 \pm 7$ | $88.26 \pm 0.05$ | $(3.77 \pm 0.08)10^4$ |
| Tight | $64.22 \pm 0.07$ | $(9.9 \pm 0.2)10^4$ | $67.53 \pm 0.06$ | $(1.26 \pm 0.05)10^5$ |
| Tight (no iso.) | $61.66 \pm 0.07$ | $(8.9 \pm 0.2)10^4$ | $68.71 \pm 0.06$ | $(1.46 \pm 0.06)10^5$ |

Table 4.15: Expected electron efficiencies for a fixed jet rejection and jet rejections for a fixed electron efficiency, as obtained from the likelihood discriminant method. The quoted errors are statistical [81].

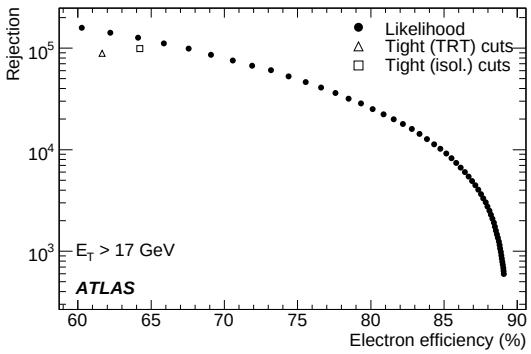


Figure 4.31: Jet rejection versus isolated electron efficiency obtained with a likelihood method (full circles) compared to the results from the two sets of tight cuts (open triangle and open square) [81].

plateau around their integrated values for $E_{\mathrm{T}} \approx 40$ GeV. Table 4.14 lists the jet rejections for each $|\eta|$ bin. Figure 4.30 shows the differential cross-sections as function of $E_{\mathrm{T}}$ after the tight set of cuts has been applied.

### 4.5.3 Multivariate techniques

In addition to the standard cut-based method, several multivariate techniques have been developed and implemented in the ATLAS software. These include a likelihood discriminant, a discriminant called H-matrix, a boosted decision tree and a neural network.
Table 4.15 summarises the gains in efficiency and rejection which may be expected with respect to the cut-based method by using the likelihood discriminant method. The gains appear to be artificially large in the case of the loose and medium cuts. This is due to the fact that these cuts do not make use of all the information available in terms of electron identification, as they were designed for robustness and ease of use with initial data. Nevertheless, they indicate how much the electron efficiency may be improved once all the discriminant variables will be understood in the data.

Figure 4.31 shows the rejection versus efficiency curve obtained using the likelihood discriminant method, compared to the results obtained for the two sets of tight cuts. The likelihood discriminant method provides a gain in rejection of about 20–40% with respect to the cut-based method for the same efficiency of 61–64%. Alternatively, it provides a gain in efficiency of 5–10% (tight and medium cuts) for the same rejection. Multivariate methods of this type will of course only be used once the detector performance has been understood using the simpler cut-based electron identification criteria.

### 4.5.4 In-situ determination of the efficiency

The experimental uncertainty on the electron identification efficiency is expected to be the source of one of the main systematic errors in many measurements, and in particular in cross-section determinations. In addition, a reliable monitoring of the electron identification efficiency is important in the commissioning phase of the detector and software.

The tag-and-probe method allows for an in-situ determination of electron efficiencies. It consists in tagging a clean sample of events using one electron, and then measuring the efficiency of interest using the second electron from the $Z$ boson decay. The tag condition typically requires an electron identified with tight cuts. The invariant mass of the lepton pair is then used to identify the number of tagged events, $N_1$ (containing $Z \to ee$ decays), and a sub-sample $N_2$, where the second pre-selected electron further passes a given set of identification cuts. The efficiency for a given signature is given by the ratio between $N_2$ and $N_1$. To account for background, the lepton-pair invariant mass spectrum is fitted around the $Z$ mass peak using a Gaussian distribution convoluted with a Breit-Wigner plus an exponential function. The dominant background arises from QCD but its contribution is small in general and its impact on the measurement is therefore very limited.

Figure 4.32 shows the electron identification efficiency for the medium set of cut obtained on $Z \to ee$ events using the tag-and-probe method and the Monte Carlo truth as a function of $p_{\mathrm{T}}$ and $|\eta|$. The relative difference between the two methods is less than 0.5% in regions where the efficiency is flat. The size of the available $Z$ boson sample is a source of systematic error. With an integrated luminosity of 100 pb$^{-1}$, the error is expected to be in the range 1–2% for $p_{\mathrm{T}} > 25$ GeV, and $\sim 4\%$ in the low–$p_{\mathrm{T}}$ bin. Another source of systematic error comes from varying the selection criteria. For instance, uncertainties introduced by varying the cut on the $Z$ boson mass or requiring an isolation criterion for the probe electron were evaluated. The magnitude of the uncertainty introduced is smaller than 0.5% for $p_{\mathrm{T}} > 40$ GeV. At low $p_{\mathrm{T}}$, this uncertainty is estimated to be in the 1–2% range.

### 4.5.5 Efficiencies in $t\bar{t}$ events

In the early phases of data-taking, electron efficiencies will have to be estimated from real data in order to cross-check results obtained using MC generated samples. For

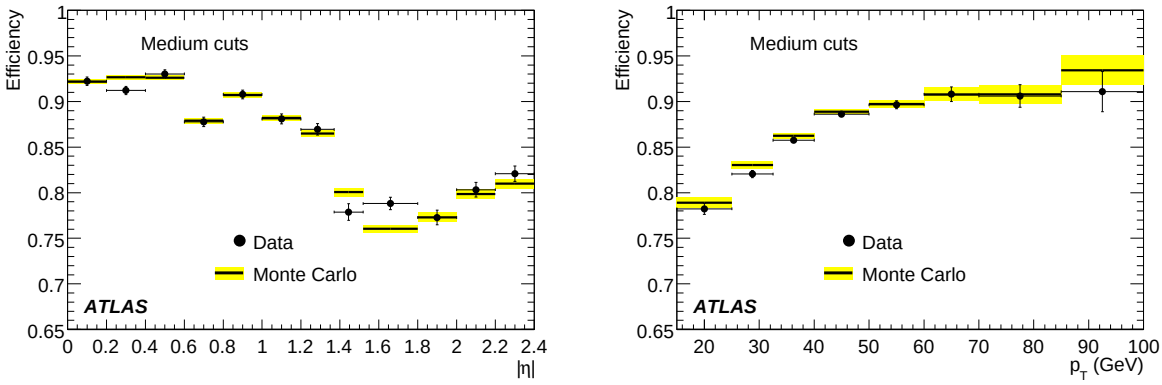


Figure 4.32: Electron identification efficiency for the medium set of cut obtained on $Z \rightarrow ee$ events using the tag-and-probe method and the Monte Carlo truth as a function of $p_{\mathrm{T}}$ (left) and $|\eta|$ (right) for an integrated luminosity of 100 pb$^{-1}$.

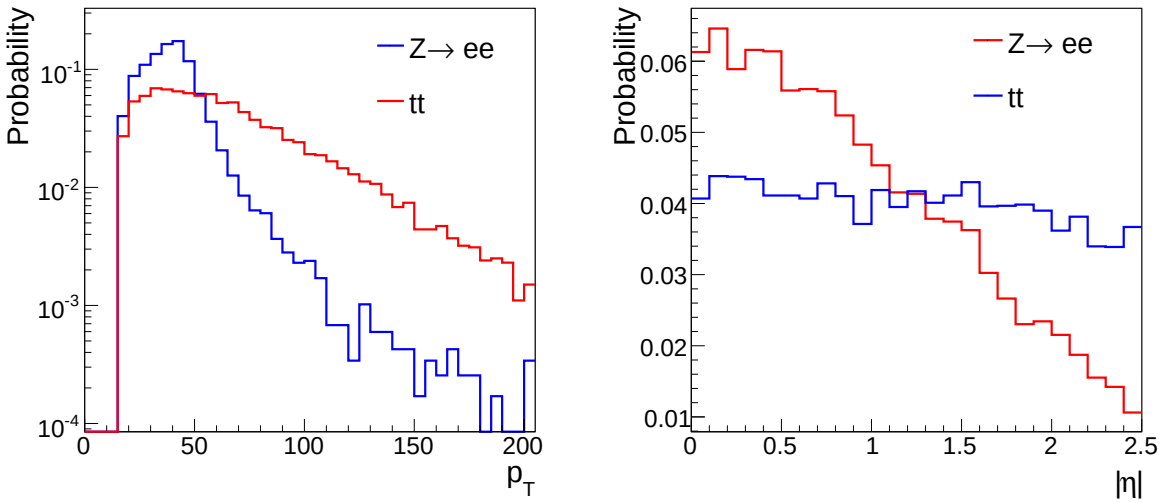


Figure 4.33: Distributions of the $p_{\mathrm{T}}$ (left) and $|\eta|$ (right) of electrons found in $Z \rightarrow ee$ (blue) and $t\bar{t}$ events (red).

| Process | $\sigma$ | BR | $f$ | $\sigma$ |
|---|---|---|---|---|
| $Z \to ee$ | 1430 pb | 100% | 32% | 458 pb |
| $t\bar{t}$ | 833 pb | $(qqe\nu) = 14\%$ | 58% | 68 pb |

Table 4.16: Cross-sections for the production of at least one electron with $p_{\mathrm{T}} > 50$ GeV in $Z$ and $t\bar{t}$ events at the LHC. $f$ is the fraction of events with at least one electron with $p_{\mathrm{T}} > 50$ GeV.

| $N$ jets | fraction (%) | Loose | Medium | Tight |
|---|---|---|---|---|
| 0 | 46 | 87±0.5 | 77±0.6 | 67±0.7 |
| 1 | 33 | 87±0.5 | 79±0.7 | 69±0.8 |
| 2 | 14 | 88±0.8 | 78±1 | 68±1 |
| ≥3 | 7 | 86±1 | 77±2 | 68±2 |

Table 4.17: Electron identification efficiencies as a function of the number of true jets in $Z \to ee$ events.

that purpose, the tag-and-probe method was described in section 4.5.4. It relies on electrons from $Z \to ee$ decays and takes advantage of the excellent knowledge of the $Z$ line-shape obtained at LEP.

$t\bar{t}$ events constitute one of the main background to all analyses requiring several high–$p_{\mathrm{T}}$ jets, missing transverse energy and leptons. That includes most of the signatures investigated in the context of the search for supersymmetry. A trustworthy knowledge of the electron identification efficiency in $t\bar{t}$ events is thus of major importance for a correct estimation of the background.

Figure 4.33 shows the transverse momentum and pseudo-rapidity distributions of isolated electrons found in $Z \to ee$ events (blue) and $t\bar{t}$ events (red). For the latter, electrons arise from the decay $t \to bW \to be\nu$. Whereas electrons from $Z$ decays are mostly gathered in the 15–70 $p_{\mathrm{T}}$–range, the $p_{\mathrm{T}}$–spectrum for electrons from $t\bar{t}$ decays is much broader and extends up to 200 GeV. More than 10% of these electrons have $p_{\mathrm{T}} > 100$ GeV. Also, these $t\bar{t}$ electrons mostly appear in the central part of the detector ($|\eta| = 0$) whereas $Z$ electrons are almost uniformly distributed across the whole acceptance of the detector.

Electrons from $Z$ and $t\bar{t}$ decays lie in different domains of phase-space. Table 4.16 shows the cross-sections for the production of at least one electron with $p_{\mathrm{T}} > 50$ GeV in $Z$ and $t\bar{t}$ events at the LHC. $Z$ events will provide almost seven times as many high–$p_{\mathrm{T}}$ electrons than $t\bar{t}$ events. Hence, the tag-and-probe method applied on $Z \to ee$ events allows to probe secluded regions in phase-space.

Figure 4.34 shows the electron identification efficiency as a function of the transverse momentum of the leading jet in $Z \to ee$ events for the three standard sets of cuts. Jets were reconstructed with a cone algorithm with $R = 0.4$ based on true partonic information. Efficiencies are slightly higher than the numbers shown in 4.5.1 as the

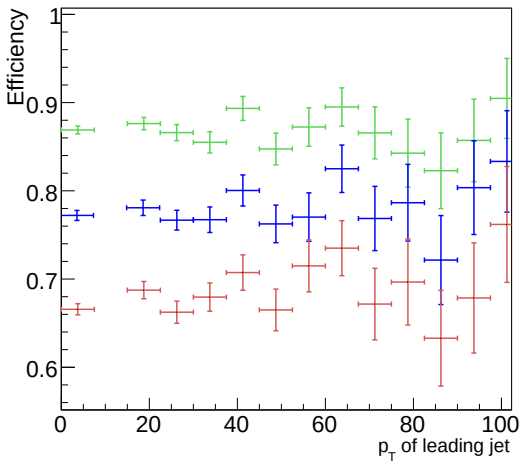


Figure 4.34: Electron identification efficiency as a function of the $p_{\mathrm{T}}$ of the leading jet in $Z \rightarrow ee$ events for the loose (green), medium (blue) and tight sets (red). The first bin on the left corresponds to the case where no jet is present in the event.

study was performed with a later version of the `Athena` software (release 14), which incorporated a number of improvements. Although statistical error bars stretch as the $p_{\mathrm{T}}$ of the leading jet increases, no dependence of the efficiencies on the latter can be argued.
Table 4.17 shows the identification efficiencies as a function of the number of true jets in the event. Again, although statistical errors increase with the number of jets, no dependence can be shown. In addition, it was shown in section 4.5.1 that identification efficiencies do not depend on the promiscuity between electrons and jets in the event.

After a careful study of the dependence of the electron identification efficiencies on various characteristics of $t\bar{t}$ and $Z \rightarrow ee$ events, no reason was found to distrust the estimation of the electron identification efficiency provided by the tag-and-probe method as applied on $Z \rightarrow ee$ events.

# Chapter 5

# Search for supersymmetry

*"I'm not fat, I'm big boned"*

Eric Cartman – *SouthPark*

*"There's nothing an agnostic can't do if he doesn't know whether he believes in anything or not"*

Graham Chapman – *Monty Python's Flying Circus*

The search for supersymmetry (SUSY) is one of the main goals of the LHC experiments. The estimation of the potential for the discovery, for the measurement and determination of the underlying parameters of as many phenomenologically realistic models as possible has been estimated. The MSSM and in particular mSUGRA, GMSB and AMSB were extensively explored among the ATLAS and CMS collaborations. The investigated signatures cover a large panorama of possible models and showed that, if realized in nature, SUSY will most likely be discovered at the LHC. If discovered, the underlying parameters of the theory will have to be determined. However, the busy environment in which SUSY events may occur as well as the rarity of some processes will disfavour a precise determination of the most secluded sectors. In such cases, future colliders such as the ILC or CLIC should provide valuable measurements towards a full comprehension of the theory.

Two studies are presented. Firstly, the potential for a discovery at the LHC of a model in which scalars are decoupled from the weak scale is discussed. Possible observables are investigated. A detailed study with Monte Carlo generated samples is performed to evaluate the uncertainties on their measurements. The precision to which the parameters of the model can be determined is estimated using the dedicated `SFitter` program. Secondly, the determination of the parameters of the MSSM at future linear colliders is studied. The improvement provided by the International Linear Collider (ILC) or a Compact LInear Collider (CLIC) to the determination of the parameters of the MSSM is estimated in the case of a specific parameter set (SPS1a). After a review of the observable sectors including a calculation of the gluino production cross-section at CLIC, the model is investigated using `SFitter`.

## 5.1 Decoupled scalars at the LHC

The preparation for the search for supersymmetry at the LHC was mostly realized in the framework of the MSSM and in particular in mSUGRA. Typical parameter sets provide reasonable cross-sections and present a wide spectrum of new particles at the LHC. Gluinos and squarks are produced and decay into charginos, neutralinos and quarks. Neutralinos and charginos can also be produced directly. Heavy Higgs bosons may also be produced and detected. With all new particles lighter than a few TeV, these models allow for a cancellation of quadratic and logarithmic divergences in the corrections to the Higgs boson mass (see section 1.6). Also, it is possible to provide a candidate for dark matter and unify gauge couplings at $M_{\mathrm{GUT}}$.

Although many signatures have been investigated, the case in which new scalars (squarks, sleptons and heavy Higgs bosons) are not produced at the LHC has raised less attention as it does not occur naturally in the MSSM. Indeed, as scalars get heavy, a large contribution from $\mu$ drives neutralino and chargino masses to very small values. In order to generate scalar masses above the reach of the LHC, they have to be decoupled from the low energy spectrum.

A complementary motivation for decoupling scalars lies in the claim that the naturalness of the weak scale should not be a guiding principle for SUSY model building [104, 105, 106]. It is argued that since supersymmetry does not address the problem of the naturalness of the cosmological constant [104], it should not be required to maintain the weak scale where it is. Both issues may find a solution via anthropic or so-called galactic principles [107]. Models in which supersymmetry is broken at a very large scale ($10^4 - 10^{16}$ GeV) may also provide solutions to a number of disturbing aspects of the MSSM (section 5.1.1) as well as a candidate for dark matter and unify gauge couplings at the high scale (section 5.1.3).

### 5.1.1 Problems with weak-scale supersymmetry

Weak-scale SUSY and in particular the MSSM are usually the most studied realization of supersymmetry. However, these models contain a number of disturbing features:

#### The Higgs boson mass

As mentioned in section 2.2.1, in the context of the MSSM, the mass of the lightest Higgs boson $m_h$ is bounded from above by $m_Z$ at tree-level. Radiative corrections from fermion and sfermion loops induce non-negligible contributions to $m_h$ and the upper bound can rise to 130 GeV [63] if sfermions are lighter than 1 TeV and the tree-level $m_h$ is close to its upper bound. Also, the triviality argument discussed in section 1.4 states that if SUSY appears at the TeV scale, the Higgs boson should be heavier than $\approx 70$ GeV in order for the Higgs quartic coupling $\lambda$ to remain positive.
Hence, a theoretically comfortable mass range for the light Higgs boson is between 70 and 130 GeV. Experimentally, $m_h$ is bounded from below by the LEP experiments with $m_h > 92.8$ GeV at 95% confidence level [24] when MSSM couplings are included.

Thus, about half of the allowed region is already excluded experimentally. This shows that a soft fine-tuning may already be at play in the Higgs sector of the MSSM.

#### Cosmological constant problem

As mentioned in the introduction, some sort of vacuum energy is necessary to account for the observed acceleration of the expansion of the Universe. This energy density should be of gravitational scale in order to produce the desired effects. If gravity is to be described by a local quantum field theory, contributions to the vacuum energy may arise from the quantum fluctuations of the gravity gauge boson, the graviton. However, if this is to be valid up to the Planck scale $M_P$, the resulting vacuum energy is larger than the observed one by some 120 orders of magnitude. A cancellation of these contributions similar to that of the quadratic divergences in the Higgs boson mass would require the occurrence of new physics at the $10^{-3}$ eV scale. This fine-tuning is of much larger magnitude than that of the weak scale. It was suggested that both of these may be realized in the anthropic selection of the vacuum within the enormous landscape of vacua appearing in string theory [107, 104].

#### Dimension–5 proton decay

In the MSSM, requiring $R$–parity to be conserved prevents dimension–4 operators $ql\tilde{d}^c$ and $u^c d^c \tilde{d}^c$ from mediating proton decay faster than experimental upper limits. However, in the context of supersymmetric Grand Unified Theories [50], dimension–5 operators of the form $ff\tilde{f}\tilde{f}$ can also accelerate proton decay. In such cases, the decay rate of the proton scales as $m_{1/2}^2/m_0^4$ [108], where $m_{1/2}$ and $m_0$ are the universal gaugino and scalar masses, respectively. Hence, if scalars are taken to be very heavy, this rate is suppressed.

#### Flavour and CP problems

The SM prevents flavour-changing interaction and none was observed experimentally. Also, the only observed occurrence of CP–violation (in weak decays of $K$ and $B$–mesons) are also correctly described by the SM. In the constrained MSSM, new flavour-changing terms and CP–violating phases in the Lagrangian are assumed to be negligible in order to build a phenomenologically viable model. Yet, no symmetry prevents the existence of these terms. Notably, large flavour changing neutral current due to the exchange of sfermions are generally expected to enhance $K^0 - \overline{K^0}$ mixing or the $\mu \to e\gamma$ decay. Also, CP–violating contributions to the electric dipole moment of fermions are expected. Again, if scalars are very heavy, these effects are suppressed.

### 5.1.2 Decoupled Scalars Supersymmetry

In Decoupled Scalars Supersymmetry (DSS), all scalars are degenerate with mass $m_S$

$$m_{\tilde{l}} = m_{\tilde{q}} = m_{H,H^\pm,A} \equiv m_S \gtrsim 10^4 \text{ GeV}$$

and are all decoupled from the low energy spectrum. The latter consists of the usual SM fields, the remaining SUSY fields, i.e. the gluino $\tilde{g}$, the wino $\tilde{W}$, the bino $\tilde{B}$ and the higgsinos components $\tilde{H}_{u,d}$. Omitting gauge-invariant kinetic terms and non-renormalizable operators, the Lagrangian density of the low energy effective theory reads [106]

$$\begin{aligned} L \supset\ & m^2 H^\dagger H - \frac{\lambda}{2}\left(H^\dagger H\right)^2 - \left[\kappa_u \bar{q} u \epsilon H^* + \kappa_d \bar{q} d H + \kappa_e \bar{\ell} e H\right. \\ & + \frac{1}{2}\left(M_3 \hat{g}\hat{g} + M_2 \tilde{W}\tilde{W} + M_1 \tilde{B}\tilde{B}\right) + \mu \tilde{H}_u^T \epsilon \tilde{H}_d \\ & \left. + \frac{H^\dagger}{\sqrt{2}}\left(\hat{g}_u \sigma \tilde{W} + \hat{g}'_u \tilde{B}\right)\tilde{H}_u + \frac{H^T \epsilon}{\sqrt{2}}\left(\hat{g}'_d \tilde{B} - \hat{g}_d \sigma \tilde{W}\right)\tilde{H}_d + \text{h.c.}\right] \end{aligned} \tag{5.1}$$

where $\sigma^a$ are the Pauli matrices, $\epsilon = i\sigma^2$. $\kappa^{u,d,e}$ are effective Yukawa couplings. $H$ is the light Higgs boson doublet. It is fine-tuned to have a small mass term $m^2$

$$H = -\cos\beta \epsilon H_d^* + \sin\beta H_u.$$

At the scale $m_S$, the low-energy effective theory is matched with the full MSSM to determine effective couplings

$$\begin{aligned} \lambda(m_S) &= \tfrac{1}{4}\left[\tfrac{3}{5} g_1^2(m_S) + g_2^2(m_S)\right]\cos^2 2\beta + \Delta_{\text{th}}, \\ k_u(m_S) &= y_u^*(m_S)\sin\beta, & k_{d,e} &= y_{d,e}^* \cos\beta \\ \hat{g}_u(m_S) &= g_2(m_S)\sin\beta, & \hat{g}_d(m_S) &= g_2(m_S)\cos\beta \\ \hat{g}'_u(m_S) &= \sqrt{\tfrac{3}{5}} g_1(m_S)\sin\beta, & \hat{g}'_d(m_S) &= \sqrt{\tfrac{3}{5}} g_1(m_S)\cos\beta \end{aligned} \tag{5.2}$$

where $g_1$ and $g_2$ are the U(1) and SU(2) gauge couplings. It is important to note that $\tan\beta$ only appears in the boundary conditions and therefore is not a parameter of the low-energy effective theory. $\tan\beta$ is interpreted as the fine-tuned angle that rotates the two Higgs doublets into one heavy and one light rather than as the ratio of two vacuum expectation values.

In order to keep gauginos and higgsinos light, it is argued that they are protected by an $R$–symmetry and a Peccei-Quinn symmetry, respectively. If $M_i = \mu = 0$ simultaneously, the low-energy effective theory remains invariant under a global U(1) symmetry that is the product of an $R$–symmetry and a PQ symmetry.
One of the corrections to the tree-level Higgs boson mass $m_h^2 = 2\lambda v$ arises from the threshold correction to the quartic Higgs coupling $\Delta_{\text{th}}$

$$\Delta_{\text{th}} = \frac{3y_t^4}{8\pi^2}\left[\left(1 - \frac{\frac{3}{5}g_1^2 + g_2^2}{8y_t^2}\right)\frac{X_t^2}{m_S^2} - \frac{X_t^4}{12 m_S^4}\right]$$

where $y_t = m_t/v$ is the top Yukawa coupling and $X_t = A_t - \mu/\tan\beta$, with $A_t$ the trilinear Higgs-stop coupling. $\Delta_{\text{th}}$ is suppressed for large values of $m_S$ and $A_t$ must be small for the same reasons as gaugino and higgsino masses.

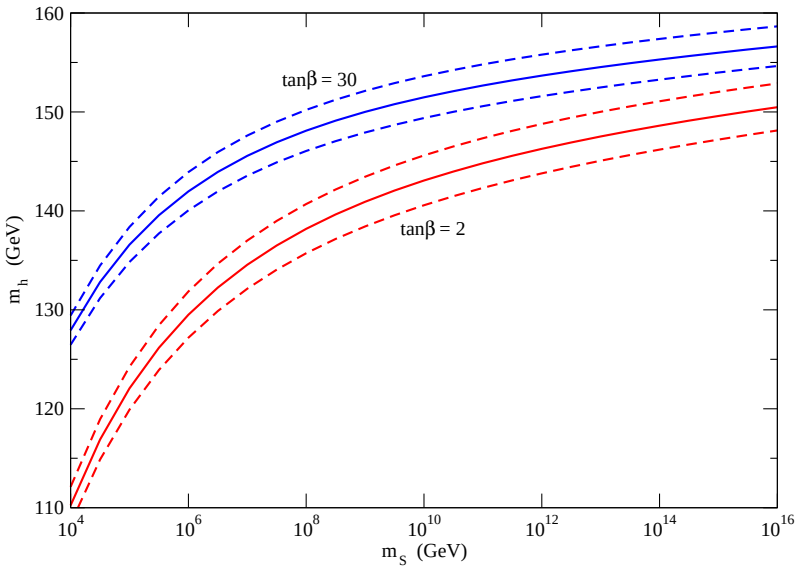


Figure 5.1: Mass of the light Higgs boson as a function of the scalar mass $m_S$ for $A_t = 0$, $\mu = m_{1/2} = 500$ GeV [110]. The dashed lines correspond to a $\pm 1$ $\sigma$ variation of the top quark mass.

The gaugino masses are given as input at the GUT scale and assumed to be universal: $M_i(M_{\mathrm{GUT}}) = m_{1/2}$. They are evolved down to the scale $m_S$ by the `SuSpect` code [109, 110] using the one-loop Renormalization Group Equations (RGEs) of the MSSM. $\mu$ is provided as an independent input parameter at the scale $m_Z$. From $m_S$, scalars are integrated out and the modified RGEs [106] are run down to the desired scale.

`SuSpect` includes one-loop corrections from both the SM and charginos and neutralinos in the computation of the mass of the light Higgs boson $m_h$. Figure 5.1 shows the logarithmic dependence of $m_h$ on the scalar mass $m_S$ for a given set of input parameters and two values of $\tan\beta$. This dependence on $m_S$ is due to the running of $\lambda$ from $m_S$ to the weak scale. For low $m_S$, the variation of $\tan\beta$ can change $m_h$ by almost 20 GeV. This is the largest effect of $\tan\beta$ on the low-energy effective theory and is due to the $\cos^2 2\beta$ in 5.2.

The tree-level chargino and neutralino mass matrices read

$$M_{\tilde{C}} = \begin{pmatrix} M_2 & \hat{g}_u v \\ \hat{g}_d v & \mu \end{pmatrix} \quad \text{and} \quad M_{\tilde{N}} = \begin{pmatrix} M_1 & 0 & -\frac{\hat{g}'_d v}{\sqrt{2}} & -\frac{\hat{g}'_u v}{\sqrt{2}} \\ 0 & M_2 & \frac{\hat{g}_d v}{\sqrt{2}} & -\frac{\hat{g}_u v}{\sqrt{2}} \\ -\frac{\hat{g}'_d v}{\sqrt{2}} & \frac{\hat{g}_d v}{\sqrt{2}} & 0 & -\mu \\ \frac{\hat{g}'_u v}{\sqrt{2}} & -\frac{\hat{g}_u v}{\sqrt{2}} & -\mu & 0 \end{pmatrix}.$$

`SuSpect` includes one-loop corrections to the chargino and neutralino masses in order to reduce the dependence on the renormalization scale. The gluino mass is related to $M_3$ by

$$m_{\tilde{g}} = M_3(Q) \left[ 1 + \frac{\alpha_S}{4\pi} \left( 12 + 9 \log \frac{Q^2}{M_3^2} \right) \right].$$

| | |
|---|---|
| Scalar mass scale | $m_S$ |
| Gaugino mass parameter at $M_{\mathrm{GUT}}$ | $m_{1/2}$ |
| Higgsino mass parameter at $m_Z$ | $\mu$ |
| Matching parameter | $\tan\beta$ |
| Higgs-stop trilinear coupling | $A_t$ |

Table 5.1: Input parameters of the DSS model

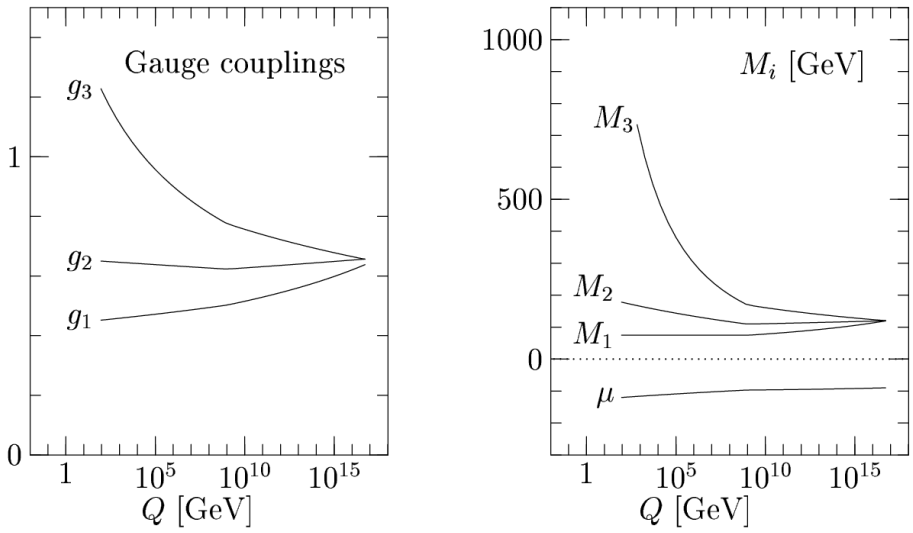


Figure 5.2: Running of the gauge couplings (left) and of the gaugino mass parameters (right) using the DSS RGEs [106] below $m_S$ [113]. The following parameters were used: $m_S = 10^9$ GeV, $m_{1/2} = 120$ GeV, $\mu = -120$ GeV and $\tan\beta = 4$.

Table 5.1 summarizes the input parameters of the DSS model.

### 5.1.3 Properties of DSS

#### Gauge couplings unification

It is shown in [111, 112] that new particles entering the RGEs at an intermediate scale $m_S$ ($m_Z < m_S < M_{\mathrm{GUT}}$) contribute identically to the running of the three gauge couplings if they compose complete representations of the unification group. All sfermions in the MSSM form complete SU(5) representations. Hence, the gauge couplings unification scheme exposed in the case of the MSSM (section 2.2.2) is unchanged.

Figure 5.2 shows the running of the gauge couplings (left) and of the gaugino mass parameters (right) using the standard MSSM RGEs above $m_S$ and the DSS RGEs below.

### Fine-tuning of the Higgs boson mass

The mass matrix for the two Higgs doublets reads

$$\begin{pmatrix} |\mu|^2 + m_{H_u}^2 & b \\ b & |\mu|^2 + m_{H_d}^2 \end{pmatrix}$$

whose eigenvalues are

$$\langle m_H^2 \rangle \pm \sqrt{\Delta^2 + b^2}$$

$$\text{with} \quad \langle m_H^2 \rangle = \frac{m_{H_u}^2 + m_{H_d}^2}{2} + |\mu|^2 \quad \text{and} \quad \Delta = \frac{m_{H_u}^2 - m_{H_d}^2}{2}.$$

Requiring the lightest Higgs boson mass to be of the order of the weak scale amounts to constraining the lightest of the eigenvalues to the range $[-m_{\text{EW}}^2 : 0]$. These bounds translate into

$$\sqrt{\Delta^2 + b^2} - m_{\text{EW}}^2 < \langle m_H^2 \rangle < \sqrt{\Delta^2 + b^2}. \tag{5.3}$$

The $b$ term in the Lagrangian density breaks a Peccei-Quinn symmetry and can therefore be kept small as opposed to $\Delta$ and $\langle m_H^2 \rangle$ who can vary on a range of size $\sim m_S$. However, in order for the light Higgs boson mass to be at the electroweak scale, $\langle m_H^2 \rangle$ can only vary on a range of size $m_{\text{EW}}^2$ as shown in 5.3. Hence, the fraction of the $(\langle m_H^2 \rangle, \Delta)$ space that is tuned, i.e. satisfies equation 5.3, corresponds to

$$\frac{V_{\text{tuned}}}{V_{\text{total}}} \sim \frac{m_{\text{EW}}^2 m_S^2}{m_S^4} \sim \frac{m_{\text{EW}}^2}{m_S^2}.$$

For a scalar mass scale of $10^4$ GeV, a fine-tuning of one part in $10^4$ is necessary. For $m_S \sim 10^{10}$ GeV, a fine-tuning of one part in $10^{16}$ is required.

### Dark matter

DSS leaves the chargino and neutralino spectrum untouched, hence still providing a good candidate for dark matter in the form of the lightest neutralino. The requirement that the experimental measurement of the density of dark matter in the universe be reproduced imposes a constraint on $\mu$. Unlike in mSUGRA, $\mu$ is not determined by electroweak symmetry breaking.
The density of dark matter as measured by the WMAP satellite ($\Omega_{\text{DM}} h^2 = 0.111^{+0.006}_{-0.008}$ [26]) can be reproduced in small regions of parameter space shown in red in figure 5.3. They can be classified as follows

- The "mixed region" where $M_1 \approx \mu$ and the LSP is a higgsino-gaugino mixture. In this region $\tilde{N}_1\tilde{N}_1$ annihilation is enhanced into final states containing gauge and/or Higgs bosons and top quarks : $\tilde{N}_1\tilde{N}_1 \to WW,\ ZZ,\ hZ,\ hh$ and $t\bar{t}$. This corresponds to the diagonal region in figure 5.3.

- The "pure higgsino" and "pure wino" regions where the LSP is almost degenerate in mass with the $\tilde{C}_1$ and the $\tilde{N}_2$, leading to an enhanced destruction of sparticles for the $\tilde{C}_1$ and $\tilde{N}_2$ co-annihilation cross-sections are much larger than that of the LSP. This region generally requires a LSP heavier than 1 TeV.

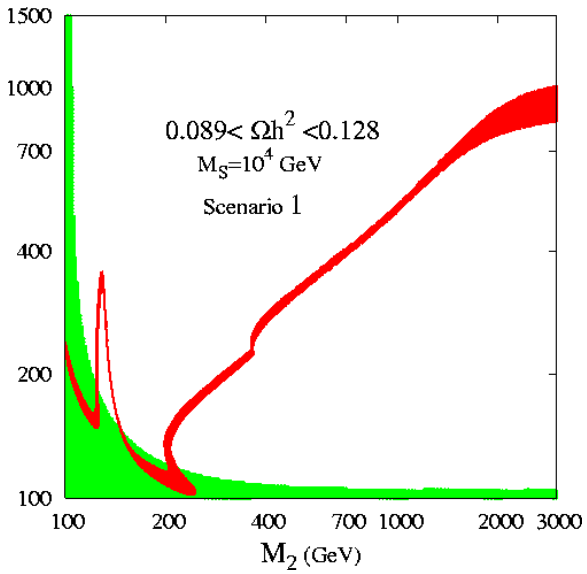


Figure 5.3: Regions of the $(\mu, M_2)$ space allowed by WMAP constraints (red) and excluded by direct searches (green) [110]. The following parameters were used : $m_S = 10^4$ GeV, $\tan\beta = 30$ and gaugino masses are universal at the GUT scale.

- The "$h$–pole" region in which the LSP is rather light, $m_{\tilde{N}_1} \approx \frac{1}{2} m_h$ and the $s$–channel $h$ exchange is nearly resonant allowing neutralinos to annihilate rapidly. This corresponds to the peak region in figure 5.3.

### Long-lived gluinos

In the MSSM, if gluinos are lighter than squarks, they will mainly decay through virtual squark exchange into quarks and charginos/neutralinos [114]. In DSS, quantum corrections to the gluino decay processes can be very significant because they are enhanced by the potentially large logarithm of the ratio between the gluino mass $m_{\tilde{g}}$ and the scale $m_S$ at which the interactions responsible for gluino decay are mediated. In order to obtain a reliable prediction for the gluino decay width, the large logarithmic corrections have to be re-summed by means of standard renormalization group techniques [115]. The gluino lifetime is approximately given by

$$\tau_{\tilde{g}} = \frac{\hbar}{\Gamma_{\tilde{g}}} \approx 4\text{sec.} \left(\frac{m_S}{10^9 \text{ GeV}}\right)^4 \left(\frac{1 \text{ TeV}}{m_{\tilde{g}}}\right)^5 .$$

Figure 5.4 compares the gluino lifetime with other relevant scales. If the scalar mass scale is larger than $10^6$ GeV, the gluino is potentially sufficiently stable to form so-called $R$–hadrons [116]. As a colour octet, the gluino can be fitted into a colour-singlet hadron along with two or three quarks coupled as an octet. $R$–hadrons could be stable and, if produced, escape detectors and be stopped in the surrounding material. For even higher values of $m_S$, $R$–hadrons could become relevant on cosmological scales since they would affect nucleosynthesis if their abundance in the early Universe is sufficiently high. Limits on the scalar mass scale can be set by big bang nucleosynthesis. A TeV mass

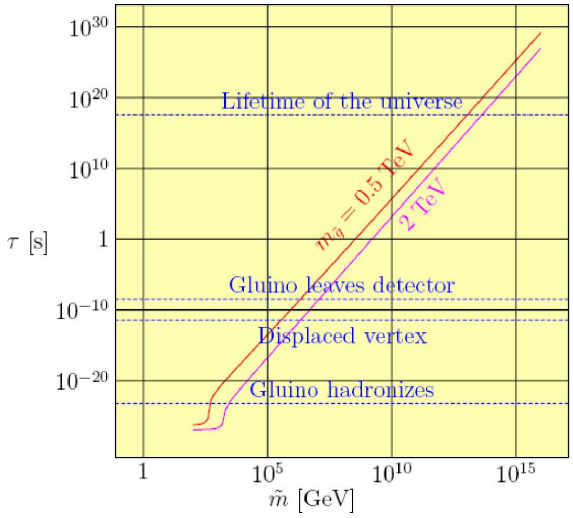


Figure 5.4: Gluino lifetime as a function of the scalar mass scale $\tilde{m} \equiv m_S$.

| | DSS1 | DSS2 |
|---|---|---|
| $m_S$ | 10 TeV | |
| $\tan\beta(m_S)$ | 30 | |
| $A_t(m_S)$ | 0 | |
| $m_{1/2}(M_{\text{GUT}})$ | 132.4 GeV | 296.5 GeV |
| $\mu(m_Z)$ | 290 GeV | 200 GeV |

Table 5.2: DSS1 and DSS2 parameter points chosen for the study of the phenomenology of DSS at the LHC.

gluino must have a lifetime shorter than 100 seconds to avoid altering the abundances of deuterium and lithium 6. This sets an upper limit of $m_S < 10^9$ GeV [117].
The study presented in this thesis will focus on short-lived gluinos to avoid exotic phenomenologies.

### 5.1.4 Parameter sets

Two points in the parameter space are chosen in agreement with known constraints from both dark matter observations and collider searches in order to study the potential for discovery, measurements and determination of the parameters of DSS at the LHC.

Table 5.2 presents the parameter values for DSS1 and DSS2.
In both case, the scalar mass scale $m_S$ is set to 10 TeV. This is the lower edge of the region of application of DSS. It allows for a soft fine-tuning of the mass of the Higgs boson, only one part in $10^4$, and sets the gluino lifetime to reasonably short length of

| | **DSS1** | **DSS2** |
|---|---|---|
| $h$ | 129 | 129 |
| $\tilde{g}$ | 438 | 880 |
| $\tilde{N}_1$ | 60 | 125 |
| $\tilde{N}_2$ | 117 | 185 |
| $\tilde{N}_3$ | 296 | 206 |
| $\tilde{N}_4$ | 310 | 317 |
| $\tilde{C}_1$ | 117 | 175 |
| $\tilde{C}_2$ | 313 | 317 |

Table 5.3: Mass spectrum for DSS1 and DSS2 as computed by a modified version of `SuSpect` [110].

time in order to avoid non-standard phenomenology or undesirable cosmological effects. Yet, squarks, sleptons and heavy Higgs bosons still lie beyond the mass reach of the LHC ($\sim 3.5$ TeV).
$\tan\beta$ is set to 30 for both points to allow for a light Higgs boson mass above the LEP limit. The only influence of $\tan\beta$ in the low-energy theory is on $m_h$. Similarly, the only impact of the trilinear coupling $A_t$ on $m_h$ are suppressed as $m_S^{-2}$ and $m_S^{-4}$. It is therefore set to 0 for all point.
The most relevant parameters for the low-energy effective theory are $\mu$ and $m_{1/2}$. They define the mass spectrum as well as the field content of the neutralinos and charginos and most notably the LSP. We chose two $(\mu, m_{1/2})$ combinations in order to cover most of the parameter space allowed by LEP and WMAP and relevant at the LHC. With $\mu = 290$ GeV and $m_{1/2} = 132.4$ GeV, DSS1 lies in the "Higgs pole" region of figure 5.3. At this point, the LSP ($\tilde{N}_1$) is mostly bino but still has a non-vanishing higgsino component. With $\mu = 200$ GeV and $m_{1/2} = 296.5$ GeV, DSS2 is in the "mixed region" of figure 5.3 and the LSP is a higgsino-gaugino mixture.

Table 5.3 presents the sparticle mass spectra for DSS1 and DSS2. For both points, the Higgs boson is SM-like. With a mass of 129 GeV, the dominant decay is to $b\bar{b}$, $\tau^+\tau^-$ and $WW^*$. However, it is also the mass were the branching fraction of the decay into a pair of photons reaches its maximum. The $h \to \gamma\gamma$ channel is especially suitable for a precise measure of the Higgs boson mass using the reconstructed invariant mass of the two photons. The LSP is the $\tilde{N}_1$ which is very light and $m_{\tilde{N}_1} < m_h$ leading to a $\sim 1\%$ branching ratio of the invisible decay $h \to \tilde{N}_1\tilde{N}_1$. In DSS1, the gluino, the $\tilde{N}_2$ and $\tilde{C}_1$ are fairly light leading to an enhanced production of gluino pairs and chargino-neutralino associated production at the LHC (see table 5.5). With a larger $m_{1/2}$, DSS2 has a much heavier gluino and LSP.

Table 5.4 shows the field content of neutralinos and charginos in DSS1 and DSS2. In DSS1, the $\tilde{N}_1$ and $\tilde{N}_2$ are bino and wino, respectively. In DSS2, the $\tilde{N}_1$ is mostly bino but still has a higgsino component. The $\tilde{N}_2$ is everything. The $\tilde{C}_1$ is mostly wino in DSS1 and higgsino in DSS2.

| | DSS1 | | | | DSS2 | | | |
|---|---|---|---|---|---|---|---|---|
| | $\left\|\tilde{B}\right\|^2$ | $\left\|\tilde{W}^0\right\|^2$ | $\left\|\tilde{H}_u^0\right\|^2$ | $\left\|\tilde{H}_d^0\right\|^2$ | $\left\|\tilde{B}\right\|^2$ | $\left\|\tilde{W}^0\right\|^2$ | $\left\|\tilde{H}_u^0\right\|^2$ | $\left\|\tilde{H}_d^0\right\|^2$ |
| $\left\|\tilde{N}_1\right\|^2$ | 0.97 | 0 | 0.03 | 0 | 0.74 | 0.02 | 0.17 | 0.07 |
| $\left\|\tilde{N}_2\right\|^2$ | 0.01 | 0.89 | 0.09 | 0.01 | 0.19 | 0.25 | 0.3 | 0.25 |
| $\left\|\tilde{N}_3\right\|^2$ | 0 | 0.02 | 0.47 | 0.51 | 0.01 | 0.01 | 0.47 | 0.51 |
| $\left\|\tilde{N}_4\right\|^2$ | 0.02 | 0.09 | 0.41 | 0.48 | 0.01 | 0.78 | 0.06 | 0.15 |

| | DSS1 | | DSS2 | |
|---|---|---|---|---|
| | $\left\|\tilde{W}^\pm\right\|^2$ | $\left\|\tilde{H}_{u,d}^\pm\right\|^2$ | $\left\|\tilde{W}^\pm\right\|^2$ | $\left\|\tilde{H}_{u,d}^\pm\right\| 2$ |
| $\left\|\tilde{C}_1\right\|^2$ | 0.89 | 0.11 | 0.21 | 0.79 |
| $\left\|\tilde{C}_2\right\|^2$ | 0.11 | 0.89 | 0.79 | 0.21 |

Table 5.4: Neutralinos and charginos field content for DSS1 and DSS2 as computed by `SuSpect` [109]. For charginos, components from $\tilde{C}_i^+$ and $\tilde{C}_i^-$ are averaged.

Table 5.5 lists the next-to-leading order cross-sections for direct production of sparticles at the LHC for DSS1 and DSS2 as computed by `Prospino2` [118, 119, 120]. As expected, the light gluino of DSS1 yields a relatively large cross-section for the production of gluino pairs. In DSS2, gluinos are fairly heavy and the gluino pair cross section is low. The second largest contribution to SUSY production is due to the associated production of charginos and neutralinos with 12 pb and 2 pb in DSS1 and DSS2, respectively. In DSS1, this channel is very much dominated by the $\tilde{C}_1\tilde{N}_2$ channel while in DSS2, equivalent contributions arise from $\tilde{C}_1\tilde{N}_{1,2,3}$ and $\tilde{C}_2\tilde{N}_4$. This is due to the fact that the mass splittings between the first three neutralinos are larger in DSS1 resulting in a less degenerate production of charginos and neutralinos. Furthermore, in DSS2, the $\tilde{C}_1$ is mostly higgsino of which there is a large fraction in all neutralinos. The total $\tilde{C}\tilde{N}$ direct production cross-section is lower for DSS2 due to a larger $m_{1/2}$. The lower $\mu$ increases the $\tilde{C}_1\tilde{N}_3$ production rate but fails to keep up with the very light $\tilde{N}_{1,2}$ in DSS1. The only other significant contribution to SUSY production in DSS1 is due to the production of $\tilde{C}_1$ pairs. DSS2 production also receives contributions from neutralino pairs.

Table 5.6 lists the branching fraction of DSS sparticles as computed by `SDECAY` [121]. Most gluino decays contain three particles in the final state as they proceed through a very virtual squark. Due to its wino-like nature, $\tilde{N}_2$ mostly decays as a $Z$ boson. The higgsino component in DSS2 opens the decay to charginos. Also, the $\tilde{C}_1$ decays like a $W$ boson.

| Channel | $\sigma_{\text{NLO}}$ | | | |
|---|---|---|---|---|
| | **DSS1** | | **DSS2** | |
| $\tilde{g}\tilde{g}$ | 62.8 pb | | 954 fb | |
| $\tilde{C}_1\tilde{N}_1$ | 227 fb | | 451 fb | |
| $\tilde{C}_1\tilde{N}_2$ | 11.67 pb | | 848 fb | |
| $\tilde{C}_1\tilde{N}_3$ | 41 fb | | 496 fb | |
| $\tilde{C}_1\tilde{N}_4$ | 17 fb | 12.2 pb | 37 fb | 2.2 pb |
| $\tilde{C}_2\tilde{N}_1$ | 7 fb | | 0.6 fb | |
| $\tilde{C}_2\tilde{N}_2$ | 15 fb | | 41 fb | |
| $\tilde{C}_2\tilde{N}_3$ | 100 fb | | 40 fb | |
| $\tilde{C}_2\tilde{N}_4$ | 104 fb | | 296 fb | |
| $\tilde{C}_1\tilde{C}_1$ | 5.9 pb | | 642 fb | |
| $\tilde{C}_1\tilde{C}_2$ | 18 fb | 6 pb | 38 fb | 827 fb |
| $\tilde{C}_2\tilde{C}_2$ | 56 fb | | 147 fb | |
| $\tilde{N}_1\tilde{N}_1$ | 7 fb | | 3 fb | |
| $\tilde{N}_1\tilde{N}_2$ | 2 fb | | 2 fb | |
| $\tilde{N}_1\tilde{N}_3$ | 6 fb | | 119 fb | |
| $\tilde{N}_1\tilde{N}_4$ | 1 fb | | $\sim 0$ | |
| $\tilde{N}_2\tilde{N}_2$ | 12 fb | 99 fb | 0.08 fb | 310 fb |
| $\tilde{N}_2\tilde{N}_3$ | 18 fb | | 166 fb | |
| $\tilde{N}_2\tilde{N}_4$ | 2 fb | | 0.2 fb | |
| $\tilde{N}_3\tilde{N}_3$ | 0.01 fb | | 0.09 fb | |
| $\tilde{N}_3\tilde{N}_4$ | 51 fb | | 20 fb | |
| $\tilde{N}_4\tilde{N}_4$ | 0.06 fb | | 0.06 fb | |
| $\tilde{C}_1\tilde{g}$ | 290 fb | 310 fb | 0.02 fb | 0.07 fb |
| $\tilde{C}_2\tilde{g}$ | 20 fb | | 0.05 fb | |
| $\tilde{N}_1\tilde{g}$ | 71 fb | | 0.01 fb | |
| $\tilde{N}_2\tilde{g}$ | 140 fb | 223 fb | 0.01 fb | 0.04 fb |
| $\tilde{N}_3\tilde{g}$ | 4 fb | | 0.001 fb | |
| $\tilde{N}_4\tilde{g}$ | 8 fb | | 0.02 fb | |
| Total | 81.6 pb | | 4.3 pb | |

Table 5.5: Next-to-leading order cross-sections for direct production of sparticles at the LHC for DSS1 and DSS2 as computed by `Prospino 2` [118, 119, 120].

| Decay | | **DSS1** | | **DSS2** | |
|---|---|---|---|---|---|
| | | BR (%) | | | |
| $\tilde{N}_1$ | | stable | | stable | |
| $\tilde{g} \to$ | $\tilde{N}_1\ q\overline{q}$ | 15 | 45 | 8 | 37 |
| | $\tilde{N}_2\ q\overline{q}$ | 30 | | 11 | |
| | $\tilde{N}_3\ q\overline{q}$ | $< 1$ | | 6 | |
| | $\tilde{N}_4\ q\overline{q}$ | $< 1$ | | 12 | |
| | $\tilde{C}_1\ q\overline{q}$ | 55 | 55 | 24 | 52 |
| | $\tilde{C}_2\ q\overline{q}$ | $< 1$ | | 28 | |
| | $\tilde{N}_1\ g$ | 0 | | $< 1$ | 11 |
| | $\tilde{N}_2\ g$ | | | 3 | |
| | $\tilde{N}_3\ g$ | | | 6 | |
| | $\tilde{N}_4\ g$ | | | 1 | |
| $\tilde{N}_2 \to$ | $\tilde{N}_1\ q\overline{q}$ | 69 | | 68 | |
| | $\tilde{N}_1\ \ell\ \ell$ | 7 | | 7 | |
| | $\tilde{N}_1\ \tau\ \tau$ | 3 | | 3 | |
| | $\tilde{N}_1\ \nu\ \overline{\nu}$ | 21 | | 20 | |
| | $\tilde{C}_1\ q\overline{q}$ | 0 | | 1 | |
| $\tilde{N}_3 \to$ | $\tilde{N}_1\ Z$ | 9 | 30 | $\tilde{N}_1\ q\overline{q}$ | 65 |
| | $\tilde{N}_2\ Z$ | 21 | | $\tilde{N}_1\ \ell\ \ell$ | 7 |
| | $\tilde{C}_1\ W$ | 64 | | $\tilde{C}_1\ q\overline{q}$ | 3 |
| | | | | $\tilde{C}_1\ \ell\ \nu$ | 1 |
| | $\tilde{N}_1\ h$ | 2 | 4 | $\tilde{N}_1\ \nu\ \nu$ | 20 |
| | $\tilde{N}_2\ h$ | 2 | | $\tilde{N}_1\ \tau\ \tau$ | 3 |
| $\tilde{N}_4 \to$ | $\tilde{N}_1\ Z$ | 4 | 9 | 0 | |
| | $\tilde{N}_2\ Z$ | 5 | | 2 | |
| | $\tilde{N}_1\ h$ | 6 | 20 | $\tilde{N}_3\ Z$ | 9 |
| | $\tilde{N}_2\ h$ | 14 | | 4 | |
| | $\tilde{C}_1\ W$ | 70 | | 86 | |
| $\tilde{C}_1 \to$ | $\tilde{N}_1\ q\overline{q}$ | 67 | | $\tilde{N}_1\ q\overline{q}$ | 66 |
| | $\tilde{N}_1\ \ell\ \nu$ | 22 | | $\tilde{N}_1\ \ell\ \nu$ | 22 |
| | $\tilde{N}_1\ \tau\ \nu$ | 11 | | $\tilde{N}_1\ \tau\ \nu$ | 11 |
| $\tilde{C}_2 \to$ | $\tilde{C}_1\ Z$ | 32 | | $\tilde{C}_1\ Z$ | 32 |
| | $\tilde{N}_1\ W$ | 8 | 48 | $\tilde{C}_1\ h$ | 9 |
| | $\tilde{N}_2\ W$ | 40 | | $\tilde{N}_2\ W$ | 38 57 |
| | $\tilde{C}_1\ h$ | 20 | | $\tilde{N}_3\ W$ | 19 |

Table 5.6: Branching fraction of DSS sparticles as computed by `SDECAY` [121].

| Process | Generator | Hadronization/Underlying event |
|---|---|---|
| SUSY | HERWIG [83] | JIMMY [89] |
| QCD jets | PYTHIA | PYTHIA |
| $t\bar{t}$ | MC@NLO [88] | HERWIG/JIMMY |
| $W/Z+$jets | ALPGEN [86] | HERWIG/JIMMY |
| $WW/WZ/ZZ$ | HERWIG | JIMMY |

Table 5.7: Codes used for the generation of signal background samples.

### 5.1.5 Generation and simulation

Leading-order and, when available, next-to-leading-order Monte Carlo (MC) generators were used for the generation of signal and background processes. All LO-generated samples were normalized to NLO cross-sections using $K$–factors. The most relevant SM background processes to SUSY searches are $t\bar{t}$, $W+$jets, $Z+$jets, $WW/WZ/ZZ$ and jet production from QCD processes. Corresponding generators were chosen to optimize the fidelity of MC samples to potential real data. For LO and NLO cross-sections, the CTEQ6L and CTEQ6M [47] sets of parton density functions were used, respectively.

General-purpose leading-order generators include PYTHIA [82] and HERWIG [83]. The latter proposes a better treatment of additional jets due to initial/final state radiation or to the hard scattering, includes spin correlations in the decay of heavy fermions and azimuthal correlations within and between jets. It was used for the generation of SUSY samples for both parameter sets and of $WW/WZ/ZZ$ samples. The generation of the underlying event was achieved by the JIMMY package [89]. Cross-sections were normalized to the next-to-leading-order calculations realized by the MCFM program [122]. Most of the background arising from QCD jets production is expected to be suppressed in the early stages of the analysis by cuts on, e.g, the transverse missing energy. For that reason, a highly accurate generation of those processes is not crucial and the PYTHIA program can be used. QCD jets samples were produced in slices of $p_{\mathrm{T}}$ of the hard scattering. A filter was applied at generation level, requiring for the hardest jet a transverse momentum above 80 GeV, for the second jet transverse momentum above 40 GeV and missing transverse energy above 100 GeV.

When available, exact matrix-elements calculators and MC generators were used and matched to parton shower generators. For the generation of heavy-quark pairs, the MC@NLO program [88] calculates next-to-leading-order matrix elements and generates final states. It was used for the production of $t\bar{t}$ samples. It provides a quite stable absolute cross-section prediction and a good description of the final state kinematics for events with up to one additional QCD jet.
The ALPGEN program [86] calculates leading-order and generates final states for multi-parton processes. It was used for the generation of $W/Z+$jets samples. Those samples were matched to HERWIG for the generation of parton showers. JIMMY was used for the underlying event. The underlying-event parameters were tuned to published data from the TeVatron and other experiments. The parton-matching between event generators

| | DSS1 | DSS2 | $t\bar{t}$ | $W/Z$ + jets | $WW/WZ/ZZ$ | QCD |
|---|---|---|---|---|---|---|
| events | 1M | 500k | 8M | 3M/2M | 700k/30k/60k | 2M |
| $\int \mathcal{L}dt$ (fb$^{-1}$) | 11 | 113 | 9 | 1/3 | 10/1/5 | 1 |

Table 5.8: Number of events used in this study.

and parton showers generators was achieved using the MLM scheme [123] with the jet matching cut set at 40 GeV. Contributions from processes with matrix-element parton multiplicities between one and five were summed to produce the multi-jet sample. A filter was applied at the generator level requiring at least four jets with transverse momentum above 40 GeV, with at least one of these having a transverse momentum above 80 GeV, and with missing transverse energy above 80 GeV.

The decay of $\tau$-leptons was treated by the `TAUOLA` program [96] and the radiation of photons by charged leptons by `PHOTOS` [97]. Pile-up and cavern background simulations were not included. Events were generated and simulated on the WLCG grid. Table 5.7 summarizes the different program used for the generation of signal and background samples.

The background samples used in this work were generated as part of the ATLAS official production with release 12 of the ATLAS software in the context of the CSC effort. Table 5.8 shows the number of events used in this study along with the corresponding integrated luminosities.

The amount of signal events required for this study as well as the non-mainstream character of the model forbids a time-consuming full simulation of the ATLAS detector on the Grid. On the other hand, the historic tool for fast simulation of physics events in ATLAS (ATLFast [124]) is based on a smearing of the four-momenta of particles in the final state. Therefore, it overestimates the reconstruction efficiencies of all objects and underestimate bias that could alter the estimations of the position and momentum of a particle such as material effects or noise.

Instead, events (signal and background) were submitted to a semi-fast simulation of the detector. The inner detector was simulated by the FATRAS package [125] and the calorimeter by the FastCaloSim package [126]. The response of the detector to muons was simulated using the usual ATLFast [124] parametrization. FATRAS and FastCaloSim are implemented within the standard `athena` event data model (EDM). Therefore, standard reconstruction algorithm such as those presented in chapter 4 can be applied. ATLFast uses a separate data model. It should be noted that although the FATRAS/FastCaloSim combination provides more faithful performance with respect to a full simulation, it is still under development and has not been fully validated yet. On the other hand, ATLFast is fully validated and its limitations are well understood.

| | Simulation | |
|---|---|---|
| | fast | full |
| Reconstruction | $89.6 \pm 0.2$ | $91.0 \pm 0.2$ |
| Loose | $88.2 \pm 0.2$ | $89.5 \pm 0.3$ |
| Medium | $79.9 \pm 0.2$ | $79.7 \pm 0.3$ |
| Tight | $69.7 \pm 0.3$ | $68.8 \pm 0.4$ |

Table 5.9: Electron identification efficiencies obtained on $Z \to ee$ with the Fast Calorimeter Simulation package or with the standard full simulation of the detector. Efficiencies are quoted for the three standard sets of cuts described in chapter 4.

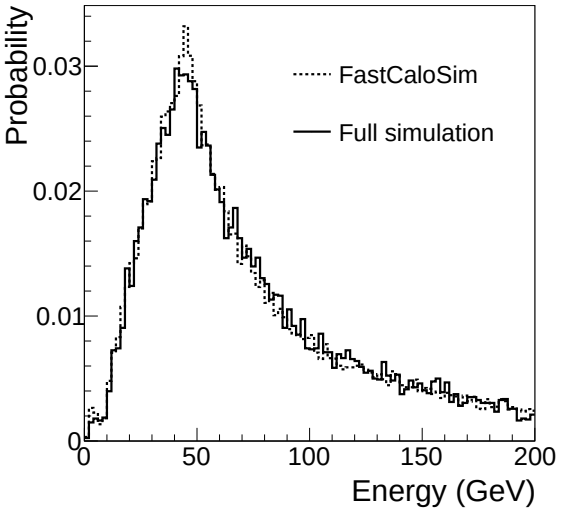


Figure 5.5: Energy spectra of electrons in $Z \to ee$ events obtained with the Fast Calorimeter Simulation package or with the standard full simulation of the detector.

### Fast ATLAS TRAck Simulation

The full simulation of the inner detector is the most time-consuming part of the full Geant 4 simulation because it tracks charged particles through the full complex geometry of the inner detector. FATRAS [125] makes use of a number of standard techniques together with a simplified geometry of the inner tracker. It accounts for material effects such as multiple scattering, energy loss, bremsstrahlung, hadronic interaction as well as noise effects. FATRAS is about fifty times faster than the standard full simulation.

### Fast Calorimeter Simulation

The aim of the FastCaloSim package [126] is to provide a parametrized simulation of the particle energy response and distribution in the calorimeter to reduce the simulation time. FastCaloSim simulates only the average shower properties and uncorrelated fluctuations (fluctuations from calorimeter cell energy resolution and electronic noise). The particle shower is described by two parametrizations, one providing the total energy deposited in each calorimeter layer and the other providing the energy distribution within a specific calorimeter layer. The calorimeter response to electrons and photons are based on a parametrization of a Geant 4 simulation of photons while the response to hadrons is parametrized on simulated charged pions. Muons are ignored. Cells in the calorimeter are described as cuboids in the $r - \eta - \phi$ space. The parametrizations are binned in pseudo-rapidity and energy.
Table 5.9 shows the identification performance obtained $Z \to ee$ with the Fast Calorimeter Simulation package or with the standard full simulation of the detector. Efficiencies

are quoted for the three standard sets of cuts described in chapter 4. All discrepancies are within the errors. Figure 5.5 shows the energy spectra of electrons in $Z \rightarrow ee$ events obtained with the Fast Calorimeter Simulation package or with the standard full simulation of the detector. No discrepancy can be seen.

#### ATLFast

The muon spectrometer is to a large degree decoupled from the rest of the detector. It is therefore well isolated from the overall event activity. For that reason, it is assumed that the response of the detector to muons as parametrized by the ATLFast software [124] is a good approximation.
Muon reconstruction is carried out using an analytical evaluation of the muon momentum resolution. This approach properly takes into account the detailed geometry of the muon spectrometer and the distribution of the material contained in the magnets and in the muon chambers, as well as resolution effects. The algorithm provides the momentum resolution as a function of $p_{\mathrm{T}}$, $\eta$ and $\phi$. This method neglects non-Gaussian effects such as multiple-scattering tails and pattern-recognition errors, excellent agreement has been found between its results and those of a full detector simulation. The muon momentum is corrected for energy loss before the spectrometer by using a parametrization which takes into account the contribution from fluctuations in the calorimeters. In ATLFAST, isolated muon candidates are searched for in the MC truth. The muon momentum is smeared using a $p_{\mathrm{T}}$, $\eta$ and $\phi$–dependent resolution function. The resolution in the spectrometer is evaluated by an interpolation between eight tables produced at four $p_{\mathrm{T}}$ values.

### 5.1.6 Objects for SUSY analysis

The objects used for the analysis of SUSY events and referred to in section 5.1.7 are described.

#### Jets

Because of the relatively large multiplicity of jets in SUSY events, a narrow cone is preferable in the reconstruction of jets. The algorithm used to reconstruct jets in the analysis documented here is the cone algorithm with a cone size of 0.4.

#### Missing transverse energy

$\not\!\!E_{\mathrm{T}}$ is calculated from the calorimeter cells, with calibration weights derived separately for cells associated to different objects (jets, electrons, photons, taus, and non-associated clusters due to the soft part of the event). Sources of fake missing energy, such as dead or noisy parts of the calorimeter, fake muons, beam-gas and beam-halo events, cosmic rays and electronics problems are not considered here. The contribution from non-Gaussian tails in the $\not\!\!E_{\mathrm{T}}$ measurement can be strongly suppressed by requiring a minimum angular separation between the $\not\!\!E_{\mathrm{T}}$ vector and the jets in the event. This cut also suppresses the contributions from jets containing hard neutrinos from the

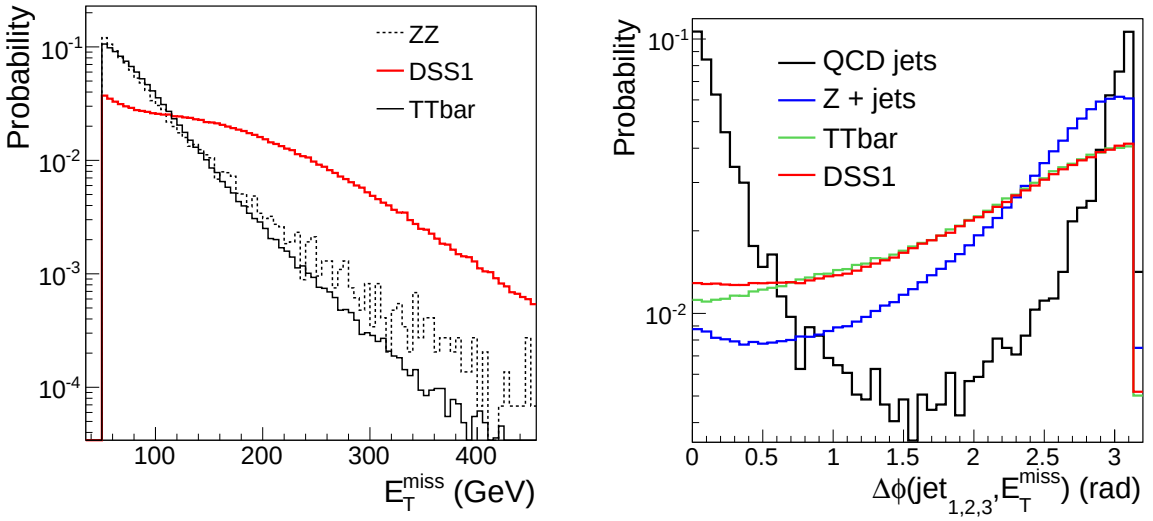


Figure 5.6: Distributions of the missing transverse energy (left) and $\phi$–difference between the $\not\!\!E_{\mathrm{T}}$ vector and the three leading jets (right) for SUSY DSS1 events and SM processes ($t\bar{t}$, $ZZ$, QCD jets and $Z+$jets).

leptonic decays of charmed and beauty mesons. The right-side plot in figure 5.6 shows the distribution of the $\phi$-difference between the $\not\!\!E_{\mathrm{T}}$ vector and the three leading jets in the event. In most QCD events, at least one of the three leading jets is very close to the $\not\!\!E_{\mathrm{T}}$ vector.
The distribution of $\not\!\!E_{\mathrm{T}}$ for SUSY DSS1 events and SM processes is shown in the left-side plot of figure 5.6. For SUSY events, the distribution is clearly shifted toward higher values while for SM processes, it is mainly gathered below 100 GeV.

### Electrons

For typical SUSY analyses the background from the production of QCD jets can be reduced by requirements on $\not\!\!E_{\mathrm{T}}$ or the transverse sphericity. Therefore stringent rejection against jets is not needed in SUSY studies, and relatively soft electron identification cuts can be applied, leading to a significant gain in efficiency especially for searches involving many leptons. The medium set of cuts defined in chapter 4 is used. However, the busy environment surround electrons in SUSY events suggests the use of an additional isolation cut. The $R_{\mathrm{cone}}$ cut is applied in addition to the standard medium set. Only electrons with transverse momentum larger than 20 GeV are considered.

### Muons

All ATLFast muons with transverse momentum larger than 20 GeV are included. An additional isolation criteria is required. Namely, the sum of the transverse momentum of all tracks with a distance $R = \sqrt{\eta^2 + \phi^2} = 0.2$ of a muon is required to be lower than 10 GeV.

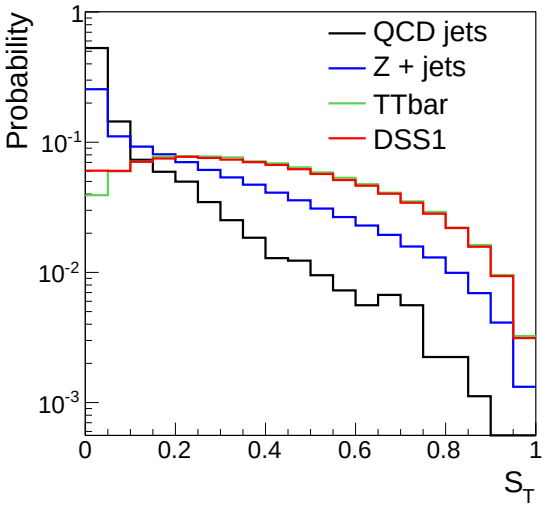


Figure 5.7: Distribution of the transverse sphericity for SUSY DSS1 events and SM processes.

### Overlap removal

Candidates can be reconstructed in parallel by different algorithms. For instance, all true electrons will be reconstructed as jets, muons can also be reconstructed as electrons. In order to remove the overlap between the candidates, electrons passing the medium set of cuts are taken as basis. All jets within a distance $R = \sqrt{\eta^2 + \phi^2}$ of 0.2 of an electron are discarded. It was shown in chapter 4 that the electron identification efficiency is uniform as a function of $R$ for $R > 0.4$. Thus, electrons within a distance $R = 0.4$ of the remaining jets are rejected. Finally, electrons within a distance of 0.2 of a muon are discarded.

### Effective mass

The effective mass $M_{\text{eff}}$ is a measure of the total activity in the event. It is defined as

$$M_{\text{eff}} \equiv \not{E}_{\text{T}} + \sum_{i \leq 4} p_{\text{T}}(\text{jet}) + \sum p_{\text{T}}(\text{lepton})$$

where the sums run respectively over the four highest–$p_{\text{T}}$ jets and over all of the identified leptons. This variable is useful to discriminate SUSY from SM events. It also has the interesting properties that, for SUSY events, $M_{\text{eff}}$ is strongly correlated with the mass of the pair of SUSY particles produced in the proton-proton interaction. It can therefore be used to quantify the mass-scale of SUSY events [127].

### Transverse sphericity

The transverse sphericity ($S_T$) is defined as

$$S_T \equiv \frac{2\lambda_2}{\lambda_1 + \lambda_2}$$

| | jets + $\not{E}_{\mathrm{T}}$ + | | | |
|---|---|---|---|---|
| | $0\ell$ | $1\ell$ | $2\ell$ | $3\ell$ |
| **DSS1** | $\gtrsim 70\%$ | $\gtrsim 20\%$ | $\gtrsim 5\%$ | $\gtrsim 3\%$ |
| **DSS2** | $\gtrsim 70\%$ | $\gtrsim 23\%$ | $\gtrsim 5\%$ | $\gtrsim 1\%$ |

Table 5.10: Most frequent final states in the production of DSS at the LHC. Leptons include electrons and muons.

where $\lambda_i$ are the eigenvalues of the $2 \times 2$ sphericity tensor $S_{ij} = \sum_k p_{ki} p_{kj}$. The tensor is computed using all jets with $p_{\mathrm{T}} > 20$ GeV, and all selected leptons. SUSY events tend to be relatively spherical ($S_T \sim 1$) since the initial heavy particles are usually produced approximately at rest in the detector and their cascade decays emit particles in many different directions. QCD events are dominated by back-to-back configurations ($S_T \sim 0$). The distribution of $S_T$ for SUSY DSS1 events and SM processes is shown in figure 5.7. In DSS1, sparticles are fairly light, resulting in a fairly uniform distribution between 0.1 and 0.6. For QCD jets or $Z$ + jetsevents, the distribution peaks at zero. A cut on $S_T$ does not discriminate against $t\bar{t}$ events as the distribution is very similar to signal events.

### 5.1.7 Collider observables

The potential for the discovery of DSS at the LHC is described in the case of the DSS1 and DSS2 parameter sets. In order to estimate the precision on the determination of the DSS parameters at the LHC, a number of quantitative observables are shown.

#### Discovery potential

Table 5.10 shows the most frequent final states occurring in the production of DSS at the LHC in terms of the number of isolated leptons in the final state. All production channels are included and leptons include electrons and muons. All channels include some amount of missing transverse energy resulting from the non-detection of the $\tilde{N}_1$. The number of jets in the cascade, i.e. not counting jets from the underlying event or initial and final state radiation, can vary from zero in the case of the direct production of $\tilde{C}_1\tilde{N}_2$ both decaying leptonically to eight in the case of gluino pairs. The most common channel for both points is the no-lepton channel $\tilde{g}\tilde{g} \rightarrow \tilde{C}_1\tilde{C}_1 + 4$ jets $\rightarrow$ 8 jets + $\not{E}_{\mathrm{T}}$ + 0 leptons. This channel is used for the estimation of the discovery potential of both points. The following standard cuts [81] are applied to both signal and background samples:

1. At least one jet with $p_{\mathrm{T}} > 100$ GeV, three other jets with $p_{\mathrm{T}} > 50$ GeV and $\not{E}_{\mathrm{T}} > 100$ GeV
2. $\not{E}_{\mathrm{T}} > 0.2 \times M_{\mathrm{eff}}$
3. $S_T > 0.2$
4. $\Delta\phi(\text{jet}, \not{E}_{\mathrm{T}}) > 0.2$ for the three leading jets

| Process | cut 1 | cut 2 | cut 3 | cut 4 | cut 5 | $M_{\text{eff}} >$ 800 GeV | $M_{\text{eff}} >$ 1000 GeV |
|---|---|---|---|---|---|---|---|
| DSS1 | 31495 | 19849 | 16985 | 15759 | 12631 | 4701 | |
| DSS2 | 504 | 313 | 251 | 231 | 145 | 112 | 97 |
| $t\bar{t}$ | 18031 | 11542 | 8981 | 8219 | 5161 | 274 | |
| QCD | 27330 | 7231 | 4632 | 851 | 848 | 15 | |
| $W+$jets | 2517 | 1561 | 1149 | 1028 | 769 | 195 | |
| $Z+$jets | 1532 | 933 | 645 | 538 | 422 | 128 | |
| $WZ$ | 58 | 38 | 34 | 31 | 20 | 4 | 62 |
| $WW$ | 84 | 53 | 42 | 42 | 12 | 3 | |
| $ZZ$ | 21 | 13 | 8 | 6 | 2 | 2 | |
| | | | | | Total SM | 621 | |
| | | | | | DSS1 significance | 18 | |
| | | | | | DSS2 significance | 0.8 | 6 |

Table 5.11: Number of events remaining for each process after the successive application of each cuts. Numbers are normalized to NLO cross-sections and for an integrated luminosity of 1 fb$^{-1}$.

5. no electrons and no muons

6. $M_{\text{eff}} > 800$ GeV

Most of the background samples have been filtered at generation level with various requirements on $\not\!\!E_{\text{T}}$ and jet multiplicity. The first cut in the analysis flow applies harder requirements than any of the ones applied at the filter level to minimise the bias to the study from the use of filtered samples.
The main background at this point is from QCD events where $\not\!\!E_{\text{T}}$ is produced either by a fluctuation in the measurement of the energy of one or more jets, or by a real neutrino from the decay of a $B$–hadron produced in the fragmentation process. Since the statistical fluctuation on the $\not\!\!E_{\text{T}}$ measurement grows with increasing $M_{\text{eff}}$, the second cut above eliminates the Gaussian part of the $\not\!\!E_{\text{T}}$ fluctuations. In SUSY events the jets are produced from the decay of heavy particles produced approximately at rest, and are thence distributed isotropically in space, whereas for the QCD events the direction of the two partons from the hard scattering provides a privileged direction. The cut on sphericity is intended to exploit this fact. Both for jet mis-measurement and $b$ decays, the $\not\!\!E_{\text{T}}$ vector will be close the direction of one jets. The $\Delta\phi$ cuts are very efficient in reducing the QCD background.

Table 5.11 shows the number of events remaining after the successive application of each cuts. Numbers are normalized to NLO cross-sections and for an integrated luminosity of 1 fb$^{-1}$. The QCD background is dominant after the first cut but is reduced to a level similar to the backgrounds containing real neutrinos by subsequently requiring $\not\!\!E_{\text{T}} > 0.2 M_{\text{eff}}$ (cut 2). The cuts on the sphericity and $\Delta\phi$ strongly reduce the QCD background, which becomes concentrated in the region of low $M_{\text{eff}}$. After all cuts $t\bar{t}$ is the dominant background, but there are also significant contributions from $W+$jets and

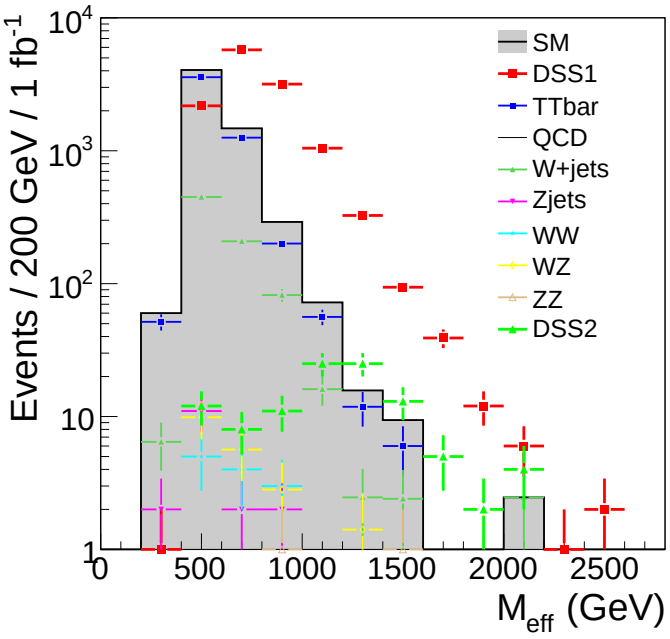


Figure 5.8: Distributions of $M_{\text{eff}}$ for signal and background processes after the application of cuts 1 to 5 for an integrated luminosity of 1 fb$^{-1}$.

$Z+$jets. The final cut, $M_{\text{eff}} > 800$ GeV, reduces the background to below the level of the signal for DSS1.
The systematic uncertainties on the number of background events for 1 fb$^{-1}$ was taken to be 50% for QCD multi-jet events and 20% for $t\bar{t}$, $W+$jets, $Z+$jets, $WW$, $WZ$ and $ZZ$. These are estimations of what could be obtained using procedures for background evaluation based on a combination of data-driven and Monte Carlo methods [81].
Systematic and statistical uncertainties are incorporated in the calculation of the significance by convoluting a Poisson probability density with a Gaussian probability density with the number of background events $N_b$ as mean and $\delta_b$ (systematic uncertainties) as standard deviation [128, 129]. The probability that the background fluctuates to the observed number of events $N_{\text{obs}} = N_{\text{signal}} + N_{\text{b}}$ or above is

$$p = A \int_0^\infty db \text{Gauss}(N_b, \delta_b) \sum_{i=N_{\text{obs}}}^{\infty} \frac{e^{-b} b^i}{i!}$$

where $A$ normalizes the integral. Then the significance of the signal reads

$$Z_n = \sqrt{2}\text{erf}^{-1}(1-2p).$$

In the case where $N_{\text{obs}}$ is very large compared to $N_b$, the significance is approximated by [130]

$$Z_0 = \frac{2}{\sqrt{1+\delta_b^2/N_b}} \left( \sqrt{N_{\text{obs}} + \frac{3}{8}} - \sqrt{N_b + \frac{3}{8}\frac{\delta_b^2}{N_b}} \right).$$

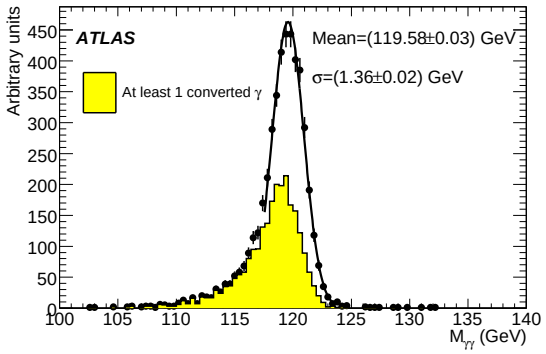


Figure 5.9: Distribution of the invariant mass of the photon pair in $h \to \gamma\gamma$ events for $m_h = 120$ GeV [81].

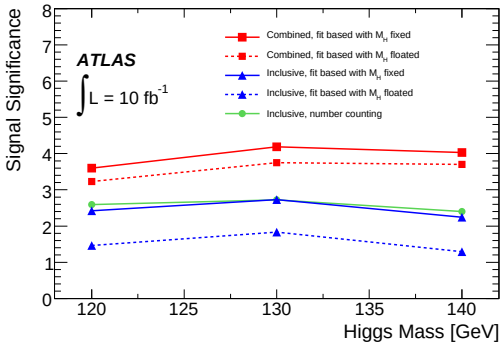


Figure 5.10: Expected signal significance for a Higgs boson using the $h \to \gamma\gamma$ decay for 10 fb$^{-1}$ of integrated luminosity as a function of the mass [81].

By convention, the discovery of new physics can be claimed if the number of observed events exceeds 25 and the significance larger than 5. The significance of the observation of DSS1 with an integrated luminosity of 1 fb$^{-1}$ is 18. Hence, this point in parameter space can be discovered very quickly at the LHC, within one year of data taking at low luminosity. For DSS2, the significance is very low and, for this set of cuts, does not increase with statistics. However, if $M_{\text{eff}}$ is required to be larger than 1 TeV, the significance for 1 fb$^{-1}$ is 6.

### Higgs boson mass

In DSS1 and DSS2, the lightest Higgs boson is essentially equivalent to that of the SM. Its production through supersymmetric cascades only occurs through the decay of $\tilde{N}_3$, $\tilde{N}_4$ and $\tilde{C}_2$. The production cross-sections of these sparticles are small and the resulting contribution to the total cross-section for Higgs boson production is of the order of 100 fb, i.e. negligible compared to SM channels.
The next-to-leading order production cross-section for a 130 GeV Higgs boson is 39 pb [81]. It is computed by the `HIGLU` code for the gluon fusion channel [131], the `VV2HF` for the vector boson fusion (VBF) channel and `V2HV` for the production in association with a vector boson. This number includes NLO electroweak and QCD corrections. At $m_h \approx 130$ GeV, the Higgs boson mostly decay to $b\bar{b}$ (53%), then to $WW^*$ (29%), $\tau\tau$ (5%), $ZZ$ (4%) and finally to $\gamma\gamma$ (2‰). Nevertheless, thanks to its two isolated photons in the final state, this channel bears less background than others and is the most suitable for the measurement of the Higgs boson mass. The analysis is not part of this thesis [81]. Figure 5.10 shows the significance for the $h \to \gamma\gamma$ signal for 10fb$^{-1}$ as a function of $m_h$.

Figure 5.9 shows the distribution of the invariant mass of the photon pair in $h \to \gamma\gamma$ events. The main source of systematic uncertainties on the measurement of the Higgs boson mass in this channel arise from the knowledge of the electromagnetic energy

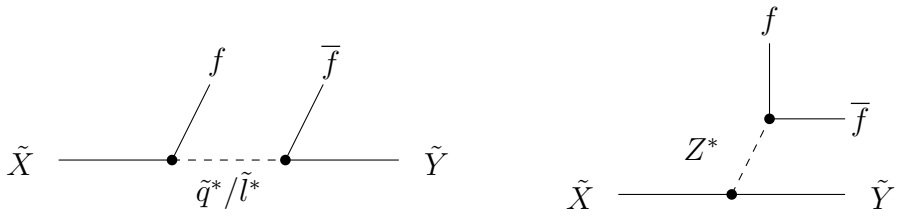


Figure 5.11: Possible three-bodies decays of sparticles.

scale. In the early phases of data-taking, the calibration of the photon energy scale will be derived from that of the electron energy scale realized on $Z \to ee$ events (see chapter 4) in combination with Monte Carlo simulations. Later, $Z \to \mu\mu\gamma$ events can be used to reconstruct the $Z$ boson mass and constrain the photon energy scale. It should eventually be known to 0.1%.
The measurement of the mass of the Higgs boson provides a strong constraint on the value of $\tan\beta$ in DSS.

### Di-lepton end-point

Three-bodies decay of sparticles can provide valuable information to constrain their masses. If the mass splitting between two sparticles, $\tilde{X}$ and $\tilde{Y}$ with $m_{\tilde{X}} > m_{\tilde{Y}}$, is smaller than the mass of the $Z$ boson, then $\tilde{X}$ may decay to $\tilde{Y}$ through a virtual squark, slepton or $Z$ boson along with a fermion pair. Figure 5.11 shows these decays. In DSS, squark and slepton masses are very large and the graph with slepton or squark exchange is negligible. If only the graph with the exchange of a $Z$ boson contributes, the differential rate of these decay with respect to the invariant mass of the fermion pair reads [132]

$$\frac{d\Gamma}{dM} = CM\frac{\sqrt{M^4 - M^2(D^2+S^2) + (DS)^2}}{(M^2 - m_Z^2)^2}\left[M^2(2S^2+D^2) - 2M^4 + (SM)^2\right] \quad (5.4)$$

where $M \equiv M_{f\overline{f}}$ is the invariant mass of the fermion pair, $D = m_{\tilde{X}} - m_{\tilde{Y}}$, $S = m_{\tilde{X}} + m_{\tilde{Y}}$ and $C$ is a normalization factor. If it is experimentally possible to establish the distribution of the invariant mass of the fermion pair, it will show a triangular shape with a sharp end-point at $M_{f\overline{f}} = D = m_{\tilde{X}} - m_{\tilde{Y}}$. A fit of the distribution to equation 5.4 provides the difference and sum of the masses of the two sparticles in the decay. However the determination of the sum is much less precise, since the dependence of the distribution shape on $m_{\tilde{Y}}$ becomes very weak when this mass is larger than the mass difference.

$\tilde{N}_3$ in DSS1 and $\tilde{N}_{3,4}$ and charginos in DSS2 decay through an on-shell $Z$. The $M_{\ell\ell}$ distribution will thus show a $Z$ peak rather than a triangular shape. However, the end-point technique can be applied to two decays : $\tilde{N}_2 \to \tilde{N}_1\ell\ell$ in both points and $\tilde{N}_3 \to \tilde{N}_1\ell\ell$ in DSS2. Leptons in $\ell\ell$ pairs have Opposite Signs and Same Flavour (OSSF). Even if $\tilde{N}_2$ and $\tilde{N}_3$ decay mostly into a quark pair, the use of OSSF leptons

| Process | $e^+e^-$ | $\mu^+\mu^-$ | OSSF | OSOF |
|---|---|---|---|---|
| DSS1 | 264 | 359 | 623 | 61 |
| $t\bar{t}$ | 128 | 214 | 342 | 327 |
| $W/Z+$jets | 1 | 5 | 6 | 4 |
| $WW/WZ/ZZ$ | 1 | 13 | 14 | 7 |
| Total SM | 130 | 232 | 362 | 338 |

Table 5.12: Number of lepton pairs passing the event selection for 1 fb$^{-1}$.

dramatically reduces the combinatorial background in the constitution of the fermion pair. Furthermore, the lepton energy scale is expected to be known to the per-mil level while the jet energy scale is only determined to the percent level. Although the direct production of $\tilde{N}_2$ via the $\tilde{C}_1\tilde{N}_2$ channel bears little background due to the small number of jets in the final state, it is important to include the production of $\tilde{N}_2$ via the decay of a gluino in order to increase statistics. The total cross section for the decay of interest is $\sigma(\tilde{N}_2 \to \tilde{N}_1\ell\ell) \approx 3.5$ pb in DSS1 and 93 fb in DSS2 and $\sigma(\tilde{N}_3 \to \tilde{N}_1\ell\ell) \approx 75$ fb in DSS2.

Events are selected by requiring a missing transverse energy larger than 100 GeV, the leading jet with $E_T > 100$ GeV and a next-to-leading jet with $E_T > 50$ GeV. Also, events are required to contain at least two Opposite-Sign-Same-Flavour (OSSF) leptons. Leptons refer to electrons or muons with $p_{\mathrm{T}} > 20$ GeV and $|\eta| < 2.5$. In order to improve the sensitivity to the signal, only lepton pairs with an invariant mass $M_{\ell\ell} < m_{\tilde{N}_2} - m_{\tilde{N}_1} + 10$ GeV are considered. Since the true value of the endpoint is a priory unknown, this choice implies that the edge has already been observed. The number of remaining lepton pairs for signal and backgrounds are listed in able 5.12. The QCD background is removed by the lepton and $\not{E}_{\mathrm{T}}$ cuts. The remaining background is mostly composed of $t\bar{t}$ events but also contains $W+$jets, $Z+$jets, $WW$, $WZ$ and $ZZ$ events. Figure 5.12 shows the distribution of the invariant mass of OSSF lepton pairs for DSS1 and all SM backgrounds for an integrated luminosity of 1 fb$^{-1}$.

In order to remove combinatorial background, the flavour subtraction method is applied. It is based on the fact that the signal contains two OSSF leptons, while the background leptons come from different decay chains, which can be of the same flavour or of different flavour with the same probability. The background thus cancels in the subtraction

$$N(e^+e^-)/\beta + \beta N(\mu^+\mu^-) - N(e^\pm\mu^\mp)$$

where $\beta$ is an efficiency correction factor equal to the ratio of the electron and muon reconstruction efficiencies. The dominant SM background arise from $t\bar{t}$ events in which each lepton in the pair comes from the decay of a $W$ boson. In such a case, the number of events containing an OSSF lepton pair is theoretically equal to the number of events containing an Opposite-Sign-Opposite-Flavour (OSOF) lepton pair. Hence, the flavour subtraction technique also cancels contributions from $t\bar{t}$ events. Figure 5.13 shows the distribution of the invariant mass of lepton pairs after suppression of the SM and combinatorial backgrounds for DSS1 with 10 fb$^{-1}$ and DSS2 with 100 fb$^{-1}$. In the case of DSS2, the lowest end-point corresponds to the mass splitting $m_{\tilde{N}_2} - m_{\tilde{N}_1}$ while

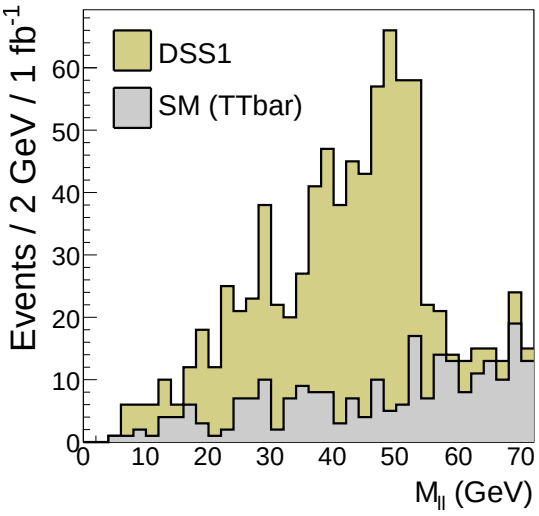


Figure 5.12: Distribution of the invariant mass of OSSF lepton pairs for DSS1 and all SM backgrounds for an integrated luminosity of 1 fb$^{-1}$. DSS1 is superimposed on the background.

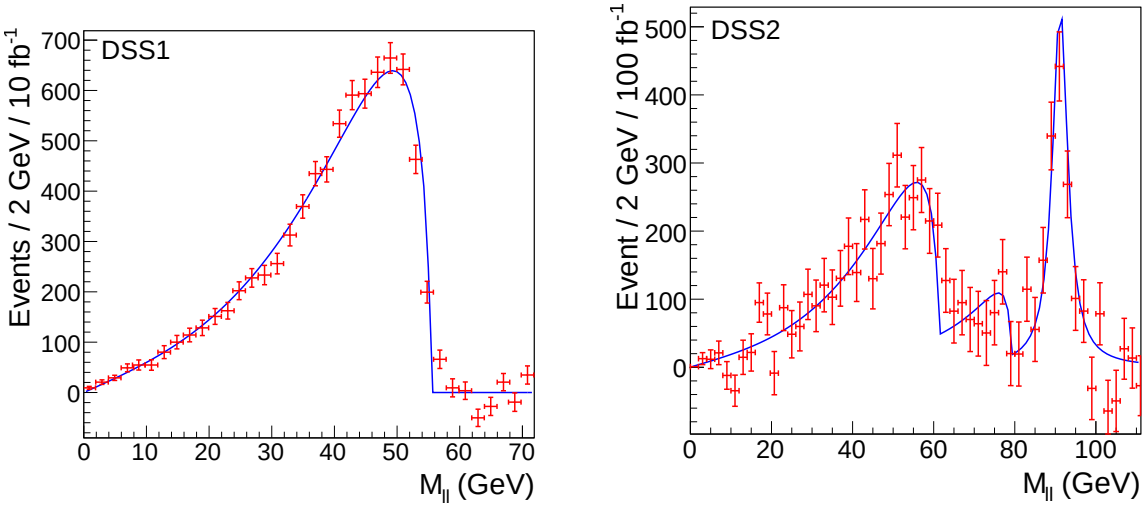


Figure 5.13: Distributions of the invariant mass of lepton pairs after suppression of the SM and combinatorial backgrounds for DSS1 with 10 fb$^{-1}$ (left) and DSS2 with 100 fb$^{-1}$ (right). Error bars include contributions from the SUSY and SM backgrounds subtraction. The fit is superimposed.

| | | Theoretical value (GeV) | Fit value (GeV) | Statistical error (GeV) |
|---|---|---|---|---|
| DSS1 | $m_{\tilde{N}_2} - m_{\tilde{N}_1}$ | 55.1 | 55.2 | $\pm 0.6$ / 10 fb$^{-1}$ |
| DSS2 | $m_{\tilde{N}_2} - m_{\tilde{N}_1}$ | 60.7 | 60.2 | $\pm 2$ / 100 fb$^{-1}$ |
| | $m_{\tilde{N}_3} - m_{\tilde{N}_1}$ | 81.9 | 79.0 | $\pm 3$ / 100 fb$^{-1}$ |

Table 5.13: Results of the fit to the invariant mass distribution.

the second corresponds to $m_{\tilde{N}_3} - m_{\tilde{N}_1}$. The distribution is fitted with a superposition of three components, two corresponding to equation 5.4 and a Breit-Wigner corresponding to the $Z$ line-shape. The $Z$ peak will be exploited later.
Table 5.13 compares the results of the fit with the theoretical values. The corresponding statistical errors are directly provided by the fit. The fit value for $m_{\tilde{N}_2} - m_{\tilde{N}_1}$ are in good agreement with the theoretical values for DSS1 and in reasonable agreement for DSS2. It can be argued that the $m_{\tilde{N}_3} - m_{\tilde{N}_1}$ edge is not clearly visible but the domain between the $m_{\tilde{N}_2} - m_{\tilde{N}_1}$ edge and the beginning of the $Z$ peak has a $5\sigma$ significance with respect to the background.

The assignment of the value of this end-points to sparticle mass splittings necessitates a few assumptions. In DSS1, lepton pairs are quite frequent with respect to the overall SUSY production. This suggests that the neutralino triggering this decay is somewhat light. In addition, a decay through a 296 GeV $\tilde{N}_3$ is rather unlikely, and in such a case additional structure would be seen. In DSS2, with two end-points and a $Z$ peak, the interpretation is slightly more complicated. Indeed, in addition to the assumption that the end-points arise from the decay of $\tilde{N}_3$ and $\tilde{N}_2$, we have to assume that $\tilde{N}_3$ decays preferably to $\tilde{N}_1$. Otherwise, the largest end-point could correspond to $m_{\tilde{N}_3} - m_{\tilde{N}_2}$ and the $Z$ peak to the decay $\tilde{N}_3 \to \tilde{N}_1 Z$.

The main source of systematic uncertainty in the measurement of di-lepton end-points arises from the knowledge of the lepton energy scale. Assuming that the error is dominated by the electromagnetic energy scale, the systematic uncertainty is of the order or the per-mil.
The measurement of the mass splitting between the lightest neutralinos provides a direct constraint on gaugino mass parameters $M_1$ and $M_2$ as well as the higgsino mass parameter $\mu$.

### Di-jet end-point

The application of the aforementioned technique to measure mass splittings is not applicable to decays involving quark pairs. The lack of information as to the flavour of the reconstructed jets implies a very large combinatorial background and washes out the end-point feature in the invariant mass distributions. However it is possible to identify jets from $b$–quarks (see chapter 3).

In DSS1, 1.7% of gluinos decay to the LSP with two $b$–quarks. Events are selected by requiring at least four jets with $E_T > 50$ GeV, no leptons and $\not{E}_{\mathrm{T}} > 100$ GeV. If

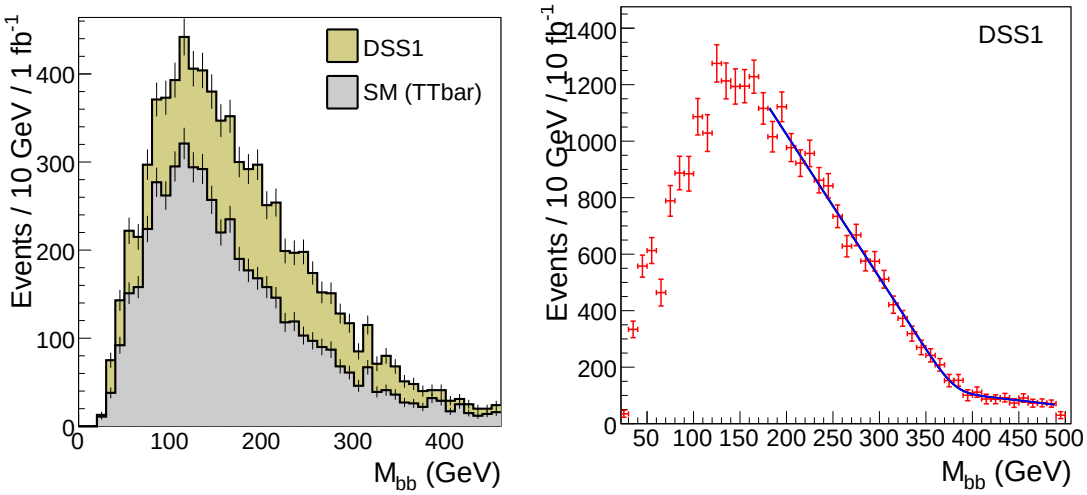


Figure 5.14: Distribution of the invariant mass of $b$–jet pairs. On the left-side plot, the DSS1 signal for 1 fb$^{-1}$ is superimposed on the SM background. On the right-side plot, the background has been subtracted and the signal is shown for 10 fb$^{-1}$.

| | Theoretical value GeV | Fit value GeV | Statistical error GeV |
|---|---|---|---|
| $m_{\tilde{g}} - m_{\tilde{N}_1}$ | 383.0 | 380.6 | $\pm$5.2 / 10 fb$^{-1}$ |

Table 5.14: Result of the fit of the $M_{bb}$ distribution.

two jets with a $b$–tagging weight larger than 10 are present in the event, the invariant mass $M_{bb}$ is computed. The background is mostly constituted of $t\bar{t}$ events as well as combinations due to decays other than $\tilde{g} \rightarrow \tilde{N}_1 b\bar{b}$.
Figure 5.14 shows the distribution of the $M_{bb}$ invariant mass in DSS1 and SM events for 1 fb$^{-1}$(left) and after subtraction of the background for 10 fb$^{-1}$(right). The distribution is fitted from the peak with a sum of two straight lines and a Gaussian smearing to account for the smooth transition. The fit function reads

$$\frac{d\Gamma}{dm} = \int_0^D dt \text{Gauss}(t,\sigma) \max\{A(t-D),0\} + \max\{B+Cm,0\}$$

where $D = m_{\tilde{g}} - m_{\tilde{N}_1}$ and $A$, $B$ and $C$ are the parameters of the two straight lines. The smearing parameter $\sigma$ is fixed to 15 GeV. Table 5.14 compares the result of the fit with the theoretical value. The statistical uncertainty is quoted for 10 fb$^{-1}$. The value obtained by fitting the distribution is in good agreement with the theoretical value.
The main source of systematic uncertainty on the measurement of the end-point arise from the knowledge of the hadronic energy scale. It is expected to be known to the percent level once the detector will have been understood.

The measurement of this observable is important for the determination of $M_3$ as it gives an indication on the gluino mass scale.

| DSS1 | $\sigma$ | BR | $\sigma(3\ell)$ |
|---|---|---|---|
| Direct | 11.7 pb | 1.54% | 180 fb |
| Via $\tilde{g}\tilde{g}$ | 10.4 pb | | 160 fb |
| | | Total | 340 fb |

| DSS2 | $\sigma$ | BR | $\sigma(3\ell)$ |
|---|---|---|---|
| Direct | 1390 fb | 1.54% | 21.4 fb |
| Via $\tilde{g}\tilde{g}$ | 166 fb | | 2.6 fb |
| | | Total | 24 fb |

Table 5.15: Cross-section of the tri-lepton signal in DSS.

| Process | $\not{E}_{\mathrm{T}}$ cut | $3\ell$ cut | OSSF cut | $M_{\ell\ell}$ cut | jet veto |
|---|---|---|---|---|---|
| DSS1 | 617,326 | 807 | 775 | 681 | 43 |
| DSS2 | 27,362 | 135 | 127 | 87 | 4 |
| $t\bar{t}$ | 4,682,866 | 1,920 | 1,350 | 1,106 | 59 |
| QCD | 14,023,358 | 0 | 0 | 0 | 0 |
| $W/Z+$jets | 10,227,119 | 27 | 27 | 14 | 0 |
| $WW/WZ/ZZ$ | 397,569 | 2,499 | 2,493 | 235 | 73 |
| | | | | $Z_n = 2.5$ | $Z_n = 1.5$ |

Table 5.16: Number of events remaining after the successive application of each cut for 10 fb$^{-1}$.

### Tri-lepton cross-section

The use of leptons in SUSY observables reduces backgrounds and increases the precision of the measurement. In DSS, many charginos and neutralinos may be produced at the LHC resulting in many final states with numerous isolated leptons. The tri-lepton final state is very well known as it allows for a large background rejection by requiring that two lepton be OSSF. Indeed, this signature arise in the case where a chargino (usually $\tilde{C}_1$) and a neutralino (usually $\tilde{N}_2$) are produced in two parallel SUSY cascades. If they decay as $\tilde{N}_2 \to \tilde{N}_1\ell\ell$ and $\tilde{C}_1 \to \tilde{N}_1\ell\nu$, three leptons will be detected two of which (from the decay of $\tilde{N}_2$) will be OSSF. If SM and SUSY backgrounds, PDFs, luminosity and lepton identification performances are well understood and a large signal sample is gathered, it may be possible to measure the cross-section of such a process.

Table 5.15 shows the components of the tri-lepton signal in DSS1. $\tilde{C}_1\tilde{N}_2$ pairs can be produced directly or through the decay of a gluino pair.
Events are selected by requiring at least one OSSF pair and exactly three leptons. In case of direct production, $\tilde{N}_1$ will be emitted essentially back-to-back, hence cancelling the missing transverse energy. The cut $\not{E}_{\mathrm{T}} > 50$ GeV is applied. An optional upper cut of 20 GeV on the $p_{\mathrm{T}}$ of the leading jet can be applied in order to select events from direct $\tilde{C}_1\tilde{N}_2$ production rather than $\tilde{g}$ pair decays. In the former case, no jets are produced from the SUSY cascade. Only jets resulting from initial state radiation or from the underlying event will be found in the event. In order to reject lepton pairs arising from decays of $Z$ bosons, the invariant mass of all OSSF pairs in the event are required to satisfy $M_{\ell\ell} < 81.2$ GeV and $M_{\ell\ell} > 102.2$ GeV. For the signal, $M_{\ell\ell}$ is expected to be lower than about 56 GeV due to the mass splitting between the $\tilde{N}_2$ and $\tilde{N}_1$.

Table 5.16 presents the number of events remaining after the successive application of each cut for an integrated luminosity of 10 fb$^{-1}$. Significances for the last two cuts are also quoted. After the three-leptons requirement, only $t\bar{t}$ and $WW/WZ/ZZ$ remain significant. The latter is partly removed by the $M_{\ell\ell}$ cut while the former is removed by the jet veto cut. A study performed on fully simulated data shows that additional cuts on the isolation of lepton tracks enables a further rejection of the background [81].

A somewhat precise determination of the number of tri-lepton events due to the signal relies on a good knowledge of the backgrounds and a complete understanding of detector effects, luminosity and PDFs. Once this is achieved, the efficiency of each cut must be known. Theoretically, once the end-point has been observed, it should be clear that the cut applied on the invariant mass $M_{\ell\ell}$ should only remove background events. The signal efficiency should be 1. The cut on the number of leptons and on the number of OSSF pairs only relies on lepton identification efficiencies. In order to estimate the exact factors to include in the analysis, lepton efficiencies including trigger and reconstruction will have to be determined precisely as a function of $p_{\mathrm{T}}$ and $|\eta|$ using $Z \to \ell\ell$ events (see chapter 4). Also, the $p_{\mathrm{T}}$ and $|\eta|$ spectrum of leptons stemming from $\tilde{C}_1$ and $\tilde{N}_2$ decays should be established. This can be achieved assuming that the majority of leptons found in SUSY events decay from the latter and that a somewhat pure SUSY sample will have been assembled using cuts detailed in the inclusive study detailed above. Using a similar approach, it should be possible to establish the $\not\!\!E_{\mathrm{T}}$ spectrum of SUSY tri-lepton events and thus estimate the efficiency $\epsilon_{\not\!\!E_{\mathrm{T}}}$ of the associated cut. The number of combinatorial background events can be estimated by counting events containing three leptons but no OSSF pairs $N_{3\ell}^{\overline{\mathrm{OSSF}}}$.

Once SM backgrounds have been removed and all efficiency factors estimated, the SUSY tri-lepton cross section should read

$$\sigma(\mathrm{SUSY} \to 3\ell) = \frac{4\left(N_{3\ell}^{\mathrm{OSSF}} - N_{3\ell}^{\overline{\mathrm{OSSF}}}\right)}{(\epsilon_e^2 + \epsilon_\mu^2)(\epsilon_e + \epsilon_\mu)\epsilon_{\mathrm{acc}}\epsilon_{\not\!\!E_{\mathrm{T}}} \int \mathcal{L}dt}.$$

The systematic uncertainty on $\sigma(\mathrm{SUSY}3\ell)$ is bounded from below by the knowledge of the luminosity $\mathcal{L}$ which will be measured with an accuracy of 5% [133]. In order to take into account other contributions, systematic errors of 5, 10 and 20% are considered. The statistical uncertainty scale with the square root of the number of selected events.

### Gluino pairs cross-section

The gluino pair channel constitutes the largest part of the SUSY signal in both DSS points (77% in DSS1 and 22% in DSS2). A number of analysis can be established in order to select $\tilde{g}\tilde{g}$ events and reject SM and SUSY backgrounds. Each of them are very model-dependent as they require a knowledge of the gluino decays branching fraction. One could for instance take advantage of the very short cascade $\tilde{g}\tilde{g} \to \tilde{N}_1\tilde{N}_1 q\bar{q}q\bar{q}$. This 0–lepton mode can help remove SUSY background from chargino and neutralino channels. This channel uses the assumption of a single gluino branching ratio, i.e. that of the decay $\tilde{g} \to \tilde{N}_1 q\bar{q}$.

| | DSS1 | DSS2 |
|---|---|---|
| $R_Z$ | $< 0.004 \sim 0$ | 0.196 |

Table 5.17: Theoretical values for $R_Z$.

Again, the systematic uncertainty is bounded from below by the knowledge of the luminosity which is expected to be measured to within 5% [133]. In order to take into account other contributions, systematic errors of 5, 10 and 20% are considered. The statistical uncertainty scale with the square root of the number of selected events.

#### Ratio of on-shell to off-shell $Z$ bosons

If the mass difference between two neutralinos or two charginos is larger than $m_Z$, the $Z$ boson in figure 5.11 will be on-shell. Consequently, the distribution of the invariant mass of its decay products will exhibit a very sharp peak around $m_Z$. Otherwise, if the mass difference between the two sparticles is smaller than $m_Z$, the distribution of $M_{\ell\ell}$ will exhibit a triangular shape with a sharp end-point below $m_Z$. Both feature can be seen in figure 5.13 where, on the left-side (DSS1), only the end-point appears while on the right (DSS2) a non-negligible fraction of the SUSY production decays through an on-shell $Z$ boson and a large peak is observed at $M_{\ell\ell} = m_Z$. This effect can provide valuable information as to the mass of the neutralinos and charginos as well as their couplings to the $Z$ boson. Such a study suffers from a very large SM background due to the production of $Z$ boson. These SM channels will have to be measured to a very high accuracy.

The measurement of the $Z$ cross-section in SUSY events $\sigma(\text{SUSY} \rightarrow Z)$ requires a good knowledge of the luminosity, lepton efficiencies and background rates. Some of these source of systematic uncertainties can be cancelled if instead of simply counting the number of events in the $Z$ peak, the ratio

$$R_Z = \frac{N\left(M_{\ell\ell} > \text{endpoint}\right)}{N\left(M_{\ell\ell} < \text{endpoint}\right)} \tag{5.5}$$

is measured. This quantity measures the fraction of on-shell to off-shell $Z$ bosons in SUSY events. Table 5.17 presents the values of $R_Z$ for DSS1 and DSS2 as obtained from the cross-sections and branching ratios in tables 5.5 and 5.6. Potential systematic uncertainties on $R_Z$ arise if the $p_{\mathrm{T}}$ spectra of leptons from the $Z$ peak or from the triangular shape are different, and if the identification efficiencies for this two spectra are different. As shown in chapter 4, electron identification efficiencies are reasonably flat for $p_{\mathrm{T}} > 25$ GeV. Leptons from the $Z$ peak will have $p_{\mathrm{T}}$'s around 45 GeV. Those in the triangular shape have their $p_{\mathrm{T}}$ bounded from below from the analysis cut $p_{\mathrm{T}} > 20$ GeV. Another source of systematic error arises from the SM $Z$ cross-section. SM processes containing a $Z$ boson are assumed to be removed in the course of the analysis with cuts on e.g. $\not\!\!E_{\mathrm{T}}$. An overall 1% systematic error is included to account for lepton identification uncertainties.

### 5.1.8 Parameter determination

Once supersymmetry will have been discovered, models will have to be discriminated and the parameters of the underlying theory will have to be determined in a consistent manner. Also, it will be necessary to combine new observables with external constraints such as the measurement of the relic density, the magnetic moment of the muon or the $b \to s\gamma$ decay.
The observables described in section 5.1.7 can be used to constrain the parameters of the model. This analysis can be realized using the `SFitter` program.

#### The `SFitter` program

`SFitter` [134] is a global code for the study of supersymmetric models. It is a European collaboration including collider experimentalists and SUSY phenomenologists. It is designed to solve the task of mapping up to 20-dimensional highly complex parameter spaces onto a large set of observables of different quality, which can be highly correlated. `SFitter` uses combinations of elaborate minimization techniques to scan the parameter space of a given SUSY model. At each point, observables are predicted with a set of well-known tools. The best parameter set is found and errors on the determination of the model parameters are estimated in a consistent manner.
Coded in `C++`, it is very flexible and modular. It supports the SUSY Les Houches Accord format (SLHA [135, 136]) and can be easily and quickly adapted to any model and any experimental constraint. `SFitter` is useful to estimate the determination potential of a given model at a given experiment but it will also be used once physics analysis will have been realized to work a "bottom-up" approach to determine the parameters of the theory.

As input, `SFitter` takes experimental observables with errors and a model. Observables can be in the form of a fixed measured value with an error or a limit with a confidence level. Supported observables include measurements of particle masses, cross-sections, branching ratios, couplings or external constraints (relic density, $b \to s\gamma$, $g_\mu - 2$, etc...). In fact, any SLHA entry can serve as input. Also, any analytical function constructed on the latter can be used as observable. This allows to input e.g. cascade cross-sections, the ratio of the rates of two channels, etc...
`SFitter` can fit six SUSY models. The MSSM (see chapter 2) is used in its phenomenological form, i.e. when the number of parameters has been reduced to about 20 in order to minimize undesired effects such as flavour-changing currents and additional CP-violation. The parameters of the MSSM can be defined at the weak scale or at the GUT scale. mSUGRA is included. SUSY models with gauge mediated breaking (GMSB) or anomaly mediated breaking (AMSB) are also available. In the context of this thesis, I have implemented DSS in `SFitter` and added it to the list of available input models.
`SFitter` can predict a large variety of observables thanks to a number of tools. For the prediction of mass spectra, three generators can be used, `SoftSUSY` [137], `SuSpect` [109] and `ISASUSY` [138]. Next-to-leading-order cross sections for LHC are calculated by the program `Prospino2` [118, 119, 120] and branching ratios can be included via

links to `Msmlib` [139] and SUSY-HIT (`HDECAY` and `SDECAY`) [121, 140]. Also the dark matter content of the relic density is readily available by an interface to `micrOMEGAs` [141]. The communication of parameters and results between the different programs is performed by the SLHA data format using the implementation of `SLHAio` [142].

Comparing the experimental data $d_i$ and the theoretical prediction $\overline{d}_i$, where the index $i$ runs over the different data, a likelihood value is assigned to every point in parameter space. Hereby we follow the RFit scheme of [143] and assume the theoretical errors $\sigma_i^{\text{th}}$ as box-shaped. This scheme interprets theoretical errors as a lack of knowledge on a parameter. As long as the deviation between theory and experiment is within the theoretical error, this must not have any influence on the total likelihood. In combination with the experimental error $\sigma_i^{\text{exp}}$ the total log-likelihood $\log L = -\frac{\chi^2}{2}$ is given by

$$\chi^2 = \begin{cases} 0 & \text{for } |d_i - \overline{d}_i| < \sigma_i^{\text{th}} \\ \left(\frac{|d_i - \overline{d}_i| - \sigma_i^{\text{th}}}{\sigma_i^{\text{exp}}}\right)^2 & \text{for } |d_i - \overline{d}_i| \geq \sigma_i^{\text{th}} \end{cases}$$

The experimental error is a combination of three different sources. All three are considered as Gaussian and are summed quadratically. The statistical error is assumed to be uncorrelated between different measurements. The first systematic error originates from the lepton energy scale and the second from the hadronic energy scale. They are treated separately. Each is taken as 99% correlated between different observables.

In order to determine the underlying parameters, a scan of the parameter space is performed. Three method can be combined. The first scan on a fixed grid. Secondly, the Minuit fitter [144] is included as a minimum finder. It makes use of a steepest-descent hill-climbing algorithm. The third option uses the technique of Weighted Markov Chains (WMC). Markov chains are defined as a sequence of points which are the result of a stochastic process. In SFitter the Metropolis-Hastings [145, 146] algorithm is used for choosing the next point, which works in the following way. In the first part of the algorithm a new point is suggested, based on the current one using a probability distribution function. The latter can be freely chosen as long as it satisfies the property that the probability from being at point $x$ and proposing $x'$ is the same as being at $x'$ and proposing $x$. It can for example be chosen flat, then the Markov-Chain algorithm has no dependence between points at all and reduces to a simple Monte-Carlo fitting. A good performance was found using a Breit-Wigner or Cauchy-shaped function. This type of function has more pronounced tails than a Gaussian distribution and provides a better balance to avoid random-walk behaviour. The second part of Metropolis-Hastings consists of the acceptance stage. It is decided whether the suggested point is accepted or rejected based on a potential, which in our case is $\chi^{-2}$. So if the log-likelihood of the suggested point is larger than that of the previous one, it is always accepted, else, it is accepted if the ratio of the two log-likelihoods is larger than a random number $r$ chosen uniformly between 0 and 1. In all other cases the old point is added to the Markov chain another time. The resulting Markov chain has the property that the density of points is proportional to the potential, i.e. to $\chi^{-2}$ which can then be used to obtain likelihood maps by binning the points.

| | Observables | | Uncertainties (%) | | | |
|---|---|---|---|---|---|---|
| | | | Stat. | Systematic | | Th. |
| | | | | Value | Source | |
| DSS1 | $m_h$ | 129 GeV | 0.1 | 0.1 | energy scale | 4 |
| | $m_{\tilde{N}_2} - m_{\tilde{N}_1}$ | 55.2 GeV | 1 | 0.1 | energy scale | 1 |
| | $m_{\tilde{g}} - m_{\tilde{N}_1}$ | 382.8 GeV | 1.5 | 1 | energy scale | 1 |
| | $\sigma(3\ell)$ | 340 fb | 2 | $> 5$ | luminosity | 12 |
| | $R_Z$ | $< 0.004$ | 0.01 | 1 | lepton id. | 1 |
| | $\sigma(\tilde{g}\tilde{g})$ | 62.8 pb | 0.1 | $> 5$ | luminosity | 30 |
| DSS2 | $m_h$ | 129 GeV | 0.1 | 0.1 | energy scale | 4 |
| | $m_{\tilde{N}_2} - m_{\tilde{N}_1}$ | 61.3 GeV | 3.3 | 0.1 | energy scale | 1 |
| | $m_{\tilde{N}_3} - m_{\tilde{N}_1}$ | 76.4 GeV | 3.7 | 0.1 | energy scale | 1 |
| | $\sigma(3\ell)$ | 24 fb | 14 | $> 5$ | luminosity | 12 |
| | $R_Z$ | 0.195 | 0.7 | 1 | lepton id. | 1 |
| | $\sigma(\tilde{g}\tilde{g})$ | 954 fb | 3 | $> 5$ | luminosity | 30 |

Table 5.18: Summary of available collider observables in DSS1 and DSS2. Statistical errors are quoted for an integrated luminosity of 100 fb$^{-1}$.

### Results

The collider observables investigated in section 5.1.7 can be used to determine the parameters of the model using a global fit. Table 5.18 summarizes the observables along with the expected uncertainties for DSS1 and DSS2. The chosen integrated luminosity for this study is 100 fb$^{-1}$. It corresponds to one year of data-taking[1] of the LHC at the design luminosity of $10^{34}$ cm$^{-2}$s$^{-1}$. For the observables for which a detailed study was performed ($m_{\tilde{N}_2} - m_{\tilde{N}_1}$, $m_{\tilde{N}_3} - m_{\tilde{N}_1}$ and $m_{\tilde{g}} - m_{\tilde{N}_1}$), the outcome of the result of the analysis is used as central value. For the others, a potential study is assumed to provide the correct central value and the theoretical value is used.
In both points, the lightest Higgs boson can be discovered and its mass measured in the $h \to \gamma\gamma$ channel. The statistical uncertainty for 100 fb$^{-1}$ is estimated to 0.1% by [148]. The systematic uncertainty is dominated by the electromagnetic energy scale (0.1%). The theoretical uncertainty is due to the knowledge of higher-order SUSY corrections to $m_h$ and is estimated to be 4%. The mass splittings $m_{\tilde{N}_2} - m_{\tilde{N}_1}$ and $m_{\tilde{N}_3} - m_{\tilde{N}_1}$ (for DSS2 only) are measured using end-points in the invariant mass distribution of OSSF lepton pairs. The statistical errors are extracted from the fit to the reference function. Systematic uncertainties are dominated by the lepton energy scale (0.1%). Theoretical errors are due to non-calculated higher-order contributions as well as discrepancies between different codes. They are estimated to be of the order of a percent. The tri-lepton signal can be detected and its cross-section measured. Systematic errors are bounded from below by the luminosity (5%) and the theoretical uncertainty is estimated to be of the order of 12%. The ratio of on-shell to off-shell $Z$ bosons produced in SUSY cascades can be measured using again the invariant mass distribution of OSSF lepton pairs. Systematic uncertainties due to lepton identification efficiencies

[1] That is 200 days of running and 3 months of winter shutdown [147].

| | | Nominal values | Starting point | WMC minimum | MIGRAD minimum |
|---|---|---|---|---|---|
| DSS1 | $M_1$ | 132.4 GeV | 100 | 225 | 132.4 |
| | $M_2$ | 132.4 GeV | 100 | 176 | 132.2 |
| | $M_3$ | 132.4 GeV | 100 | 150 | 132.3 |
| | $\tan\beta$ | 30 | 50 | 69 | 30 |
| | $\mu$ | 290 GeV | 100 | 381 | 289 |
| | $m_S$ | $10^4$ | fixed | | |
| | $A_t$ | 0 | | | |
| DSS2 | $M_1$ | 296.5 GeV | 100 | 282 | 296.4 |
| | $M_2$ | 296.5 GeV | 100 | 279 | 296.5 |
| | $M_3$ | 296.5 GeV | 100 | 293 | 296.5 |
| | $\tan\beta$ | 30 | 50 | 64 | 30 |
| | $\mu$ | 200 GeV | 100 | 186 | 200 |
| | $m_S$ | $10^4$ | fixed | | |
| | $A_t$ | 0 | | | |

Table 5.19: Results of the WMC and Minuit minimization for DSS1 and DSS2.

and lepton energy scale are cancelled in the ratio. The theoretical uncertainty is due to the generation of branching ratios by SDECAY and is taken to be of the order of 1%. The systematic error on the measurement of the gluino pair cross-section is bounded from below by the knowledge of the luminosity (5%). Theoretical uncertainties from higher order contributions are very large due to the strongly-interacting nature of gluinos. They are assumed to be of the order of 30%.

The determination of the parameters proceeds in two steps. In a first stage, the likelihood is maximized to find the best point in parameter space. Then the minimization is started from the correct point in order to estimate the error on the parameters. All SFitter jobs were run on the WLCG grid.
For the first stage, the Weighted Markov Chain (WMC) method is used to find the approximate region of the minimum. The starting point is arbitrary and the search is repeated several times to ensure the convergence of the procedure. Then, the minimum found by the WMC algorithm serves as starting point for a higher resolution local search with the Minuit MIGRAD minimization technique.
No information on the squark and slepton sector is available except for the absence thereof. Consequently, $m_S$ and $A_t$ remain undetermined. They are fixed to their nominal value throughout the study. The three gaugino mass parameters are fitted independently.
Table 5.19 presents the results of the minimization procedure. For both points, the starting point is chosen randomly. The minimum found by the WMC algorithm is fairly distant from the nominal point but proves to stay in the correct domain. From there, Minuit recovers correctly the nominal parameter sets.

Three scenarios are layed out in order to estimate the precision on the determination

| | | STAT | | SYST | | TH | |
|---|---|---|---|---|---|---|---|
| | | $\Delta$ | % | $\Delta$ | % | $\Delta$ | % |
| DSS1 | $M_1$ | 1.9 | 1.4 | 0.2 | 0.2 | 4 | 3.0 |
| | $M_2$ | 0.9 | 1.4 | 0.1 | 0.1 | 2 | 1.5 |
| | $M_3$ | 0.3 | 0.2 | 0.1 | 0.1 | 4 | 1.5 |
| | $\mu$ | 0.5 | 0.2 | 0.2 | 0.1 | 10 | 3.4 |
| | $\tan\beta$ | 12.7 | 42.3 | 1.3 | 4.4 | undet. | |
| DSS2 | $M_1$ | 21.3 | 7.2 | 0.9 | 0.3 | 6.1 | 2.1 |
| | $M_2$ | 9.8 | 3.3 | 0.4 | 0.1 | 0.8 | 0.3 |
| | $M_3$ | 2.3 | 0.8 | 1.6 | 0.5 | undet. | |
| | $\mu$ | 10.5 | 5.3 | 0.4 | 0.2 | 4.4 | 2.2 |
| | $\tan\beta$ | 17.6 | 58.7 | 1.4 | 4.7 | undet. | |

Table 5.20: Errors on the determination of the parameters for three fitting strategies.

of the DSS parameters. This scenarios aim at evaluating the effect from each error set. The starting point of the minimization is the best point found by `MIGRAD`, in the last column of table 5.19. From there, the Minuit `MINOS` technique is used to estimate the errors. `MINOS` performs a consistent estimation of the uncertainties taking into account the various correlation between measurements and parameters. Table 5.20 displays the resulting uncertainties for the three scenarios :

- Scenario STAT : Statistical errors. In order to evaluate the impact of the statistical uncertainties on the determination of the DSS parameters, no theoretical errors are included.

  Firstly, with a $\sim$ 50% error, the determination of $\tan\beta$ is imprecise in both points. This is expected since with all heavy Higgs bosons at $m_S$, the only leverage available on this parameter is the Higgs boson mass. $\mu$ is determined to less than 1% in DSS1 and 5% in DSS2. In the former, leverage is provided by large rates of neutralino and chargino productions. In the latter, higgsinos are more equally spread over all neutralinos. Hence, $m_{\tilde{N}_2} - m_{\tilde{N}_1}$ provides sufficient leverage. Thanks to very small statistical uncertainties on $m_{\tilde{N}_2} - m_{\tilde{N}_1}$ and $m_{\tilde{g}} - m_{\tilde{N}_1}$ in DSS1, the gaugino mass parameters are determined within 2%. This is not the case in DSS2 and they are determined to $\sim$ 10%. It was mentioned in section 5.1.7 that the visibility of the $m_{\tilde{N}_3} - m_{\tilde{N}_1}$ edge was arguable. In order to consolidate the results, the DSS2 fit was performed without this observable and no obvious difference was noted.

- Scenario SYST : Systematic errors. This scenario assumes that a very large statistic has been gathered at the LHC ($\geq$ 300 fb$^{-1}$) and that statistical uncertainties are negligible. Also by that time, it is assumed that theoretical progress will have been achieved in the calculation of higher-orders contributions to $m_h$ and SUSY cross-sections rendering theoretical errors negligible. This is indeed an idealized scenario but it is useful to measure the impact of systematic errors on the determination of the parameters.

All parameters are determined within 1% except for $\tan\beta$ which still suffers from an almost invisible Higgs sector. Systematic errors on cross-section measurements of 5, 10 and 20% are considered. In DSS1, the determination is not affected as all parameters are already well constrained by mass measurements. In DSS2, a 20% systematic error on $\sigma(\tilde{g}\tilde{g})$ doubles the uncertainty on the determination of $M_3$ with respect to the case where it is dominated by the knowledge of the luminosity (5% systematic error). A 20% systematic error on $\sigma(3\ell)$ has no effect on the determination of the parameters as mass constraints $m_{\tilde{N}_2} - m_{\tilde{N}_1}$ and $m_{\tilde{N}_3} - m_{\tilde{N}_1}$ determine the same parameters.

- Scenario TH : Theoretical errors. In this scenario, statistic is assumed to be infinite but theoretical errors are included. This more realistic scenario gives a flavour of what is achievable after at least five years of operation of the LHC.

  With a 4% theoretical uncertainty on $m_h$, $\tan\beta$ is largely undetermined in both points. The interplay of neutralinos mass splittings, $R_Z$ and the tri-lepton cross-section provides a somewhat tight constraint on the neutralino and chargino sector, leading to a determination of $M_1$, $M_2$ and $\mu$ within 4%. In DSS1, $M_3$ is mostly determined by the mass splitting $m_{\tilde{g}} - m_{\tilde{N}_1}$ and is, hence, very well determined. However, in DSS2, the only available handle on $M_3$ comes from the gluino pair cross-section which suffers from a 30% theoretical uncertainty, rendering $M_3$ undetermined.

### 5.1.9 Summary

Decoupled scalars supersymmetry is an attractive extension to the SM. While discarding SUSY as a means of stabilizing the weak scale, it still provides a number of desirable features such as a candidate for dark matter and gauge couplings unification. The absence of squarks and sfermions in the low energy theory suppresses features of the general MSSM such as proton decay mediating processes, flavour-changing interactions and additional CP-violation. The stabilization of the weak scale together with the cosmological constant are expected to be achieved through a fine-tuning of some sort.

A phenomenological model was constructed with a limited number of parameters. Two points were chosen in phase-space in order to analyse the potential of DSS at the LHC. They were designed to provide a reasonable fine-tuning of the Higgs boson mass and satisfy current experimental constraints such as measurements of the relic density or lower mass bounds set by previous collider experiments. With a very large SUSY cross-section, the first point was shown to be discoverable within a year of data-taking at the LHC. The second point necessitates a finer analysis but may be discovered within a few years. A number of observables were established for both points. The statistical and systematic errors on their measurement and the theoretical uncertainties on their prediction was estimated.

It was shown that a global fit of the DSS parameters to the experimental observables using elaborate minimization techniques together with well-known prediction tools is

able to determine the correct central value of all parameters. A study of the errors on their determination showed that the systematic uncertainties on the observables are not dominant on the determination of the parameters. However, the estimation of such errors prior to a full-fledged analysis on real data should be taken with care. Large theoretical uncertainties on the SUSY production cross-sections were shown to be non-dominant as long as another leverage is provided on the parameters in the form of mass constraints. Cross-sections alone cannot be used for the determination. The partial visibility of the Higgs sector in DSS does not allow an accurate estimation of $\tan\beta$. Together with $m_S$ and $A_t$, this parameters has few prospects at the LHC. The ILC is not expected to provide further information on the scalar sector, considering that the mass of the lightest Higgs boson was already well measured at the LHC and that 10 TeV scalars will not be produced at the ILC. As expected, the non-coloured sector of DSS ($M_1$, $M_2$ and $\mu$) can be fairly well determined at the LHC with accuracies of the order of a few percent when all errors have been included.

| | | | | | | | |
|---|---|---|---|---|---|---|---|
| $M_1$ | 103.1 | $m_{\tilde{e}_L}$ | 194.4 | $m_{\tilde{u}_R}$ | 508.1 | $m_{\tilde{q}_L^1}$ | 526.6 |
| $M_2$ | 192.9 | $m_{\tilde{e}_R}$ | 135.8 | $m_{\tilde{d}_R}$ | 505.9 | $m_{\tilde{q}_L^2}$ | 526.6 |
| $M_3$ | 567.9 | $m_{\tilde{\mu}_L}$ | 194.4 | $m_{\tilde{c}_R}$ | 508.1 | $m_{\tilde{q}_L^3}$ | 480.8 |
| $\mu$ | 353.7 | $m_{\tilde{\mu}_R}$ | 135.8 | $m_{\tilde{s}_R}$ | 505.9 | $A_{\tilde{\tau}}$ | -249.4 |
| $m_A$ | 394.9 | $m_{\tilde{\tau}_L}$ | 193.6 | $m_{\tilde{t}_R}$ | 408.3 | $A_{\tilde{t}}$ | -490.9 |
| $\tan\beta$ | 10.0 | $m_{\tilde{\tau}_R}$ | 133.4 | $m_{\tilde{b}_R}$ | 502.9 | $A_{\tilde{b}}$ | -763.4 |

Table 5.21: Low-energy MSSM parameters for the SPS1a point. Masses and couplings are GeV.

## 5.2 Determination of the MSSM at future linear colliders

If supersymmetry is discovered at the LHC, the parameters of the underlying theory will have to be determined. In this analysis, the study-case of the MSSM, and its universal branch mSUGRA, are used to compare the expected precision on the determination of the parameters between the LHC and future linear colliders. This study was realized in the case of the SPS1a parameter set. The latter represent a fairly favorable case for supersymmetry at the LHC and was already used in many prospective studies [149]. In addition to the LHC, the precision on the determination of the supersymmetric parameters was estimated at two future linear colliders: The International Linear Collider (ILC) is a project for an $e^+e^-$ collider with a center-of-mass energy of 500 GeV, extensible to 1 TeV. The Compact LInear Collider (CLIC) is a feasibility study for an $e^+e^-$ collider with 3 TeV in the center-of-mass. In order to estimate the potential for the measurement of the gluino mass at CLIC, the cross-section for the production of gluinos in $e^+e^-$ collisions was calculated.

### 5.2.1 The SPS1a parameter point

The *Snowmass Points and Slopes* (SPS) [150] are sets of benchmark points and parameter lines in the MSSM parameter space corresponding to different scenarios in the search for supersymmetry at present and future experiments. The SPS1a reference point is a "typical" parameter point of the minimal supergravity (mSUGRA) scenario. It gives rise to a particle spectrum where many states are accessible both at the LHC and the ILC, corresponding to a rather favourable scenario for phenomenology. The SPS1a benchmark scenario has been studied with experimental simulations at both colliders.

The mSUGRA parameters for the SPS1a point are

$$m_0 = 100 \text{ GeV}, \quad m_{1/2} = 250 \text{ GeV}, \quad A_0 = -100 \text{ GeV}, \quad \tan\beta = 10, \quad \text{sign}\mu = +.$$

All but $\tan\beta$ are defined at the GUT scale. The corresponding low-energy MSSM parameters are listed in table 5.21. The SPS1a scenario yields the sparticle spectrum reported in table 5.22. The dominant production channel for the SPS1a point at the

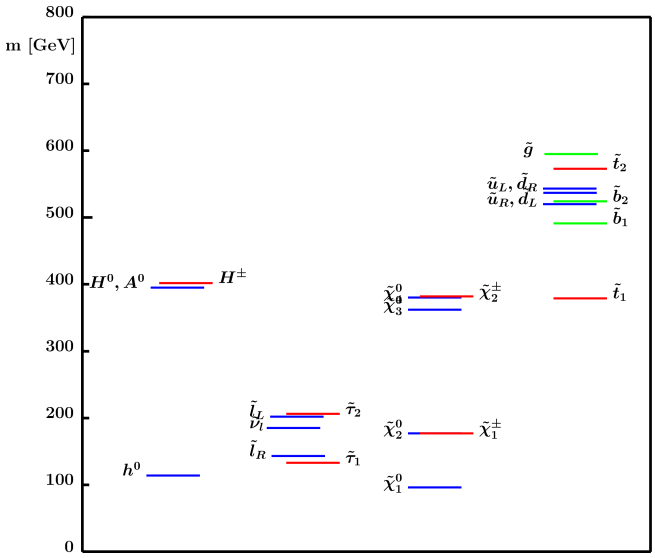


| | | | | | | | |
|---|---|---|---|---|---|---|---|
| $h$ | 110.8 | $\tilde{N}_1$ | 97.2 | $\tilde{e}_1,\ \tilde{\mu}_1$ | 142.9 | $\tilde{b}_1$ | 516.3 |
| $A$ | 398.9 | $\tilde{N}_2$ | 180.8 | $\tilde{e}_2,\ \tilde{\mu}_2$ | 200.8 | $\tilde{b}_2$ | 546.4 |
| $H$ | 399.3 | $\tilde{N}_3$ | 363.1 | $\tilde{\tau}_1$ | 133.2 | $\tilde{u}_1,\ \tilde{c}_1$ | 546.1 |
| $H^\pm$ | 407.3 | $\tilde{N}_4$ | 381.9 | $\tilde{\tau}_2$ | 205.0 | $\tilde{u}_2,\ \tilde{c}_2$ | 562.4 |
| $\tilde{g}$ | 606.3 | $\tilde{C}_1$ | 180.2 | $\tilde{t}_1$ | 399.6 | $\tilde{d}_1,\ \tilde{s}_1$ | 544.8 |
| | | $\tilde{C}_2$ | 382.2 | $\tilde{t}_2$ | 586.0 | $\tilde{d}_2,\ \tilde{s}_2$ | 567.9 |

Table 5.22: Mass spectrum in GeV for the SPS1a point obtained with `SuSpect`.

LHC is the squark-gluino channel with 28 pb (`Prospino2`) followed by squark pairs with 21 pb and gluino pairs with 8 pb. At the LHC squarks and gluinos will be produced abundantly. The gluino is the heaviest particle and decays to a squark and a quark. The squarks decay to neutralinos and charginos, which in turn decay to sleptons or lighter neutralinos and charginos. The sleptons then decay into the LSP, the $\tilde{N}_1$. Since the LSP will escape detection, it is not a straightforward task to reconstruct SUSY events. A possible approach is to use kinematic edges. Particularly interesting is the decay $\tilde{N}_2 \to \tilde{l}_R \ell \to \ell^+\ell^-\tilde{N}_1$. The two leptons in the final state provide a natural trigger, and the energy resolution is high. While right-handed squarks decay directly to the LSP, due to the bino-like nature of the $\tilde{N}_1$ in SPS1a, left-handed squarks decay to $\tilde{N}_2$ with a branching ratio of one third. The decay $\tilde{q}_L \to q\tilde{N}_2 \to q\ell^\pm\tilde{l}^\pm_R \to q\ell^\pm\ell^\mp\tilde{N}_1$, where $\tilde{q}_L$ can be $\tilde{u}_L$, $\tilde{d}_L$ or a $\tilde{b}$, is particularly useful to measure kinematic edges or threshold, leading to measurements of squark and neutralino masses [151, 149].

### 5.2.2 Future linear colliders

As a high-luminosity hadronic collider, the LHC is very useful to probe rare signals such as the production of Higgs bosons or new particles from physics beyond the SM. It is a discovery-oriented collider. The very busy environment in which hard scatterings take place due to the underlying event and pile-up as well as the large uncertainties introduced by parton density functions render precision tests challenging.
In $e^+e^-$ colliders, the four-momenta of the initial state of the hard scattering is known with great accuracy and no underlying event occurs. If the Higgs boson and supersymmetry are discovered at the LHC, such machines will be necessary to perform a full survey of the mass spectrum, couplings, spins and potential unexpected features of the underlying models. It may even be impossible to identify new phenomena that may occur at the LHC as supersymmetry before the properties of the new particles are measured with an $e^+e^-$ collider.

The International Linear Collider (ILC) [152] is a project for a 30 km long $e^+e^-$ linear accelerator with a center-of-mass energy of 500 GeV and a peak luminosity of $2 \times 10^{34}$ $\mathrm{cm}^{-2}\mathrm{s}^{-1}$. Electrons will be accelerated by 1.3 GHz superconducting radio-frequency cavities. There is a world-wide consensus that the ILC will be the next large experimental facility for high-energy physics. Designs for this machine have been developed in a world-wide effort, and it has been demonstrated that a ILC can be built and reliably operated. The project is now in the preparatory phase. No hosting site has emerged yet, but sample sites were studied in the USA (Fermilab), Europe (CERN, Switzerland) and Asia (Japan). If approved (around 2012), the ILC is expected to be operational in 2020–2025. A possible extension of the center-of-mass energy to 1 TeV is included in the design of the machine. This will be denoted $\mathrm{ILC}_{1000}$ hereafter.
The 1000 $\mathrm{fb}^{-1}$ that may be accumulated during the first running phase would help measure the physical parameters of the new particles discovered at the LHC. The couplings and spin of the Higgs boson may be measured along with a thorough survey of new SUSY particles or other new particles such as heavy gauge bosons.

The Compact LInear Collider (CLIC) is a feasibility study realized by CERN [153, 154].

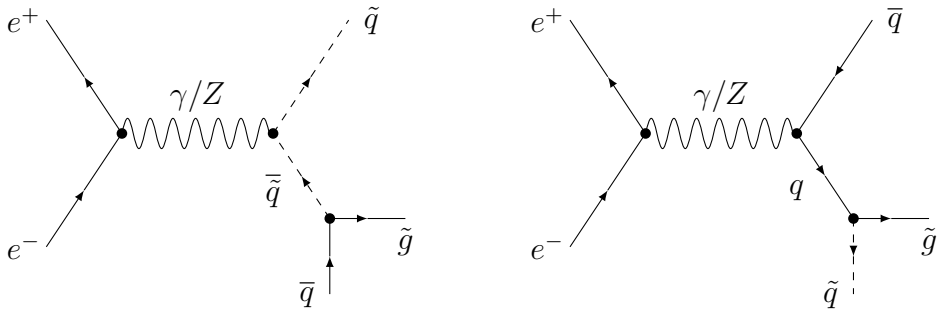


Figure 5.15: Feynman diagrams contributing to the associated production of gluino with quarks and squarks in $e^+e^-$ collisions.

It would be built after the LHC and differs from the ILC in its use of more novel technology to achieve a higher center-of-mass energy. It would use a 48 km long, 12 GHz acceleration system to bring electrons and positrons in collision with an energy in the center-of-mass of 3 TeV at a luminosity of $6 \times 10^{34}$ cm$^{-2}$s$^{-1}$. Currently, research is in progress to develop cavities that can sustain the required alternating electric field. The aim is to demonstrate the feasibility of the technology in the year 2010.
The novel feature of the CLIC proposal is its use of two-beam acceleration. The design involves coupled RF cavities to transfer energy from a high-current, low-energy drive beam to a low-current, high-energy beam to be used in collisions. It is hoped that this design will allow acceleration to significantly higher energies (3 to 5 TeV) in a shorter distance than the more conventional acceleration cavities of the ILC design.
The increased cross-section for the production of the Higgs boson at CLIC would allow for a study of its rare decays such as $H \to \ell\ell$. Also CLIC could produce heavy Higgs bosons that arise in the MSSM with masses up to 1100 GeV.

### 5.2.3 Gluino production in $e^+e^-$ collisions

Gluinos cannot be produced in pairs at leading-order in $e^+e^-$ collisions as they only couple to strongly interacting particles. The only way to produce gluino pairs is via quark-squark triangular loops and results in cross-sections of the order of $10^{-2}$ fb [155]. Another way to produce gluinos in $e^+e^-$ collisions is in association with quarks and squarks. This can proceed via the two graph shown in figure 5.15. The three-body final state $q\tilde{q}\tilde{g}$ is produced through an intermediate virtual quark or squark.

In order to estimate the precision on a potential measurement of the gluino mass at a linear collider, it is necessary to calculate its production cross-section. The total amplitude $M$ of the process is

$$M = \sum_{\mathrm{X=A,B}} \sum_{V=\gamma,Z} M_{\mathrm{X}}^{V}$$

where $M_{\rm X}^V$ corresponds to the amplitude of the graph X in figure 5.15 with the exchange of the $V$ gauge boson. The following momenta are defined

$$e^+(p_1)\ e^-(p_2) \to \tilde{q}(p_3)\ \tilde{g}(p_4)\ \overline{q}(p_5).$$

The $e^+e^-\gamma$ and $e^+e^-Z$ vertices have the form, respectively

$$-ie\overline{v}_e(p_1)\gamma_\mu u_e(p_2) \qquad \text{and} \qquad -\frac{ig}{2c_W}\overline{v}_e(p_1)\gamma^\mu\left(c_V^e - c_A^e\gamma^5\right)u_e(p_2)$$

where $\gamma_\mu$ are the Dirac matrices, $g$ is the SU(2) coupling, $\{s,c\}_W = \{\sin,\cos\}\theta_W$, $c_V^e = 2s_W^2 - \frac{1}{2}$, $c_A^e = -\frac{1}{2}$ and $u$ and $v$ are Dirac spinors for incoming fermions and outgoing anti-fermion, respectively. The photon and $Z$ propagators read

$$\frac{-ig^{\mu\nu}}{(p_1+p_2)^2} \qquad \text{and} \qquad -i\frac{g_{\mu\nu} - (p_1+p_2)_\mu(p_1+p_2)_\nu/m_Z^2}{(p_1+p_2)^2 - m_Z^2}$$

where $g_{\mu\nu}$ is the metric. The $\tilde{q}\overline{\tilde{q}}\gamma$ and $\tilde{q}\overline{\tilde{q}}Z$ vertices take the form, respectively

$$-ieQ_{\tilde{q}}(p_4+p_5-p_3)_\nu \qquad \text{and} \qquad \frac{ig}{c_W}\left(Q_{\tilde{q}}s_W^2 - T_{\tilde{q}}^3\right)(p_4+p_5-p_3)^\nu$$

where $Q_{\tilde{q}}$ and $T_{\tilde{q}}^3$ are the electric charge and third component of the weak isospin, respectively. The squark and quark propagators are, respectively

$$\frac{i}{(p_4+p_5)^2 - m_{\tilde{q}}^2} \qquad \text{and} \qquad i\frac{\not{p}_3 + \not{p}_4 + m_q}{(p_3+p_4)^2 - m_q^2}.$$

Finally, the $\tilde{q}_n q\tilde{g}$ vertex is

$$-i\sqrt{2}g_S\overline{u}_{\tilde{g}}^a(p_4)\lambda_a\left(P_{\rm R}M_{nR} - P_{\rm L}M_{nL}\right)v_{\bar{q}}(p_5)$$

where $P_{L,R}$ are left and right helicity projectors, $M_{nL,nR}$ are elements of the mass/helicity eigenstates mixing matrix and $\lambda_a$ are the Gell-Mann matrices. Then, the amplitudes $M_{\rm X}^V$ read

$$\begin{aligned}
M_A^\gamma &= -\sqrt{2}e^2Q_{\tilde{q}}g_S\sum_n \frac{\bar{v}_e(p_1)(\not{p}_4 + \not{p}_5 - \not{p}_3)u_e(p_2)\bar{u}_{\tilde{g}}^a(p_4)\lambda_a(P_{\rm R}M_{nR} - P_{\rm L}M_{nL})v_{\bar{q}}(p_5)}{(p_1+p_2)^2\left[(p_4+p_5)^2 - m_{\tilde{q}}^2\right]} \\
M_A^Z &= \frac{e^2g_S}{\sqrt{2}s_W^2c_W^2}\sum_n \frac{\bar{v}_e(p_1)(\not{p}_4 + \not{p}_5 - \not{p}_3)(c_{\rm L}^eP_{\rm L} + c_{\rm R}^eP_{\rm R})u_e(p_2)}{\left[(p_1+p_2)^2 - m_Z^2\right]\left[(p_4+p_5)^2 - m_{\tilde{q}}^2\right]} \\
&\quad \times(Qs_W^2 - T_3)\bar{u}_{\tilde{g}}^a(p_4)\lambda_a(P_{\rm R}M_{nR} - P_{\rm L}M_{nL})v_{\bar{q}}(p_5)
\end{aligned}$$

$$\begin{aligned}
M_B^\gamma &= -\sqrt{2}e^2Q_qg_s\sum_n \frac{\bar{v}_e(p_1)\gamma^\mu u_e(p_2)\bar{u}_{\tilde{g}}^a(p_4)\lambda_a(P_{\rm R}M_{nR} - P_{\rm L}M_{nL})(\not{p}_3 + \not{p}_4 + m_q)\gamma_\mu v_{\bar{q}}(p_5)}{(p_1+p_2)^2\left[(p_3+p_4)^2 - m_q^2\right]} \\
M_B^Z &= \frac{e^2g_S}{2\sqrt{2}s_W^2c_W^2}\sum_n \frac{\bar{v}_e(p_1)\gamma^\mu(c_{\rm L}^eP_{\rm L} + c_{\rm R}^eP_{\rm R})u_e(p_2)\bar{u}_{\tilde{g}}^a(p_4)\lambda_a(P_{\rm R}M_{nR} - P_{\rm L}M_{nL})}{\left[(p_1+p_2)^2 - m_Z^2\right]\left[(p_3+p_4)^2 - m_{\tilde{q}}^2\right]} \\
&\quad \times(\not{p}_3 + \not{p}_4 + m_q)\gamma_\mu(c_{\rm L}^qP_{\rm L} + c_{\rm R}^qP_{\rm R})v_{\bar{q}}(p_5)
\end{aligned}$$

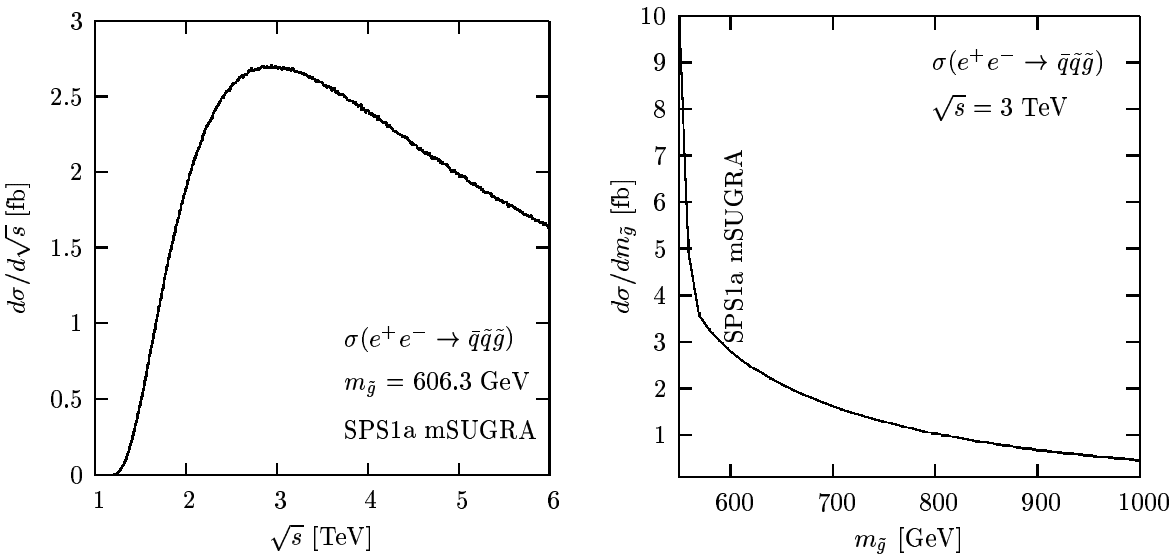


Figure 5.16: Cross-section for the production of gluino in association with a quark and a squark in $e^+e^-$ collisions as a function of the center-of-mass energy (left) and of the gluino mass (right).

The amplitudes were checked against [156]. The total spin-averaged and color-summed squared amplitude reads

$$|\mathcal{M}|^2 = \frac{1}{4} \sum_{\text{spins, colors}} \left| M_A^\gamma + M_A^Z + M_B^\gamma + M_B^Z \right|^2$$

and the differential cross-section obtained by dividing by the flux and multiplying by the phase-space

$$d\sigma = \frac{1}{2s} \times \frac{1}{(2\pi)^5} \frac{d^3p_3}{2E_3} \frac{d^3p_4}{2E_4} \frac{d^3p_5}{2E_5} \delta^4(p_1 + p_2 - p_3 - p_4 - p_5) \times |\mathcal{M}|^2. \tag{5.6}$$

The integration is achieved numerically using the `RAMBO` Monte Carlo final state generator [157].
Figure 5.16 shows the cross-section for the production of gluino in association with a quark and a squark in $e^+e^-$ collisions as a function of the center-of-mass energy and of the gluino mass. The leading-order cross-section for the production of gluinos at CLIC ($\sqrt{s} = 3$ TeV) in the case of the SPS1a scenario is

$$\sigma^{\text{LO}}(\text{CLIC} \to \tilde{g}) \approx 2.7 \text{ fb}.$$

At the LHC, the gluino mass can be measured thanks to the $\tilde{g} \to q\tilde{q}_{\text{L}} \to qq\tilde{N}_2$ decay where the momentum of the $\tilde{N}_2$ can be reconstructed [158]. In such a case, the invariant mass of the $qq\tilde{N}_2$ system will show a peak at $m_{\tilde{g}}$. Systematic uncertainties are mainly due to the knowledge of the hadronic energy scale (1%) and of the leptonic energy scale (0.1%) in the reconstruction of the $\tilde{N}_2$. A statistical error of the order of 0.5% was obtained using 1000 gluino events, after analysis cuts [149] were applied to suppress

| | SPS1a | LHC | ILC | CLIC |
|---|---|---|---|---|
| $h$ | 110.8 | 0.25 | 0.05 | 0.05 |
| $A$ | 398.9 | | | 1.5 |
| $H$ | 399.3 | | | 1.5 |
| $H^+$ | 407.3 | | | 1.5 |
| $\tilde{g}$ | 606.3 | 8 | | 6.5 |
| $\tilde{C}_1$ | 180.2 | | 0.55 | 0.55 |
| $\tilde{C}_2$ | 382.2 | | | 3 |
| $\tilde{N}_1$ | 97.2 | 4.8 | 0.05 | 0.05 |
| $\tilde{N}_2$ | 180.8 | 4.7 | 1.2 | 1.2 |
| $\tilde{N}_3$ | 363.1 | | 4 | 4 |
| $\tilde{N}_4$ | 381.9 | 5.1 | 4 | 4 |
| | GeV | | | |

| | SPS1a | LHC | ILC | CLIC |
|---|---|---|---|---|
| $\tilde{e}_1$ | 142.9 | 4.8 | 0.05 | 0.05 |
| $\tilde{e}_2$ | 200.9 | 5 | 0.2 | 0.2 |
| $\tilde{\mu}_1$ | 142.9 | 4.8 | 0.2 | 0.2 |
| $\tilde{\mu}_2$ | 200.8 | 5 | 0.5 | 0.5 |
| $\tilde{\tau}_1$ | 133.2 | 6.5 | 0.3 | 0.3 |
| $\tilde{\tau}_2$ | 205.0 | | 1.1 | 1.1 |
| $\tilde{t}_1$ | 399.6 | | | 2 |
| $\tilde{t}_2$ | 586.0 | | | 2.8 |
| $\tilde{b}_1$ | 516.3 | 14 | | 2.6 |
| $\tilde{b}_2$ | 546.4 | 14 | | 2.7 |
| $\tilde{u}_1$, $\tilde{c}_1$ | 546.1 | 19 | | 5.5 |
| $\tilde{u}_2$, $\tilde{c}_2$ | 562.4 | 17.4 | | 5.5 |
| $\tilde{d}_1$, $\tilde{s}_1$ | 544.8 | 19 | | 5.5 |
| $\tilde{d}_2$, $\tilde{s}_2$ | 567.9 | 17.4 | | 5.5 |
| | GeV | | | |

Table 5.23: Uncertainties on the measurement of the mass of Higgs bosons and sparticles at the LHC, ILC [149] and CLIC. Systematic and statistical error are included for 300 fb$^{-1}$.

backgrounds. In order to improve this uncertainty, a potential similar analysis at CLIC should be performed on at least 1000 events. Assuming an efficiency of the analysis of 10%, $10^4$ gluino events should be produced corresponding to an integrated luminosity of about 4000 fb$^{-1}$. With a luminosity of $6 \times 10^{34}$ cm$^{-2}$s$^{-1}$, approximately 1000 fb$^{-1}$ are expected every year. Hence, after four years of operation, CLIC will improve the statistical precision on the measurement of the gluino mass with respect to the LHC.

### 5.2.4 The MSSM at linear colliders

#### Mass measurements

In order to evaluate the precision on the determination of the parameters of the MSSM at future linear colliders, it is necessary to estimate the uncertainties on the measurement of sparticle masses.
Several studies [149] investigated the measurement of the mass of the particles of the MSSM at the LHC and ILC. Table 5.23 lists the experimental uncertainties on these measurements, including systematic errors and 300 (500) fb$^{-1}$ systematic uncertainties for the LHC (ILC). Essentially, the errors for CLIC are the same as for the ILC but extended to a broader spectrum (squarks and gluinos).

In the Higgs sector, only the mass of the lightest Higgs boson is measured at the LHC. The energy available at the ILC will not be sufficient to produce heavy Higgs bosons with mass of the order of 400 GeV. The lightest Higgs boson can be produced and measured in the Higgsstrahlung channel. At the ILC$_{1000}$ and CLIC, all Higgs bosons

may be produced via Higgsstrahlung, fusion processes or in pairs.

The gluino is reconstructed at the LHC using the $\tilde{g} \to \tilde{b}b \to \tilde{N}_2 bb$ decay. If the four-momentum of the $\tilde{N}_2$ can be reconstructed, the distribution of the invariant mass of the $\tilde{N}_2 bb$ shows a peak at $m_{\tilde{g}}$. As mentioned in section 5.2.3, gluinos are not produced at the ILC but the $\text{ILC}_{1000}$ and CLIC may provide a measurement of the mass, the error on which is estimated to be 6.5 GeV.

It is well known that chargino masses are not measurable at the LHC. At the ILC, the heaviest chargino is too heavy to be produced in pairs. $\tilde{C}_1$ may be produced and would most likely decay into a tau-lepton. Its mass can be measured from the energy spectra of hadronic $\tau$ decays. At $\text{ILC}_{1000}$ and CLIC, both charginos may be produced and their mass measured.

Sleptons are produced in pairs and in the $\tilde{q}_\text{L}$ cascade at the LHC. Two OSSF lepton pairs is the key signature to such events. However, due to the LSP present in the cascade, a direct measurement of the mass is not possible. It was shown that $\tilde{l}_2$ masses ($\ell = e,\ \mu$) can be derived from a study of the so-called stransverse mass variable $M_{T2}$ [149, 159]. $\tilde{l}_1$ masses can be measured using the invariant mass distribution of OSSF lepton pairs arising from $\tilde{N}_2$ decays. The $\tilde{\tau}_1$ mass can be measured similarly but relies on an efficient tagging of $\tau$–leptons. At linear colliders, all sleptons may be produced in pairs and their mass reconstructed using the energy spectra of leptons arising in the cascades or thanks to a threshold scan of the cross-section as a function of $\sqrt{s}$.

$\tilde{q}_1$ are produced in gluino decays and, for the first two generations, decay almost exclusively to the LSP along with a quark. Given $m_{\tilde{N}_1}$, the stransverse mass method allows to measure the mass of $\tilde{q}_1$s for the first two generations. Sbottom masses can be measured in their decay to $\tilde{N}_2 b$, assuming again that the four-momentum of the $\tilde{N}_2$ can be reconstructed. In the case of the SPS1a point, no squark can be produced at a $\sqrt{s} = 500$ GeV linear collider. Top squarks exhibit non-trivial decay patterns. The reconstruction of their mass necessitates high $b$ and $\tau$–tagging efficiencies in addition to assumptions on chargino masses. They are not included for the LHC. At $\text{ILC}_{1000}$ and CLIC, it was shown [149] that the $\tilde{t}_1$ mass can be obtained via the energy spectra of $b$–jets arising in its decay to charginos. A 1% error on the mass was established. This error was scaled to the mass of other squarks for CLIC.

Table 5.23 summarizes the available mass measurement at the LHC, ILC and CLIC.

### mSUGRA determination

In order to have a global view on the sensitivity of the parameters of the model to the different mass measurement, the mSUGRA parameter set is fitted using the `SFitter` program described in section 5.1.8. The starting point of all fits is the SPS1a nominal parameter set. The `MINOS` Minuit package is used to estimate the error on the determination of the parameters.

| | SPS1a | LHC | ILC | $\text{ILC}_{1000}$ | CLIC |
|---|---|---|---|---|---|
| $m_0$ | 100 | 3.9 | 0.16 | 0.2 | 0.2 |
| $m_{1/2}$ | 250 | 0.7 | 0.06 | 0.05 | 0.05 |
| $\tan\beta$ | 10 | 10.4 | 3.11 | 1.3 | 1.3 |
| $A_0$ | $-100$ | 31.6 | 16.6 | 4.8 | 4.4 |
| | GeV | % | | | |

Table 5.24: Result of the fit of the mSUGRA parameter set on the mass measurement available at the LHC, ILC and CLIC. For the ILC, two energy configuration are considered. ILC corresponds to the nominal center-of-mass energy of 500 GeV while $\text{ILC}_{1000}$ corresponds to a potential center-of-mass energy of 1 TeV.

Table 5.24 shows the result of the fits performed on the observables available at the LHC, ILC and CLIC. In the case of the ILC, energies in the center-of-mass of 500 GeV (ILC) and 1 TeV ($\text{ILC}_{1000}$) are considered.

The scalar mass parameter $m_0$ can be determined at the LHC with a precision better than 5% despite large errors on the measurement of squark masses. The squark and slepton sectors are almost completely surveyed, providing good constraints on $m_0$. At the ILC, no squark can be produced. Yet, $m_0$ is determined with a precision better than 0.2% due to the very good accuracy on the measurement on slepton masses. This is confirmed by the $\text{ILC}_{1000}$ and CLIC, for which no improvement is seen on $m_0$. Hence, it is already fully determined by the slepton sector.

The gaugino mass parameter $m_{1/2}$ can be determined at the LHC with a precision better than 1% thanks to the interplay of the measurement of the $\tilde{N}_1$, $\tilde{N}_2$ and $\tilde{N}_4$. The addition of the measurement of the $\tilde{N}_3$ and $\tilde{C}_1$ mass at the ILC and $\tilde{C}_2$ at the $\text{ILC}_{1000}$ pulls the precision on $m_{1/2}$ below 0.1%. No further information on gauginos is provided by CLIC and the precision on $m_{1/2}$ is not improved.

At the LHC, heavy Higgs boson masses cannot be measured. This results in a determination of $\tan\beta$ with a precision larger than 10%. The ILC does not provide a measurement of the mass of heavy Higgs boson either but improves the precision on $m_h$ leading to a 3% precision on $\tan\beta$. $\text{ILC}_{1000}$ and CLIC are able to measure the mass of all Higgs boson, yielding a $\sim 1\%$ determination of $\tan\beta$.

The determination of the trilinear coupling $A_0$ at the LHC suffers from the partial and imprecise measurements in the scalar sector and especially from the absence of stop and stau mass measurements. The ILC does not improve the picture as the whole squark spectrum is absent. The $\text{ILC}_{1000}$ and CLIC provide a determination of $A_0$ better than 5% thanks to a full and somewhat precise coverage of the scalar sector.

At the LHC, $m_0$ and $m_{1/2}$ can be determined within 5%. Due to the absence of measurement in the heavy Higgs sector and to rather large errors on the measurement of squark masses, $\tan\beta$ and $A_0$ cannot be determine. With errors of the order of 0.1%, the ILC improves the determination of $m_0$ and $m_{1/2}$ mostly due to an increase of the

precision on the measurements rather than an increase of the number of measurements. The $\text{ILC}_{1000}$ and CLIC both provide a very good determination of all parameters thanks to a complete survey of the SUSY spectrum. The $\sqrt{s} = 1$ TeV barrier seems to be crucial for the determination of mSUGRA parameters.

### MSSM determination

The mSUGRA models has very few parameters compared to the number of observables available. Even if most of the latter are highly correlated, the fits presented above are over-constrained. If the condition of universality is released, many more parameters have to be included in the fits. With respect to the MSSM, the pMSSM assumes the absence of flavour-changing neutral currents or additional CP–violation reducing the number of parameters from 105 to 24 (see chapter 2). The pMSSM is more realistic phenomenologically and more suitable to include in a fitting procedure.

The parameters of the pMSSM were adjusted using `SFitter` with five different sets of uncertainties. First, the LHC and the $\text{ILC}_{1000}$ error sets are considered. Then a combination of both is included. The combination is realized in [149] using a fit to the many kinematic observables provided by both the LHC and the ILC. Finally, the error set corresponding to CLIC observables are included, with and without the gluino.
Table 5.25 presents the results of the fit of the parameters to the five sets of uncertainties. Absolute and relative errors are quoted.
At the LHC, the number of available observables is smaller than the number of parameters. The least sensitive parameters have to fixed. In the Higgs sector, only the mass of the lightest Higgs boson may be measured. Hence, no sensitivity is expected on the mass of the $A$ Higgs boson $m_A$ and it can be fixed. In the slepton sector, the mass of the heaviest stau $\tilde{\tau}_2$ is not measurable. As $\tilde{\tau}_2$ mostly corresponds to the $\tilde{\tau}_\text{L}$ field, no sensitivity is expected on the corresponding mass $m_{\tilde{\tau}_\text{L}}$ and it can be fixed. In the squark sector, no stop mass is measurable. The parameters corresponding to the stop masses are $m_{\tilde{q}^3_\text{L}}$ and $m_{\tilde{t}_\text{R}}$. The former may be determined by the measurement of sbottom masses whereas no measurement constraint the latter and it can be fixed. The situation is slightly more complex for trilinear couplings $A_{\tilde{f}}$ for which the correlations with the observables is not straightforward. Cross-sections and branching ratios may be necessary to investigate these parameters. Indications presented in [149] are followed and $A_{\tilde{t}}$ and $A_{\tilde{\tau}}$ are fixed.

The nominal value to which these parameters should be fixed is a priory unknown. In order to study the impact of the choice of value, parameters to be fixed are varied within some range, one at a time. For each value, a fit is performed and the deviation of other parameters from their nominal value is investigated. Table 5.26 shows the variation of the value of $\tan\beta$ output by the fit when parameters are varied on a broad range. Each parameter is varied independently by steps of 100 GeV and the maximal variation of $\tan\beta$ is reported. While the fixing $m_{\tilde{\tau}_\text{L}}$, $A_{\tilde{\tau}}$ and $m_A$ to some random values have little impact on the fit, the effect of fixing $m_{\tilde{t}_\text{R}}$ and $A_{\tilde{t}}$ is not negligible.

After fixing some parameters, the pMSSM can be determined at the LHC with precisions ranging from a few to 25%. Despite the absence of charginos, $M_1$, $M_2$ and $\mu$ are

| | SPS1a | LHC | | $\text{ILC}_{1000}$ | | LHC + $\text{ILC}_{1000}$ | | CLIC w/out $\tilde{g}$ | | CLIC w/ $\tilde{g}$ | |
|---|---|---|---|---|---|---|---|---|---|---|---|
| | GeV | GeV | % | GeV | % | GeV | % | GeV | % | GeV | % |
| $M_1$ | 103.1 | 5.1 | 4.9 | 0.2 | 0.2 | 0.1 | 0.1 | 0.2 | 0.2 | 0.2 | 0.2 |
| $M_2$ | 192.9 | 5.5 | 2.8 | 0.9 | 0.5 | 0.3 | 0.2 | 0.9 | 0.5 | 0.9 | 0.5 |
| $M_3$ | 567.9 | 10.0 | 1.8 | fixed | | 147.1 | 25.9 | undet. | | 7.8 | 1.4 |
| $\mu$ | 353.7 | 6.1 | 1.7 | 2.4 | 0.7 | 1.9 | 0.5 | 2.3 | 0.7 | 2.3 | 0.7 |
| $\tan\beta$ | 10.0 | 1.1 | 11.3 | 1.2 | 11.9 | 0.6 | 5.7 | 1.2 | 11.9 | 1.2 | 11.9 |
| $m_A$ | 394.9 | fixed | | 0.9 | 0.2 | 1.5 | 0.4 | 0.9 | 0.2 | 0.9 | 0.2 |
| $m_{\tilde{e}_\text{L}}$ | 194.4 | 4.9 | 2.5 | 0.06 | 0.03 | 0.05 | 0.03 | 0.06 | 0.03 | 0.06 | 0.03 |
| $m_{\tilde{\mu}_\text{L}}$ | | | | 0.2 | 0.1 | 0.2 | 0.1 | 0.2 | 0.1 | 0.2 | 0.1 |
| $m_{\tilde{e}_\text{R}}$ | 135.8 | 5.2 | 3.9 | 0.2 | 0.1 | 0.2 | 0.1 | 0.2 | 0.1 | 0.2 | 0.1 |
| $m_{\tilde{\mu}_\text{R}}$ | | | | | | 0.5 | 0.4 | 0.5 | 0.4 | 0.5 | 0.4 |
| $m_{\tilde{\tau}_\text{L}}$ | 193.6 | fixed | | 2.8 | 1.4 | 2.1 | 1.1 | 2.8 | 1.4 | 2.8 | 1.4 |
| $m_{\tilde{\tau}_\text{R}}$ | 133.4 | 7.2 | 5.4 | 3.6 | 2.7 | 2.6 | 1.9 | 3.6 | 2.7 | 3.6 | 2.7 |
| $m_{\tilde{u}_\text{R}}$ $m_{\tilde{c}_\text{R}}$ | 508.1 | 18.4 | 3.6 | fixed | | 14.6 | 2.9 | 13.2 | 2.6 | 5.8 | 1.1 |
| $m_{\tilde{d}_\text{R}}$ $m_{\tilde{s}_\text{R}}$ | 505.9 | | | | | | | | | | |
| $m_{\tilde{q}^1_\text{L}}$ $m_{\tilde{q}^2_\text{L}}$ | 526.6 | 14.3 | 2.7 | | | 15.7 | 3.0 | 12.8 | 2.4 | 4.2 | 0.8 |
| $m_{\tilde{q}^3_\text{L}}$ | 480.8 | 129.0 | 26.8 | 56.6 | 11.8 | 53.3 | 11.1 | 17.3 | 3.6 | 11.9 | 2.5 |
| $m_{\tilde{t}_\text{R}}$ | 408.3 | fixed | | 8.0 | 2.0 | 23.2 | 5.7 | 15.5 | 3.8 | 11.6 | 2.8 |
| $m_{\tilde{b}_\text{R}}$ | 502.9 | 123.1 | 24.5 | fixed | | 47.2 | 9.4 | 16.6 | 3.3 | 12.1 | 2.4 |
| $A_{\tilde{t}}$ | -490.9 | fixed | | 18.4 | 3.7 | 9.3 | 1.9 | 18.6 | 3.8 | 18.6 | 3.8 |
| $A_{\tilde{b}}$ | -763.4 | undet. | | fixed | | undetermined | | | | | |
| $A_{\tilde{\tau}}$ | -249.4 | fixed | | undet. | | undetermined | | | | | |

Table 5.25: Results of the fit of the pMSSM parameters to five sets of uncertainties. Errors are presented in absolute and relative values.

| | $m_{\tilde{\tau}_\text{L}}$ | $m_{\tilde{t}_\text{R}}$ | $A_{\tilde{\tau}}$ | $A_{\tilde{t}}$ | $m_A$ |
|---|---|---|---|---|---|
| range | [0 : 2000] | [0 : 2000] | [−4000 : 4000] | [−4000 : 4000] | [0 : 2000] |
| $\Delta\tan\beta$ | 1.68 | 5.95 | 0.64 | 2.5 | 0.55 |

Table 5.26: Impact of the fixation of some parameters on the fit.

determined within 5% due to the interplay of the three neutralino masses. The slepton sector as well as the first two generations of squarks are also determined within about 5%. The third generation sector, masses and couplings, are not determined.

At the ILC, no measurement of the gluino mass is expected. $M_3$ is fixed. Similarly, the squark sector is mostly invisible and the parameters corresponding to the first two generations and the sbottom are fixed. The stau trilinear coupling is released but undetermined. $\tan\beta$ is determined thanks to the measurement of heavy Higgs bosons mass but still suffers from a 12% error. With all chargino and neutralino masses measured within one percent, $M_1$ and $M_2$ are very well determined. Also, the slepton sector is fully visible and the associated parameters are determined very precisely. With respect to the LHC, the ILC provides valuable information in the slepton, gaugino and heavy Higgs's sectors. A combination of measurements realized at both experiments allows for a release of fixed parameters, achieving a fairly good determination (within less than 5%) of these sectors. These statements are valid for an energy in the center-of-mass of 1 TeV at the ILC. The determination of $M_3$ in the combination is worth than that for the LHC alone because all parameters are released. CLIC provides valuable information in the squark sectors. The determination of squark masses is better (about 1%) than the combination of LHC and ILC data. In the gaugino and slepton sectors, CLIC is equivalent to the ILC. However, CLIC is important for the determination of $M_3$ thanks to the measurement of the gluino mass demonstrated in section 5.2.3. $A_{\tilde{b}}$ and $A_{\tilde{\tau}}$ are still undetermined and will necessitate measurements such as cross-section or branching fractions to be determinable.

### 5.2.5 Summary

The determination of the MSSM at several colliders was investigated in the constrained cases of the pMSSM and mSUGRA. The SPS1a parameter set yields rather light new particles and constitutes a favourable scenario at the LHC and the ILC. The improvement in the determination of the supersymmetric parameters brought by potential future linear colliders such as the ILC or CLIC with respect to the LHC was studied.

The reach for sparticle mass measurements and associated uncertainties was investigated for the LHC, the ILC with $\sqrt{s} = 500$ GeV and $\sqrt{s} = 1$ TeV and CLIC. In a parameter set such as SPS1a where all squarks and sleptons have their mass between 200 and 570 GeV, the $\sqrt{s} = 1$ TeV barrier seems crucial to achieve an exhaustive survey of the supersymmetric particle spectrum. In order to estimate whether an 600 GeV gluino could be produced, detected and measured in $e^+e^-$ collisions, the leading-order cross-section for its production in association with a quark and a squark was computed. It was found that for $m_{\tilde{g}} = 606.3$ GeV and $\sqrt{s} = 3$ TeV, the gluino production cross-section is of the order of 2.7 fb at leading-order. A measurement of the gluino mass with a better precision than that realized at the LHC was estimated to be attainable for an integrated luminosity of 4000 fb$^{-1}$, corresponding to about four years of operation of CLIC at nominal luminosity.

Mass measurements and uncertainties were input into the `SFitter` program in order

to realize a global fit of the supersymmetric parameters. In the case of the mSUGRA reduced parameter set, it was shown that the gaugino sector ($m_{1/2}$) can already be determined within one percent at the LHC. The squark and slepton sector is determined within 5% at the LHC but may require the ILC to pass the 1% barrier. The determination of $\tan\beta$ at the LHC and the ILC with $\sqrt{s} = 500$ GeV suffers from the invisibility of heavy Higgs masses. In such a case, the 1 TeV barrier is very important.

In the case of the less constrained pMSSM parameter set, some parameters had to be fixed in order to obtain a solvable system. The effect of the choice of fixation value was shown to be non-negligible but limited. Errors of the order of 5% can be achieved at the LHC. The ILC with $\sqrt{s} = 1$ TeV alone provides a weak determination of the scalar sector but the combination of LHC and ILC information yields a precision better than the percent on the determination of the gaugino and slepton sectors and better than 5% on the squark sector. CLIC provides valuable input in the squark and gluino sectors, yielding a percent determination for both. The inclusion of further measurements such as cross-sections or branching fraction is necessary in order to constrain couplings and other parameters to a better level.

# Conclusion

*"Well what starts out as a warm breeze turns into something more*
*Like the lightning that burns down houses or the wind that blows down doors*
*I see it in the distance, it moves much faster than I think*
*Yes this storm will wreak much havoc, bring my sanity to the brink [...]*
*Now the wooden gate is creaking and the windows loudly rattle*
*Yet I still venture towards it like I'm marching into battle*
*I could heed your good advice and stay in comfort back at home*
*But there it is in its splendour and it's chilling me down to the bone [...]*
*The storm is coming, it's gonna make a beautiful sound,*
*I hope it turns your life upside down."*

Ed Harcourt – *The storm is coming*

The LHC is set to start producing proton-proton collisions in 2009. The ATLAS experiment, installed on the LHC, is fully functional and ready to record data. The analysis of produced events will most likely unveil new kinds of physics. If it exists, the particle supposed to account for the mass of the Standard Model fields, the Higgs boson, will be produced and detected at the LHC. In order to stabilize its mass, the Higgs boson should be accompanied by an extension to the SM, including new particles. The most popular extension to the SM is supersymmetry. Again, if supersymmetry is realized in Nature, it will most likely be produced and detected at the LHC.

In this thesis, I presented my contribution to the preparation of the ATLAS experiment. Firstly, I exposed the improvements I brought to the reconstruction and identification of electrons in the ATLAS detector. Electrons are of major importance for many physics studies such as the search for the Higgs boson into its decay into four leptons, for heavy gauge bosons occurring in models with extra-dimensions, for supersymmetry in decay cascades producing many leptons or in the measurement of the $W$ and top quark masses. In addition, the analysis of electrons in standard processes such as $Z, \Upsilon, J/\Psi \rightarrow ee$ decays provide robust constraints on the absolute electromagnetic energy scale. The study of electrons from photon conversions and of the bremsstrahlung activity in the tracking detector constitutes a solid probe of the amount of matter present before the electromagnetic calorimeter.
I showed that an electron identification efficiency of about 70% (for electrons with $p_{\mathrm{T}} > 25$ GeV and in the central region of the detector) was reached for a jet rejection

of $10^5$ (for jets with $p_{\mathrm{T}} > 17$ GeV). This was achieved thanks to the analysis of many identification variables on both signal and background. The correspondence between tracks left by electrons in the tracking detector and electromagnetic showers left by their decay in the calorimeter was fully exploited to reject photons and neutral mesons. Furthermore, converted photons were correctly identified thanks to information from the vertexing layer of the tracking detector. In the latter, the electron identification efficiency was optimized using the ratio of the energy deposit in the calorimeter and the momentum of the track. The fraction of high-threshold hits on electron tracks in the Transition Radiation Tracker was also exploited. In the calorimeter, the isolation of the electrons showers was studied with the $R_{\mathrm{cone}}$ variable in order to optimize the jet rejection.
All improvements were incorporated in the unified `athena` framework in order to be used in various physics analysis. The performance of the identification process was assessed, documented and maintained throughout many successive software releases. The performance was measured and cross-checked using different physics process such as single electrons, supersymmetric events, $Z \rightarrow ee$ decays or $t\bar{t}$ events and confronted to independent studies in order to provide physics groups with robust results.
With collisions expected in the LHC at the end 2009, the improvement and monitoring of reconstruction and identification performances are of major importance. The first few month of collision data will help gather large samples of di-electron resonances ($Z, \Upsilon, J/\Psi \rightarrow ee$), the use of which will help assess the electron identification efficiencies for various kinematic configurations. They will also be very useful to gain knowledge on the absolute electromagnetic energy scale. On the achievement of these tasks will depend the reactivity of physics group to potential signal for the Higgs boson or new physics.

Secondly, I presented my contribution to the preparation for the search for supersymmetry at the LHC.
If the stabilization of the weak scale is abandoned as a motivation for supersymmetry, phenomenological models can be constructed in which new scalar particles (squarks, sleptons and heavy Higgs bosons) are very heavy, beyond the reach of the LHC. In such models, scalars are decoupled from the weak scale, where an effective theory containing the rest of the supersymmetric spectrum is established. A candidate for dark matter is provided in the form of the lightest supersymmetric particle (LSP) and gauge couplings are unified at the high scale. In addition, the absence of sfermions at the weak scale highly suppresses flavour-changing neutral current and additional CP-violation processes usually associated with weak-scale supersymmetric models.
The Decoupled Scalars Supersymmetry (DSS) model is a heavy-scalars model with only five parameters. DSS was studied in two points in parameter space, covering the entire domain of interest at the LHC. In this framework, supersymmetry may be produced at the LHC through gluino or gaugino pairs. They sign in the detector by a large amount of missing transverse energy due to the non-detection of the LSP, many jets with large transverse momenta and leptons in the case of gaugino decays. Thanks to an analysis based on the Monte Carlo generation of signal and background samples and a semi-fast simulation of the ATLAS detector, I showed that both points can be

discovered or excluded at the LHC. I investigated a number of observables that may be measured at the LHC such as the mass splitting between the two lightest neutralinos, the cross-section for the production of gluino pairs and the tri-lepton signal, the ration of on-shell to off-shell $Z$ bosons produced in supersymmetric cascades, etc... The uncertainties on the measurement of these observables was evaluated in order to estimate the precision on the determination of the DSS parameters that may be achieved at the LHC. This task was realized in the framework of the `SFitter` program, in which the DSS model was implemented. I showed that a global fit of the DSS parameters to the observables was able to determine the correct central value of parameters. I also showed that the gaugino sector may be determined within a few percent thanks to the use of leptonic observables. However, the partial visibility of the Higgs sector and the complete invisibility of the scalar sector prevents a determination of their parameters. In order to establish even tighter constraints on DSS models, the inclusion of indirect measurements such as that arising from the $b \to s\gamma$ decay, $g_\mu - 2$, the relic density or other cosmological quantities may be useful.

Finally, I investigated the impact of future linear colliders on the determination of the parameters of the MSSM in the case of the SPS1a parameter set. LHC potential results were compared to input from $e^+e^-$ linear colliders with energies in the center of mass of 500 GeV, 1 TeV (ILC) and 3 TeV. The 1 TeV barrier seems important in the case of the SPS1a where squarks and sleptons have masses in the 200 to 600 GeV range. The cross-section for the production of gluinos in $e^+e^-$ collisions was calculated at leading-order in order to estimate the capacity of a 3 TeV $e^+e^-$ collider to measure its mass. It was shown to be possible within a few years of operation of the collider. After fixing indeterminable parameters, the MSSM may be determined at the LHC with a precision of the order of 5%. In some sectors, the ILC improves this precision by one order of magnitude. The combination of LHC and ILC data allows for a 1% determination of most sectors of the MSSM. If the center-of-mass energy of the ILC is upgraded to 1 TeV, the impact of a 3 TeV $e^+e^-$ collider on the determination of the MSSM resides mostly in the heaviest sectors : scalars and gluinos. Such a collider may be necessary for the measurement of masses above 300 GeV and an exhaustive determination of the MSSM.

# Bibliography


[1] S. L. Glashow. Partial symmetries of weak interactions. *Nucl. Phys.*, 22:579–588, 1961.

[2] A. Salam and J. C. Ward. Electromagnetic and weak interactions. *Phys. Lett.*, 13:168–171, 1964.

[3] S. Weinberg. A model of leptons. *Phys. Rev. Lett.*, 19:1264–1266, 1967.

[4] C.-N. Yang and R. L. Mills. Conservation of isotopic spin and isotopic gauge invariance. *Phys. Rev.*, 96:191–195, 1954.

[5] A. Einstein. On the electrodynamics of moving bodies. *Annalen Phys.*, 17:891–921, 1905.

[6] R. P. Feynman. Space-time approach to non-relativistic quantum mechanics. *Rev. Mod. Phys.*, 20:367–387, 1948.

[7] F. J. Hasert et al. Observation of neutrino-like interactions without muon or electron in the Gargamelle neutrino experiment. *Phys. Lett.*, B46:138–140, 1973.

[8] G. Arnison et al. Experimental observation of isolated large transverse energy electrons with associated missing energy at $\sqrt{s} = 540$ GeV. *Phys. Lett.*, B122:103–116, 1983.

[9] G. Arnison et al. Experimental observation of lepton pairs of invariant mass around 95 GeV/$c^2$ at the CERN SPS collider. *Phys. Lett.*, B126:398–410, 1983.

[10] P. Renton. Global electroweak fits and the Higgs boson mass. *Proceedings of ICHEP 2008, Philadephia*, 2008. `arXiv:0809.4566v1 [hep-ph]`.

[11] The TEVNPH Working Group. Combined CDF and DØ upper limits on Standard Model Higgs boson production with up to 4.2 fb$^{-1}$ of data. *CDF/DØ note*, (FERMILAB-PUB-09-060-E), march 2009.

[12] M. Gell-Mann. A schematic model of baryons and mesons. *Phys. Lett.*, 8:214–215, 1964.

[13] G. Zweig. An SU(3) model for strong interaction symmetry and its breaking; Part I. In *Developments In The Quark Theory Of Hadrons*, volume 1, pages 22–101. Lichtenberg and Rosen, jan 1964.

[14] M. Y. Han and Y. Nambu. Three-triplet model with double SU(3) symmetry. *Phys. Rev.*, 139:B1006–B1010, 1965.

[15] O. W. Greenberg. Spin and unitary spin independence in a paraquark model of baryons and mesons. *Phys. Rev. Lett.*, 13:598–602, 1964.

[16] D. J. Gross and F. Wilczek. Ultraviolet behavior of non-abelian gauge theories. *Phys. Rev. Lett.*, 30:1343–1346, 1973.

[17] H. D. Politzer. Reliable perturbative results for strong interactions? *Phys. Rev. Lett.*, 30:1346–1349, 1973.

[18] D. P. Barber et al. Discovery of Three Jet Events and a Test of Quantum Chromodynamics at PETRA Energies. *Phys. Rev. Lett.*, 43:830, 1979.

[19] S. Abachi et al. Observation of the top quark. *Phys. Rev. Lett.*, 74:2632–2637, 1995. `arXiv:hep-ex/9503003`.

[20] F. Abe et al. Observation of top quark production in $\bar{p}p$ collisions. *Phys. Rev. Lett.*, 74:2626–2631, 1995. `arXiv:hep-ex/9503002`.

[21] P. W. Higgs. Broken symmetries and the masses of gauge bosons. *Phys. Rev. Lett.*, 13:508–509, 1964.

[22] P. W. Higgs. Spontaneous symmetry breakdown without massless bosons. *Phys. Rev.*, 145:1156–1163, 1966.

[23] F. Englert and R. Brout. Broken symmetry and the mass of gauge vector mesons. *Phys. Rev. Lett.*, 13:321–322, 1964.

[24] R. Barate et al. Search for the standard model Higgs boson at LEP. *Phys. Lett.*, B565:61–75, 2003. `arXiv:hep-ex/0306033`.

[25] LEP Electroweak working group. `http://lepewwg.web.cern.ch/LEPEWWG/`.

[26] D. N. Spergel et al. Wilkinson Microwave Anisotropy Probe (WMAP) three year results: Implications for cosmology. *Astrophys. J. Suppl.*, 170:377, 2007. `arXiv:astro-ph/0603449`.

[27] S. Perlmutter et al. Measurements of $\Omega$ and $\Lambda$ from 42 high-redshift supernovae. *Astrophys. J.*, 517:565–586, 1999. `arXiv:astro-ph/9812133`.

[28] A. G. Riess et al. Observational evidence from supernovae for an accelerating Universe and a cosmological constant. *Astron. J.*, 116:1009–1038, 1998. `arXiv:astro-ph/9805201`.

[29] ATLAS Collaboration. The ATLAS Experiment at the CERN Large Hadron Collider. *JINST*, 3:S08003, 2008.

[30] G. 't Hooft. Renormalizable lagrangians for massive Yang–Mills fields. *Nucl. Phys.*, B35:167–188, 1971.

[31] T. Hambye and K. Riesselmann. Matching conditions and Higgs mass upper bounds revisited. *Phys. Rev.*, D55:7255–7262, 1997. `arXiv:hep-ph/9610272`.

[32] B. W. Lee, C. Quigg, and H. B. Thacker. Weak interactions at very high energies: The role of the Higgs boson mass. *Phys. Rev.*, D16:1519, 1977.

[33] J. M. Cornwall, D. N. Levin, and G. Tiktopoulos. Derivation of gauge invariance from high energy unitarity bounds on the $S$–matrix. *Phys. Rev.*, D10:1145, 1974.

[34] N. Cabibbo, L. Maiani, G. Parisi, and R. Petronzio. Bounds on the fermions and Higgs boson masses in Grand Unified Theories. *Nucl. Phys.*, B158:295, 1979.

[35] G. Altarelli and G. Isidori. Lower limit on the Higgs mass in the standard model: An update. *Phys. Lett.*, B337:141–144, 1994.

[36] S. Weinberg. Problems in gauge field theories. Talk presented at XVII Int. Conf. on High Energy Physics, London, Eng., July 3, 1974.

[37] S. Weinberg. Implications of dynamical symmetry breaking. *Phys. Rev.*, D13:974–996, 1976.

[38] E. Gildener and S. Weinberg. Symmetry Breaking and Scalar Bosons. *Phys. Rev.*, D13:3333, 1976.

[39] L. Susskind. Dynamics of spontaneous symmetry breaking in the Weinberg-Salam theory. *Phys. Rev.*, D20:2619–2625, 1979.

[40] A. Djouadi. The anatomy of electro-weak symmetry breaking. II: The Higgs bosons in the minimal supersymmetric model. *Phys. Rept.*, 459:1–241, 2008. `arXiv:hep-ph/0503173`.

[41] V. N. Gribov and L. N. Lipatov. Deep inelastic $ep$ scattering in perturbation theory. *Sov. J. Nucl. Phys.*, 15:438–450, 1972.

[42] G. Altarelli and G. Parisi. Asymptotic freedom in parton language. *Nucl. Phys.*, B126:298, 1977.

[43] Y. L. Dokshitzer. Calculation of the structure functions for deep inelastic scattering and $e^+e^-$ annihilation by perturbation theory in quantum chromodynamics. (In Russian). *Sov. Phys. JETP*, 46:641–653, 1977.

[44] L. N. Lipatov. Reggeization of the vector meson and the vacuum singularity in nonabelian gauge theories. *Sov. J. Nucl. Phys.*, 23:338–345, 1976.

[45] E. A. Kuraev, L. N. Lipatov, and V. S. Fadin. The Pomeranchuk singularity in nonabelian gauge theories. *Sov. Phys. JETP*, 45:199–204, 1977.

[46] I. I. Balitsky and L. N. Lipatov. The Pomeranchuk singularity in quantum chromodynamics. *Sov. J. Nucl. Phys.*, 28:822–829, 1978.

[47] J. Pumplin et al. New generation of parton distributions with uncertainties from global QCD analysis. *JHEP*, 07:012, 2002. `arXiv:hep-ph/021195`.

[48] A. D. Martin, R. G. Roberts, W. J. Stirling, and R. S. Thorne. Physical gluons and high–$E_T$ jets. *Phys. Lett.*, B604:61–68, 2004. `arXiv:hep-ph/0410230`.

[49] H. Goldberg. Constraint on the photino mass from cosmology. *Phys. Rev. Lett.*, 50:1419, 1983.

[50] S. Dimopoulos and H. Georgi. Softly Broken Supersymmetry and SU(5). *Nucl. Phys.*, B193:150, 1981.

[51] S. R. Coleman and J. Mandula. All possible symmetries of the $S$–matrix. *Phys. Rev.*, 159:1251–1256, 1967.

[52] Yu. A. Golfand and E. P. Likhtman. Extension of the algebra of Poincare group generators and violation of $p$ invariance. *JETP Lett.*, 13:323–326, 1971.

[53] J. Wess and B. Zumino. Supergauge transformations in four dimensions. *Nucl. Phys.*, B70:39–50, 1974.

[54] A. Salam and J. A. Strathdee. Supergauge transformations. *Nucl. Phys.*, B76:477–482, 1974.

[55] R. Haag, J. T. Lopuszanski, and M. Sohnius. All possible generators of supersymmetries of the $s$–matrix. *Nucl. Phys.*, B88:257, 1975.

[56] P. Fayet. Supersymmetry and weak, electromagnetic and strong interactions. *Phys. Lett.*, B64:159, 1976.

[57] P. Fayet. Spontaneously broken supersymmetric theories of weak, electromagnetic and strong interactions. *Phys. Lett.*, B69:489, 1977.

[58] S. Coleman. Trouble with relativistic SU(6). *Phys. Rev.*, 138(5B):B1262–B1267, Jun 1965.

[59] S. Weinberg. Comments on relativistic supermultiplet theories. *Phys. Rev.*, 139(3B):B597–B601, Aug 1965.

[60] L. Michel and B. Sakita. Group of invariance of a relativistic supermultiplet theory. *Annales Poincare Phys. Theor.*, A11:167–170, 1965.

[61] S. Weinberg. *The quantum theory of fields. Vol. 3: Supersymmetry.* Cambridge University Press, 2000.

[62] P. C. West. *Introduction to supersymmetry and supergravity.* Singapore, Singapore: World Scientific, 1990.

[63] Y. Okada, M. Yamaguchi, and T. Yanagida. Upper bound of the lightest Higgs boson mass in the minimal supersymmetric standard model. *Prog. Theor. Phys.*, 85:1–6, 1991.

[64] J. R. Ellis, G. Ridolfi, and F. Zwirner. Radiative corrections to the masses of supersymmetric Higgs bosons. *Phys. Lett.*, B257:83–91, 1991.

[65] D. Pierce and A. Papadopoulos. The Complete radiative corrections to the gaugino and Higgsino masses in the minimal supersymmetric model. *Nucl. Phys.*, B430:278–294, 1994. arXiv:hep-ph/9403240.

[66] A. H. Chamseddine, R. L. Arnowitt, and P. Nath. Locally supersymmetric grand unification. *Phys. Rev. Lett.*, 49:970, 1982.

[67] R. Barbieri, S. Ferrara, and C. A. Savoy. Gauge models with spontaneously broken local supersymmetry. *Phys. Lett.*, B119:343, 1982.

[68] L. J. Hall, J. D. Lykken, and S. Weinberg. Supergravity as the messenger of supersymmetry breaking. *Phys. Rev.*, D27:2359–2378, 1983.

[69] Nobuyoshi Ohta. Grand Unified Theory based on local supersymmetry. *Prog. Theor. Phys.*, 70:542, 1983.

[70] M. Drees and S. P. Martin. Implications of SUSY model building. In T. L. Barklow, editor, *Electroweak symmetry breaking and new physics at the TeV scale*, pages 146–215. march 1995. arXiv:hep-ph/9504324.

[71] J. R. Ellis, K. A. Olive, Y. Santoso, and V. C. Spanos. Supersymmetric dark matter in light of WMAP. *Phys. Lett.*, B565:176–182, 2003. arXiv:hep-ph/0303043.

[72] LEPSUSYWG (ALEPH, DELPHI, L3 and OPAL experiments), note LEPSUSYWG/01-03.1 (2001). http://lepsusy.web.cern.ch/lepsusy/.

[73] DØcollaboration. Search for associated production of charginos and neutralinos in the trilepton final state using 2.3 fb$^{-1}$ of data. 2009. arXiv:0901.0646 [hep-ex].

[74] CDF collaboration. Search for gluino-mediated sbottom production in $p\bar{p}$ collisions at $\sqrt(s) = 1.96$ TeV. 2009. arXiv:0903.2618 [hep-ex].

[75] CDF collaboration. Inclusive search for squark and gluino production in $p\bar{p}$ Collisions at $\sqrt{s} = 1.96$ TeV. 2008. arXiv:0811.2512 [hep-ex].

[76] G. W. Bennett et al. Measurement of the Positive Muon Anomalous Magnetic Moment to 0.7 ppm. *Phys. Rev. Lett.*, 89:101804, 2002. arXiv:hep-ex/0208001.

[77] S. Ferrara and E. Remiddi. Absence of the anomalous magnetic moment in a supersymmetric Abelian gauge theory. *Phys. Lett.*, B53:347, 1974.

[78] R. Bernabei et al. First results from DAMA/LIBRA and the combined results with DAMA/NaI. *Eur. Phys. J.*, C56:333–355, 2008. arXiv:0804.2741 [astro-ph].

[79] J. Chang et al. An excess of cosmic ray electrons at energies of 300800 GeV. *Nature*, 456:362–365, 2008.

[80] J. R. Ellis, T. Falk, and K. A. Olive. Neutralino-Stau coannihilation and the cosmological upper limit on the mass of the lightest supersymmetric particle. *Phys. Lett.*, B444:367–372, 1998. arXiv:hep-ph/9810360.

[81] ATLAS Collaboration. Expected performance of the atlas experiment detector, trigger, physics. Technical Report CERN-OPEN-2008-020. ISBN978-92-9083-321-5, CERN, Geneva, Sep 2008. arXiv:0901.0512 [hep-ex].

[82] T. Sjostrand, S. Mrenna, and P. Skands. PYTHIA 6.4 physics and manual. *JHEP*, 05:026, 2006. arXiv:hep-ph/0503175.

[83] G. Corcella et al. HERWIG 6.4 release note. 2001. arXiv:hep-ph/0201201.

[84] T. Gleisberg et al. SHERPA 1.alpha, a proof-of-concept version. *JHEP*, 02:056, 2004. arXiv:hep-ph/0311263.

[85] B. P. Kersevan and E. Richter-Was. The Monte Carlo event generator AcerMC version 1.0 with interfaces to PYTHIA 6.2 and HERWIG 6.3. *Comput. Phys. Commun.*, 149:142–194, 2003. arXiv:hep-ph/0201302.

[86] M. L. Mangano, M. Moretti, F. Piccinini, R. Pittau, and A. D. Polosa. ALPGEN, a generator for hard multiparton processes in hadronic collisions. *JHEP*, 07:001, 2003. arXiv:hep-ph/0206293.

[87] J. Alwall et al. MadGraph/MadEvent v4: The new web generation. *JHEP*, 09:028, 2007. arXiv:0706.2334 [hep-ph].

[88] S. Frixione and B. R. Webber. The MC@NLO 3.3 event generator. 2006. arXiv:hep-ph/0612272.

[89] J. M. Butterworth, J. R. Forshaw, and M. H. Seymour. Multiparton interactions in photoproduction at HERA. *Z. Phys.*, C72:637–646, 1996. arXiv:hep-ph/9601371.

[90] M. R. Whalley, D. Bourilkov, and R. C. Group. The Les Houches Accord PDFs (LHAPDF) and Lhaglue. 2005. arXiv:hep-ph/0408110.

[91] J. Allison et al. Geant4 developments and applications. *IEEE Trans. Nucl. Sci.*, 53:270, 2006.

[92] S. Agostinelli et al. G4–a simulation toolkit. *Nuclear Instruments and Methods in Physics Research Section A: Accelerators, Spectrometers, Detectors and Associated Equipment*, 506(3):250–303, 2003.

[93] M. Cacciari and G. P. Salam. Dispelling the N**3 myth for the k(t) jet-finder. *Phys. Lett.*, B641:57–61, 2006. arXiv:hep-ph/0512210.

[94] *ATLAS computing: Technical Design Report*. Technical Design Report ATLAS. CERN, Geneva, 2005.

[95] Worldwide LHC Computing Grid. `http://lcg.web.cern.ch/LCG/`.

[96] S. Jadach, Z. Was, R. Decker, and J. H. Kuhn. The tau decay library TAUOLA: Version 2.4. *Comput. Phys. Commun.*, 76:361–380, 1993.

[97] E. Barberio and Z. Was. PHOTOS: A Universal Monte Carlo for QED radiative corrections. Version 2.0. *Comput. Phys. Commun.*, 79:291–308, 1994.

[98] E. Bouhova-Thacker and V. Kartvelishvili. Electron bremstrahlung recovery in ATLAS tracking using dynamic noise adjustment. *PoS*, ACAT:046, 2007.

[99] V. Kartvelishvili. Electron bremsstrahlung recovery in ATLAS. *Nucl. Phys. Proc. Suppl.*, 172:208–211, 2007.

[100] W. Lampl, S. Laplace, D. Lelas, P. Loch, H Ma, S. Menke, S. Rajagopalan, D. Rousseau, S. Snyder, and G. Unal. Calorimeter clustering algorithms: description and performance. Technical Report ATL-LARG-PUB-2008-002. ATL-COM-LARG-2008-003, CERN, Geneva, Apr 2008.

[101] ATLAS Collaboration. ATLAS calorimeter performance. CERN-LHCC-96-40.

[102] D Banfi, L Carminati, and L Mandelli. Calibration of the atlas electromagnetic calorimeter using calibration hits. Technical Report ATL-LARG-PUB-2007-012. ATL-COM-LARG-2007-007, CERN, Geneva, Jul 2007.

[103] P. Pralavorio. Pile-up effect on electron reconstruction in $t\bar{t}$ and $z$ events. egamma meeting, november 2007.

[104] N. Arkani-Hamed and S. Dimopoulos. Supersymmetric unification without low energy supersymmetry and signatures for fine-tuning at the LHC. *JHEP*, 06:073, 2005. `arXiv:hep-th/0405159`.

[105] N. Arkani-Hamed, S. Dimopoulos, G. F. Giudice, and A. Romanino. Aspects of split supersymmetry. *Nucl. Phys.*, B709:3–46, 2005. `arXiv:hep-ph/0409232`.

[106] G. F. Giudice and A. Romanino. Split supersymmetry. *Nucl. Phys.*, B699:65–89, 2004. `arXiv:hep-ph/0406088`.

[107] S. Weinberg. Anthropic bound on the cosmological constant. *Phys. Rev. Lett.*, 59:2607, 1987.

[108] R. Dermisek, A. Mafi, and S. Raby. SUSY GUTs under siege: Proton decay. *Phys. Rev.*, D63:035001, 2001. `arXiv:hep-ph/0007213`.

[109] A. Djouadi, J.-L. Kneur, and G. Moultaka. SuSpect: A Fortran code for the supersymmetric and Higgs particle spectrum in the MSSM. *Comput. Phys. Commun.*, 176:426–455, 2007. `arXiv:hep-ph/0211331`.

[110] N. Bernal, A. Djouadi, and P. Slavich. The MSSM with heavy scalars. *JHEP*, 07:016, 2007. arXiv:0705.1496 [hep-ph].

[111] S. Dawson and H. Georgi. Generalized gauge hierarchies. *Phys. Rev. Lett.*, 43:821, 1979.

[112] M. B. Einhorn and D. R. T. Jones. The weak mixing angle and unification mass in supersymmetric SU(5). *Nucl. Phys.*, B196:475, 1982.

[113] W. Kilian, T. Plehn, P. Richardson, and E. Schmidt. Split supersymmetry at colliders. *Eur. Phys. J.*, C39:229–243, 2005. arXiv:hep-ph/0408088.

[114] A. Djouadi and Y. Mambrini. Three-body decays of SUSY particles. *Phys. Lett.*, B493:120–126, 2000. arXiv:hep-ph/0007174.

[115] P. Gambino, G. F. Giudice, and P. Slavich. Gluino decays in split supersymmetry. *Nucl. Phys.*, B726:35–52, 2005. arXiv:hep-ph/0506214.

[116] G. R. Farrar and P. Fayet. Phenomenology of the production, decay, and detection of new hadronic states associated with supersymmetry. *Phys. Lett.*, B76:575–579, 1978.

[117] A. Arvanitaki, C. Davis, P. W. Graham, A. Pierce, and J. G. Wacker. Limits on split supersymmetry from gluino cosmology. *Phys. Rev.*, D72:075011, 2005.

[118] W. Beenakker, R. Hopker, and M. Spira. PROSPINO: A program for the PROduction of Supersymmetric Particles In Next-to-leading Order QCD. 1996. arXiv:hep-ph/9611232.

[119] W. Beenakker et al. The production of charginos/neutralinos and sleptons at hadron colliders. *Phys. Rev. Lett.*, 83:3780–3783, 1999. arXiv:hep-ph/9906298.

[120] W. Beenakker, R. Hopker, M. Spira, and P. M. Zerwas. Squark and gluino production at hadron colliders. *Nucl. Phys.*, B492:51–103, 1997. arXiv:hep-ph/9610490.

[121] M. Muhlleitner, A. Djouadi, and Y. Mambrini. SDECAY: A Fortran code for the decays of the supersymmetric particles in the MSSM. *Comput. Phys. Commun.*, 168:46–70, 2005. arXiv:hep-ph/0311167.

[122] J. M. Campbell and R. K. Ellis. An update on vector boson pair production at hadron colliders. *Phys. Rev.*, D60:113006, 1999. arXiv:hep-ph/9905386.

[123] J. Alwall et al. Comparative study of various algorithms for the merging of parton showers and matrix elements in hadronic collisions. *Eur. Phys. J.*, C53:473–500, 2008. arXiv:0706.2569 [hep-ph].

[124] D. Cavalli, D. Costanzo, S. Dean, M. Dhrssen, S. Hassani, M. Heldmann, K. Jakobs, A. Nairz, A. Phillips, S. Resconi, E. Richter-Was, P. Sherwood, L. Vacavant, I. Vivarelli, J.-B. De Vivie, and I. Wingerter-Seez. Performance of the atlas fast simulation atlfast. Technical Report ATL-PHYS-INT-2007-005. ATL-COM-PHYS-2007-012, CERN, Geneva, Jan 2007.

[125] K. Edmonds, S. Fleischmann, T. Lenz, C. Magass, J. Mechnich, and A. Salzburger. The fast atlas track simulation (fatras). Technical Report ATL-SOFT-PUB-2008-001. ATL-COM-SOFT-2008-002, CERN, Geneva, Mar 2008.

[126] M. Duhrssen. The fast calorimeter simulation fastcalosim. Technical Report ATL-PHYS-INT-2008-043. ATL-COM-PHYS-2008-093, CERN, Geneva, Jul 2008.

[127] D. R. Tovey. Inclusive SUSY searches and measurements at ATLAS. *Eur. Phys. J. direct*, C4:N4, 2002.

[128] R. D. Cousins and V. L. Highland. Incorporating systematic uncertainties into an upper limit. *Nucl. Instrum. Meth.*, A320:331–335, 1992.

[129] J. T. Linnemann. Measures of significance in HEP and astrophysics. 2003. `arXiv:0312059 [physics]`.

[130] S. N. Zhang and D. Ramsden. Statistical data analysis for gamma-ray astronomy. *Exp. Astro.*, 1(3):145–163, may 1990.

[131] M. Spira. HIGLU: A program for the calculation of the total Higgs production cross section at hadron colliders via gluon fusion including QCD corrections. 1995. `arXiv:9510347 [hep-ph]`.

[132] U. De Sanctis, T. Lari, S. Montesano, and C. Troncon. Perspectives for the detection and measurement of Supersymmetry in the focus point region of mSUGRA models with the ATLAS detector at LHC. *Eur. Phys. J.*, C52:743–758, 2007. `arXiv:0704.2515 [hep-ex]`.

[133] ATLAS Collaboration. *ATLAS forward detectors for measurement of elastic scattering and luminosity*. Technical Design Report. CERN, Geneva, 2008.

[134] R. Lafaye, T. Plehn, M. Rauch, and D. Zerwas. Measuring supersymmetry. *Eur. Phys. J.*, C54:617–644, 2008. `arXiv:0709.3985 [hep-ph]`.

[135] P. Skands et al. SUSY Les Houches accord: Interfacing SUSY spectrum calculators, decay packages, and event generators. *JHEP*, 07:036, 2004. `arXiv:hep-ph/0311123`.

[136] B. Allanach et al. SUSY Les Houches Accord 2. *Comp. Phys. Commun.*, 180:8–25, 2009. `arXiv:0801.0045 [hep-ph]`.

[137] B. C. Allanach. SOFTSUSY: A C++ program for calculating supersymmetric spectra. *Comput. Phys. Commun.*, 143:305–331, 2002. `arXiv:hep-ph/0104145`.

[138] H. Baer, F. E. Paige, S. D. Protopopescu, and X. Tata. Simulating supersymmetry with ISAJET 7.0 / ISASUSY 1.0. 1993. arXiv:hep-ph/9305342.

[139] G Ganis. http://ganis.web.cern.ch/ganis/MSMLIB/msmlib.html.

[140] A. Djouadi, M. M. Muhlleitner, and M. Spira. Decays of supersymmetric particles: the program SUSY-HIT (SUspect-SdecaY-Hdecay-InTerface). *Acta Phys. Polon.*, B38:635–644, 2007. arXiv:hep-ph/0609292.

[141] G. Belanger, F. Boudjema, A. Pukhov, and A. Semenov. micrOMEGAs2.0: A program to calculate the relic density of dark matter in a generic model. *Comput. Phys. Commun.*, 176:367–382, 2007. arXiv:hep-ph/0607059.

[142] S. Kreiss. http://www.svenkreiss.com/SLHAio.

[143] A. Hocker, H. Lacker, S. Laplace, and F. Le Diberder. A new approach to a global fit of the CKM matrix. *Eur. Phys. J.*, C21:225–259, 2001. arXiv:hep-ph/0104062.

[144] F. James and M. Roos. Minuit: A system for function minimization and analysis of the parameter errors and correlations. *Comput. Phys. Commun.*, 10:343–367, 1975.

[145] N. Metropolis, A. W. Rosenbluth, M. N. Teller, and E. Teller. Equation of state calculations by fast computing machines. *Journal of Chemical Physics*, 21:1087–1092, 1953.

[146] W. K. Hastings. Monte carlo sampling methods using markov chains and their applications. *Biometrika*, 57(1):97–109, 1970.

[147] L. Evans (ed.) and P. Bryant (ed.). LHC Machine. *JINST*, 3:S08001, 2008.

[148] G. L. Bayatian et al. CMS technical design report, volume II: Physics performance. *J. Phys.*, G34:995–1579, 2007.

[149] LHC/LC Study Group. Physics interplay of the LHC and the ILC. *Phys. Rept.*, 426:47–358, 2006. arXiv:hep-ph/0410364.

[150] B. C. Allanach et al. The Snowmass points and slopes: Benchmarks for SUSY searches. *Eur. Phys. J.*, C25:113–123, 2002. arXiv:hep-ph/0202233.

[151] B. K. Gjelsten, D. J. Miller, and P. Osland. Measurement of SUSY masses via cascade decays for SPS1a. *JHEP*, 12:003, 2004. arXiv:hep-ph/0410303.

[152] J. Brau (ed.) et al. International Linear Collider reference design report. 1: Executive summary. 2: Physics at the ILC. 3: Accelerator. 4: Detectors. 2007. ILC-REPORT-2007-001.

[153] CLIC Study Team. CLIC 2008 parameters. 2008. CERN-OPEN-2008-021.

[154] J. Ellis. The physics prospects for CLIC. 2008. arXiv:0811.1366 [hep-ph].

[155] S. Berge and M. Klasen. Gluino pair production at linear $e^+e^-$ colliders. *Phys. Rev.*, D66:115014, 2002. arXiv:hep-ph/0208212.

[156] A. Datta and A. Djouadi. Associated production of sfermions and gauginos at high- energy $e^+e^-$ colliders. *Eur. Phys. J.*, C25:523–537, 2002. arXiv:hep-ph/0111466.

[157] R. Kleiss, W. James Stirling, and S. D. Ellis. A new Monte Carlo treatment of multiparticle phase space at high-energies. *Comput. Phys. Commun.*, 40:359, 1986.

[158] B. K. Gjelsten, D. J. Miller, and P. Osland. Measurement of the gluino mass via cascade decays for SPS1a. *JHEP*, 06:015, 2005. arXiv:hep-ph/0501033.

[159] C. G. Lester and D. J. Summers. Measuring masses of semi-invisibly decaying particles pair produced at hadron colliders. *Phys. Lett.*, B463:99–103, 1999. arXiv:hep-ph/9906349.